Characterisation of exoplanetary upper atmospheres undergoing hydrodynamic atmospheric escape

---

Manuel Lampón González-Albo

2 February 2021

Universidad de Granada

Programa de doctorado en Física y Ciencias del Espacio

Dissertation for the degree of Doctor of Philosophy

Characterisation of exoplanetary upper atmospheres undergoing hydrodynamic atmospheric escape

Manuel Lampón González-Albo

Supervisor: Manuel López Puertas

2 February 2021

Manuel Lampón González-Albo
Characterisation of exoplanetary upper atmospheres undergoing hydrodynamic atmospheric escape
Dissertation for the degree of Doctor of Philosophy , 2 February 2021

Supervisor:
Manuel López Puertas
Departamento del Sistema Solar
Instituto de Astrofísica de Andalucía - CSIC

Universidad de Granada
Programa de doctorado en Física y Ciencias del Espacio
Escuela Internacional de Posgrado
Avenida de Madrid, 13.
18071, Granada

Instituto de Astrofísica de Andalucía - CSIC
Departamento del Sistema Solar
Glorieta de la Astronomía s/n.
18008, Granada

DECLARATION

El doctorando Manuel Lampón González-Albo y el director de la tesis doctoral Manuel López Puertas

Garantizamos, al firmar esta tesis doctoral, que el trabajo ha sido realizado por el doctorando bajo la dirección del director de la tesis y hasta donde nuestro conocimiento alcanza, en la realización del trabajo, se han respetado los derechos de otros autores a ser citados, cuando se han utilizado sus resultados o publicaciones.

Asimismo, garantizamos que el doctorando ha realizado una estancia de investigación en Alemania por un periodo de 3 meses en los centros "Centre of Astronomy and Astrophysics of the Technische Universitat Berlin", y "Deutsches Zentrum für Luft-und Raumfahrt", en Berlín del 10 de abril al 11 de julio de 2018.

The doctoral candidate Manuel Lampón González-Albo and the thesis supervisor Manuel López Puertas

Guarantee, by signing this doctoral thesis, that the work has been done by the doctoral candidate under the direction of the thesis supervisor and, as far as our knowledge reaches, in the performance of the work, the rights of other authors to be cited (when their results or publications have been used) have been respected.

Likewise, we guarantee that the doctoral candidate did a research stay in Germany of three months in "Centre of Astronomy and Astrophysics of the Technische Universitat Berlin", and "Deutsches Zentrum für Luft- und Raumfahrt", in Berlin from 10 to April to 11 of July of 2018.

Granada, 1 de Febrero de 2021 / *Granada, 1 February 2021*

Director de la tesis/*Thesis supervisor*

LOPEZ PUERTAS MANUEL - 23771249J

Firmado digitalmente por LOPEZ PUERTAS MANUEL - 23771249J
Fecha: 2021.02.01 22:19:45 +01'00'

Manuel López Puertas

Doctorando/*Doctoral candidate*

Firmado por LAMPON GONZALEZ-ALBO MANUEL - 05675612V el día 01/02/2021 con un certificado emitido por AC FNMT Usuarios

Manuel Lampón González-Albo

Abstract

Many planets undergo hydrodynamic atmospheric escape at some stage of their lifetime. During this blow-off stage, these planets could significantly change their atmospheric composition; their bulk planetary mass; their radius-mass relationship; and even they could evolve to a different planetary class. Therefore, this mechanism plays a central role in planetary evolution, formation and diversity. Scarcity of observations of planets currently undergoing hydrodynamic escape prevents a better atmospheric characterisation and limits the knowledge of this mechanism. One of the main gaps in the knowledge of the hydrodynamic escape is the non-confirmation of the three regimes theoretically identified: energy-limited, recombination-limited, and photon-limited, as no observational evidence of these regimes has been reported to date. However, high-resolution measurements of the He I triplet lines at 10830 Å of highly irradiated planets have been recently reported, which provide a new means of studying their atmospheric escape.

The main goal of this thesis is to contribute to the knowledge in planetary science through the study of the upper atmosphere of giant planets undergoing hydrodynamic escape. We aim at 1) to improve the characterisation of the upper atmospheres of a sample of exoplanets currently undergoing hydrodynamic escape: the hot Jupiters HD 209458 b and HD 189733 b, and the warm Neptune GJ 3470 b; 2) to perform a comparative analysis of these exoplanets to better understand this mechanism; and 3) to investigate their hydrodynamic regime.

To fulfil those objectives, we participate in the CARMENES He I survey, a collaboration within the CARMENES Consortium for observing the He I triplet in a sample of exoplanets with the CARMENES high-resolution spectrograph. As part of the Working Group of Atmospheres of the Consortium, we were one of the first groups worldwide in taking those measurements, which opened a new window for studying the atmospheric escape. A series of measurements were taken of several exoplanets including the three planets studied here, HD 209458 b9, HD 189733 b, and GJ 3470 b. In order to analyse this wealth of unique measurements, we developed a 1D hydrodynamic spherically symmetric model for exoplanetary upper atmospheres coupled with a non-local thermodynamic model for the population of the He I triplet state. In addition, we performed high-resolution radiative transfer calculations of synthetic spectra for the He I triplet lines to analyse the measured absorption spectrum and to retrieve information about the atmospheric parameters, as the mass-loss rate,

the thermospheric temperature, the He I triplet density profile, and the degree of ionisation. In order to break the degeneracy in some of those parameters we also used the H density derived from Lyα observations.

Among the most important results we find that the upper atmosphere of HD 189733 b is compact and hot, with a maximum temperature of $12\,400^{+400}_{-300}$ K, with a very low mean molecular mass (H/He=(99.2/0.8)$\pm$0.1), with small gas radial velocities, which is almost fully ionised above 1.1 $R_{\rm P}$, and with a mass-loss rate of $1.07^{+0.08}_{-0.09} \times 10^{11}$ g s^{-1}. In contrast, the upper atmosphere of GJ 3470 b is highly extended and relatively cold, with a maximum temperature of 5100$\pm$900 K, also with a very low mean molecular mass (H/He=$(98.5/1.5)^{+1.0}_{-1.5}$), with large radial outflow velocities, which is not strongly ionised and with a mass-loss rate of $(1.87\pm1.13) \times 10^{11}$ g s^{-1}. HD 209458 b seems an intermediate case between HD 189733 b and GJ 3470 b, as its upper atmosphere is extended, although not as GJ 3470 b, with an intermediate temperature of 7625$\pm$500 K, a mean molecular weight of $\sim$ 98/2, with intermediate gas radial velocities, and a mass-loss rate of $(0.71\pm0.29) \times 10^{11}$ g s^{-1}. Attending to the derived H density profiles we find that while the recombination is the process governing the whole upper atmosphere of HD 189733 b, advection dominates in GJ 3470 b, and both processes are not negligible in HD 209458 b.

In addition to constrain the main atmospheric parameters of these exoplanets we confirm that GJ 3470 b undergoes hydrodynamic escape, and provide the first observational derivation of the H/He ratio of an exoplanet. Moreover, our results suggest that the upper atmospheres of giant planets undergoing hydrodynamic escape tend to have very low mean molecular mass (H/He $\gtrsim$ 97/3). Furthermore, we report observational evidence of the hydrodynamic escape regimes in H/He atmospheres. In particular, we demonstrate that HD 209458 b is in the energy-limited regime, HD 189733 b is in the recombination-limited regime and GJ 3470 b is in the photon-limited regime. Accordingly, we propose these exoplanets as benchmark cases for their respective regimes. We conclude that this work significantly improves the atmospheric characterisation of this sample of exoplanets and enhances our knowledge of the hydrodynamic escape mechanism.

Resumen

Muchos planetas sufren escape atmosférico hidrodinámico en alguna etapa de su vida. Durante esta etapa de gran expansión atmosférica, estos planetas podrían sufrir un gran cambio en su composición atmosférica; en su masa planetaria; en su relación masa-radio; e incluso podrían evolucionar a una clase planetaria diferente. Por lo tanto, este mecanismo juega un papel crucial en la evolución, formación y diversidad planetaria. La falta de observaciones en planetas que actualmente sufren escape hidrodinámico evita que se mejore la caracterización de sus atmósferas, y limita la comprensión de este proceso. Una de las deficiencias principales en el conocimiento del escape hidrodinámico es la falta de confirmación de los tres regímenes hidrodinámicos que han sido identificados de forma teórica: limitado por la energía, limitado por recombinación y limitado por el número de fotones (en inglés, "energy-limited", "recombination-limited", y "photon-limited"), debido a que no se han obtenido pruebas observacionales a fecha de hoy. Sin embargo, medidas de alta resolución de las líneas del He I triplete a 10830 ,Å, en planetas intensamente irradiados por su estrella, han sido tomadas recientemente, lo que proporciona una nueva forma de estudiar su escape atmosférico.

La finalidad de esta tesis consiste en contribuir al conocimiento en ciencias planetarias a través del estudio de la alta atmósfera de planetas gigantes que sufren escape atmosférico hidrodinámico. Nuestros objetivos son 1) mejorar la caracterización de las altas atmósferas de una muestra de exoplanetas que actualmente sufren escape hidrodinámico, compuesta por los exoplanetas tipo Júpiter caliente HD 209458 b, y HD 189733 b, y por el exoplaneta tipo Neptuno caliente GJ 3470 b; 2) realizar un análisis comparativo con los exoplanetas de la muestra para comprender mejor el proceso de escape hidrodinámico; y 3) investigar su régimen hidrodinámico.

Para alcanzar estos objetivos, hemos participado en el proyecto CARMENES He I, una colaboración dentro del Consorcio de CARMENES para observar el He I en una muestra de exoplanetas, mediante el espectrógrafo de alta resolución CARMENES. Como parte del grupo de trabajo dedicado al estudio de atmósferas dentro del consorcio, hemos sido de los primeros a nivel mundial en obtener este tipo de medidas, que han abierto una nueva ventana para el estudio del escape atmosférico. El grupo de trabajo ha llevado a cabo una serie de observaciones entre las que se encuentran los exoplanetas que se estudian en esta tesis, HD 209458 b, HD 189733 b y GJ 3470 b. Para analizar estas observaciones, hemos desarrollado un modelo hidrodinámico

1D con simetría esférica para describir la alta atmósfera de los exoplanetas, y lo hemos acoplado a un modelo termodinámico de desequilibrio para el cálculo de la población del He triplete. Además, hemos realizado un modelo de transferencia radiativa de alta resolución para calcular el espectro sintético de las líneas del He triplete y de esta forma analizar el espectro de absorción medido. De este análisis extraemos información de los parámetros atmosféricos como, la tasa de pérdida de masa, la temperatura de la termosfera, el perfil de densidad del He triplete y su grado de ionización. Para romper la degeneración existente entre algunos de estos parámetros, hemos utilizado las observaciones de la línea Lyα ya observada en estos exoplanetas.

Entre los resultados más importantes que hemos obtenido, encontramos que la alta atmósfera de HD 189733 b es caliente y compacta, con una temperatura máxima de $12\,400^{+400}_{-300}$ K, una masa molecular media de (H/He=(99.2/0.8)$\pm$0.1), que se desplaza con una baja velocidad radial, que está altamente ionizada por encima de 1.1 $R_{\rm P}$, y que sufre una tasa de pérdida de masa de $1.07^{+0.08}_{-0.09} \times 10^{11}$ g s^{-1}. Por el contrario, la alta atmósfera de GJ 3470 b está muy extendida y es relativamente fría, con una temperatura máxima de 5100$\pm$900 K, una masa molecular media de (H/He=(98.5/1.5)$^{+1.0}_{-1.5}$), que se expande con una velocidad radial muy alta, que está moderadamente ionizada y que pierde masa a un ritmo de (1.87$\pm$1.13) $\times 10^{11}$ g s^{-1}. La alta atmósfera de HD 209458 b parece un caso intermedio entre las de HD 189733 b y GJ 3470 b, ya que está moderadamente extendida, tiene una temperatura máxima de 7625$\pm$500 K, una masa molecular media de $\sim$ 98/2, se desplaza con una velocidad radial moderada y sufre una tasa de pérdida de masa de (0.71$\pm$0.29) $\times 10^{11}$ g s^{-1}. Atendiendo a los perfiles de densidad del H, encontramos que mientras la recombinación es el proceso que gobierna toda la atmósfera de HD 189733 b, la advección domina completamente la de GJ 3470 b, no siendo ninguno de estos procesos despreciable en la alta atmósfera de HD 209458 b. A parte de obtener buenas estimaciones de los principales parámetros atmosféricos de estos exoplanetas, hemos podido confirmar que GJ 3470 b sufre escape hidrodinámico. Además, hemos proporcionado la primera estimación observacional de la proporción de H/He en un exoplaneta. Las estimaciones de esta proporción en los tres exoplanetas, sugieren que la alta atmósfera de planetas gigantes que sufren escape hidrodinámico tienden a tener una masa molecular media muy baja (H/He $\gtrsim$ 97/3). Por otro lado, presentamos pruebas observacionales de los diferentes regímenes hidrodinámicos en atmósferas ricas en hidrógeno (del tipo H/He). En concreto, demostramos que HD 209458 b se encuentra en el régimen limitado por la energía, HD 189733 b en el régimen limitado por la recombinación y GJ 3470 b en el limitado por el número de fotones. De acuerdo con estos resultados, proponemos estos exoplanetas como arquetipos para sus respectivos regímenes. Concluimos que este trabajo mejora significativamente la caracterización de la alta atmósfera de los exoplanetas que forman nuestra muestra, al igual que mejora nuestro conocimiento sobre el proceso de escape atmosférico hidrodinámico.

Acknowledgement

La enorme satisfacción que me ha producido la realización de esta tesis doctoral es comparable a la dureza de las dificultades con las que me he encontrado. No habría sido posible, de ninguna forma, haber terminado este proyecto sin el apoyo incondicional de mis padres, de mis hermanos, de mi hermana y de Eva, a quienes tanto debo. Tampoco podría haberlo hecho sin la alegría que me transmiten mis sobrinos y sobrinas.

Dedico este trabajo a mi familia y a mis buenos amigos. Tanto a los que están, como a los que ya nos han dejado y tanto echo de menos.

Esta tesis también me ha brindado la oportunidad de hacer nuevos amigos, mis compañeros de fatigas científicas, con los que he convivido y compartido experiencias que siempre quedarán en mi recuerdo. También he compartido momentos muy agradables con otros muchos compañeros de trabajo que he tenido la suerte de conocer, que de tantos, no tendría espacio para nombrar. Este proyecto también me ha dado la oportunidad de aprender mucho, más de lo que en un principio pensé. Una gran parte de lo aprendido se lo debo a la dedicación, paciencia y sabiduría de mi supervisor, Manuel, excelente científico y mejor persona.

Contents

1 Introduction **1**

1.1 Planetary nature 1

1.2 Hydrodynamic atmospheric escape 4

1.2.1 Thermal escape regimes 4

1.2.2 Hydrodynamic escape regimes 6

1.2.3 Modelling the hydrodynamic escape 7

1.2.4 The role of the hydrodynamic atmospheric escape in planetary evolution 10

1.2.5 Observations of the hydrodynamic escape 13

1.3 Thesis motivation 18

1.3.1 Thesis objectives 19

1.3.2 Thesis outline 19

2 A He I upper atmosphere around the warm Neptune GJ 3470 b **23**

3 Characterisation of the upper atmosphere of HD 209458 b **33**

4 Characterisation of the upper atmospheres of HD 189733 b and GJ 3470 b **49**

5 Observational evidence of hydrodynamic escape regimes **67**

6 Conclusions **77**

6.1 Summary 77

6.2 Conclusion remarks 80

6.3 Future work 81

Bibliography **83**

1 Introduction

1.1 Planetary nature

Since the confirmed detection of the first exoplanets[1] PSR 1257 12 b and PSR 1257 12 c by Wolszczan and Frail (1992), which orbit a pulsar, and the first confirmed detection of an exoplanet orbiting a main-sequence star, the hot Jupiter 51 Pegasi b (Mayor and Queloz, 1995), about 4400 exoplanets have been discovered to date[2] (Schneider et al., 2011:exoplanet.eu catalog)[3].

Bulk planetary and stellar parameters (e.g., planetary and stellar mass and radius, planetary orbital properties and stellar effective temperature and luminosity) reveal a very diverse and exotic population of exoplanets, most of them very different to the planets of the Solar System. Exoplanets have been detected around every type of star, including advanced evolutionary stages (e.g., white dwarfs and pulsars) and binaries; with orbital separations closer to 0.01 AU and beyond 1000 AU (as reference, Mercury is at $\sim$0.39 AU and Neptune at $\sim$30 AU). Also, exoplanets have orbital periods from less than 1 day to more than 1000 years; orbital eccentricities from 0 to larger than 0.9 (the largest in the Solar System is $\sim$0.2 for Mercury); and with distances to the Sun from $\sim$1.3 pc (Proxima Centaury, the closest star to the Sun) to beyond 3000 pc.

Statistical analysis of population shows that planetary systems are ubiquitous, with an estimation of an exoplanet or more per star in the Milky Way on average (Cassan et al., 2012). Derivation of occurrence rates (number of planets per star) depends on the parameters used for the study, as for example the spectral type of host stars or the range of orbital separations of the planetary sample. Nevertheless, these demographic studies provide key insights. Fig. 1.1 shows the occurrence rate of planets around main-sequence FGKM stars with an orbital period lower than 85 days, derived from *Kepler* data by Fressin et al. (2013). They defined different planetary classes as: Earths (0.8–1.25 $R_\oplus$), super-Earths (1.25–2 $R_\oplus$), small Neptunes (2–4 $R_\oplus$), large Neptunes (4–6 $R_\oplus$) and giant planets (6–22 $R_\oplus$). Intermediate size planets, i.e. super-Earths and small-Neptunes, are the most common. Paradoxically,

[1] Planets outside the Solar System, also known as extra-solar planets.
[2] January of 2021.
[3] http://exoplanet.eu/

there are not intermediate size planets in the Solar System. Small planets are also very abundant. In particular, Bryson et al. (2021) estimated an occurrence rate of about 0.16–0.69 rocky planets (0.5–1.5 $R_\oplus$) in the habitable zone (HZ)[4] per Sun-like star (FGK spectral types), which implies that on average four of these planets are within 10 pc from the Sun. Most M dwarf host at least one small or intermediate size planet (0.5–4 $R_\oplus$) and, more specifically, about 0.21–0.43 rocky planets in the HZ per M dwarf star (Hsu et al., 2020). Occurrence rates of hot Jupiters estimates are around ∼0.004–0.016 planets per Sun-like star (Wright et al., 2012; Fressin et al., 2013; Zhou et al., 2019). Giant planets beyond 10–50 AU are rare, and at separations of $\lesssim$ 2.5 AU the occurrence rate increases with host star mass and metallicity (Gaudi et al., 2020).

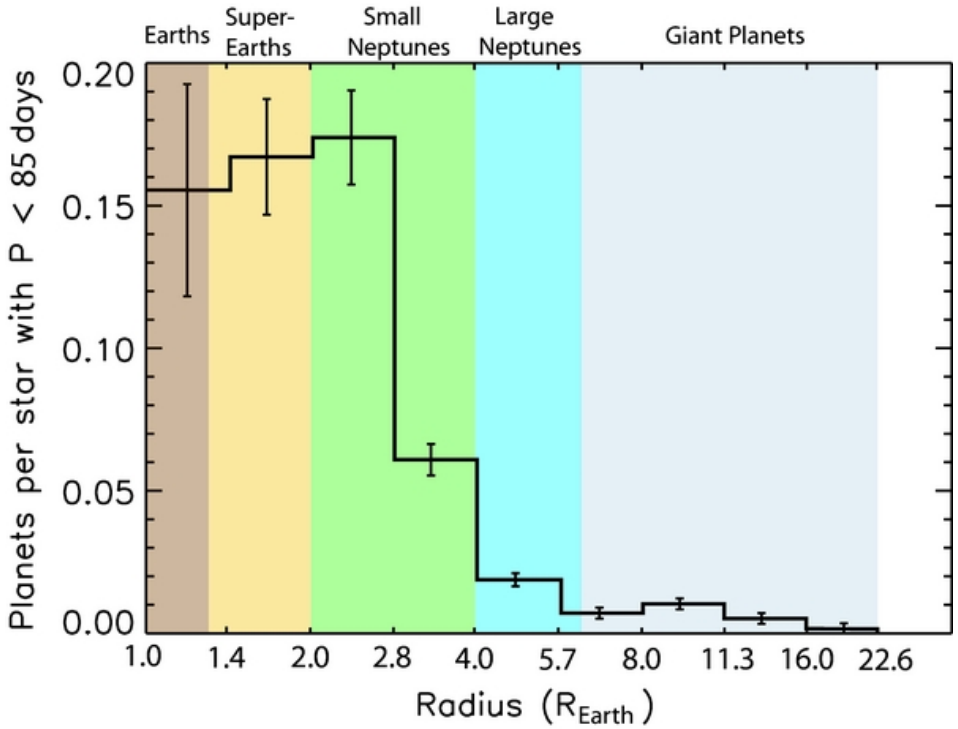

Fig. 1.1 Occurrence rate of planets of different classes with orbital periods lower than 85 days around main-sequence FGKM stars from *Kepler* data. After Fressin et al. (2013).

Besides, demographic studies are biased by the detection methods, and then we have to be cautious with the interpretation of the current census. The main detection methods are radial velocity (RV), primary transit, direct imaging and microlensing. Essentially almost all discoveries from 1995 to 2003 were by means of the RV method. The first exoplanet observed by primary transit was HD 209458 b in 2020 (Henry et al., 2000; Charbonneau et al., 2000) and, currently, due to the NASA Kepler mission, this technique is the most productive so far with ∼ 3100 detections (compared with

[4]Defined as the region around a star in which a rocky-mass/size planet with an Earth-like atmospheric composition (CO_2, H_2O, and N_2) can sustain liquid water on its surface (Bryson et al., 2021). See that reference for more specific definitions of the HZ.

the $\sim$1000 by RV, $\sim$140 by direct imaging and $\sim$130 by microlensing)[5]. Primary transit technique is restricted to relatively small orbital separations (compared with microlensing and direct imaging). Direct imaging detection are limited to gas giants with masses $> 1\ M_{\rm Jup}$ beyond 10 AU around nearby young stars, generally at 15–150 pc from the Sun (Gaudi et al., 2020). Microlensing is sensitive to planets orbiting low-mass and solar-like mass host stars.

With measurements of mass and radius we can derive the density of the planet, which is the first clue about the planet interior composition. Interior structure models predict very different types of planets, for example solid planets without atmosphere, gaseous hydrogen dominated or water worlds. While it is known that giant planets have large hydrogen/helium (H/He) atmospheres, composition of atmospheres of intermediate and low-planets are not obvious. However, derivation of planetary densities from observations and model estimations point that a high number of low-mass planets have large H/He atmospheres (see, e.g., Owen et al., 2020).

The detection of the first exoplanetary atmosphere (Charbonneau et al., 2002) was another breaking point in planetary science history. By primary transit spectrophotometry with the *Hubble Space Telescope* (HST) Charbonneau et al. (2002) observed the Na I absorption line in the atmosphere of HD 209458 b (although this has been recently call into question, see Casasayas-Barris et al. (2020)). Since then, several techniques have been developed for observing exoplanetary atmospheres. Among those we have the transmission spectroscopy in the primary transit, which provides absorption spectra from the day-night terminator of the planet; and emission spectroscopy, in the secondary transit, which provides emission spectra from the day-side of the planet. The most interesting technique for this work is the transmission spectroscopy, as it is the method used for observing escaping atmospheres. Then, we only will briefly explain some basic foundations about the transmission spectroscopy (see, e.g., Madhusudhan (2019) for a detailed review of the atmospheric observational methods).

As the planet passes in front of the star (as seen from the observer, see sketch in Fig. 1.2), a fraction of the stellar photons goes through the atmosphere of the planet, some of them being absorbed by the species populating the atmosphere. Therefore, the transmission spectrum of the planetary atmosphere can be derived by measuring the spectrum in transit and dividing it by the spectrum of the star (measured out of the planetary transit). As the starlight decreases by the planet-to-star area ratio, photons absorbed by the atmosphere increase the area of the planet (see blue ring in Fig. 1.1) at the corresponding wavelengths (i.e. the absorption radius of the

[5]Analysed from the exoplanet.eu catalog data in January 2021.

planet $R_{\rm abs}$). Therefore, the absorption depth, δ, of an absorption line of a species can be defined as

$$\delta = \left(\frac{R_{\rm abs}}{R_\star}\right)^2, \tag{1.1}$$

where $R_\star$ is the radius of the star. Besides, if the radius of the star is known, it is possible to derive the planetary radius for the corresponding wavelength.

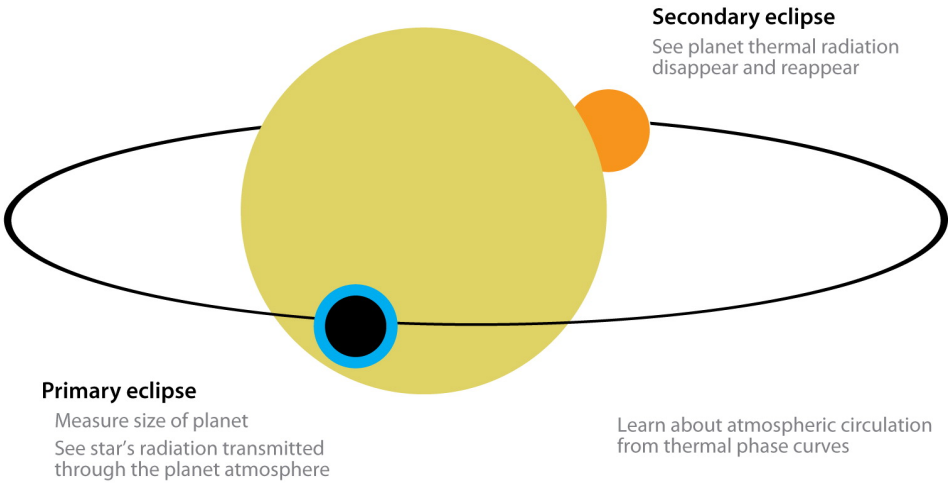

Fig. 1.2 Sketch of the primary and secondary planetary transits by Seager and Deming (2010).

1.2 Hydrodynamic atmospheric escape

Planetary atmospheric escape is produced by thermal and non-thermal processes. Thermal escape processes are linked to the local temperature of the atmosphere, and we can find two different mechanisms, the Jeans escape and the hydrodynamic escape. Non-thermal escape processes are produced by other mechanisms as, for example, ion pick-up by the stellar wind, ion-neutral atoms collisions or photochemical escape. Our study focuses on the most effective atmospheric mechanism of mass-loss, the hydrodynamic escape; hence we do not review here the non-thermal escape (see, e.g., Pierrehumbert (2010) for a complete review) and describe the Jeans mechanism only very briefly.

1.2.1 Thermal escape regimes

Upper atmospheres in hydrostatic equilibrium are composed by a collisional region located in the lower part, the thermosphere, and a non-collisional region[6] at the upper part, the exosphere. In the transition region from the thermosphere to the

[6]The region where collisions between molecules are infrequent, that is, where the Knudsen number, K_n, defined as the ratio between the mean free path of molecules/atoms/ions and the scale height, is larger than 1.

exosphere (the exobase)[7], the local velocity distribution of particles follows the Maxwellian distribution. Those particles in the high tail of the distribution with radial velocities greater than the escape velocity of the planet escape from the atmosphere. This is the Jeans escape mechanism (Jeans, 1905), and this scenario is called the Jeans regime. The escape flux (number of escaping particles per unit area per unit time), Φ_{Jeans}, can be estimated approximating that particles escape from the exobase, which is also assumed that is located at a single altitude (Öpik and Singer, 1961; Chamberlain, 1963; Johnson et al., 2009),

$$\Phi_{Jeans} = \frac{n_{\text{exo}}\, v_0}{2\sqrt{\pi}} \left(\frac{v_{\text{esc}}^2}{v_0^2} + 1 \right) \exp\left(-\frac{v_{\text{esc}}^2}{v_0^2} \right), \tag{1.2}$$

where n_{exo} is the exobase number density; $v_0 = \sqrt{2\,k\,T/m}$ is the most probable velocity of the distribution, k the Boltzmann constant, m the mass of the particle and T the local kinetic temperature; v_{esc} is the escape velocity of the planet, given by $v_{esc} = \sqrt{2\,G\,M_{\text{P}}/r}$ with G being the gravitational constant, M_{P} the mass of the planet and r the distance from the centre of the planet.

A planetary upper atmosphere is in hydrodynamic escape (also known as blow-off escape)[8] when the gas, heated via photo-ionisation, has a pressure gradient that overcomes the gravity of the planet. Therefore, the stellar irradiation, mainly X-ray and extreme ultraviolet (XUV) radiation, as well as the near-ultraviolet (NUV) radiation in exoplanets orbiting hot stars (García Muñoz and Schneider, 2019), triggers hydrodynamic atmospheric escape generating a strong wind that expands substantially the thermosphere and ejects the gas beyond the Roche lobe. The bulk velocity of the outflow is accelerated from subsonic to supersonic velocity (i.e., so-called transonic outflow). This scenario is known as hydrodynamic regime. The escape flux of this mechanism, Φ_{HD}, can be expressed as:

$$\Phi_{\text{HD}} = \rho(r)\, \text{v}(r)/\mu, \tag{1.3}$$

where $\rho(r)$ and μ are the density and the mean molecular mass of the gas respectively; and v(r) is the bulk radial velocity of the flow.

Transition between the hydrostatic Jeans escape and the hydrodynamic escape is not well understood yet. This transition regime, known as the slow hydrodynamic thermal regime (e.g., Volkov, 2016; Zhang, 2020)[9], describes an outgoing flux with an intermediate gas bulk velocity, lower than the bulk velocity of the hydrodynamic escape but higher than the zero bulk velocity of the Jeans escape. As a consequence,

[7] Usually defined as the region where $K_n \sim 1$.
[8] We will use both names indistinctly.
[9] There are several different terminologies of thermal regimes. For example, slow hydrodynamic escape regime is also known as the controlled hydrodynamic escape. In this work, we follow the terminology of Johnson et al. (2009).

the upper atmosphere expands and the velocity at the exobase can be described by a shifted Maxwellian distribution (e.g., Tian, 2015). We will refer to this mechanism as the enhanced Jeans escape.

A raw estimation about which thermal regime governs the upper atmosphere of a planet, can be done with the so-called exobase Jeans parameter (or simply the Jeans parameter), λ,

$$\lambda = \frac{G\, M_{\rm P}\, \mu}{k\, T_{\rm exo}\, r_{\rm exo}}, \tag{1.4}$$

where $r_{\rm exo}$ is the distance from the centre of the planet to the exobase, and $T_{\rm exo}$ is the temperature at the exobase. Jeans parameter is the ratio of the gravitational energy to the thermal energy of a particle at the exobase. λ is $\gtrsim 10$ in hydrostatic equilibrium (stable) atmospheres, so that the escape is produced by Jeans escape (e.g., Zhang, 2020). In contrast, λ is $\lesssim 2$ in non-hydrostatic equilibrium (unstable) atmospheres, so that the escape is hydrodynamic. The transition regime is roughly estimated as the very narrow range of $\lambda \sim$2–10 (see, e.g., Johnson et al., 2009; Volkov, 2016). As a reference, the exobase Jeans parameters of current Venus, Earth, Mars, and Jupiter atmospheres are $\lambda \sim 350$, 130, 200, and 430, respectively (Johnson et al., 2009).

1.2.2 Hydrodynamic escape regimes

The atmospheric mass-loss of hot Jupiters have been intensively studied in recent years. In that line, Murray-Clay et al. (2009) have studied how the atmospheric mass-loss of a prototype hot Jupiter varies according to the incident ultra-violet (UV) flux. Their results show that, under high levels of irradiation, the mass-loss rate is not limited by the radiative energy absorbed in the atmosphere, but by the radiation-recombination processes that occur in the atmosphere. In the cases where the mass-loss rate is limited by the energy deposition of the absorbed radiation, it scales linearly with the incident UV flux. This happens because that energy is efficiently spent in the work required to expel the gas. However, if the mass-loss rate is limited by the radiation-recombination processes, it is then approximately given by the square root of the incident UV flux. In this case, a large fraction of the absorbed energy is lost by radiative cooling and hence it is not available for lifting the gas.

Owen and Alvarez (2016) found theoretically that the mass-loss rate of moderately irradiated low gravity planets can be limited by the incoming flux that ionises the gas. In these cases, the mass-loss rate scales to the square of the effective absorption radius of the planet, that is, the radius where the incoming flux is near completely absorbed. Hence, all those theoretical studies suggest that planets with hydrogen-dominated

atmospheres and undergoing hydrodynamical escape might be under three very distinct atmospheric escape regimes: energy-limited, recombination-limited[10], and photon-limited.

We should note that this classification of the hydrodynamic atmospheric escape regimes is important not only for a better understanding the different mass-loss rates processes of the planetary atmospheres, but it is also very useful for estimating accurately the planetary mass-loss rate when using the very common energy-limited approximation (see, e.g., Murray-Clay et al., 2009; Bear and Soker, 2011; Owen and Alvarez, 2016; Salz et al., 2015; Wang and Dai, 2018; Lampón et al., 2021a). This approximation, when used jointly with an estimated heating efficiency[11] in the range of 10–20% (the most probable range in hydrogen-dominated atmospheres, Shematovich et al., 2014), largely overestimates the mass-loss rate of planets that are in the recombination-limited regime. It might also lead to significantly inaccurate results when applied to atmospheres in the photon-limited regime. The reason is that the effective absorption radius could be very different from the actual planetary radius. Therefore, the accuracy of the application of this approach very much depends on the hydrodynamic escape regime of the planet in question.

1.2.3 Modelling the hydrodynamic escape

By definition, hydrodynamic escape occurs only in the collisional regions, where the gas behaves as a fluid , and hence, it is naturally described by the hydrodynamical equations. In this section, we focus on 1D spherically symmetric models, as this is the approach we used in this work. We will explain the 1D hydrodynamical equations and then we will discuss the comparison with 3D models.

The hydrodynamical equations for a multi-component gas composed for s species and assuming a spherical symmetry are (e.g., Koskinen et al., 2013),

$$\frac{d\rho_s}{dt} + \frac{1}{r^2}\frac{d}{dr}(r^2\,\rho_s\,\mathrm{v}) + \frac{1}{r^2}\frac{d}{dr}(r^2\,F_s) = \sum_s P_s + \sum_s L_s, \tag{1.5}$$

$$\frac{d\,(\rho_s \mathrm{v})}{dt} + \frac{1}{r^2}\frac{d}{dr}(r^2\,\rho_s\,\mathrm{v}^2) = -\rho\,g - \frac{dp}{dr} + f_\mu, \tag{1.6}$$

$$\begin{aligned}&\frac{d\,(\rho_s E)}{dt} + \frac{1}{r^2}\frac{d}{dr}(r^2\,\rho_s\,E\,\mathrm{v}) \\ &= \rho\,Q_R - p\,\frac{1}{r^2}\frac{d}{dr}(r^2\,\mathrm{v}) + \frac{1}{r^2}\frac{d}{dr}\left(r^2\kappa\frac{dT}{dr}\right) + \Phi_\mu\end{aligned} \tag{1.7}$$

[10] Also known as radiation/recombination limited.
[11] Defined in Chapter 3, Sec. 2.2.

where r is the distance from the centre of the planet; t is the time; ρ and v are the mass density and bulk radial velocity of the gas, respectively; $g = G\,M_P/r^2$; G is the gravitational constant, and M_P is the planetary mass; p is the gas pressure; ρ_s is the mass density for the species s, and $\rho = \sum_s \rho_s$ is the total density of the gas; F_s is the species diffusive flux; P_s and L_s are species production and losses terms; f_μ is the viscosity term; E is the specific internal energy of the gas; Q_R is the specific net radiative heating; κ is the coefficient of heat conduction; and Φ_μ is the viscous dissipation functional.

Equation (1.5) is the species continuity equation for each species, Eqs. (1.6) and (1.7) are the momentum and the energy continuity equations for the gas as a whole respectively. Under this approach, the momentum equation contains only forces induced by the planet's gravity and the gas pressure, neglecting other forces like the stellar gravitational pull. When we sum all the species continuity equations, we obtain the mass continuity equation of the gas as a whole,

$$\frac{d\rho}{dt} + \frac{1}{r^2}\frac{d}{dr}(r^2\,\rho\,\mathrm{v}) = 0. \tag{1.8}$$

as the sum over all the species production and losses, and the sum over all species diffusive fluxes, are zero, that is $\sum_s (P_s + L_s) = 0$ and $\sum_s F_s = 0$. In stationary state, we can reduce the continuity equations to

$$\frac{d\,[r^2\,\rho(r)\,\mathrm{v}(r)]}{dr} = 0, \tag{1.9}$$

$$\frac{1}{r^2}\frac{d}{dr}(r^2\,\rho\,\mathrm{v}^2) = -\rho\,g - \frac{dp}{dr} + f_\mu, \tag{1.10}$$

$$\frac{1}{r^2}\frac{d}{dr}(r^2\,\rho_s\,E\,\mathrm{v}) = \rho\,Q_R - \,p\,\frac{1}{r^2}\frac{d}{dr}(r^2\,\mathrm{v}) + \frac{1}{r^2}\frac{d}{dr}\left(r^2\kappa\frac{dT}{dr}\right) + \Phi_\mu. \tag{1.11}$$

Now, by deriving the LHS of the momentum continuity equation, Eq. (1.10), using Eq. (1.9), and rearranging we obtain.

$$\mathrm{v}\,\frac{d\mathrm{v}}{dr} = -g - \frac{1}{\rho}\,\frac{dp}{dr} + \frac{1}{\rho}\,f_\mu. \tag{1.12}$$

If we assume an inviscid gas (i.e. the viscosity is equal to zero),

$$\mathrm{v}\,\frac{d\mathrm{v}}{dr} + \,\frac{1}{\rho}\,\frac{dp}{dr} + \frac{G\,M_P}{r^2} = 0, \tag{1.13}$$

$$\frac{1}{r^2}\frac{d}{dr}(r^2\,\rho_s\,E\,\mathrm{v}) = \rho\,Q_R - \,p\,\frac{1}{r^2}\frac{d}{dr}(r^2\,\mathrm{v}). \tag{1.14}$$

As explained above we already took into account several assumptions for obtaining this form of the 1D hydrodynamical equations. However, they are still complex to solve. For this reason, more simplifications have to be done. The most simple approach is the so-called energy-limited approach, which assumes some important approximations in the energy equation (see Sec.4.2. of Chapter 3 where we describe this approach). Although the energy-limited approach can give us a good estimation of the mass-loss rate when the required input parameters have appropriate values, we need additional approaches in order to characterise the upper atmospheres undergoing hydrodynamic escape. The majority of the hydrodynamic models developed to date are 1D spherically symmetric models and solve the hydrodynamic equations by using other more complex approaches (see, e.g., Watson et al., 1981; Lammer et al., 2003; Yelle, 2004; Tian et al., 2005; García Muñoz, 2007; Murray-Clay et al., 2009; Owen and Alvarez, 2016; Salz et al., 2016).

Further to those difficulties, the upper atmospheres can comprise not only the region of hydrodynamic escape, fully collisional, but also some regions where the atmosphere becomes no-collisional and the hydrodynamic equations do not fully apply. In this region, gas particles behave as bullets, not as a fluid. This case especially applies to the slow-hydrodynamic escape and Jeans regimes (see Sect. 1.2.1). Some authors use a hydrostatic model for the thermosphere, and a particle (ballistic) model for the exosphere and the unbound region (beyond the Roche lobe), simulating an enhanced Jeans escape (e.g. Bourrier and Lecavelier des Etangs, 2013). Monte Carlo simulations can describe auto-consistently all thermal regimes, as they can represent the fluid and the ballistic behaviour of the gas (Johnson et al., 2009; Volkov, 2016). These models are specially suitable for simulating the slow-hydrodynamic escape regime. However, this treatment is computationally very expensive even for a 1D approach. A simplification of these kinds of models is to compute only the region of slow-hydrodynamic regime, or the exobase, and to use other models for describing the thermosphere and the exosphere. As shown in the next chapters, all our studied exoplanets are in the hydrodynamic regime and our results show that their no-collisional region is well beyond the Roche lobe. Hence, we do not need to resort to these kinds of models in this work.

Some hydrodynamic 3D models have been recently developed for modelling hydrodynamic escape (see e.g., Tripathi et al., 2015; Shaikhislamov et al., 2020). These models can simulate the gas not only in the upper atmosphere of an exoplanet undergoing hydrodynamic escape but also beyond the Roche lobe (if the gas continues being collisional). Nevertheless, multidimensional models also have to assume simplifications in order to reduce their computational cost and, even though, they still remain computationally too expensive for being used in parameter space studies.

Deriving constraints for the parameters of the evaporating atmospheres from absorption spectra observations requires an exploration of the space parameters. As reference, in this work, for a three parameters study (mass-loss rate, temperature, and H/He composition), we needed to run several grids with more than 2000 simulations for every planet. Hence, we run more than 35 000 simulations (excluding the many tests performed).

The main concerns about the use of 1D hydrodynamic spherically symmetric models are the simulation of the outflow geometrical deviations (by e.g. Coriolis force and stellar tidal force) at distances near or beyond the Roche lobe, and the asymmetric irradiance of the planet which could generate for example day-to-night temperature gradients. Owen et al. (2020) analysed these differences by comparing the comprehensive 3D hydrodynamic model of Shaikhislamov et al. (2020) with the 1D model of Parke Loyd et al. (2017), and found that the main parameters can be accurately simulated by 1D models. As they argue, this is because the day side heating by stellar XUV is efficiently redistributed over the whole atmosphere, and because the maximum heating rate is located at lower altitudes. This result agrees with previous analysis that compare 3D and 1D models (Murray-Clay et al., 2009; Stone and Proga, 2009; Tripathi et al., 2015; Salz et al., 2016). Since our study is essentially focused in the upper atmosphere (i.e. below the Roche lobe), the main region where the He triplet absorption takes place, we do not need to accurately model the unbound gas, neither its possible interactions with the stellar wind, the interaction with ENAs[12] or with the radiation pressure.

As our aim is to retrieve information from observed He(2^3S) absorption spectra, which takes place mainly in the upper atmosphere under the hydrodynamic regime, and as we need to compute tens of thousand of simulations, our best solution is a 1D hydrodynamical symmetric model able to solve the hydrodynamic equations very efficiently. In Chapter 3, Sec. 3, we describe the model and the approach for improving its computational efficiency.

1.2.4 The role of the hydrodynamic atmospheric escape in planetary evolution

Hydrodynamic atmospheric escape has a high impact on the evolution of planets that undergo this process at some stage in their history (the so-called blow-off stage). Many planets suffer a blow-off stage during their lifetime. As bulk parameters of planets and their host stars depend on age, planets could experience different thermal escape regimes during their lifetimes (see Sec. 1.2.1). Young planets are usually very

[12]Energetic neutral atoms.

extended, which lead to a higher absorption of the XUV stellar radiation and thus favouring the hydrodynamic regime. Subsequent cooling in their evolution stages produces a contraction of the atmosphere which does not favour the hydrodynamic regime. On the other hand, young stars emit more high-energy radiation, especially during their saturation phase[13], which also favours the hydrodynamic regime (see e.g., Jackson et al., 2012). In addition, large mass-loss rates could also reduce the size of the planet with time, which does not favour the continuity of the hydrodynamic regime. In conclusion, hydrodynamic escape is more probable and with larger mass-loss rates in the first Gyr of the lifetime of the planet, specially in the first 100–200 Myr, during the saturation phase of the host star (see e.g., Jackson et al., 2012).

The change of the thermal escape regime with time has also important consequences. For example, planets with late migration, which occurs at $\gtrsim$100 Myr are less exposed to high irradiation from their young host stars and then could experience a shorter blow-off stage. Hence, the relation of hydrodynamic escape with migration could provide hints about the different migration mechanisms and on the epoch at which migration occurs (Jackson et al., 2012). Another illustrative example is the case of hydrogen-rich super-Earths orbiting a solar-like star in the HZ, which are in hydrodynamic regime due to the strong XUV stellar fluxes, which are several tens higher than the ones of the current Sun. That is actually the case of early evolution of Solar-like stars. However, hydrogen-rich Earth-like planets in the same scenario, are in hydrodynamic regime only for XUV fluxes ten times higher than the Solar one. Therefore, as the stellar XUV flux decreases with time, super-Earths would have a shorter blow-off stage than Earth-like planets and, consequently, a larger stage in the slow-hydrodynamic regime.

Hydrodynamic escape is the most efficient atmospheric mechanism of planetary mass-loss. This process can lead to a loss from a small fraction of the original atmosphere to its complete removal (see e.g., Baraffe et al., 2004; Baraffe et al., 2005; García Muñoz and Schneider, 2019). In consequence it can be very important in shaping the current planetary population. The most relevant consequences about the influence of hydrodynamic escape on planetary demography are the formation of the so-called evaporation desert, a remarkably lack of large low-mass planets ($\lesssim$20 $M_\oplus$) in very short orbital separations, and the so-called evaporation valley, an empty band starting about $2R_\oplus$ at 0.03 AU and declining up to $\sim$0.1 AU (Owen, 2019).

Figure 1.3 shows the radius-separation distribution resulting from a simulation of an exoplanetary population with core masses ranging from $15M_\oplus$ to $6.5M_\oplus$, initial total masses $<20M_\oplus$ and hydrogen/helium atmospheres that evolved up to 10 Gyr (Owen and Wu, 2013; Owen, 2019). This simulation predicts clearly the evaporation

[13] Period of the star in which the X-ray luminosity is higher. The X-ray luminosity is roughly constant with time until about 100 Myr, when it starts decreasing.

desert, where only exoplanets with higher core masses can retain a part of their atmospheres, and that the closer to their host star, the lower the atmospheric fraction is retained. The evaporation valley is algo noticeably predicted. Planets below the empty band have lost their atmospheres (i.e., they evolved to solid cores). See Owen and Wu (2013) and Lopez and Fortney (2013) for more details about these simulations.

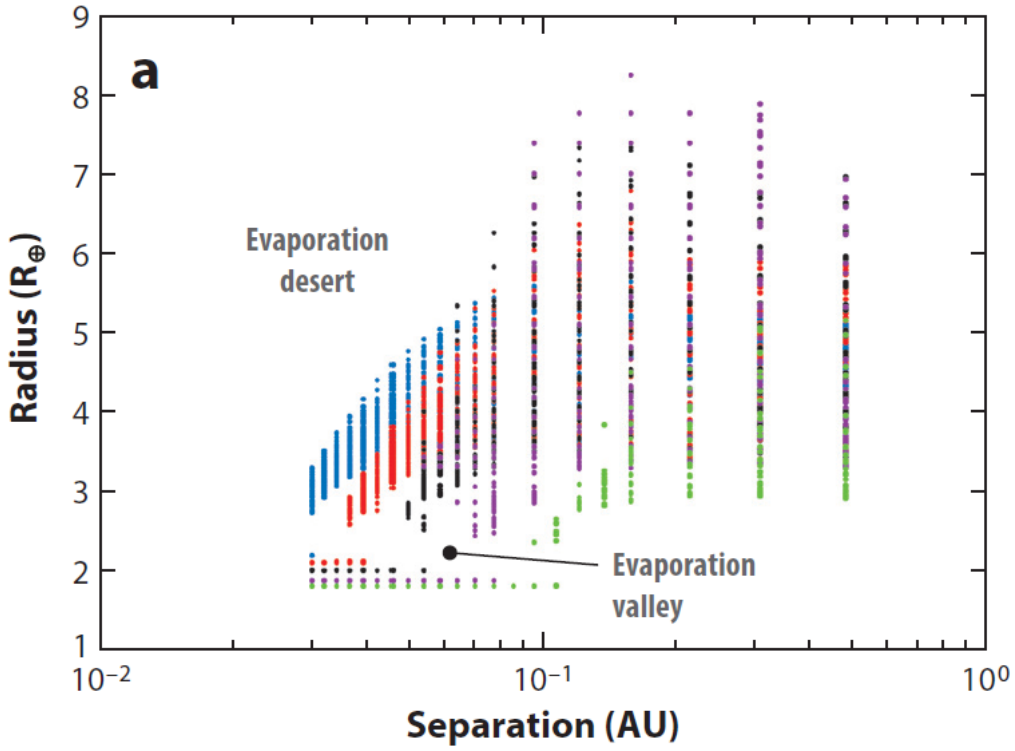

Fig. 1.3 Radius–separation distribution resulting from a simulation of an exoplanetary population undergoing hydrodynamic escape. Core masses are ranging from $15M_\oplus$ (blue dots) to $6.5M_\oplus$ (green dots). Red points have intermediate core masses. After Owen (2019) and adapted from Owen and Wu (2013).

Analogously to the evaporation desert, we have the Neptune desert[14], a significant lack of planets with a mass range of $\sim$20–200$M_\oplus$ in orbital periods of $\sim$3 days (Szabó and Kiss, 2011; Mazeh et al., 2016; Owen, 2019). Although the process(es) leading to the formation of the upper limit of the Neptune desert is not clear (Owen, 2019), the hydrodynamic escape can at least explain the formation of the lower boundary (Owen and Lai, 2018).

As discussed above, migration of planets to closer separations of their host star favour the hydrodynamic escape, as its atmospheres receive more stellar irradiation. Recent studies have pointed out that the opposite is also possible, i.e. hydrodynamic escape can favour the migration (Kurbatov et al., 2020; Kurbatov and Bisikalo, 2021). These authors argue that the ejected gas from the planet by hydrodynamic escape can form

[14]Also known as the sub-Jovian desert.

a torus around the star. This gaseous torus could interchange angular momentum with the planet inducing its migration towards the star. As a reference, these authors found that the migration of a HD 209458 b-like planet took about 4.5 Gyr to migrate from an orbit at $\gtrsim$ 0.67 AU to its current orbit at 0.045 AU.

Hydrodynamic escape might also significantly change the metallicity of the atmosphere via mass fractionation (e.g. Zahnle and Kasting, 1986; Hunten et al., 1987), generating critical changes in their composition and in the planetary mass-radius relationship (e.g. Catling et al., 2001; Hu et al., 2015; Malsky and Rogers, 2020). Besides, hydrodynamic escape can also be relevant for affecting the interior composition structure of the planets. Although by considering only the planetary mass and radius it is possible to constrain the ranges of plausible interior composition, the information supplied by other processes such as the formation mechanisms or the atmospheric escape could help to obtain a better constraint (Rogers and Seager, 2010). For example, the preferential loss of hydrogen causes the oxidation of the martial surface (Lammer et al., 2020b).

It is also very relevant to mention that Solar System planets as Venus, Mars and the Earth could experience hydrodynamic escape in early stages of their evolution (e.g., Watson et al., 1981; Zahnle and Kasting, 1986; Hunten et al., 1987; Lammer et al., 2020b; Lammer et al., 2020a).

1.2.5 Observations of the hydrodynamic escape

Hydrodynamic atmospheric escape can only be observed from exoplanets, as no planet in the Solar System is currently undergoing this process. This fact reduces considerably our available observational capabilities. Indeed atmospheric escape has been observed only in a few exoplanetary atmospheres of giant planets, mini-Neptunes and super-Earths.

Exoplanetary atmospheres are mainly detected by transmission spectra (see Sect. 1.1). Therefore, extended atmospheres are detected when the absorption depth of the line(s) of a species is/are significantly larger than the broadband optical absorption depth during the transit, or equivalently when the absorption radius of the line (See Eq. 1.1) is larger than the absorption radius of the optical broadband (optical radius).

However, the detection of an extended atmosphere does not prove the existence of atmospheric escape. To confirm atmospheric escape, it is necessary to detect gas

beyond the Roche lobe of the planet; for instance, finding an absorption line whose absorption radius is higher than the Roche lobe (Owen, 2019),

$$\delta \geqslant \left(\frac{R_{\rm lobe}}{R_\star} \right)^2 . \tag{1.15}$$

For proving hydrodynamic atmospheric escape, it is also necessary to constrain the velocity of the gas in the upper atmosphere, as the gas outside the Roche lobe could be supplied by the Jeans escape or by the enhanced Jeans escape (see Sec.1.2). Essentially, hydrodynamic escape can be proved if the velocity of the gas is about or larger than the speed of sound, as this demonstrates the transonic outflow. From the broadening of the line and an upper limit of the density, it is possible to constrain the radial velocity of the gas, and then to compare with the estimated speed of sound (see e.g., discussion in VidalMadjar2004, and also in this work, in Chapters 2, 4 and 5).

The H I Lyα line is an excellent feature to prove atmospheric escape due to its large absorption cross-section, specially in giant planets, where hydrogen is the most abundant element in their atmosphere. In fact, the first detection of atmospheric escape in an exoplanet (in the hot Jupiter HD 209458 b) was obtained by the measurement of the Lyα absorption with the HST (Vidal-Madjar et al., 2003). These authors found an absorption depth in the Lyα of $\sim$ 15%, much higher than the absorption depth in the visible broadband, $\sim$ 1.5%, with an absorption radius higher than the Roche lobe of the planet. Therefore, they concluded that the signal originated from escaping hydrogen. Since then, a few more Lyα observations have been done in exoplanetary atmospheres with the HST, for instance of the hot Jupiter HD 189733 b (Lecavelier des Etangs et al., 2010) with an absorption depth of 5% compared to its broadband optical absorption depth of $\sim$2.4%; of the warm Neptune GJ 436 b (Ehrenreich et al., 2015) with an absorption depth of 56% compared to its broadband optical absorption depth of 0.69%; and of the warm Neptune GJ 3470 b (Bourrier et al., 2018) with absorption depth of $\sim$35%.

However, Lyα observations are restricted to space-based telescopes, reducing our observational capabilities. Moreover, geocoronal emission contamination and interstellar medium absorption dominate the core of the line, leaving only their wings with potential exoplanetary information (see e.g., Vidal-Madjar et al., 2003; Ehrenreich et al., 2008). The lack of information from the core of the Lyα line produces a high degeneracy when deriving the main parameters of the upper atmosphere (e.g., density and velocity of the escaping gas) and prevents it from probing its type of escape mechanism. Nevertheless, important information about the upper atmosphere and processes as stellar wind interaction, ENAs or radiation pressure can be derived from Lyα observations (see e.g., Bourrier et al., 2016). In Fig. 1.4, we show the Lyα transmission spectra of GJ 436 b measured by Ehrenreich et al. (2015). Observations

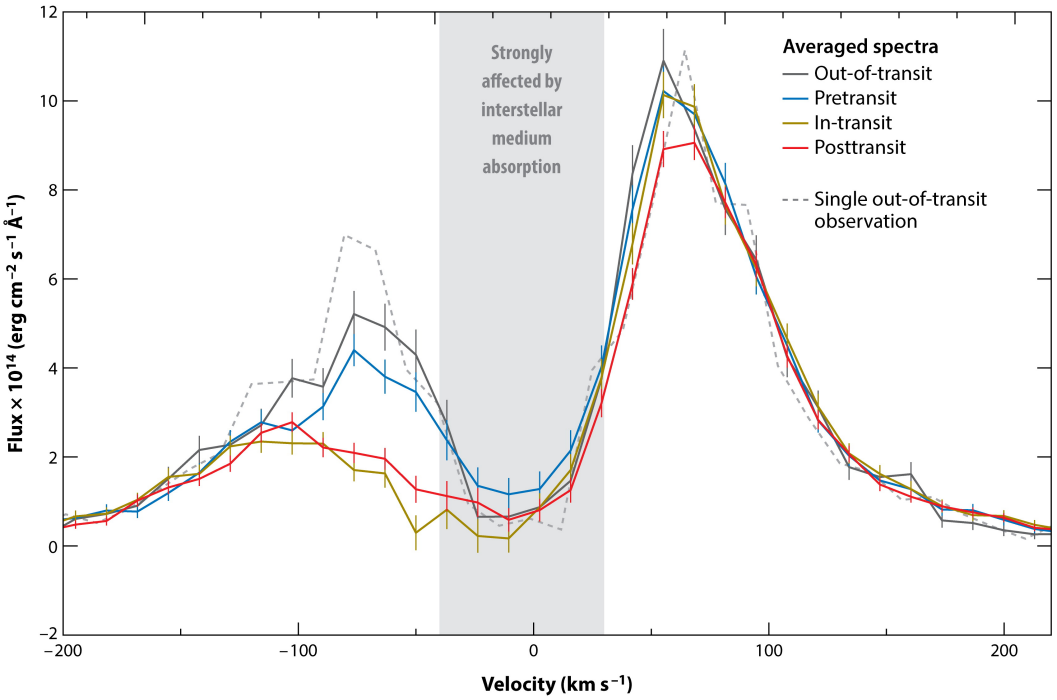

Fig. 1.4 Lyα transmission spectra of GJ 436 b measured by Ehrenreich et al. (2015). Solid lines show the averaged spectra from several observations. After Owen (2019), adapted from Ehrenreich et al. (2015).

of ultraviolet (UV) lines from heavy elements (e.g., O I, C II) are partially affected by the interstellar absorption medium (see e.g. Vidal-Madjar et al., 2004). With part of the core of the line available, and constraining the density of the heavy element (e.g. by means of the hydrogen density from Lyα absorption), it is possible to constrain the radial velocity of the escaping gas. Comparing these with the speed of sound in the upper atmosphere, it is then possible to probe the hydrodynamic escape (as seen before). Indeed, by observing the absorption spectra of O I and C II lines, Vidal-Madjar et al. (2004) proved that the escape in the atmosphere of HD 209458 b is hydrodynamic. In this scenario, the presence of heavy species in the upper atmosphere flowing at high radial velocities can be explained as hydrodynamic drag by outflow of the hydrogen atoms.

Others UV detection in excess of absorption have been detected in other exoplanets, for example in HD 189733 b (Ben-Jaffel and Ballester, 2013), and GJ 436 b (Kulow et al., 2014; Ehrenreich et al., 2015; Lavie et al., 2017). However, since UV lines can only be detected from space telescopes; heavy elements are in a much lower densities than H in the upper atmospheres of giant planets, and also they have lower absorption cross-sections than the Lyα line; they are less favorable for detection.

In addition to the UV absorption lines, broadband X-ray observations are also valuable for supporting the presence of heavy metals in extended atmospheres, as

observed in HD 189733 b (Poppenhaeger et al., 2013) with an absorption depth of ∼6–8%.

Hydrogen lines in the Balmer series, e.g. Hα, Hβ and Hγ, are not limited by interstellar absorption and can then be measured from ground telescopes. The first detection of Hα in an exoplanetary atmosphere was observed in the hot Jupiter HD 189733 b by Jensen et al. (2012) with HET[15]. Since then, the Hα line (the main line of Balmer series) has been detected in six more exoplanetary atmospheres: in the hot Jupiter WASP–52 b (Chen et al., 2020) with ESPRESSO[16], and in five ultra-hot Jupiters: MASCARA–2 b/KELT–20 b (Casasayas-Barris et al., 2018) with HARPS-N[17], WASP–12 b (Jensen et al., 2018) with HET, KELT–9 b (Yan and Henning, 2018; Wyttenbach et al., 2020) with HARPS-N, WASP–121 b (Cabot et al., 2020) with HARPS[18], WASP–33 b (Yan et al., 2021) with CARMENES[19] and HARPS-N. These observations suggest extended atmospheres and then are a very important source of information for escape studies (see e.g. García Muñoz and Schneider, 2019; Wyttenbach et al., 2020). Nevertheless, all these exoplanets exhibit very hot upper atmospheres, which suggest that observations of H lines in the Balmer series are restricted to these conditions.

The He I 2^3S–2^3P transition from metastable states, hereafter He(2^3S), is composed of three lines at 10830.33, 10830.25, and 10829.09 Å[20], is not strongly absorbed by the interstellar medium (Indriolo et al., 2009; Spake et al., 2018), and therefore could be in principle observed from ground-based telescopes. Additionally, He is the second element more abundant in the upper atmosphere of giant planets and hence might be detectable in the upper atmospheres of giant planets. The major problem for detection is that it originates from a metastable excited state, usually with a much smaller population than the ground state and, hence we need a strong pumping mechanism (stellar irradiation) to populate it. These characteristics make the He(2^3S) observations, whenever feasible, very promising for probing the hydrodynamic escape and for characterising the escaping atmospheres. Observation of the He(2^3S) lines were proposed originally by Seager and Sasselov (2000), who studied transmission spectra for close-in planets and estimated a significant absorption of these lines, particularly when the planet has an extended atmosphere.

[15]The high resolution spectrograph on the 9.2 m Hobby-Eberly Telescope.
[16]The high-resolution spectrograph at the Very Large Telescope array.
[17]HARPS-North spectrograph at the 3.58 m Telescopio Nazionale Galileo.
[18]High-Accuracy Radial-velocity Planet Searcher echelle spectrograph, located at the ESO, La Silla 3.6 m telescope.
[19]Calar Alto high-Resolution search for M dwarfs with Exoearths with Near-infrared and optical Échelle Spectrographs, at the 3.5 m Calar Alto Telescope (Quirrenbach et al., 2016; Quirrenbach et al., 2018).
[20]Wavelengths in the air, often referred to as wavelengths of 10830 Å. Corresponding wavelengths in the vacuum are 10832.06, 10833.22 and 10833.31 Å.

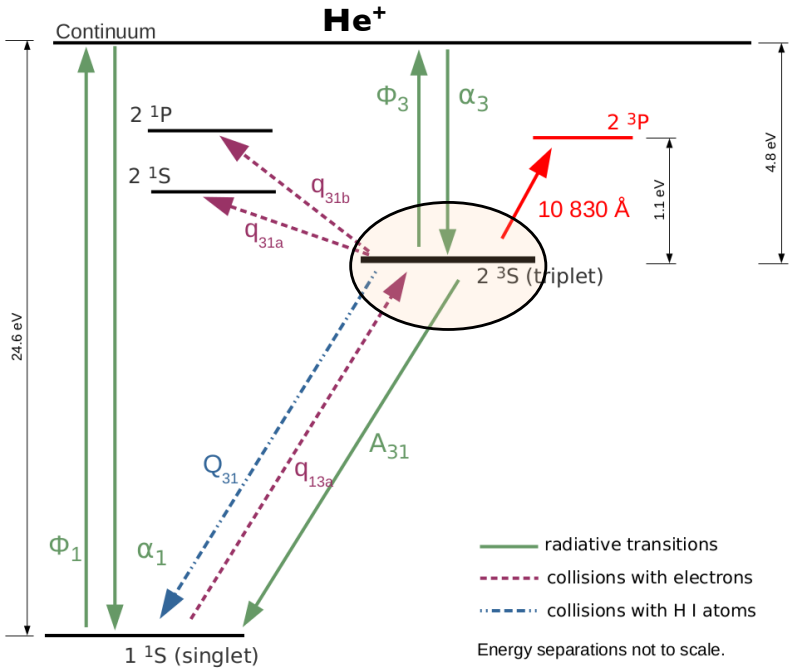

Fig. 1.5 Sketch of the most relevant electronic transitions in the atom of He for the analysis of the observed He(2^3S) absorption spectra. The triplet states are encircled with an orange oval. Adapted from Oklopčić and Hirata (2018).

More recently, Oklopčić and Hirata (2018) developed a model suitable for estimating He(2^3S) absorption in extended atmospheres.

The measurements of the He(2^3S) absorption has become a reality only a couple of years ago. It was detected for the first time in the atmosphere of WASP-107 b from space with the WFC3[21] with a moderate spectral resolution (Spake et al., 2018) and, almost simultaneously, from ground based observations in the atmospheres of WASP–69 b (Nortmann et al., 2018), HAT–P–11 b (Allart et al., 2018), and HD 189733 b (Salz et al., 2018) with the high-resolution spectrograph CARMENES. Since then, a few more observations have been performed, e.g. HAT–P–11 b (Mansfield et al., 2018) with WFC3; WASP-107 b (Allart et al., 2019) and HD 209458 b (Alonso-Floriano et al., 2019) with CARMENES; HD 189733 b (Salz et al., 2018; Guilluy et al., 2020) with CARMENES and GIANO-B[22] respectively; GJ 3470 b by Pallé et al. (2020) and Ninan et al. (2020) with CARMENES and HPF[23] respectively.

[21] The Wide Field Camera 3 on board the HST.
[22] GIANO-B high-resolution spectrograph at the Telescopio Nazionale Galileo.
[23] Habitable Zone Planet Finder near-infrared spectrograph, on the 10 m Hobby–Eberly Telescope at the McDonald Observatory.

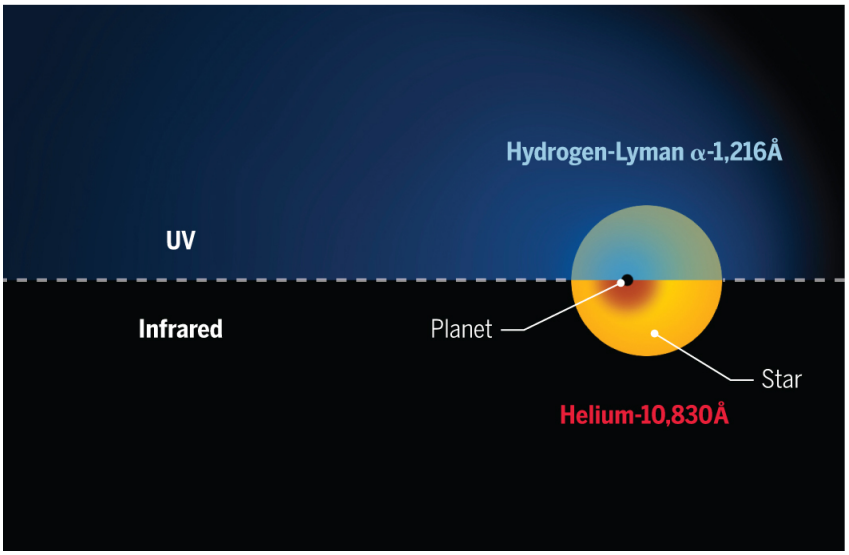

Fig. 1.6 Sketch showing the dimensions of the probing regions of the upper atmospheres of giant planets by the hydrogen Lyα line in the UV and by the He(2^3S) lines in the NIR. After Brogi (2018).

1.3 Thesis motivation

Many planets undergo hydrodynamic atmospheric escape at some stage of their lifetime. During this stage, these planets could significantly change their atmospheric composition; their bulk planetary mass; their radius-mass relationship; and even evolve to a different planetary class. Characterisation of atmospheres of exoplanets currently undergoing hydrodynamic escape, provide critical information of their nature; hints about its origin and evolution; and clues to understand the formation of the current planetary population and the origin and evolution of the Solar System. However, only a few observations of this process were available until very recently. Consequently, our knowledge about the hydrodynamic atmospheric escape is very limited.

The new observations of the He(2^3S) absorption spectra have opened a new window in the study of the atmospheric escape (see, Nortmann et al., 2018; Brogi, 2018), allowing to significantly improve the characterisation of the upper atmosphere of exoplanets undergoing hydrodynamic escape. Apart from the larger sensitivity that offers the He(2^3S) signature, one further key point is that, in contrast to the H Lyα line, it probes the root of the origin of atmospheric escape (see Fig. 1.6). Detailed studies of the absorption line profile are nowadays feasible and the diversity in bulk parameters of exoplanets with the recent available observations of He(2^3S) and Lyα lines, allows us to perform deeper studies and to investigate their hydrodynamic regimes. In this thesis we aim at exploiting these new measurements of He(2^3S) in conjunction to previous measurements of the H Lyα line. This, constitutes one of the

very first (if not the first) dedicated studies of the evaporating atmospheres of gas giants by using the recent He(2^3S) and Lyα absorption measurements.

1.3.1 Thesis objectives

The main goal of this thesis is to contribute to the knowledge in planetary science through the study of the upper atmospheres of giant exoplanets undergoing hydrodynamic escape.

The specific objectives are:

1. To improve the characterisation of the upper atmosphere of a representative sample of giant exoplanets currently undergoing hydrodynamic escape (the hot Jupiters HD 209458 b and HD 189733 b, and the warm Neptune GJ 3470 b).

2. To perform a comparative analysis between the planets in the sample.

3. To investigate the hydrodynamic atmospheric regimes of the planets in the sample.

1.3.2 Thesis outline

The framework of this thesis is the CARMENES He I survey, a collaboration to study the He(2^3S) in exoplanetary atmospheres within the CARMENES Atmospheric Working Group. This collaboration, that involves more than 30 scientist from 11 institutions (see e.g. acknowledgments in Chapters 3, 2, 4, and 5), is essentially divided in two main tasks, observations of high-resolution He(2^3S) absorption spectra with the CARMENES spectrograph, and their physical interpretation. This thesis is mainly focussed on the physical interpretation of the He(2^3S) measurements acquired within this collaboration.

Within the CARMENES He I survey collaboration, the research focused on: a) the observations of the He(2^3S) absorption spectra of the exoplanets WASP-69 b, HD 189733 b, HD 209458 b and GJ 3470 b published in Nortmann et al. (2018), Salz et al. (2018), Alonso-Floriano et al. (2019) and Pallé et al. (2020) respectively, and of the exoplanet HATP-32b, currently submitted for publication; and b) the analysis and physical interpretation of those observations that lead to three studies about the upper atmospheres of HD 189733 b, HD 209458 b, and GJ 3470 b, published in Lampón et al. (2020) and Lampón et al. (2021b) and in a recently submitted article (Lampón et al., 2021a). In this thesis we focus on the study of HD 189733 b,

HD 209458 b, and GJ 3470 b, as they have very different planetary and stellar bulk parameters, and the absorption measurements of both He(2^3S) and Lyα lines are available.

This thesis is presented as a compendium of articles. It is composed of the articles by Pallé et al. (2020); Lampón et al. (2020); Lampón et al. (2021b) and Lampón et al. (2021a) (the last one submitted to Astronomy and Astrophysics). By including the article by Pallé et al. (2020), we provide with the necessary description of the observations of the He(2^3S) absorption spectra, of the CARMENES spectrograph, and of the methodology followed to obtain the He(2^3S) signature. We have not included the publications by Salz et al. (2018) and Alonso-Floriano et al. (2019) as we aim to present a concise work focussed on the physical interpretation of the observations.

The methodology used in this thesis is described in Chapters 2, 3, and 4 . We observed the high-resolution transit spectroscopy with the CARMENES instrument. We corrected spectra of contamination by telluric absorption from atmospheric water vapor and OH^- emission, and used two different ways for calculating the transmission spectrum, masking the OH-affected regions of the spectrum, and correcting for OH^- contamination. We also calculated the transit light curves for He I absorption in order to monitor the temporal behavior of the excess. These methods are described in more detail in Sec. 2 of Chapter 2. Concerning the methodology used for modelling exoplanetary upper atmospheres, we used a 1D hydrodynamic model with spherical symmetry, coupled with a non-LTE model for calculating the population of the metastable He(2^3S) state. The He(2^3S) concentration profiles were included into a radiative transfer model to calculate He(2^3S) absorption spectra. By comparing the calculated and measured He(2^3S) spectra, we constrained key parameters of the upper atmosphere of these planets as the mass-loss rate, the thermospheric temperature, the He(2^3S) density profile, and the degree of ionisation. We also compared our derived H densities with previous profiles derived from the Lyα absorption to further constrain the H/He ratio. This methodology is described in more detail in Sec. 2 of Chapter 3. In Sec. xx of Chapter 4 we also introduced the Markov Chain Monte Carlo (MCMC) analysis.

Chapter 2

In this chapter we report the observations of the He(2^3S) absorption spectra of the atmosphere of GJ 3470 b. We describe the characteristics of the CARMENES spectrograph, and the basics of the transmission spectroscopic technique that lead to the observation of the He(2^3S) signature. A preliminary analysis of the physical interpretation of the He(2^3S) absorption spectra is included in this article, and a more in-depth study is presented in Chapter 4.

Chapter 3

In this chapter we characterise the upper atmosphere of the hot Jupiter HD 209458 b. We describe the model we developed for studying the upper atmosphere of planets undergoing hydrodynamic escape, and the method we used for retrieving information from observations of the He(2^3S) and Lyα absorption spectra.

Chapter 4

In this chapter we characterise the upper atmospheres of the hot Jupiter HD 189733 b and the warm Neptune GJ 3470 b. We used the same methods than in the previous chapter for modelling the upper atmospheres of these exoplanets, and, in addition, we included another method for retrieving constraints from observations, the MCMC analysis. The important results from the comparison of the three planets are discussed in this Chapter.

Chapter 5

In this chapter we investigate the hydrodynamic escape regimes of HD 209458 b, HD 189733 b and GJ 3470 b. Accordingly, we present observational evidence of the three hydrodynamic escape regimes in planetary H/He atmospheres predicted theoretically.

Chapter 6

In this chapter we present the thesis conclusions.

2

A He I upper atmosphere around the warm Neptune GJ 3470 b

This Chapter has been published in the journal Astronomy and Astrophysics with the title “A He I upper atmosphere around the warm Neptune GJ 3470 b”. Palle et al. A&A, 638, A61 (2020), reproduced with permission ©ESO.

A&A 638, A61 (2020)
https://doi.org/10.1051/0004-6361/202037719
© ESO 2020

Astronomy & Astrophysics

A He I upper atmosphere around the warm Neptune GJ 3470 b

E. Palle[1,2], L. Nortmann[1,2], N. Casasayas-Barris[1,2], M. Lampón[3], M. López-Puertas[3], J. A. Caballero[4], J. Sanz-Forcada[4], L. M. Lara[3], E. Nagel[5,6], F. Yan[7], F. J. Alonso-Floriano[8], P. J. Amado[3], G. Chen[1,2,9], C. Cifuentes[4], M. Cortés-Contreras[4], S. Czesla[5], K. Molaverdikhani[10], D. Montes[11], V. M. Passegger[5], A. Quirrenbach[12], A. Reiners[7], I. Ribas[13,14], A. Sánchez-López[3], A. Schweitzer[5], M. Stangret[1,2], M. R. Zapatero Osorio[4], and M. Zechmeister[7]

[1] Instituto de Astrofísica de Canarias (IAC), 38200 La Laguna, Tenerife, Spain
e-mail: epalle@iac.es
[2] Deptartamento de Astrofísica, Universidad de La Laguna (ULL), 38206 La Laguna, Tenerife, Spain
[3] Instituto de Astrofísica de Andalucía (IAA-CSIC), Glorieta de la Astronomía s/n, 18008 Granada, Spain
[4] Centro de Astrobiología (CSIC-INTA), ESAC, Camino bajo del castillo s/n, 28692 Villanueva de la Cañada, Madrid, Spain
[5] Hamburger Sternwarte, Universität Hamburg, Gojenbergsweg 112, 21029 Hamburg, Germany
[6] Thüringer Landessternwarte Tautenburg, Sternwarte 5, 07778 Tautenburg, Germany
[7] Institut für Astrophysik, Georg-August-Universität, Friedrich- Hund-Platz 1, 37077 Göttingen, Germany
[8] Leiden Observatory, Leiden University, Postbus 9513, 2300 RA Leiden, The Netherlands
[9] Key Laboratory of Planetary Sciences, Purple Mountain Observatory, Chinese Academy of Sciences, Nanjing 210033, PR China
[10] Max-Planck-Institut für Astronomie, Königstuhl 17, 69117 Heidelberg, Germany
[11] Departamento de Física de la Tierra y Astrofísica and IPARCOS-UCM (Intituto de Física de Partículas y del Cosmos de la UCM), Facultad de Ciencias Físicas, Universidad Complutense de Madrid, 28040 Madrid, Spain
[12] Landessternwarte, Zentrum für Astronomie der Universität Heidelberg, Königstuhl 12, 69117 Heidelberg, Germany
[13] Institut de Ciències de l'Espai (ICE, CSIC), Campus UAB, c/ de Can Magrans s/n, 08193 Bellaterra, Barcelona, Spain
[14] Institut d'Estudis Espacials de Catalunya (IEEC), 08034 Barcelona, Spain

Received 12 February 2020 / Accepted 15 April 2020

ABSTRACT

High resolution transit spectroscopy has proven to be a reliable technique for the characterization of the chemical composition of exoplanet atmospheres. Taking advantage of the broad spectral coverage of the CARMENES spectrograph, we initiated a survey aimed at characterizing a broad range of planetary systems. Here, we report our observations of three transits of GJ 3470 b with CARMENES in search of He (2^3S) absorption. On one of the nights, the He I region was heavily contaminated by OH^- telluric emission and, thus, it was not useful for our purposes. The remaining two nights had a very different signal-to-noise ratio (S/N) due to weather. They both indicate the presence of He (2^3S) absorption in the transmission spectrum of GJ 3470 b , although a statistically valid detection can only be claimed for the night with higher S/N. For that night, we retrieved a $1.5 \pm 0.3\%$ absorption depth, translating into a $R_p(\lambda)/R_p = 1.15 \pm 0.14$ at this wavelength. Spectro-photometric light curves for this same night also indicate the presence of extra absorption during the planetary transit with a consistent absorption depth. The He (2^3S) absorption is modeled in detail using a radiative transfer code, and the results of our modeling efforts are compared to the observations. We find that the mass-loss rate, $\dot{M}$, is confined to a range of 3×10^{10} g s^{-1} for $T = 6000$ K to 10×10^{10} g s^{-1} for $T = 9000$ K. We discuss the physical mechanisms and implications of the He I detection in GJ 3470 b and put it in context as compared to similar detections and non-detections in other Neptune-size planets. We also present improved stellar and planetary parameter determinations based on our visible and near-infrared observations.

Key words. planetary systems – planets and satellites: atmospheres – planet-star interactions – planets and satellites: general – planets and satellites: individual: GJ 3470b

1. Introduction

High resolution spectroscopy has been established over the past few years as a major tool for the characterization of exoplanet atmospheres. The cross-correlation technique of planetary models and observed spectral time series has allowed for the detection of CO, CH_4, and H_2O molecules in the atmospheres of hot Jupiters (Snellen et al. 2010; de Kok et al. 2013; Birkby et al. 2013; Guilluy et al. 2019) and holds the key to spectroscopic characterization of rocky worlds with the upcoming extremely large telescopes (Pallé et al. 2011; Snellen et al. 2013).

Moreover, using high resolution transmission spectroscopy, we are not only able to detect chemical species in the atmosphere of exoplanets, but also to resolve their spectral lines. If the signal-to-noise ratio (S/N) of the final transmission spectrum is high enough, it is possible to obtain temperature and pressure profiles of the upper atmosphere by adjusting isothermal models to different regions of the lines (from core to wings), whose origins reside in different layers of the atmosphere (Wyttenbach et al. 2015, 2017; Casasayas-Barris et al. 2018).

The ability to measure and track line profiles can greatly help in the study of atmospheric escape, which is an important process for understanding planetary physical and chemical evolution. In the past, studies of atmospheric escape relied mostly on space-based observations of the hydrogen Lyα line in the far ultraviolet (Vidal-Madjar et al. 2003), a spectral

Table 1. Observing log of the GJ 3470 b transit observations.

Night t	Date	Start UT	End UT	t_{exp} [s]	N_{obs}	Airmass	S/N	RV [km s^{-1}]
1	2018 Dec 16	22:23	02:05	498	23	1.85→1.08→1.08	26	7.15
2	2018 Dec 26	21:38	03:13	498	34	1.9→1.079→1.136	66	12.24
3	2019 Jan 05	21:54	03:27	498	35	1.48→1.078→1.25	61	16.90

Notes. RV is the averaged barycentric Earth radial velocity during the night.

region with limited access and strongly affected by interstellar absorption.

However, the near-infrared coverage of spectrographs such as CARMENES and GIANO gives access to poorly-explored exoplanet atmospheric features, including the triplet line feature of metastable neutral helium at 10830 Å. This line was proposed as a tracer for atmospheric evaporation in general by Seager & Sasselov (2000) and for particular targets by Oklopčić & Hirata (2018). In this process, intense high-energy irradiation from the host star causes the atmosphere of a hot gas planet to continuously expand resulting in mass flowing away from the planet (Lammer et al. 2013; Lundkvist et al. 2016). With the recent detections of He I with low (Spake et al. 2018) and high resolution spectroscopy (Nortmann et al. 2018; Allart et al. 2018; Salz et al. 2018), it has been proven that this line is a powerful tool for studying the extended atmospheres, mass-loss, and winds in the upper-atmospheres, and for tracking the possible presence of cometary-like atmospheric tails.

Atmospheric erosion by high-energy stellar radiation is believed to play a major role in shaping the distribution of planet radii. Planets with H/He-rich envelopes can be strongly evaporated by stellar irradiation. The evaporation theory predicts the existence of an "evaporation valley" with a paucity of planets at $\sim$1.7 $R_\oplus$ (Seager & Sasselov 2000; Owen & Wu 2013). The radius distribution of small planets ($R_p < 4.0\,R_\oplus$) is bi-modal; small planets tend to have radii of either $\sim$1.3 $R_\oplus$ (super-Earths) or $\sim$2.6 $R_\oplus$ (sub-Neptunes), with a dearth of planets at $\sim$1.7 $R_\oplus$ (Fulton et al. 2017; Van Eylen et al. 2018; Fulton & Petigura 2018). This gap suggests that all small planets might have solid cores, while the cores of sub-Neptune planets are expected to be surrounded by H/He-rich envelopes that significantly enlarge the planetary radii as they are optically thick, while accounting for only 1% of the total planetary mass. Terrestrial cores can also be surrounded by a thin atmosphere or possess no atmosphere at all, making up the population of super-Earths centered at $R_p \sim 1.3\,R_\oplus$.

GJ 3470 b (Bonfils et al. 2012) is a warm Neptune ($R = 3.88 \pm 0.32\,R_\oplus$, $M = 12.58 \pm 1.3\,M_\oplus$), with an equilibrium temperature of 547 K and a period of 3.33 d, located very close to the Neptunian desert. Previous atmospheric studies have inferred a hazy, low-methane or metal-rich atmosphere from *Hubble* Space Telescope observations (Ehrenreich et al. 2014) and a Rayleigh slope in the visible range (Nascimbeni et al. 2013; Chen et al. 2017). While Earth-size and super-Earth planets still remain out of the reach of current instrumental capabilities for evaporation studies, GJ 3470 b is an excellent target for study of such processes. Indeed, Bourrier et al. (2018) already reported the existence of a giant hydrogen exosphere around GJ 3470b and derived a high mass-loss rate. Here we present observations of this target in search for the absorption features of the He (2^3S) triplet. During the process of writing and refereeing of this manuscript, a similar independent work was reported by Ninan et al. (2019).

2. Observations and data analysis

2.1. CARMENES spectroscopy

The transit of GJ 3470 b was observed three times with the CARMENES spectrograph (Quirrenbach et al. 2014, 2018) at the Calar Alto Observatory, on the nights of 16 and 26 December 2018, and on 5 January 2019 (nights 1, 2, and 3, hereafter). CARMENES covers simultaneously the visual (0.52–0.96 μm) and near-infrared (0.96–1.71 μm) spectral ranges with its two channels. A log of the observations, including start and ending times, airmass intervals, and S/Ns can be found in Table 1. Altogether, we collected 13, 14, and 13 in-transit spectra on each night, respectively, using the criteria that at least half the exposure time was taken inside the first and fourth contact interval. Following the same criteria, we also obtained 10, 20, and 22 out-of-transit spectra on nights 1, 2, and 3, respectively.

During the observations, fiber A was fed by the light of the GJ 3470 star and fiber B felt on the sky at about 1.5 arcmin to the target. The spectra of both fibers were extracted from the raw frames using the CARACAL pipeline (Zechmeister et al. 2018). In the standard data flow (Caballero et al. 2016), fiber A spectra are extracted using flat optimized extraction while fiber B spectra are extracted with a simple aperture. Here, we also extracted fiber B with flat optimized extraction so that the spectra of both fibers underwent the same processing scheme.

2.2. Target star parameters

The star GJ 3470 was first cataloged as a high proper motion star in the Luyten-Palomar survey (Luyten 1979). It went almost unnoticed until Bonfils et al. (2012) discovered the transiting planet around it. Since then, and especially with the advent of *Gaia* (Gaia Collaboration 2018), the stellar parameters of GJ 3470 have been better measured.

In Table 2 we compile a comprehensive list of stellar parameters of GJ 3470, either from the literature or derived by us. When there are different published parameter determinations (e.g., spectral type, proper motion), we list the most precise or the most recent ones.

We determined the photospheric parameters T_{eff}, $\log g$, and [Fe/H] following the methods described by Passegger et al. (2019), using the combined VIS+NIR spectra of the two CARMENES channels. The physical stellar parameters L, R, and M were determined following Schweitzer et al. (2019), i.e., we measured the luminosity L by using the *Gaia* DR2 parallax and integrated multi-wavelength photometry from B to $W4$, applied Stefan-Boltzmann's law to obtain the radius R, and, finally, used the linear mass-radius relation from Schweitzer et al. (2019) to arrive at the mass M.

Our photospheric parameters (T_{eff}, $\log g$, and [Fe/H]) are consistent with Demory et al. (2013). Their mass was based on the empirical mass-magnitude relation of Delfosse et al. (2000) and, hence, it differs by the same amount from our value as

Table 2. Stellar parameters of GJ 3470.

Parameter	Value	Reference
Name and identifiers		
Name	LP 424–4	Luy79
GJ	3470	GJ91
Karmn	J07590+153	AF15
Key parameters		
α	07:59:05.84	*Gaia* DR2
δ	+15:23:29.2	*Gaia* DR2
G (mag)	11.3537 ± 0.0013	*Gaia* DR2
J (mag)	8.794 ± 0.026	2MASS
Spectral type	M2.0 V	Lep13
Parallax and kinematics		
π (mas)	33.96 ± 0.06	*Gaia* DR2
d (pc)	29.45 ± 0.05	*Gaia* DR2
$\mu_\alpha \cos\delta$ (mas a^{-1})	–185.73 ± 0.11	*Gaia* DR2
μ_δ (mas a^{-1})	–57.26 ± 0.06	*Gaia* DR2
V_r (km s^{-1})$^{(a)}$	+26.5169 ± 0.0005	Bou18
U (km s^{-1})	–32.04 ± 0.21	This work
V (km s^{-1})	–12.42 ± 0.10	This work
W (km s^{-1})	–15.37 ± 0.10	This work
Kinematic population	Young disc	This work
Photospheric parameters		
$T_{\rm eff}$ (K)	3725 ± 54	This work
log g	4.65 ± 0.06	This work
[Fe/H]	+0.420 ± 0.019	This work
$v \sin i$ (km s^{-1})	$\lesssim$2	Bon12
Physical parameters		
L (10^{-4} $L_\odot$)	390 ± 5	This work
R ($R_\odot$)	0.474 ± 0.014	This work
M ($M_\odot$)	0.476 ± 0.019	This work
Age (Ga)	0.6–3.0	This work
Other parameters		
$P_{\rm rot}$ (d)	20.70 ± 0.15	Bid15
pEW(Hα) (Å)	+0.39 ± 0.09	Gai14
log $R'_{\rm HK}$	–4.91 ± 0.11	SM15
$F_{5-100\,\text{Å}}$ (10^{27} erg s^{-1})	2.3	Bou18
$F_{100-504\,\text{Å}}$ (10^{27} erg s^{-1})	2.7	Bou18

Notes. $^{(a)}$Soubiran et al. (2018) tabulated V_r = +26.341 ± 0.004 km s^{-1}, but their uncertainties did not include gravitational redshift or photospheric convection.

References. AF15: Alonso-Floriano et al. (2015); Bid14: Biddle et al. (2014); Bon12: Bonfils et al. (2012); Bou18: Bourrier et al. (2018); Gai14: Gaidos et al. (2014); GJ91: Gliese & Jahreiß (1991); Lép13: Lépine et al. (2013); Luy79: Luyten (1979); SM15: Suárez Mascareño et al. (2015); 2MASS: Skrutskie et al. (2006); *Gaia* DR2: Gaia Collaboration (2018).

results from Delfosse et al. (2000) differ from the updated mass-magnitude relation of Mann et al. (2019). Our method, however, agrees very well with the updated mass-magnitude relation (cf., Schweitzer et al. 2019). The radii determination of Demory et al. (2013) or Awiphan et al. (2016), however, were based on the average density inside the planetary orbit, which added an additional uncertainty.

In addition, we also used the latest astrometric and absolute radial velocity data of *Gaia* for determining Galactocentric space velocities UVW and assigning GJ 3470 to the Galactic young disc population. We estimated a stellar age between 0.6 and 3.0 Ga, which is consistent with its kinematic population, the presence of Hα in absorption (in spite of its M2.0 V spectral type), the faint Ca II H&K emission, the relatively slow rotation (quantified by the low rotational velocity and long rotational period), and its weak X-ray emission, as well as with previous determinations in the literature (e.g., Bourrier et al. 2018; Bonfils et al. 2012).

We also searched the literature for additional information on GJ 3470. What was of particular interest is the i'- and z'-band lucky imaging of the star by Wöllert & Brandner (2015), who derived upper limits on the existence of targets brighter than $\Delta z' \approx 4.0$ mag and 6.0 mag at 0.25 arcsec and 5 arcsec, respectively. These limits translated into the absence of objects at the substellar boundary at separations beyond 150 au and more massive than 0.1 $M_\odot$ down to 7 au, approximately.

For the system parameters, throughout the rest of the paper, we adopt the stellar velocity semi-amplitude $K_{\rm star}$ from Bonfils et al. (2012). For the planet parameters, we recalculated here the radius, mass, density, and equilibrium temperature values (see Table 4) based on the stellar parameters of Table 2. The remaining values were taken from Bourrier et al. (2018) and references therein. We calculated the velocity semi-amplitude of the planet $K_{\rm planet}$ from these values.

2.3. Telluric absorption removal

The He I λ10830 Å triplet is contaminated by telluric absorption from atmospheric water vapor and OH$^-$ emission (Nortmann et al. 2018; Salz et al. 2018). Due to the Earth's barycentric velocity, the relative position between the He I and the telluric features varies with date. To detect the weak planetary signals in the spectral time series, the telluric contribution needs to be removed from the spectra.

The water vapor removal in each individual spectrum was performed with `molecfit`, which fits synthetic transmission models to the observations (Smette et al. 2015; Kausch et al. 2015). To adapt the telluric model to the spectra, `molecfit` allows the user to convolve the model with an instrumental profile. We analyzed several thousand lines from hollow cathode lamp spectra, which are regularly used as calibration sources, and measured the Gaussian and Lorentzian FWHM components. Based on our analysis, we adopted a value of 5.26 and 0.75 pixel for the Gaussian and the Lorentzian FWHM components, respectively. The determination of the instrumental line spread function is described in more detail in Nagel et al. (priv. comm.). The effect of telluric line removal is illustrated in Fig. 1.

The He I triplet lines were also located between OH$^-$ emission lines (see also Fig. 1), which are not accounted for by `molecfit`. These lines were also observed in the spectra obtained from fiber B, which was pointed at the sky. We corrected the emission lines in fiber A by first modeling the lines in fiber B and then subtracting the model from the spectra of fiber A. In fiber B there was no detectable contamination from the stellar spectra. To construct the model, we first obtained a master spectrum for fiber B, calculated by summing up all fiber B spectra for a given night. To this spectrum, we fitted a Voigt profile to the fiber B OH$^-$ line redwards of the stellar He I lines, and two Gaussian profiles (with the same amplitude and width) to the two weakest OH$^-$ lines bluewards of the stellar He I lines. The amplitude of the fit to the strongest OH$^-$ emission could vary for every fiber B spectrum independently, but we kept the values for the positions, widths, and amplitude ratios between strong

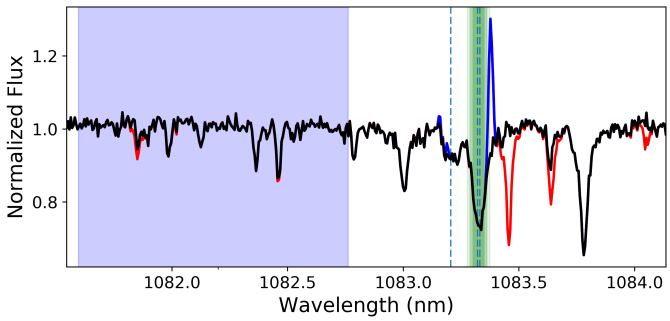

Fig. 1. Zoom of one CARMENES spectrum of GJ 3470 in the wavelength region containing the He I triplet. In red the raw spectra after standard data reduction is plotted. Over-plotted in blue is the same spectrum after removal of the telluric features (mainly water in this region) using `molecfit`. In black is the same spectrum after adjusting and removing also the OH^- spectral features. In the figure, the wavelength region used to normalize the continuum of all spectra is marked with a blue shade, and the region around the He I line cores used to calculate the spectro-photometric transit light curves is marked with a shaded green region.

and weak OH^- lines fixed for all the spectra of a given night. When allowing the widths of the lines to vary, we found no statistically significant differences in the final results. Finally, when subtracting the model fit of fiber B from fiber A, we applied a scaling factor (0.88 ± 0.05) to the model to compensate for the efficiency differences between the two fibers. This factor was calculated from a high S/N observation with CARMENES, and was fixed for all spectra and nights. The error of this factor had no significant impact on our results compared to the standard deviation.

3. Results

3.1. He I transmission spectra

After correction of the telluric absorption and emission, we normalized all spectra by the mean value of the region between 10815.962 and 10827.624 Å in vacuum. This region, which lies blue-wards of the He I lines, was almost unaffected by telluric absorption and, therefore, gave a robust reference level for the pseudo-continuum (see Fig. 1).

After normalization we aligned all the spectra to the stellar rest frame. We then calculated a master out-of-transit spectrum by computing the mean spectrum of all spectra obtained out of transit, and divided each individual spectrum (in and out) by this master. This technique has been previously applied in several works (Wyttenbach et al. 2015; Salz et al. 2018; Casasayas-Barris et al. 2018). After removal of the stellar signal, the residual spectra should contain the possible atmospheric planetary signal that, in the stellar rest frame, moves through wavelength space as time progresses, from blue-shifted at the beginning of the transit to red-shifted towards the end. To obtain the transmission spectrum, we aligned these residual spectra to the planet rest frame and calculated the mean in-transit spectrum between the second and third contacts.

In Fig. 2 (left panels) the residual maps around the He I triplet are shown for each of the three nights. Also plotted are the ingress start time (first contact) and egress end time (fourth contact), as well as the expected residual trace of a possible planetary signal. Significant positive residual indicative of He I absorption was visible for night 2, but not for the other two nights. The lack of reproducible results could be indicative of a spurious signal. However, it was not clear that this was the case. For night 1, the S/N of the measurements was low due to weather conditions (see Table 1), and while a positive signal was also seen at the expected He I wavelengths, the data quality did not allow the signal to reach the 3σ significance level required to claim a detection.

For night 3, which had a S/N as night 2, the problem was the contamination of the He I signal by telluric OH^- lines. During the night, the position of the OH^- lines with respect to the He lines changed. To illustrate this, we plot in Fig. 2 (right panels) the same residual maps. In this figure, however, the spectral regions that during the transit (T1-T4) were overlapping with OH^- lines were masked. It is readily appreciable from the figure that night 3 had the largest OH^- contamination, with practically no unaffected signal from the planet. Thus, we kept the analysis of that night for completeness, but a He I signal detection was not expected for that night even if the planetary absorption was there.

Figure 3 shows the transmission spectrum of He I derived for each of the three nights. The transmission spectrum was calculated in two different ways. The first was by simply masking the OH-affected regions of the spectrum. It is plotted in the figure in black, and it is discontinuous in these affected regions. A second way to calculate the spectra was to correct for OH^- contamination, as described in Sect. 2.1. These spectra are over-plotted in red and nothing is masked. The corrected and uncorrected spectra were identical in the common regions.

In summary, we concluded from the figure that both nights 1 and 2 showed strong absorption features centered in the He I λ 10830 Å triplet. While the scatter for night 1 was large due to the low S/N of the observations, the absorption was clear for night 2, reaching 1.5 ± 0.3%. Following Nortmann et al. (2018), and using the values in Tables 1 and 2, this translated into a planetary radius increase of $R_p(\lambda)/R_p = 1.15 \pm 0.14$, or an equivalent scale height of $\Delta R_p/H_{eq} = 77 \pm 9$.

The absorption in night 1 nearly doubled that of night 2, but there were strong residual features in the transmission spectrum, at the few percent level, that were probably associated to low S/N systematics and were affecting the absorption depth. Night 3, represented at the same scale as night 2, did not show any significant absorption feature. The nightly retrieved absorption depths from the transmission spectrum and the transit light curves (see next section) are given in Table 3.

3.2. Spectro-photometric light curves

Spectro-photometric light curves from the spectral data were useful to understand if the absorption features had a temporal variability compatible with the planetary transit. Thus, in order to monitor the temporal behavior of the excess He I absorption, we calculated the transit light curves for this line. To do this, we integrated the counts in band-passes of three different widths (0.40, 0.74, and 0.97 Å) centered on the two deepest lines of the He I triplet. This integration was done in the planet rest frame. The summation intervals are marked in Fig. 1. The methodology that we followed to build the spectro-photometric light curves was described by Nortmann et al. (2018) and Casasayas-Barris et al. (2019). For GJ 3470 b, the Rossiter-McLaughlin effect on the transmission spectrum and photometric light curves is expected to be negligible.

In Fig. 4 we plot the transit light curves for the He (2^3S) absorption for each of the three nights. As in the case of the transmission spectrum, a clear transit was detected only on night 2, while the light curves for nights 1 and 3 were mainly flat. The

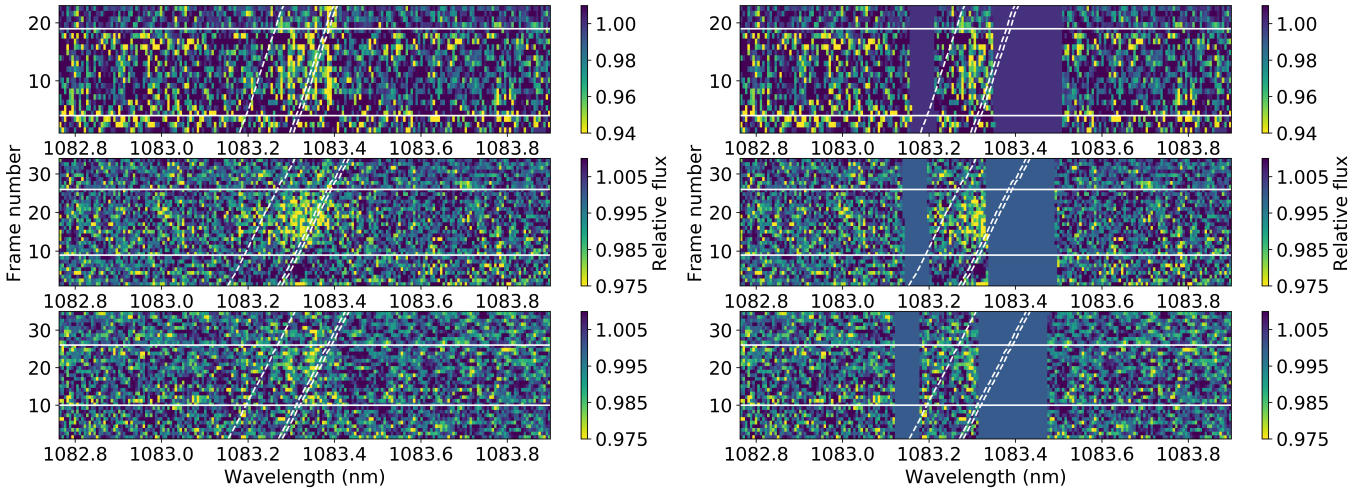

Fig. 2. Observed 2D residual maps after dividing each spectrum by the master-out spectrum. *Form top to bottom*: nights 1, 2 and 3, respectively. The data on the *right and left panels* are exactly the same, but in the *right panel*, the regions affected by OH^- contamination are masked to illustrate the amount of usable data for each night. The maps comprise the region around the He I triplet, and are shown in the stellar rest frame. The horizontal white bars mark the beginning (T1) and end (T4) of the transit. The tilted dashed lines mark the expected planetary trail of triplet. Note the different color scale between night 1 and nights 2 and 3.

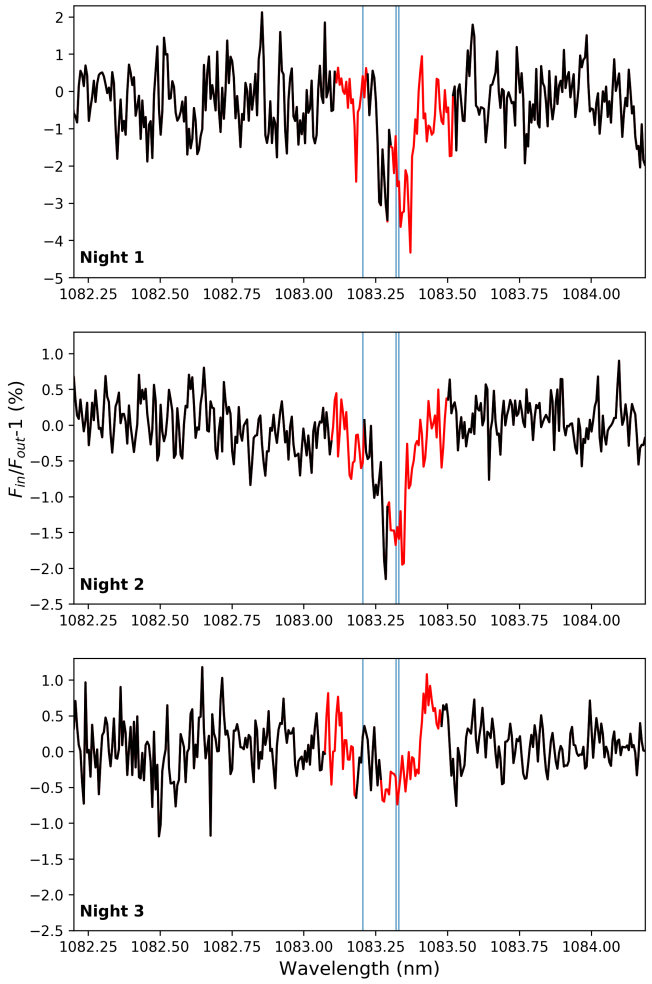

Fig. 3. Mid-transit (T2-T3) transmission spectrum around the HeI triplet for nights 1, 2 and 3, *from top to bottom*, respectively. The black line shows the spectral regions unaffected by OH^- lines, while the red line marks the spectral regions affected, and corrected for, OH^- emission. The blue vertical lines mark the helium triplet line center positions. Note the different absorption scale between night 1 and nights 2 and 3.

Table 3. Comparison table of absorption depths retrieved for each individual night.

Night	TS	TS-Nc	LC
1	2.4 ± 0.9	3.5 ± 0.9	2.1 ± 0.9
2	1.5 ± 0.3	2.2 ± 0.3	1.4 ± 0.5
3	0.4 ± 0.2	...	0.4 ± 0.3

Notes. TS means the value retrieved from the averaged absorption over a 0.4 Å-wide bin (green shadow in Fig. 1). TS-Nc is the same calculation over the transmissions spectrum without accounting for OH-corrected regions (i.e., considering black points only). LC refers to the absorption depth retrieved from the transit light curves between second (T2) and third (T3) contacts. For the transmission spectrum the error is simply calculated as the rms over the continuum region 1082.5–1083 nm.

error bars took into account the individual scatter of each spectrum and the number of points integrated. For night 1, there were a few outliers that coincided in time with ingress and egress, and may resemble of a transit feature, but there was no statistically significant additional absorption during transit. Given the low S/N of the data, this was not surprising as the construction of spectro-photometric light curves from high-dispersion spectroscopy requires a higher S/N (Casasayas-Barris et al. 2020). The non-detection of a transit signal for night 3 was consistent with the flat transmission spectrum for the same night.

For the clear transit of night 2, we observed a transit duration roughy coincident with the expected ingress and egress times. The retrieved depth of the transit was consistent with that retrieved from the transmission spectrum analysis (Table 3). An extra absorption extending further than the egress (tail structure) might be present, but it was not statistically significant within our error bars. New observations minimizing OH^- emission contamination and with larger telescopes will be needed to explore this issue. For night 2 we also observed an "emission-like" feature just before the transit, which is already visible in the 2D residual maps in Fig. 2 as a dark blue region just before the transit start. Currently, we have no explanation for this.

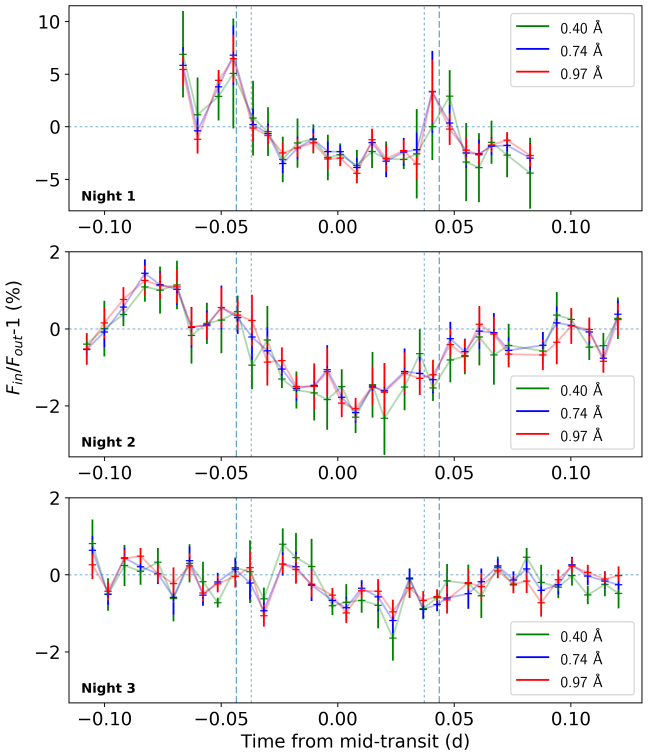

Fig. 4. Spectro-photometric light curves of the He (2^3S) absorption of the transit of GJ 3470 b for each of the three nights: 1 to 3 *from top to bottom*, respectively. The light curves have been constructed using three different wavelength integration intervals: 0.40 Å (green), 0.74 Å (blue), and 0.97 Å (red). Note the different absorption scale between night 1 and nights 2 and 3.

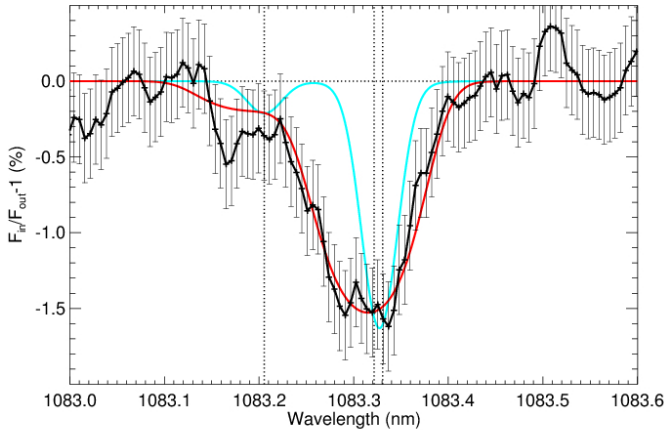

Fig. 5. Transmission spectrum of the He I triplet during transit. Measured absorption (+), and their respective estimated errors, are shown in black. The data are the same as in Fig. 3 but with a three-point running mean applied. The cyan curve shows the absorption profile when only the Doppler and turbulence broadenings are included. The red curve is the best-fit model obtained for an effective temperature of 6000 K, a mass-loss rate ($\dot{M}$) of 3×10^{10} g s^{-1} and a H/He mole-fraction ratio of 90/10. This calculation included, in addition to the Doppler and turbulence broadenings, the broadening induced by the radial velocities of the model and an additional blue net wind of –3.2 km s^{-1}. The positions of the three He I lines are marked by vertical dotted lines.

4. Modeling the He I absorption

As previously done in the case of HD 209458 b (Alonso-Floriano et al. 2019), we modeled here the He (2^3S) absorption of GJ 3470 b. Briefly, we used a one-dimensional hydrodynamic and spherically symmetric model together with a non-local thermodynamic equilibrium (non-LTE) model to calculate the He (2^3S) density distribution in the upper atmosphere of the planet (Lampón et al. 2020). The hydrodynamic equations were solved assuming that the escaping gas has a constant speed of sound, $v_s = \sqrt{kT/\mu}$, where k is the Boltzmann constant, T is temperature, and μ in the mean molecular weight. This assumption leads to the same analytical solution as the isothermal Parker wind solution. However, the atmosphere is not isothermal. Instead the temperature is such that the T/μ ratio is constant with altitude, that is, $v_s = \sqrt{kT/\mu} = \sqrt{kT_0/\bar{\mu}}$, where $\bar{\mu}$ is the average mean molecular weight calculated in the model, and T_0 is a model input parameter that is very similar to the maximum of the thermospheric temperature profile calculated by hydrodynamic models that solve the energy balance equation (see, e.g., Salz et al. 2016). The He (2^3S) absorption was later computed by using a radiative transfer code for the standard primary transit geometry (Lampón et al. 2020). The absorption coefficients and wavelengths for the three metastable He I lines were taken from the NIST Atomic Spectra Database[1]. Doppler line shapes were assumed at the atmospheric temperature used in the helium model density, and an additional broadening produced by turbulent velocities was included as described in the reference above.

[1] https://www.nist.gov/pml/atomic-spectra-database

The component of the radial velocity of the gas along the line of sight (towards the observer, i.e., arising from the planet day- and night-sides around the terminator) was also included in order to account for the motion of He (2^3S) as predicted in the hydrodynamic model. From the modeling results, we found that the He (2^3S) distribution is significantly more extended than in the case of HD 209458 b. Hence, we found it necessary to perform the integration of the He (2^3S) absorption up to 10 R_P.

Figure 5 shows the observed transmission spectrum of night 2, together with a calculation performed with the model described above for an effective temperature of 6000 K and a sub-stellar mass-loss-rate of 3×10^{10} g s^{-1}.

The inclusion of the broadening of the lines due to turbulence ($v_{turb} = \sqrt{5kT/3m}$, where m is the mass of a helium atom), in addition to the standard Doppler broadening, was not enough to explain the measured broadening in the observations (cyan line in Fig. 5). However, when we included the broadening due to the component of the radial velocities of the gas calculated in our model along the observer's line of sight, (see Eq. (15) in Lampón et al. 2020), then we were able to explain the absorption line width (red curve in Fig. 5). Because of the weak surface gravity of this planet, the obtained radial velocities were rather large, even at relatively short radii. In particular, we obtained radial velocities in the range of 5 to 20 km s^{-1} for r = 1–10 R_P. These velocities, particularly at low radii, induce a rather significant broadening as shown in Fig. 5. Nevertheless, we observed that the peak of the absorption was slightly shifted to blue wavelengths, indicating that there may be a net blue wind flowing from the day to the night side, for which we estimated a net velocity shift of -3.2 ± 1.3 km s^{-1}. This result is similar to that of –1.8 km s^{-1} found by Alonso-Floriano et al. (2019) for HD 209458b, which was also interpreted as a net day-to-night thermospheric wind. Our model, being 1D and spherically homogeneous, was not able to predict any net blue or red component. Hence, the calculation shown in Fig. 5 (red curve) was obtained by imposing a net shift of –3.2 km s^{-1} on the radial velocities computed by our model.

Table 4. Physical planet parameters for GJ 3470b, HAT-P-11 b, and GJ 436 b.

Parameter	GJ 3470 b [1–5]	HAT-P-11 b [5,6]	GJ 436 b [7–10]
Host sp. type	M2.0 V	K4 V	M2.5 V
Radius [$R_{\rm Jup}$]	0.36 ± 0.01	0.389 ± 0.005	0.374 ± 0.009
Mass [$M_{\rm Jup}$]	0.036 ± 0.002	0.0736 ± 0.0047	0.0728 ± 0.0024
Density [g cm^{-3}]	1.036 ± 0.119	1.658 ± 0.127	1.848 ± 0.163
$T_{\rm eq}$ [K]	733 ± 23	832 ± 10	686 ± 10
$F_{\rm EUV}$ [erg s^{-1} cm^{-2}]	1435 ± 80	2109 ± 153	197 ± 9
Age [Gry]	<3	6.5 ± 5.0	6.0 ± 5.0
He (2^3S) Absorption [%]	1.5 ± 0.3	1.08 ± 0.05	<0.41

References. [1]Biddle et al. (2014); [2]Kosiarek et al. (2019); [3]Dragomir et al. (2015); [4]this work; [5]Yee et al. (2018); [6]Allart et al. (2018); [7]Alonso-Floriano et al. (2015); [8]Turner et al. (2016); [9]Nortmann et al. (2018); [10]Torres et al. (2008).

Our 1D hydrodynamic and spherically symmetric model was based on the assumption of a constant sound speed and, hence, it was unable to discriminate among the temperature and the mass-loss rate. That is, both quantities are degenerate. However, it had the advantage of being computationally very efficient, which allowed us to explore a wide range of atmospheric temperatures and mass-loss rates that were compatible with the He (2^3S) absorption. Hence, this measurement significantly constrained the parameter space of those quantities. We performed calculations by covering a range of maximum temperatures from 6000 to 9000 K and found that the mass-loss rate, $\dot{M}$, is confined to a range of 3×10^{10} g s^{-1} for $T = 6000$ K to about 10×10^{10} g s^{-1} for $T = 9000$ K.

For HD 209458 b, Lampón et al. (2020) derived mass-loss rates of 1.3×10^{10} and 1.3×10^{11} g s^{-1} for those temperatures (derived for a H/He ratio of 98/2), which are slightly smaller at about 6000 K but slightly larger at a temperature of 9000 K than those derived here for GJ 3470 b for the canonical H/He ratio of 90/10. However, if considering the same H/He ratio, the mass-loss rates are about a factor of 10 larger in GJ 3470 b than in HD 209458 b.

The mass-loss rate of GJ 3470 b derived by Bourrier et al. (2018) was in the range of $(1.5–8.5)\times10^{10}$ g s^{-1}. The lower limit was derived assuming the mass-loss rate of only neutral hydrogen atoms (that is, neither H^+ nor helium were included), while the upper limit was obtained by using the energy-limited approach. Our value at 6000 K is about twice their lower limit, but both are consistent since they only include neutral hydrogen. Our rate at a temperature of 9000 K is slightly larger than their upper limit.

5. Discussion and conclusions

Here we report the detection of He I absorption in the upper atmosphere of GJ 3470 b. To understand this observation in a broader context, it is important to compare the properties of GJ 3470 b with two other well-studied Neptune planets: GJ 436 b (Butler et al. 2004; Gillon et al. 2007) and HAT-P-11 b (Bakos et al. 2010). All three planets have very close radius values (see Table 4, where the physical properties of all three planets are summarized). GJ 436 b and HAT-P-11 b have also nearly the same mass, density, and age (Demory et al. 2013; Fraine et al. 2014), while GJ 3470 b is less massive and only about half the average bulk density.

For GJ 436 b, very significant extra absorption during transit has been observed in Lyα. Both Kulow et al. (2014) and Ehrenreich et al. (2015) detected an extended transit with a comet-like tail structure, reaching a depth of almost 50% of the stellar flux. Despite this, absorption in Hα during transit has not been detected, and Cauley et al. (2017) suggested that the large cloud of neutral hydrogen surrounding GJ 436 b is almost entirely in the ground state. While a strong absorption in He (2^3S) was theoretically predicted by Oklopčić & Hirata (2018), Nortmann et al. (2018) found no detectable evidence for it. However, Salz et al. (2016) showed that the concentration of ionized hydrogen in GJ 436 b is significantly lower than in GJ 3470 b at high altitudes (at radii larger than $\sim3\,R_{\rm P}$, the region where according to our model the He (2^3S) is mainly formed). We recall that the major formation process of He (2^3S) is recombination from $He^+ + e^-$. Thus, a lower density of ionized hydrogen leads to a lower electron concentration and, consequently, to a less efficient He (2^3S) formation, which is in line with the observations of Nortmann et al. (2018). In the case of HAT-P-11 b, there are no published detections of extra absorption either in Hα or Lyα, but Allart et al. (2018) detected a strong signature of He (2^3S) absorption during transit.

For GJ 3470 b, based on ultraviolet observations of the Lyα absorption, Bourrier et al. (2018) estimated a mass-loss rate of $(1.5–8.5)\times10^{10}$ g s^{-1}, comparable to that of hot Jupiters, and concluded that the planet could already have lost up to 40% of its mass over its 2 Gyr lifetime. This observation is roughly in line (depending on the actual thermospheric temperature) with the $\dot{M}$ derived from our analysis of the observed He (2^3S) absorption described above. We obtained a value of $(3–10)\times10^{10}$ g s^{-1} for a temperature range of 6000–9000 K. Those values are also comparable to the ones obtained by Lampón et al. (2020) for He (2^3S) $\dot{M}$ of the hot Jupiter HD 209458 b. We caution, however, that there is a strong dependency of these values on the assumed H/He ratio values, which are currently unknown. Lampón et al. (2020) derived similar mass-loss rate by using H/He = 98/2, imposed by the Lyα measurements, but they had large errors as only the wings of the line were detected. If we used only the He (2^3S) measurements and assumed the same H/He = 90/10 for both HD 209458 b and GJ 3470 b, then the mass-loss rate of GJ 3470 b would be about a factor 10 larger than caculated in Sect. 4.

It is of particular interest to consider why planets with such similar physical properties display very different upper atmospheric escape properties. As discussed in Nortmann et al. (2018), the formation of the He I λ10830 Å triplet in exoplanet atmospheres is directly linked to the stellar irradiation with $\lambda < 504$ Å, which ionizes the neutral helium atoms, with

a subsequent recombination with electrons. Therefore, it is essential to know the X-ray and extreme ultraviolet (XUV) irradiation in this spectral range. The X-ray observations of GJ 3470 reveal a moderately active star ($\log L_X/L_{bol} = -4.8$) with some flaring variability (Sanz-Forcada et al., in prep.). The analysis of the X-ray spectrum and ultraviolet lines was used to construct a coronal model and calculate a spectral energy distribution in the full range 1–1200 Å (Bourrier et al. 2018, and Sanz-Forcada et al., in prep.). The XUV luminosity in the 5–504 Å range is $L_{XUV\ He} = 5 \times 10^{27}$ erg s^{-1}, yielding an irradiation in this band at the distance of GJ 3470 b of $f_{XUV\ He} = 1435$ erg s^{-1} cm^{-2}. Thus, the $f_{XUV,He}$ of GJ 3470 b is similar to that of HAT-P-11 b, but it is almost one order of magnitude larger than that of GJ 436 b (Table 4). While the youth and lower density of GJ 3470 b compared to the other two Neptunes surely plays a role, our results suggest that He (2^3S) ionization is mainly driven by XUV stellar irradiation.

As mentioned above, we previously analyzed the He (2^3S) absorption detection in the hot Jupiter HD 209458 b (Alonso-Floriano et al. 2019; Lampón et al. 2020), another CARMENES target of our He I survey. We noticed two significant differences. First, the He (2^3S) absorption profile of GJ 3470 b is significantly wider than in HD 209458 b. Secondly, our model showed that the absorption in GJ 3470 b takes place mainly in the outer regions. Both facts suggest that GJ 3470 b has a rather expanded atmosphere with strong winds prevailing in its upper thermosphere. These results are in line with its lower gravity with respect to HD 209458 b. Moreover, we found that the $\dot{M}$/T relationship derived from the measured He (2^3S) absorptions are rather different: GJ 3470 b exhibits comparable or even larger $\dot{M}$ (for the same temperature) than the hot Jupiter HD 209458 b. These results suggest that escape of GJ 3470 b is possibly driven by a different process than in HD 209458 b.

Acknowledgements. CARMENES is an instrument for the Centro Astronómico Hispano-Alemán (CAHA) at Calar Alto (Almería, Spain), operated jointly by the Junta de Andalucía and the Instituto de Astrofísica de Andalucía (CSIC). CARMENES was funded by the German Max-Planck-Gesellschaft (MPG), the Spanish Consejo Superior de Investigaciones Científicas (CSIC), the European Union through FEDER/ERF FICTS-2011-02 funds, and the members of the CARMENES Consortium. We acknowledge financial support from the Agencia Estatal de Investigación of the Ministerio de Ciencia, Innovación y Universidades and the European FEDER/ERF funds through projects ESP2016-80435-C2-2-R, ESP2016-76076-R, and BES-2015-074542, and AYA2016-79425-C3-1/2/3-P, the Deutsche Forschungsgemeinschaft through the Research Unit FOR2544 "Blue Planets around Red Stars" and the Priority Program SPP 1992 "Exploring the Diversity of Extrasolar Planets" RE 1664/16-1, the National Natural Science Foundation of China through grants 11503088, 11573073, and 11573075, and the Natural Science Foundation of Jiangsu Province through grant BK20190110. Finally, we wish to thank Dr. Vincent Bourrier and an anonymous referee for discussion and comments that helped to improve the contents of this manuscript.

References

Allart, R., Bourrier, V., Lovis, C., et al. 2018, Science, 362, 1384
Alonso-Floriano, F. J., Morales, J. C., Caballero, J. A., et al. 2015, A&A, 577, A128
Alonso-Floriano, F. J., Snellen, I. A. G., Czesla, S., et al. 2019, A&A, 629, A110
Awiphan, S., Kerins, E., Pichadee, S., et al. 2016, MNRAS, 463, 2574
Bakos, G. Á., Torres, G., Pál, A., et al. 2010, ApJ, 710, 1724
Biddle, L. I., Pearson, K. A., Crossfield, I. J. M., et al. 2014, MNRAS, 443, 1810
Birkby, J. L., de Kok, R. J., Brogi, M., et al. 2013, MNRAS, 436, L35
Bonfils, X., Gillon, M., Udry, S., et al. 2012, A&A, 546, A27
Bourrier, V., Lecavelier des Etangs, A., Ehrenreich, D., et al. 2018, A&A, 620, A147
Butler, R. P., Vogt, S. S., Marcy, G. W., et al. 2004, ApJ, 617, 580
Caballero, J. A., Guàrdia, J., López del Fresno, M., et al. 2016, SPIE Conf. Ser. 9910, 99100E
Casasayas-Barris, N., Pallé, E., Yan, F., et al. 2018, A&A, 616, A151
Casasayas-Barris, N., Pallé, E., Yan, F., et al. 2019, A&A, 628, A9
Casasayas-Barris, N., Pallé, E., Yan, F., et al. 2020, A&A, 635, A206
Cauley, P. W., Redfield, S., & Jensen, A. G. 2017, AJ, 153, 81
Chen, G., Guenther, E. W., Pallé, E., et al. 2017, A&A, 600, A138
de Kok, R. J., Brogi, M., Snellen, I. A. G., et al. 2013, A&A, 554, A82
Delfosse, X., Forveille, T., Ségransan, D., et al. 2000, A&A, 364, 217
Demory, B.-O., Torres, G., Neves, V., et al. 2013, ApJ, 768, 154
Dragomir, D., Benneke, B., Pearson, K. A., et al. 2015, ApJ, 814, 102
Ehrenreich, D., Bonfils, X., Lovis, C., et al. 2014, A&A, 570, A89
Ehrenreich, D., Bourrier, V., Wheatley, P. J., et al. 2015, Nature, 522, 459
Fraine, J., Deming, D., Benneke, B., et al. 2014, Nature, 513, 526
Fulton, B. J., & Petigura, E. A. 2018, AJ, 156, 264
Fulton, B. J., Petigura, E. A., Howard, A. W., et al. 2017, AJ, 154, 109
Gaia Collaboration (Brown, A. G. A., et al.) 2018, A&A, 616, A1
Gaidos, E., Mann, A. W., Lépine, S., et al. 2014, MNRAS, 443, 2561
Gillon, M., Pont, F., Demory, B. O., et al. 2007, A&A, 472, L13
Gliese, W., & Jahreiß, H. 1991, Preliminary Version of the Third Catalogue of Nearby Stars, Tech. rep.
Guilluy, G., Sozzetti, A., Brogi, M., et al. 2019, A&A, 625, A107
Kausch, W., Noll, S., Smette, A., et al. 2015, A&A, 576, A78
Kosiarek, M. R., Crossfield, I. J. M., Hardegree-Ullman, K. K., et al. 2019, AJ, 157, 97
Kulow, J. R., France, K., Linsky, J., & Loyd, R. O. P. 2014, ApJ, 786, 132
Lammer, H., Erkaev, N. V., Odert, P., et al. 2013, MNRAS, 430, 1247
Lampón, M., López-Puertas, M., Lara, L. M., et al. 2020, A&A, 636, A13
Lépine, S., Hilton, E. J., Mann, A. W., et al. 2013, AJ, 145, 102
Lundkvist, M. S., Kjeldsen, H., Albrecht, S., et al. 2016, Nat. Commun., 7, 11201
Luyten, W. J. 1979, New Luyten catalogue of stars with proper motions larger than two tenths of an arcsecond; and first supplement, NLTT (Minneapolis, 1979) ; Label 12 = short description; Label 13 = documentation by Warren; Label 14 = catalogue
Mann, A. W., Dupuy, T., Kraus, A. L., et al. 2019, ApJ, 871, 63
Nascimbeni, V., Piotto, G., Pagano, I., et al. 2013, A&A, 559, A32
Ninan, J. P., Stefansson, G., Mahadevan, S., et al. 2019, ApJ, 894, 97
Nortmann, L., Pallé, E., Salz, M., et al. 2018, Science, 362, 1388
Oklopčić, A., & Hirata, C. M. 2018, ApJ, 855, L11
Owen, J. E., & Wu, Y. 2013, ApJ, 775, 105
Pallé, E., Zapatero Osorio, M. R., & García Muñoz, A. 2011, ApJ, 728, 19
Passegger, V. M., Schweitzer, A., Shulyak, D., et al. 2019, A&A, 627, A161
Quirrenbach, A., Amado, P. J., Caballero, J. A., et al. 2014, Proc. SPIE, 9147, 91471F
Quirrenbach, A., Amado, P. J., Ribas, I., et al. 2018, SPIE Conf. Ser., 10702, 107020W
Salz, M., Czesla, S., Schneider, P. C., & Schmitt, J. H. M. M. 2016, A&A, 586, A75
Salz, M., Czesla, S., Schneider, P. C., et al. 2018, A&A, 620, A97
Schweitzer, A., Passegger, V. M., Cifuentes, C., et al. 2019, A&A, 625, A68
Seager, S., & Sasselov, D. D. 2000, ApJ, 537, 916
Skrutskie, M. F., Cutri, R. M., Stiening, R., et al. 2006, AJ, 131, 1163
Smette, A., Sana, H., Noll, S., et al. 2015, A&A, 576, A77
Snellen, I. A. G., de Kok, R. J., de Mooij, E. J. W., & Albrecht, S. 2010, Nature, 465, 1049
Snellen, I. A. G., de Kok, R. J., le Poole, R., Brogi, M., & Birkby, J. 2013, ApJ, 764, 182
Soubiran, C., Jasniewicz, G., Chemin, L., et al. 2018, A&A, 616, A7
Spake, J. J., Sing, D. K., Evans, T. M., et al. 2018, Nature, 557, 68
Suárez Mascareño, A., Rebolo, R., González Hernández, J. I., & Esposito, M. 2015, MNRAS, 452, 2745
Torres, G., Winn, J. N., & Holman, M. J. 2008, ApJ, 677, 1324
Turner, J. D., Pearson, K. A., Biddle, L. I., et al. 2016, MNRAS, 459, 789
Van Eylen, V., Agentoft, C., Lundkvist, M. S., et al. 2018, MNRAS, 479, 4786
Vidal-Madjar, A., Lecavelier des Etangs, A., Désert, J. M., et al. 2003, Nature, 422, 143
Wöllert, M., & Brandner, W. 2015, A&A, 579, A129
Wyttenbach, A., Ehrenreich, D., Lovis, C., Udry, S., & Pepe, F. 2015, A&A, 577, A62
Wyttenbach, A., Lovis, C., Ehrenreich, D., et al. 2017, A&A, 602, A36
Yee, S. W., Petigura, E. A., Fulton, B. J., et al. 2018, AJ, 155, 255
Zechmeister, M., Reiners, A., Amado, P. J., et al. 2018, A&A, 609, A12

3

Characterisation of the upper atmosphere of HD 209458 b

This Chapter has been published in the journal Astronomy and Astrophysics with the title “Modelling the He I triplet absorption at 10 830 Å in the atmosphere of HD 209458 b”. Lampón et al. A&A, 636, A13 (2020), reproduced with permission ©ESO.

A&A 636, A13 (2020)
https://doi.org/10.1051/0004-6361/201937175
© ESO 2020

Astronomy & Astrophysics

Modelling the He I triplet absorption at 10 830 Å in the atmosphere of HD 209458 b

M. Lampón[1], M. López-Puertas[1], L. M. Lara[1], A. Sánchez-López[1], M. Salz[2], S. Czesla[2], J. Sanz-Forcada[3], K. Molaverdikhani[4], F. J. Alonso-Floriano[5], L. Nortmann[6,7], J. A. Caballero[3], F. F. Bauer[1], E. Pallé[6,7], D. Montes[8], A. Quirrenbach[9], E. Nagel[2], I. Ribas[10,11], A. Reiners[12], and P. J. Amado[1]

[1] Instituto de Astrofísica de Andalucía (IAA-CSIC), Glorieta de la Astronomía s/n, 18008 Granada, Spain
e-mail: mlampon@iaa.es
[2] Hamburger Sternwarte, Universität Hamburg, Gojenbergsweg 112, 21029 Hamburg, Germany
[3] Centro de Astrobiología (CSIC-INTA), ESAC, Camino bajo del castillo s/n, 28692 Villanueva de la Cañada, Madrid, Spain
[4] Max-Planck-Institut für Astronomie, Königstuhl 17, 69117 Heidelberg, Germany
[5] Leiden Observatory, Leiden University, Postbus 9513, 2300 RA, Leiden, The Netherlands
[6] Instituto de Astrofísica de Canarias, Calle Vía Láctea s/n, 38200 La Laguna, Tenerife, Spain
[7] Departamento de Astrofísica, Universidad de La Laguna, 38026 La Laguna, Tenerife, Spain
[8] Departamento de Física de la Tierra y Astrofísica & IPARCOS-UCM (Instituto de Física de Partículas y del Cosmos de la UCM), Facultad de Ciencias Físicas, Universidad Complutense de Madrid, 28040 Madrid, Spain
[9] Landessternwarte, Zentrum für Astronomie der Universität Heidelberg, Königstuhl 12, 69117 Heidelberg, Germany
[10] Institut de Ciències de l'Espai (CSIC-IEEC), Campus UAB, c/ de Can Magrans s/n, 08193 Bellaterra, Barcelona, Spain
[11] Institut d'Estudis Espacials de Catalunya (IEEC), 08034 Barcelona, Spain
[12] Institut für Astrophysik, Georg-August-Universität, Friedrich-Hund-Platz 1, 37077 Göttingen, Germany

Received 22 November 2019 / Accepted 21 February 2020

ABSTRACT

Context. HD 209458 b is an exoplanet with an upper atmosphere undergoing blow-off escape that has mainly been studied using measurements of the Lyα absorption. Recently, high-resolution measurements of absorption in the He I triplet line at 10 830 Å of several exoplanets (including HD 209458 b) have been reported, creating a new opportunity to probe escaping atmospheres.
Aims. We aim to better understand the atmospheric regions of HD 209458 b from where the escape originates.
Methods. We developed a 1D hydrodynamic model with spherical symmetry for the HD 209458 b thermosphere coupled with a non-local thermodynamic model for the population of the He I triplet state. In addition, we performed high-resolution radiative transfer calculations of synthetic spectra for the helium triplet lines and compared them with the measured absorption spectrum in order to retrieve information about the atmospheric parameters.
Results. We find that the measured spectrum constrains the [H]/[H$^+$] transition altitude occurring in the range of 1.2 R_P–1.9 R_P. Hydrogen is almost fully ionised at altitudes above 2.9 R_P. We also find that the X-ray and extreme ultraviolet absorption takes place at effective radii from 1.16 to 1.30 R_P, and that the He I triplet peak density occurs at altitudes from 1.04 to 1.60 R_P. Additionally, the averaged mean molecular weight is confined to the 0.61–0.73 g mole^{-1} interval, and the thermospheric H/He ratio should be larger than 90/10, and most likely approximately 98/2. We also provide a one-to-one relationship between mass-loss rate and temperature. Based on the energy-limited escape approach and assuming heating efficiencies of 0.1–0.2, we find a mass-loss rate in the range of $(0.42–1.00) \times 10^{11}$ g s^{-1} and a corresponding temperature range of 7125–8125 K.
Conclusions. The analysis of the measured He I triplet absorption spectrum significantly constrains the thermospheric structure of HD 209458 b and advances our knowledge of its escaping atmosphere.

Key words. planets and satellites: atmospheres – planets and satellites: individual: HD 209458 b – planets and satellites: gaseous planets

1. Introduction

Close-in exoplanets receive considerable high-energy irradiation that triggers an outgoing bulk motion and expands their atmospheres. This in turn results in a very efficient mechanism for atmospheric mass loss. In some cases, the velocity reaches supersonic values that give rise to the so-called blow-off escape. This escape process is key for understanding the formation and evolution of observed (exo)planets. Lecavelier des Etangs et al. (2004) showed that such an efficient escape could lead to the loss of a significant fraction of the atmosphere in hot Jupiters, or even to a complete atmospheric loss in some hot Neptunes. In the same vein, Locci et al. (2019) showed that the occurrence of gas giants of less than 2 M_{Jup} in young stars is higher than in old ones. Furthermore, evaporation escape has also been invoked to explain the distribution with respect to the star–planet separation of super-Earths and mini-Neptunes (Jin & Mordasini 2018). Observations of extended atmospheres and their modelling are therefore essential for understanding the physical conditions that trigger evaporation escape and for obtaining a deeper understanding of planetary diversity, formation, and evolution.

The first detection of an evaporating atmosphere was reported by Vidal-Madjar et al. (2003), who observed the

Lyα line in absorption in the atmosphere of HD 209458 b and concluded that the signal originated from escaping hydrogen. Subsequent studies, both theoretical (e.g., Yelle 2004; Tian et al. 2005; Penz et al. 2008; Sanz-Forcada et al. 2010, 2011; Koskinen et al. 2013; Salz et al. 2016) and observational (Vidal-Madjar et al. 2003, 2004, 2008, 2013; Ballester et al. 2007; Ballester & Ben-Jaffel 2015; Linsky et al. 2010; Ehrenreich et al. 2008; Ben-Jaffel & Hosseini 2010; Jensen et al. 2012), supported the prediction that the extended atmosphere of HD 209458 b can be explained by a highly effective escape. Following this thread, hydrodynamic escape models were used to explain the observations of the absorption excess in Lyα and ultraviolet (UV) in other planets, such as in HD 189733 b, WASP-12 b, GJ 436 b, GJ 3470 b, and KELT-9 b (Vidal-Madjar et al. 2013; Ehrenreich et al. 2008, 2015; Lecavelier des Etangs et al. 2010, 2012; Fossati et al. 2010; Haswell et al. 2012; Bourrier & Lecavelier des Etangs 2013; Ben-Jaffel & Ballester 2013; Kulow et al. 2014; Lavie et al. 2017; Yan & Henning 2018).

Lyα observations are restricted to space-based telescopes and are significantly affected by absorption in the interstellar medium, which leads to a scarcity of observational data. The He I $2^3S - 2^3P$ triplet, hereafter He(2^3S), composed of three lines at 10 830.33, 10 830.25, and 10 829.09 Å, is not strongly absorbed by the interstellar medium (Indriolo et al. 2009) and can be observed from the ground. Seager & Sasselov (2000) studied transmission spectra for close-in planets and estimated significant absorption of He(2^3S) that could be observable, particularly when the planet has an extended atmosphere. More recently, Oklopčić & Hirata (2018) developed a model suitable for estimating He(2^3S) absorption in extended atmospheres.

He(2^3S) absorption was detected for the first time in the atmosphere of WASP-107 b with the Wide Field Camera 3 (WFC3) onboard the *Hubble* Space Telescope (HST; Spake et al. 2018), and almost simultaneously with the high-resolution spectrograph CARMENES (Calar Alto high-Resolution search for M dwarfs with Exoearths with Near-infrared and optical Échelle Spectrographs; Quirrenbach et al. 2016, 2018) at the 3.5 m Calar Alto Telescope in the atmospheres of WASP–69 b (Nortmann et al. 2018), HAT–P–11 b (Allart et al. 2018), and HD 189733 b (Salz et al. 2018). A few more observations were also recently performed. Thus, HAT–P–11 b data were acquired with WFC3 (Mansfield et al. 2018), whereas CARMENES was also used to observe WASP-107 b (Allart et al. 2019) and HD 209458 b (Alonso-Floriano et al. 2019).

In this work we analyse the new He(2^3S) observations of HD 209458 b reported by Alonso-Floriano et al. (2019). Based on the fact that this absorption probes the region where the escape originates, we aim at gaining a better understanding of the atmosphere of HD 209458 b and establishing tighter constraints on its mass-loss rate, temperature, and composition (e.g. the H/He ratio). To this end, we developed a 1D hydrodynamic and spherically symmetric model together with a non-local thermodynamic model for the He(2^3S) state similar to that reported by Oklopčić & Hirata (2018). The overall model computes the He(2^3S) radial distribution that it is then entered into a high-resolution line-by-line radiative transfer model in order to compute He(2^3S) absorption profiles. Synthetic spectra are then compared with the observed one in order to derive the properties of the escaping atmosphere.

This paper is organised as follows: Sect. 2 summarises the observations and Sect. 3 describes the modelling of the He(2^3S) radial densities and its absorption. The results, and a discussion on comparisons with previous works for the mass-loss rate, temperature, and H density, are presented in Sect. 4. The main conclusions are summarised in Sect. 5.

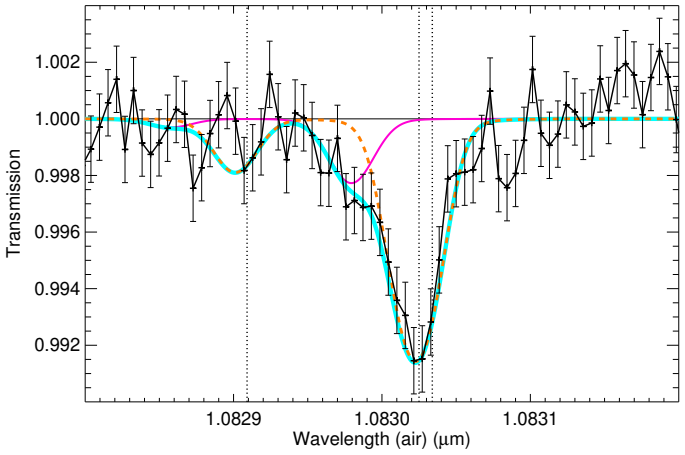

Fig. 1. Spectral transmission of the He triplet at mid transit. Data points and their respective error bars are shown in black (adapted from Alonso-Floriano et al. 2019). The orange dash curve is the best fit obtained for a temperature of 6000 K, a mass-loss rate ($\dot{M}$) of 1.9×10^9 g s^{-1}, and an H/He mole-fraction ratio of 90/10 (see Sect. 4). We note that these values have changed with respect to those reported in Alonso-Floriano et al. (2019). The magenta line is a modelled absorption of the helium triplet moving along the observer's line of sight with -13 km s^{-1} with respect to the rest-frame of the planet and using the appropriate He(2^3S) density to fit the measured spectrum. The cyan curve is the total modelled absorption. The positions of the three helium lines are marked by vertical dotted lines.

2. Observations of He I λ10 830 Å absorption

Here we briefly summarise the observations reported by Alonso-Floriano et al. (2019) of the helium excess absorption from the atmosphere of HD 209458 b using CARMENES (see Fig. 1). The He excess absorption peaks at a value of 0.91±0.10% at mid-transit. The core of the absorption shows a net blueshift of 1.8 ± 1.3 km s^{-1}, suggesting that the helium envelope moves at that velocity, in the line of sight from the Earth with respect to the rest-frame of the planet. This velocity is rather low, similar to that reported by Snellen et al. (2010) from observations of the carbon monoxide band near 2 μm that occurs in the lower thermosphere, and suggests that the He triplet absorption takes place at relatively low altitudes (within a few planetary radii, see Sect. 4 below).

Figure 1 also shows excess absorption near 10 829.8 Å. Since the absorption is well above the estimated errors, it might be caused by an additional atmospheric absorption component. However, it is largely blue shifted, by around 13 km s^{-1}, and therefore could be due to atmospheric escape occurring beyond the thermosphere. Alonso-Floriano et al. (2019) constructed the light curve of the He I signal (see their Fig. 5) and obtained an average in-transit absorption of ~0.44%, about a factor two smaller than the peak absorption. However, there is no clear evidence for pre- or post-transit absorption signals.

We assumed a one-dimensional hydrodynamic and spherically symmetric model for analysing this absorption. This simplification is justified because: (1) the bulk of the absorption takes place at relatively low radii, well below the Roche lobe height, and with rather low wind velocities; (2) there are no clear signs of asymmetry in the absorption; and (3) the light curve does not exhibit signs of pre- or post-transit absorption – for

Table 1. System parameters of HD 209458.

Parameter	Value	Reference
$R_\star$	$1.155^{+0.014}_{-0.016}\,R_\odot$	Torres et al. (2008)
$M_\star$	$1.119 \pm 0.033\,M_\odot$	Torres et al. (2008)
$T_{\rm eff}$	6065 ± 50 K	Torres et al. (2008)
[Fe/H]$_\star$	0.02 ± 0.05	Santos et al. (2004)
a	$0.04707^{+0.00046}_{-0.00047}$ au	Torres et al. (2008)
$R_{\rm P}$	$1.359^{+0.016}_{-0.019}\,R_{\rm Jup}$	Torres et al. (2008)
$M_{\rm P}$	$0.685^{+0.015}_{-0.014}\,M_{\rm Jup}$	Torres et al. (2008)

example there are no cometary-like tail features. This model also has the advantage that it is computationally very efficient with respect to 1D models that solve the energy balance equation, and is about one order of magnitude faster than the model of García-Muñoz (2007; priv. comm.) and about two orders of magnitude faster than the model of Salz et al. (2016). It also allows us to explore a wide range of atmospheric parameters, and yet gives reasonable density distributions (see, e.g. the comparison with the model of Salz et al. 2016 in Sect. 3.1 and Fig. 3 below).

The analysis of the velocity shifts in the He(2^3S) absorption is potentially interesting because it would provide us information about the 3D velocity distribution and maybe also break some of the degeneracy between temperature and mass-loss rates. Our model, as it is one dimensional and spherically symmetric, cannot explain net blue or red shifts and therefore such an analysis is beyond the scope of this paper. Nevertheless, in order to better fit the measured spectrum we assume a velocity of $-1.8\,{\rm km\,s^{-1}}$along the observational line of sight superimposed on the radial velocities of our model. In the following sections we describe the He triplet density model and the radiative absorption calculations used to constrain the characteristics of the escaping atmosphere of this planet.

3. Modelling of the helium triplet density and the absorption

We computed the He(2^3S) radial density by means of a 1D hydrodynamic and spherically symmetric model (see, e.g. Yelle 2004; Tian et al. 2005; García-Muñoz 2007; Koskinen et al. 2013; Salz et al. 2016) and following the methods discussed in Oklopčić & Hirata (2018). The hydrodynamic equations for mass and momentum conservation, for a steady-state radial atmospheric outflow are given by

$$\frac{{\rm d}\left(r^2\,\rho(r)\,v(r)\right)}{{\rm d}r} = 0, \tag{1}$$

and

$$v(r)\,\frac{{\rm d}v}{{\rm d}r} + \frac{1}{\rho(r)}\frac{{\rm d}p}{{\rm d}r} + \frac{G\,M_{\rm P}}{r^2} = 0, \tag{2}$$

where r is the distance from the centre of the planet; ρ and v are the mass density and bulk radial velocity of the gas, respectively; p is the gas pressure; G the gravitational constant; and $M_{\rm P}$ is the planet mass (see Table 1). The momentum equation contains only the forces induced by the gravity of the planet and the gas pressure, neglecting other forces such as the stellar gravitational pull and fluid viscosity. We also consider the atmosphere as an ideal gas, $p = \rho\,k\,T/\mu$, where k is Boltzmann's constant, T is temperature, and μ is the gas mean molecular weight. The pressure gradient can then be written as

$$\frac{{\rm d}p}{{\rm d}r} = \frac{k\,T(r)}{\mu(r)}\frac{{\rm d}\rho}{{\rm d}r} + \rho(r)\,\frac{\rm d}{{\rm d}r}\left(\frac{k\,T(r)}{\mu(r)}\right). \tag{3}$$

The derivative of Eq. (1) gives

$$\frac{1}{\rho(r)}\frac{{\rm d}\rho}{{\rm d}r} = -\frac{1}{v(r)}\frac{{\rm d}v}{{\rm d}r} - \frac{2}{r}, \tag{4}$$

and including Eqs. (3) and (4) into the momentum continuity equation (Eq. (2)), this becomes

$$v(r)\frac{{\rm d}v}{{\rm d}r} + v_{\rm s}^2(r)\left(-\frac{1}{v(r)}\frac{{\rm d}v}{{\rm d}r} - \frac{2}{r}\right) + \frac{{\rm d}(v_{\rm s}^2(r))}{{\rm d}r} + \frac{G\,M_{\rm P}}{r^2} = 0, \tag{5}$$

where $v_{\rm s}(r) = \left[k\,T(r)/\mu(r)\right]^{1/2}$ is the gas speed of sound.

To solve Eq. (5) we need to incorporate the energy and species continuity equations into the system, which requires the use of computationally expensive numerical methods. Our aim is to develop a very fast hydrodynamic model in order to explore and constrain the mass-loss rate and temperatures imposed by the He(2^3S) absorption measurements. To that end, we assume here a constant speed of sound, $v_{\rm s,0}$, which allows us to decouple the momentum equation from the energy budget equation and obtain a simple expression for Eq. (5) that can be solved analytically. This expression is known as the isothermal Parker wind approximation, previously studied by Parker (1958) for describing stellar winds, and can be written as

$$\frac{1}{v(r)}\frac{{\rm d}v}{{\rm d}r}\left(\frac{v^2(r)}{v_{\rm s,0}^2} - 1\right) = \frac{2}{r} - \frac{G\,M_{\rm P}}{v_{\rm s,0}^2\,r^2}. \tag{6}$$

However, our approach does not require temperature to be necessarily constant, but to have the same inverse altitude dependence as $\mu(r)$ so that the ratio $T(r)/\mu(r)$ is constant, i.e. $v_{\rm s,0} = \left[k\,T(r)/\mu(r)\right]^{1/2}$.

We obtain the constant speed of sound from

$$v_{\rm s,0} = \left(\frac{k\,T_0}{\bar{\mu}}\right)^{1/2}, \tag{7}$$

where we introduce a constant temperature T_0 and the corresponding average mean molecular weight $\bar{\mu}$ of the gas. This quantity is calculated using Eq. (A.3), which is constructed such that it provides an accurate calculation of the integrals over velocity and radius of the hydrodynamic equations.

Below we discuss (see Sect. 3.1) the validity and scope of this approach. In particular, the total density of our model closely matches that obtained by more comprehensive models when the constant speed of sound is equal to the maximum speed of sound of those models. Under these conditions, the T_0 of our model is very close to the maximum of the temperature profile obtained by those models.

Equation (6) has infinite solutions but only one has a physical interpretation in terms of escape: the transonic solution that describes a subsonic velocity of the gas at distances below the sonic point (the altitude where wind velocity is equal to the speed of sound) and supersonic beyond that point (see, e.g.

Table 2. Production and loss processes included in the He(2^3S) model.

Name	Process	Rate [a]	References
$J_{\rm H}$	$\rm H + h\nu \rightarrow H^+ + e^-$	See text	Osterbrock & Ferland (2006)
$\alpha_{\rm H}$	$\rm H^+ + e^- \rightarrow H$	$2.59\times10^{-13}(T/10^4)^{-0.700}$	Osterbrock & Ferland (2006)
$J_{\rm He^1S}$	$\rm He(1^1S) + h\nu \rightarrow He^+ + e^-$	See text	Brown (1971)
α_1	$\rm He^+ + e^- \rightarrow He(1^1S)$	$1.54\times10^{-13}(T/10^4)^{-0.486}$	Benjamin et al. (1999)
$J_{\rm He^3S}$	$\rm He(2^3S) + h\nu \rightarrow He^+ + e^-$	See text	Norcross (1971)
α_3	$\rm He^+ + e^- \rightarrow He(2^3S)$	$2.10\times10^{-13}(T/10^4)^{-0.778}$	Benjamin et al. (1999)
q_{13}	$\rm He(1^1S) + e^- \rightarrow He(2^3S) + e^-$	$2.10\times10^{-8}\sqrt{\frac{13.6}{kT}}\exp\left(-\frac{19.81}{kT}\right)\Upsilon_{13}$	Bray et al. (2000); Oklopčić & Hirata (2018)
q_{31a}	$\rm He(2^3S) + e^- \rightarrow He(2^1S) + e^-$	$2.10\times10^{-8}\sqrt{\frac{13.6}{kT}}\exp\left(-\frac{0.80}{kT}\right)\frac{\Upsilon_{31a}}{3}$	Bray et al. (2000); Oklopčić & Hirata (2018)
q_{31b}	$\rm He(2^3S) + e^- \rightarrow He(2^1P) + e^-$	$2.10\times10^{-8}\sqrt{\frac{13.6}{kT}}\exp\left(-\frac{1.40}{kT}\right)\frac{\Upsilon_{31b}}{3}$	Bray et al. (2000); Oklopčić & Hirata (2018)
Q_{31}	$\rm He(2^3S) + H \rightarrow He(1^1S) + H$	5.00×10^{-10}	Roberge & Dalgarno (1982); Oklopčić & Hirata (2018)
$Q_{\rm He^+}$	$\rm He^+ + H \rightarrow He(1^1S) + H^+$	$1.25\times10^{-15}\left(\frac{300}{T}\right)^{-0.25}$	Glover & Jappsen (2007); Koskinen et al. (2013)
$Q_{\rm He}$	$\rm He(1^1S) + H^+ \rightarrow He^+ + H$	$1.75\times10^{-11}\left(\frac{300}{T}\right)^{0.75}\exp\left(\frac{-128\,000}{T}\right)$	Glover & Jappsen (2007); Koskinen et al. (2013)
A_{31}	$\rm He(2^3S) \rightarrow He(1^1S) + h\nu$	1.272×10^{-4}	Drake (1971); Oklopčić & Hirata (2018)

Notes. [a]Units are [$\rm cm^{-3}\,s^{-1}$] for the recombination and collisional processes and [$\rm s^{-1}$] for the other processes. Υ_{ij} are the effective collision strengths taken from Bray et al. (2000) at the corresponding temperatures.

Parker 1958; Lamers & Cassinelli 1999). Integrating Eq. (6) and selecting the solutions that cross the sonic point, we have

$$\frac{v(r)}{v_{\rm s,0}}\exp\left[-\frac{v^2(r)}{2v_{\rm s,0}^2}\right] = \left(\frac{r_{\rm s}}{r}\right)^2\exp\left(-\frac{2r_{\rm s}}{r}+\frac{3}{2}\right), \tag{8}$$

where $r_{\rm s} = G\,M_{\rm P}/2\,v_{\rm s,0}^2$ is the radial distance of the sonic point. Of the two possible solutions of Eq. (8) the transonic one is the solution that provides the velocity profile of the hydrodynamic escape.

Integrating Eq. (1) and taking into account spherical symmetry, the mass-loss rate, $\dot{M}$, can be expressed by

$$\dot{M} = 4\,\pi\,r^2\,\rho(r)\,v(r), \tag{9}$$

and including the velocity profile from Eq. (8), the density profile results in

$$\frac{\rho(r)}{\rho_{\rm s}} = \exp\left[\frac{2r_{\rm s}}{r}-\frac{3}{2}-\frac{v^2(r)}{2v_{\rm s,0}^2}\right], \tag{10}$$

where $\rho_{\rm s}$ is the gas density at the sonic point.

The radial distribution of the species H, $\rm H^+$, helium singlet, hereafter He(1^1S), $\rm He^+$, and He(2^3S), are obtained by solving their respective continuity equations,

$$-\,v(r)\,\frac{\partial f_i}{\partial r} + P_i + L_i = 0, \tag{11}$$

where the first term accounts for advection, f_i is the fraction of species i (i.e. with respect to the total – neutral, ionised, and excited atom concentrations – of species i), P_i is the production, and L_i is the loss term.

The production and loss terms and corresponding rates included for the different species are essentially those considered by Oklopčić & Hirata (2018), but two additional processes have been included: the charge exchange reactions, $Q_{\rm He}$ and $Q_{\rm He^+}$, which were taken from Koskinen et al. (2013); see Table 2.

Thus, production and loss incorporate photo-ionisation and recombination processes of atomic hydrogen (processes $J_{\rm H}$ and $\alpha_{\rm H}$ in Table 2). For helium, these processes include photo-ionisation ($J_{\rm He^1S}$ and $J_{\rm He^3S}$), recombination (α_1 and α_3), collisional excitation and de-excitation with electrons (q_{13} and q_{31}), collisional de-activation with H atoms (Q_{31}), charge exchange between atoms and ions ($Q_{\rm He}$ and $Q_{\rm He^+}$), and the radiative relaxation of the helium triplet state (A_{31}). Double ionisation processes for helium were not considered, and we assume that the charge exchange reactions between helium and hydrogen do not significantly affect the concentration of the latter. Furthermore, we assume that the electrons produced from helium ionisation are negligible in comparison to the production from hydrogen ionisation.

The hydrogen photo-ionisation cross sections were taken from Osterbrock & Ferland (2006) and the photo-ionisation cross sections for the helium triplet and singlet states were taken from Norcross (1971) and Brown (1971), respectively (see Fig. 2). The photo-ionisation rates are calculated as usual,

$$J(r) = \int_{\lambda_{\rm min}}^{\lambda_{\rm max}} \sigma_\lambda\,F_\lambda\,\exp[-\tau_\lambda(r)]\,{\rm d}\lambda, \tag{12}$$

and

$$\tau_\lambda(r) = \sum_i \int_r^\infty \sigma_i(\lambda)\,n_i(r)\,{\rm d}r, \tag{13}$$

where $\lambda_{\rm min}$ and $\lambda_{\rm max}$ correspond to the wavelength range of photo-ionisation, $\tau_\lambda(r)$ is the optical depth, F_λ is the stellar flux density at the top of the atmosphere, and $\sigma_i(\lambda)$ and $n_i(r)$ are the absorption cross section and number density of species i (H and He), respectively.

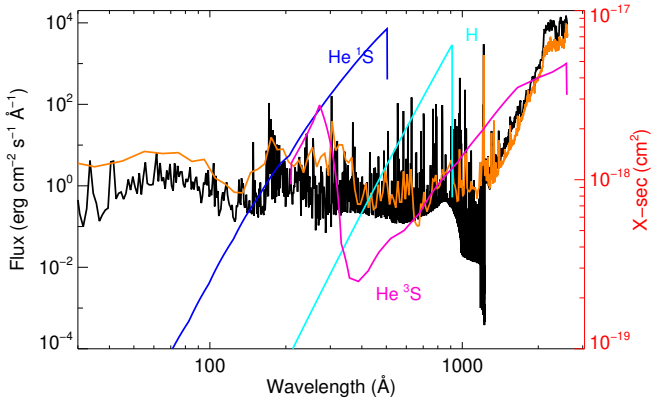

Fig. 2. Flux density for HD 209458 at 0.04707 au (left y-axis) as calculated here (black) and for the modern Sun (solar maximum) as reported by Claire et al. (2012) and scaled up to the size of HD 209458 (orange). We note that the resolution of the two spectra is different. The H, He singlet, and He triplet ionisation cross sections (right y-axis) are also shown.

The flux of HD 209458 in the 5–1230 Å range was calculated using a coronal model based on *XMM-Newton* observations of this star (Sanz-Forcada et al. 2010, 2011) that are combined to improve their statistical significance in the spectral fit, reaching a 3.2–σ detection. No substantial variability was registered in the X-rays observations, although the number of measurements is small. The coronal 1-T model, $\log T(\mathrm{K}) = 6.0^{+0.3}_{-0.0}$, $\log EM\,(\mathrm{cm}^{-3}) = 49.52^{+0.22}_{-0.48}$, $L_\mathrm{X} = 6.9 \times 10^{26}$ erg s^{-1}, is complemented with line fluxes from observations with the Cosmic Origin Spectrograph onboard HST published by France et al. (2010) in order to extend the model towards lower temperatures ($\log T(\mathrm{K}) \sim 4.0$–6.5). No substantial amount of emitting material is expected for higher temperatures. The XUV (5–920 Å) modelled luminosity is 1.5×10^{28} erg s^{-1}, which is about 2.6 times higher than in Sanz-Forcada et al. (2011). For the 1230–1700 Å range we used current observations with the Space Telescope Imaging Spectrograph taken from the HST archive[1]. At $\lambda >$ 1700 Å we used the stellar atmospheric model of Castelli & Kurucz (2004) scaled to the temperature, surface gravity, and metallicity of HD 209458 (see Table 1). The resulting stellar flux for the spectral range 5–2600 Å at the orbital separation of the planet (0.04707 au) is shown in Fig. 2. This flux shows several differences with respect to the solar flux (see, e.g. Claire et al. 2012; Linsky et al. 2014). Thus, it shows a weaker Lyα continuum but more prominent emission lines in the 600–912 Å region. Also, the continuum in the 950–1200 Å range is significantly weaker, although this is expected to have a minor effect on the He(2^3S) population. In order to analyse the effects of these phenomena on the He(2^3S) density we performed some tests as shown in Sect. 3.2.

Equations (8), (10), (A.3), and (11) are solved iteratively until convergence is reached, ensuring a fully consistent model. As the abundances of neutral and ionised species and electrons vary with r, so does the mean molecular weight. We assume pre-set neutral gas composition of H and He (we considered H/He mole-fraction ratios of 90/10, 95/5, and 98/2). To ease the numerical convergence of the model, we select the minimum value of $\bar{\mu}$ (atmosphere fully ionised in the first iteration). The $\rho(r)$ and $v(r)$ profiles derived from the solution of Eqs. (8) and (10) with this initial $\bar{\mu}$ value enter into the system of continuity equations (Eq. (11)) to obtain the abundances of the neutral and ionised species, from which we calculated a new mean molecular weight profile, $\mu(r)$. The sequence is repeated until the $\mu(r)$ profiles in two subsequent iterations differ by less than 1%. In our model we assumed the lower boundary to be the pressure level of 1 mbar, corresponding roughly to a distance of 1.04 R_P or ~3800 km above $R_\mathrm{P} = 1$ ($R_\mathrm{P} = 1$ at 1 bar).

[1] STIS/G140L combined spectra were acquired on the dates 9 Oct. 2003, 19 Oct. 2003, 6 Nov. 2003 and 24 Nov. 2003.

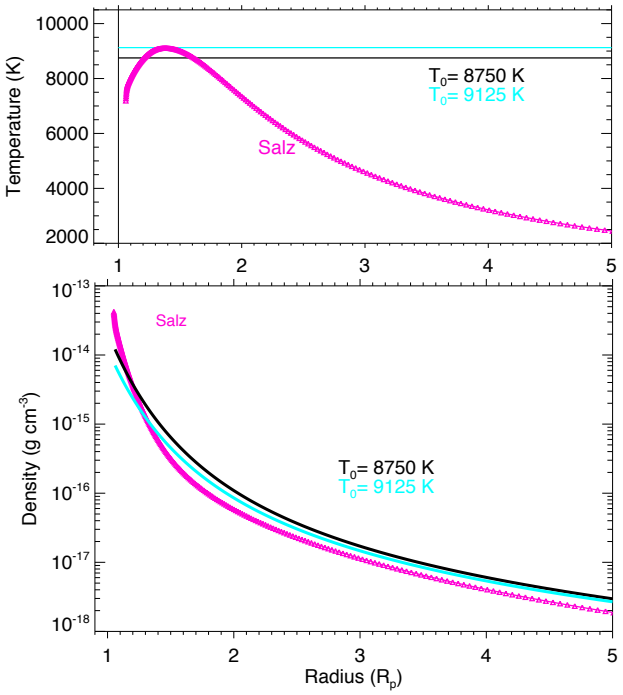

Fig. 3. Comparison of temperatures (*upper panel*) and their corresponding density profiles (*lower panel*). *Upper panel*: black line is the temperature resulting from the maximum speed of sound of Salz et al. (2016) and our averaged mean molecular weight; the cyan line is the maximum of the temperature profile of Salz et al. (2016), and magenta is their temperature profile. *Lower panel*: density profiles calculated by Salz et al. (2016) (magenta) and those calculated using our model (black and cyan).

3.1. Validity of the hydrodynamic model

In order to check the validity of our constant-speed-of-sound approach, we compared our results with those obtained by Salz et al. (2016), who solved the energy equation and did not include any assumption on temperature. For that comparison, we used the same HD 209458 b bulk parameters, mass-loss rate, H/He, and XUV stellar flux. We performed the calculations for two T_0 temperatures: (1) that obtained when considering the largest speed of sound computed by Salz et al. (2016) and the average mean molecular weight obtained in our model (Eq. (7)); and (2) the maximum of the temperature profile computed by Salz et al. (2016). Figure 3 shows these latter two temperature profiles and the one calculated by Salz et al. (2016), as well as the corresponding total density profiles. Except for altitudes very close to the lower boundary ($r < 1.15\,R_\mathrm{P}$), the density that we obtain with the temperature corresponding to the maximum speed of sound in Salz et al. (2016), 8750 K, agrees with that computed by these latter authors. This result should not be surprising because for the maximum of the speed of sound, its derivative is zero and then the equations of the full model reduce to those in our model, i.e. Eq. (5) reduces to Eq. (6).

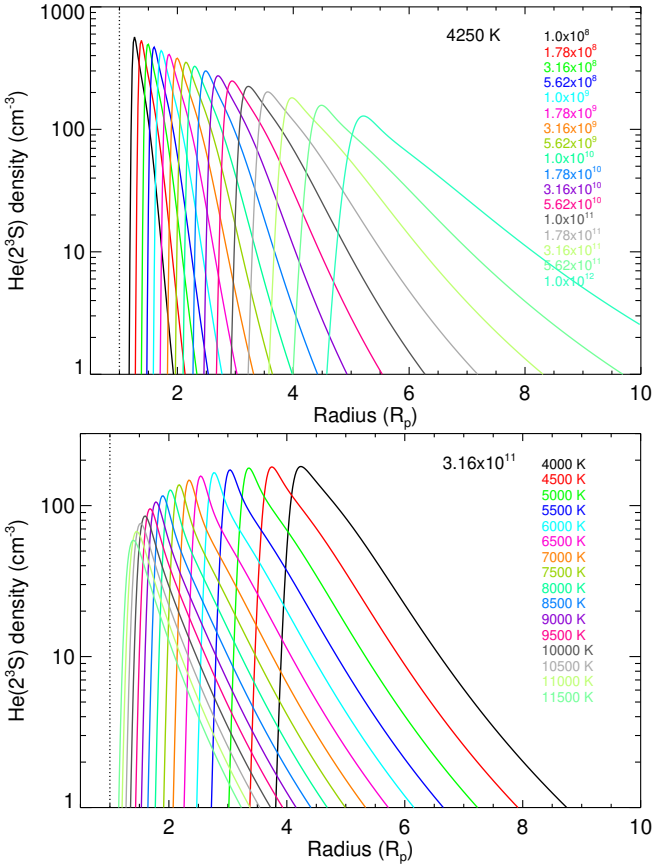

Fig. 4. Density profiles of the helium triplet state showing the mass-loss rate dependence for a temperature of 4250 K (*top panel*) and the temperature dependence for a mass-loss rate of 3.16×10^{11} g s^{-1} (*bottom panel*). An H/He ratio of 90/10 was assumed.

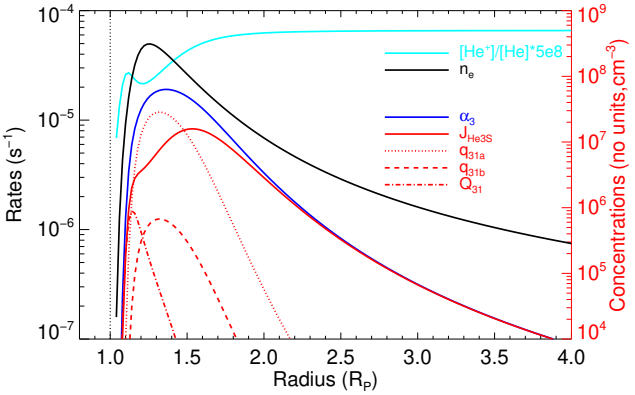

Fig. 5. Production and loss rates of He(2^3S) (labelled as in Table 2, left y-axis) for the case of 6000 K and a mass-loss rate of 4.2×10^9 g s^{-1}. The blue line corresponds to the production by recombination and the red lines to the losses. Also shown are the concentrations of the species directly involved in the recombination (right-y axis): the electrons (in cm^{-3}, black solid line) and the [He$^+$]/[He] ratio (scaled by 5×10^8 in cyan). An H/He ratio of 90/10 was assumed.

The temperature $T_0 = 8750$ K is also close to the thermospheric maximum temperature calculated by Salz et al. (2016). Moreover, the density obtained for the maximum of the temperature profile of Salz et al. (2016), $T_0 = 9125$ K, still gives very good agreement with that of Salz et al. (2016), although at altitudes close to the lower boundary, where the He(2^3S) absorption is most important (see Fig. 9), the agreement is slightly poorer. Furthermore, the temperature profile obtained in our approach, dictated by v_s, max(Salz) $= [k\,T(r)/\mu(r)]^{1/2}$, is equal to $T_0 = 8750$ K at an altitude close to 1.6 R_P, which corresponds to the location of the photo-ionisation front, that is, where most of the stellar radiation is absorbed. We also performed this comparison with two other planets, HD 189733b and GJ 3470b, which show different parameters and maximum of their temperature profiles at significantly different altitudes (Salz et al. 2016). Since we obtain similar results, the input temperature to our model, T_0, can be considered as a good proxy (within ~10%) for the maximum temperature obtained in the hydrodynamic models that also solve the energy budget equation.

3.2. He(2^3S) densities

Figure 4 shows several He(2^3S) density profiles and their dependence on the mass-loss rate (upper panel) and temperature (lower panel) for an H/He ratio of 90/10. As a general trend, for a given temperature, smaller mass-loss rates give rise to higher He(2^3S) peak densities and more compressed (narrower layers of) He(2^3S) density profiles. Conversely, at larger mass-loss rates, the He(2^3S) density has a broader shape and its maximum occurs at larger planetary radii. Regarding the effect of temperature, for a given $\dot{M}$, we can see that the peak of the He(2^3S) density occurs at smaller radii for larger temperatures, whereas colder thermospheres produce higher He(2^3S) abundances.

To understand this behaviour we analysed the production and loss terms of Eq. (11). As an example, Fig. 5 shows the production and loss terms of He(2^3S) for a temperature of 6000 K and a mass-loss rate of 4.2×10^9 g s^{-1}. The production of He(2^3S) is dominated by the recombination of He$^+$ with electrons, α_3, having its maximum contribution at about 1.2–1.4 R_P. The electron density is mainly driven by H photo-ionisation, J_H, whereas the electron productions from the photo-ionisation of He(1^1S) and He(2^3S) are negligible. In turn, the He$^+$ production is determined by the helium photo-ionisation, J_{He^1S}, and the charge exchange process, Q_{He}; and its losses are mainly controlled by the recombination with electrons, α_1 and α_3, and the charge exchange process Q_{He^+}. At high altitudes, where He ionisation is very effective, the He$^+$ concentration is dominated by its photo-ionisation, J_{He^1S}, but at lower altitudes the photo-ionisation production and the losses by recombination with electrons determine the resulting He$^+$ profile (see Fig. 5). The production of He(2^3S) by collisional excitation, q_{13}, is very small, i.e. below the lower limit of the scale of Fig. 5. We found that the inclusion of the charge-exchange processes Q_{He} and Q_{He^+} produces a net loss of He$^+$, which translates into a reduction of the He(2^3S) concentration peak (~15% for this case).

Given the importance of H photo-ionisation in the production of He(2^3S), it can be seen that a thinner atmosphere (i.e. weaker $\dot{M}$ or warmer thermosphere, see Fig. 6) produces ionisation of H at lower altitudes and hence effectively produces He(2^3S) at this region. In contrast, for larger $\dot{M}$ or colder thermospheres, the density is higher and the absorption of the stellar flux takes place mainly at higher altitudes. Additionally we observe in Fig. 4 a broader extension of [He(2^3S)] (square brackets indicate concentration) at larger $\dot{M}$, which is due to the weaker vertical gradient of the total density at higher altitudes (see Fig. 6). For these conditions, the attenuation of the stellar flux occurs more progressively with altitude than at low altitudes where the density abruptly increases (see Fig. 6). In addition to this, the hotter the gas is, the more expanded and thinner the thermosphere is.

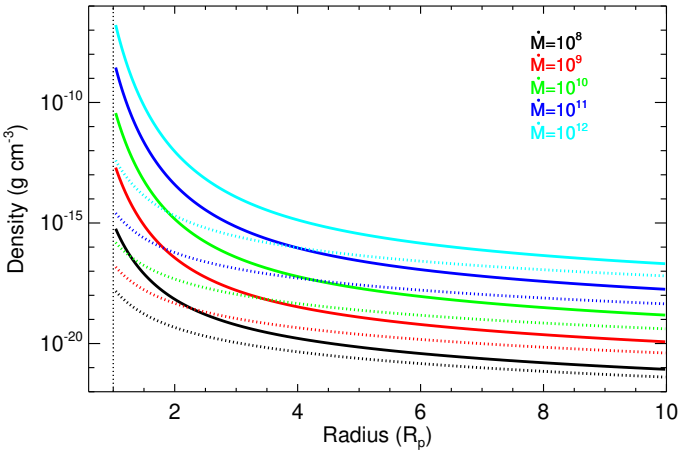

Fig. 6. Total atmospheric density profiles for several mass-loss rates and temperatures of 5000 K (solid) and 10 000 K (dotted). An H/He ratio of 90/10 was assumed.

Losses of He(2^3S) are controlled by different processes. The major loss is due to photo-ionisation, $J_{\mathrm{He^3S}}$, at higher altitudes and the collisional deactivation with electrons, q_{31a}, at lower altitudes. Collisional deactivation with H, Q_{31}, and advection are about one order of magnitude smaller than photo-ionisation and collisional deactivation with electrons. Overall, the helium triplet concentration is mainly controlled by the stellar flux: on the one hand, by the electron production from H photo-ionisation, which heavily depends on the stellar flux at 600–912 Å (see Fig. 2), and on the other hand, by the losses through photo-ionisation of He(2^3S), which mainly depends on the stellar flux at ∼1000–2600 Å (see Fig. 2). Hence, the ratio of the stellar flux in these two regions, 600–912 Å and ∼1000−2600 Å, will impact the He(2^3S) density favouring a larger He(2^3S) density as the ratio increases.

As discussed above, we performed some tests using the solar flux scaled to the size of HD 209458 (see Fig. 2) for temperatures ranging from 6000 to 10 000 K and $\dot{M}$ from 10^9 to 10^{11} g s^{-1}. When using this flux, the production terms of He(2^3S), i.e. the photo-ionisation rates J_{H} and $J_{\mathrm{He^1S}}$, change by factors of ∼0.46 and ∼2.3, respectively, while the loss term, $J_{\mathrm{He^3S}}$, decreases by a factor of ∼0.44; overall, this produces an increase in the He(2^3S) concentration of a factor of approximately 2.4.

Different He(2^3S) density profiles are obtained when considering different H/He ratios, mass-loss rates, or temperatures. However, the same mechanism described above applies. The helium triplet abundance is largely determined by the stellar flux via H photo-ionisation as well as by the density, which largely controls the atmospheric region where the stellar flux is fully absorbed.

3.3. Spectral absorption

The spectral absorption of the He triplet lines was calculated computing the radiative transfer following the usual transit geometry (see Fig. 7). The transmission, $\mathcal{T}_\nu(r)$, along the line of sight (LOS) x at a radius r over the planet reference surface for an infinitesimal field of view of the planet's atmosphere (see Fig. 7, top) at frequency ν can be written as (see, e.g., López-Puertas & Taylor 2001, p. 64)

$$\mathcal{T}_\nu(r) = \exp\left[-\int_{-\mathrm{TOA}}^{\mathrm{TOA}} k_\nu(x)\, n(x)\, \mathrm{d}x\right], \tag{14}$$

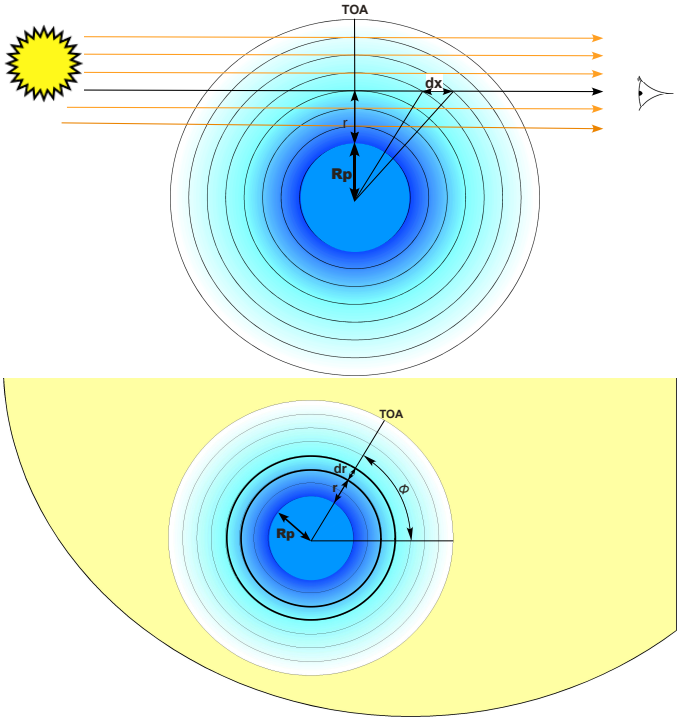

Fig. 7. Basic sketch (not to scale) of the side view (*top*) and front view (*bottom*) of the typical geometry of the primary transit.

where k_ν is the absorption coefficient of the radiative transition and $n(x)$ is the concentration of the absorbing gas, the helium triplet state in our case, and TOA stands for the top of the atmosphere.

The absorption coefficient can be expressed as $k_\nu = K\, f_\nu$, where K is the integrated absorption coefficient and f_ν is the line shape. The latter is usually taken as a Lorentz, Doppler, or Voigt profile. Here, as most of the absorption comes from low-pressure regions, we assumed a Doppler profile which in general accounts for temperature and the turbulent broadening, for example

$$f_\nu(x) = \frac{1}{\alpha_{\mathrm{D}}\sqrt{\pi}} \exp\left[-\frac{[\nu - \nu_0 + (\nu_0/c)\, v_{\mathrm{wind}}]^2}{\alpha_{\mathrm{D}}^2}\right], \tag{15}$$

where c is the speed of light and ν_0 the central frequency of the line. The Doppler line width, α_{D}, is given by

$$\alpha_{\mathrm{D}} = \frac{\nu_0}{c}\sqrt{\frac{2kT}{m} + v_{\mathrm{turb}}^2} \;\text{ with }\; v_{\mathrm{turb}}^2 = \frac{5kT}{3m}, \tag{16}$$

where v_{turb} is the turbulent velocity, and m is the mass of the atom or molecule. We note that in Eq. (15) we have included a term with v_{wind}, the mean velocity of the gas along the line of sight (towards the observer), in order to account for possible motion of the absorbing gas. This dependence can take place either along the LOS ray pencil, x (top panel of Fig. 7), or along the radial and azimuth dependencies of the v_{wind}, r and ϕ (lower panel of Fig. 7).

The absorption of the whole atmosphere, $\mathcal{A}_\nu$, is obtained by integration of the absorption for the area covered by infinitesimal spherical rings of thickness dr and then integrating over all radii r and polar angles ϕ of the atmosphere,

$$\mathcal{A}_\nu = \int_0^{2\pi}\int_0^{\mathrm{TOA}} (R_{\mathrm{p}} + r)\,[1 - \mathcal{T}_\nu(r,\phi)]\,\mathrm{d}r\,\mathrm{d}\phi, \tag{17}$$

where R_p is the radius of the planet. We include the integration over the polar angle, ϕ, in order to account for potential atmospheric inhomogeneities in the density or velocity of the helium triplet state along this coordinate.

The absorption coefficients, K, and the frequencies, ν_0, for the three lines from meta-stable helium levels were taken from the NIST Atomic Spectra Database[2]. The He(2^3S) density profiles were calculated as described above in this section. Temperature was kept constant, as given by the helium triplet density model. As most of the absorption is expected to take place at atmospheric regions below the Roche limit (see below), here we did not include the broadening of the lines due to turbulence ($v_{turb} = 0$ in Eq. (15)). The v_{wind} included in the nominal calculation corresponds to the line-of-sight component of the radial velocity outflow obtained in the density model of Sect. 3.

4. Results and discussion

To analyse the mid-transit absorption spectra of Fig. 1, the thermospheric model described in Sect. 3 has been run for a temperature range of 4000–11 500 K in steps of 125 K. The mass-loss rate interval is 10^8–10^{12} g s^{-1} in eight steps per decade. This results in a total of 2013 simulations for each set of H/He abundances.

Subsequently, we computed the spectral transmission for each of the helium triplet profiles. In these radiative transfer calculations, we included the temperature and the escape velocity profile $v(r)$ (see Eq. (8)) from the model. No turbulence term was included, as most of the absorption comes from radii below the Roche limit. Nevertheless, we performed a test for the case of Fig. 1 by including this term in the broadening of the line and found a less precise fitting; that is, the modelled line profile is wider than the measured profile.

A bulk Doppler blueshift of 1.8 km s^{-1} was included in the absorption calculation, as suggested by the observations. The additional absorption observed at around –13 km s^{-1} (the magenta curve in Fig. 1) has not been included in these calculations (e.g. in the computation of χ^2, see below). The reason is that this absorption seems to emerge from very high altitudes and possibly from material already ejected by the planet, but we are interested in determining the temperature and mass-loss rates of the bulk atmosphere.

The absorption spectra were computed at a very high resolution (wavelength step of 10^{-7} Å) and then convolved with the CARMENES line spread function. We performed the integration over the radius, r in Fig. 7, from the lower boundary condition of the He triplet model (1.04 R_P) up to the Roche lobe boundary, located at 4.22 R_P (Salz et al. 2016).

In order to analyse the extent to which absorption contributes beyond that limit, we also computed the absorption including the atmosphere extended up to 10 R_P. The results show that for $\dot{M}$ smaller than 10^{11} g s^{-1} the additional absorption for radii beyond that boundary is very small; in particular, for $\dot{M}$ of $\sim 3.7 \times 10^9$ g s^{-1} at a temperature of 6000 K (Fig. 1) it is negligible (below 0.3%). This result is consistent with the light curve shown in Fig. 5 in Alonso-Floriano et al. (2019) which does not show signs of relevant ingress or egress absorption.

We compared the synthetic spectra to the measured one (see an example in Fig. 1) and calculated the χ^2 in the spectral interval of 10 829.9–10 831.5 Å (avoiding the –13 km s^{-1} component) for each of them. In this way, we obtained all possible pairs of $\dot{M}$ and T which are compatible with the measured absorption.

[2] https://www.nist.gov/pml/atomic-spectra-database

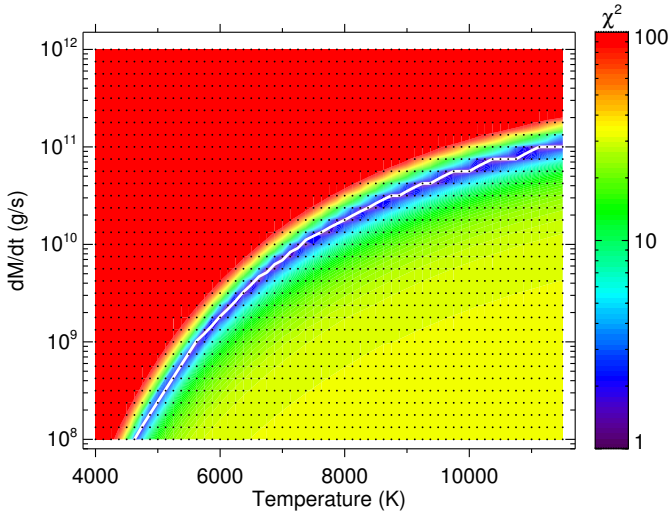

Fig. 8. Contour map of the χ^2 of the model of the helium triplet absorption compared to that measured by CARMENES as reported by Alonso-Floriano et al. (2019). The χ^2 has been scaled by 10^5 (or, equivalently, the reduced χ^2 scaled by a factor of 3.8). An H/He ratio of 90/10 was assumed. The small black dots represent the grid of models. The white curve highlights the best fitting simulations.

The results of the χ^2 computations for H/He of 90/10, our nominal case, are shown in Fig. 8. The white curve highlights the best-fitting simulations. According to these results, the measured absorption is consistent with pairs of (T, $\dot{M}$) ranging from (4625 K, 10^8 g s^{-1}) to (11500 K, 10^{11} g s^{-1}). The relationship between temperature and $\dot{M}$ is not linear, being steeper at lower T and $\dot{M}$ values, and flatter at high temperatures.

In order to better understand the escaping atmosphere we plotted a selection of the He(2^3S) densities in Fig. 9 (top panel for an H/He ratio of 90/10) that fit the observed absorption spectrum and cover the full range of temperatures and $\dot{M}$. This figure shows that the majority of the He(2^3S) profiles peak at very short distances, in the range of 1.04–1.10 R_P. The few profiles with peaks at distances greater than 1.30 R_P are more extended and generally correspond to higher temperatures and larger mass-loss rates. Another relevant feature of the atmospheres that best fit the measured absorption is that they all have a very similar averaged mean molecular weight, close to 0.69 g mole^{-1}. This value corresponds to a partially ionised thermosphere, between the fully ionised ($\bar{\mu} = 0.65$) and the neutral ($\bar{\mu} = 1.3$) thermospheres.

As the atmospheric model provides [H$^+$], we also analysed [H]/[H$^+$] for the different atmospheres that fit the observed He(2^3S) absorption. In Fig. 10 we show the H mole fraction profiles for the same atmospheres as shown in Fig. 9. We see that for an H/He of 90/10 (top panel) most of the atmospheres reproducing the measured He(2^3S) absorption have a rather sharp [H]/[H$^+$] transition region occurring at altitudes ranging from about 1.04 to 1.09 R_P. That is, the measured He(2^3S) spectrum suggests that the atmospheric hydrogen of HD 209458 b is fully ionised at altitudes above ~1.6 R_P, which is in agreement with the mean molecular weight of ~0.69 g mole^{-1} mentioned above.

4.1. Sensitivity to the H/He ratio and comparison with previous H densities

We further explored whether or not we can constrain the H concentration with the measured He(2^3S) spectrum. The H abundance in HD 209458 b has been derived from Lyα

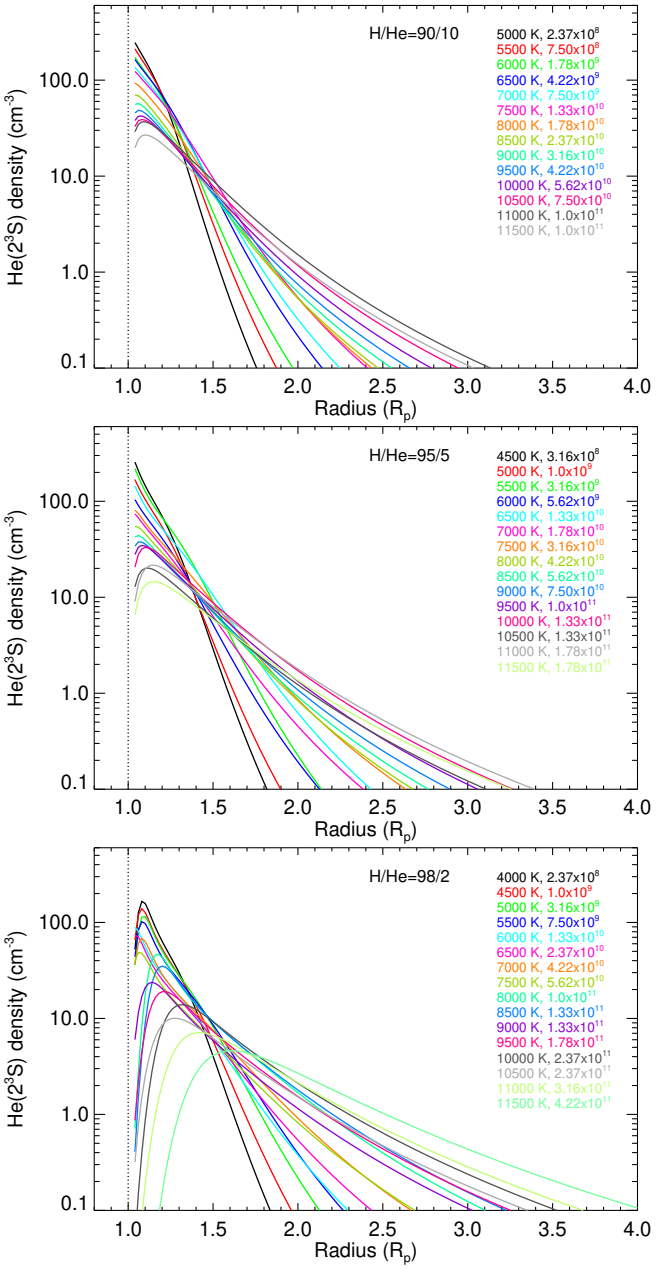

Fig. 9. He(2^3S) concentration profiles that best fit the measured absorption (see Figs. 8 and 12). Shown is a selection of the profiles along the black, cyan. and orange lines in Fig. 12, covering the whole range of temperatures and mass-loss rates of those figures. *Panels from top to bottom* are for H/He ratios of 90/10, 95/5, and 98/2, respectively.

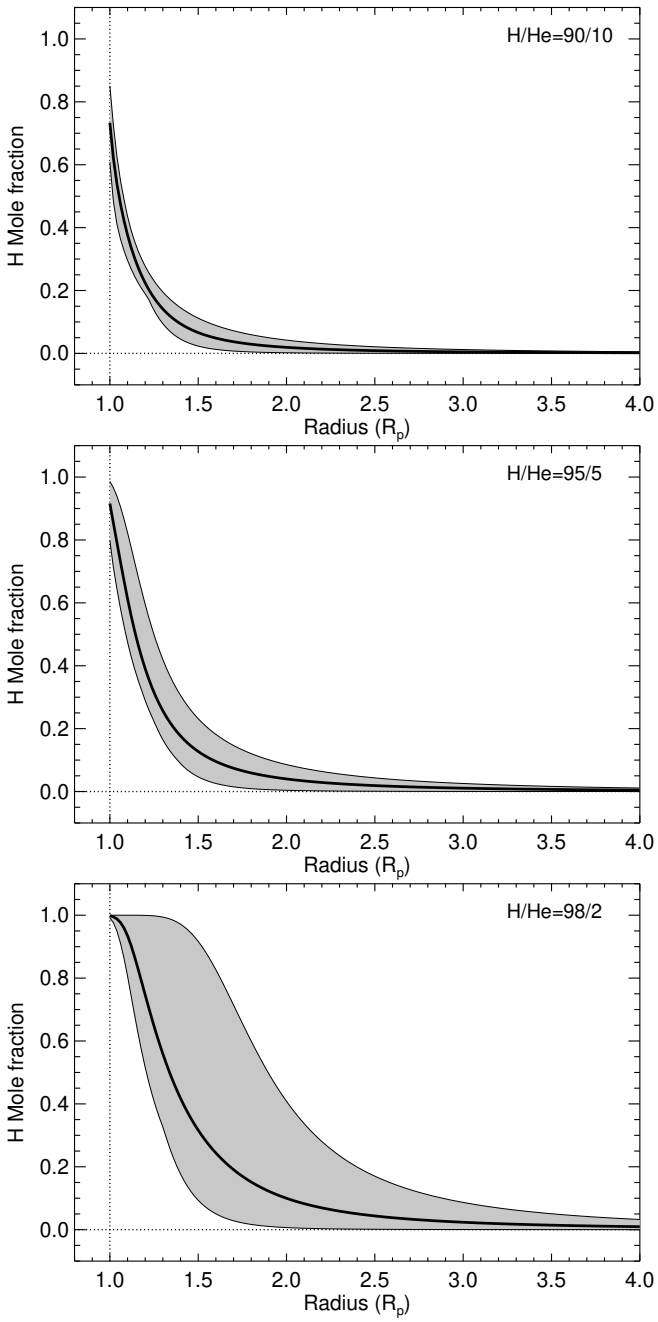

Fig. 10. Range of the hydrogen molar fraction profiles resulting from the fit of the measured absorption (see Figs. 8 and 12) for three H/He ratios, covering the whole temperature and mass-loss rate ranges of those figures. The solid thicker lines are the mean profiles.

absorption measurements in several studies (see, e.g. García-Muñoz 2007; Koskinen et al. 2013; Salz et al. 2016). We then compared our derived H density from the He(2^3S) fit with the ones reported in these latter studies. We found that, in general, our derived H densities for the usual H/He ratio of 90/10 (see Fig. 11, top panel) are significantly lower at all altitudes. This prompts us to consider other H/He densities in order to ascertain whether or not they can explain these discrepancies. Therefore, we repeated all the calculations above for the larger H/He ratios of 95/5 and 98/2. There are several processes that could lead to a larger H/He than the canonical value of 90/10. For example, as He is not chemically active, depending on the location of the He homopause, its abundance can be lower than its canonical value at lower altitudes due to diffusive separation (see, Fig. 14 in Moses et al. 2005). Another possible process of depletion He in the upper atmosphere of a giant planet is the He sequestration in the interior of the planet due to the formation of an H–He immiscibility layer (Salpeter 1973; Stevenson 1975, 1980; Wilson & Militzer 2010).

The most noticeable effect of increasing the H fraction (and thus decreasing the He abundance) is a global decrease of the thermospheric mass density. Therefore the thermosphere is lighter and, for given conditions of temperature and mass-loss rate, it is more expanded. Figure 13 (top panel) shows the change in the HD 209458 b density when assuming an H/He ratio of

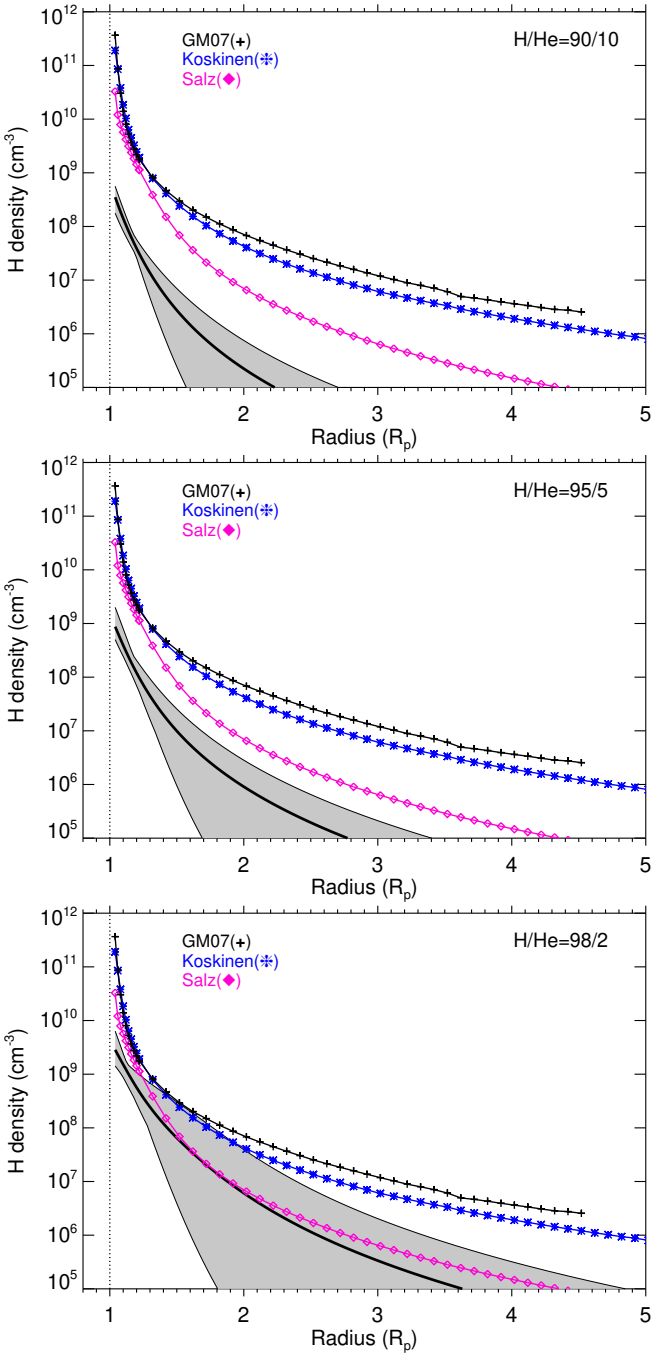

Fig. 11. Range of the neutral hydrogen concentration profiles resulting from the fit of the measured absorption (see Figs. 8 and 12) for three H/He ratios, covering the whole temperature and mass-loss rate ranges of those figures. The solid thicker lines are the mean profiles. The H density derived from Lyα measurements reported by García-Muñoz (2007), Koskinen et al. (2013), and Salz et al. (2016) is also shown.

95/5. Here we observe large changes in the density of close to two orders of magnitude for lower temperatures at low distances. The H density also shows large decreases (Fig. 13, middle panel), following the total density very closely. We also see the effects of absorption of the stellar radiation mainly for lower temperatures; that is, a change in the slope of the H density ratio at distances close to 1, 2, 3, and 4.5 R_P (for $\dot{M}$ of 10^9–10^{12} g s^{-1}) in response to the penetration of radiation to deeper altitudes for smaller H/He ratios.

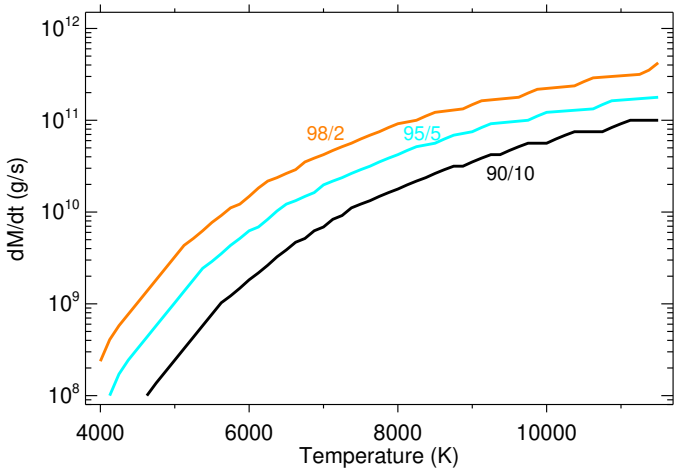

Fig. 12. Lines corresponding to the (T, $\dot{M}$) pairs of the model that best fit the helium triplet absorption as measured by CARMENES. The black curve shows the results for an H/He ratio of 90/10 (e.g. white curve in Fig. 8). The cyan and orange lines correspond to the best fit obtained when assuming H/He ratios of 95/5 and 98/2, respectively.

As a consequence of the lower total density, and lower H density, for a larger H/He ratio, the helium triplet density also mainly follows the behaviour of H, and therefore we generally obtain smaller He(2^3S) densities (Fig. 13, bottom panel). It is also worth noting that the peak of the He(2^3S) density moves to slightly lower altitudes for larger H/He.

The results of fitting the measured He(2^3S) spectrum when using H/He of 95/5 and 98/2 in the model are shown in the corresponding figures: Fig. 12 (cyan and orange lines) for the constrained ($\dot{M}$, T) pairs; Fig. 9 (middle and bottom panels) for the He(2^3S) density; and in Figs. 10 and 11 (middle and bottom panels) for the H mole fraction and H density, respectively.

Regarding the ($\dot{M}$, T) relationship, this curve moves to colder temperatures and larger mass-loss rates for higher H/He (see Fig. 12), which is the consequence of a smaller He(2^3S) density. In order to fit the measured spectrum we need to lower T or increase $\dot{M}$ in order to increase the He(2^3S) concentration (see Fig. 4). For the relatively high H/He ratio of 98/2, the measured spectrum implies relatively low temperatures and high mass-loss rates.

Figure 9 (middle and bottom panels) shows the He(2^3S) densities for the higher H/He of 95/5 and 98/2. In comparison to the result obtained for the commonly used H/He ratio of 90/10, the concentrations peak at generally lower values. These peaks are located at larger radii, and the profile shapes are wider. The chosen H/He ratio used in the fitting of the He(2^3S) absorption also dictates the ionisation level of the atmosphere. Figure 10 shows that the atmosphere of HD 209458 b is ionised at higher altitudes for larger H/He.

By inspecting the results obtained for the H density for the three H/He ratios considered here (see Fig. 11), it seems that the derived H densities that agree better with those derived from previous Lyα measurements correspond to the 98/2 ratio (lower panel).

4.2. Comparisons of temperatures and mass-loss rates to those of previous works

Several models with different approaches and assumptions have been developed for studying the processes that drive the escape in HD 209458 b. A summary is listed in Table 3 for comparison.

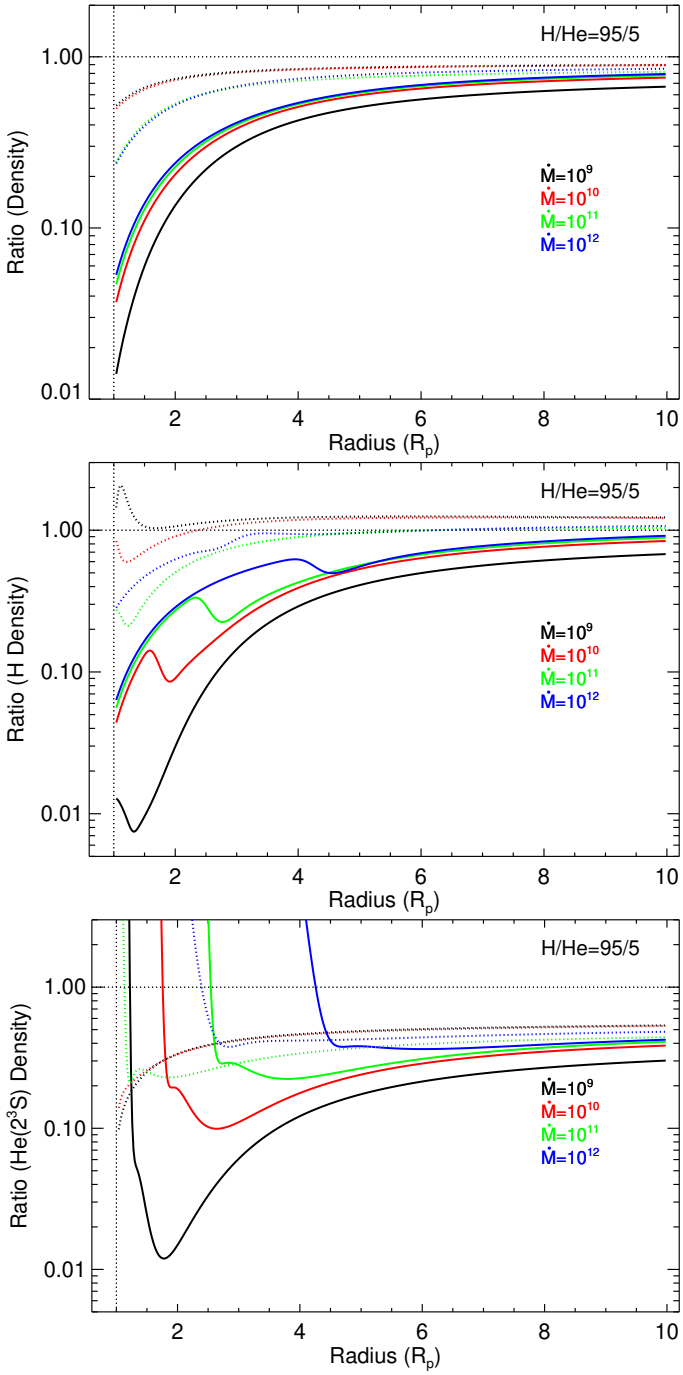

Fig. 13. Ratios of the total atmospheric mass density (*top panel*), the neutral H number density (*middle panel*), and the He(2^3S) density (*bottom panel*) for several mass-loss rates and temperatures of 5000 (solid) and 9000 K (dotted) for an H/He ratio of 95/5 relative to the densities for an H/He ratio of 90/10.

Before discussing them, we should recall that our mass-loss rates refer to the total mass of hydrogen and helium, and that they were computed at the substellar location instead of the globally averaged values reported by some authors, the latter being four times smaller. When necessary, we translate globally averaged to substellar values.

One of the approaches for escape modelling is to consider a particle model, which focuses on the exosphere or the unbound region. With the aim of interpreting HD 209458 b observations of H I Lyα, Vidal-Madjar et al. (2003) built a particle model where the atmosphere is composed of atomic hydrogen only. These latter authors considered the stellar radiation pressure and the planetary and stellar gravity. Thereby, they determined a lower limit for the substellar mass-loss rate of 0.4×10^{11} g s^{-1}. This value, when compared to those derived here (we consider that our case of an H/He ratio of 98/2 gives the better overall agreement for the He(2^3S) and Lyα absorption; see Fig. 12, orange curve) would implies a temperature of about 7000 K, which seems plausible although generally lower than those calculated in different models (e.g. Salz et al. 2016). Higher temperatures lead to stronger mass-loss rates, which is consistent with Vidal-Madjar et al. (2003) since they provide a lower limit.

Similarly, Bourrier & Lecavelier des Etangs (2013) developed a 3D model for an atomic hydrogen exosphere including stellar radiation pressure. These latter authors suggested a substellar mass-loss rate range of $(0.04-4.0) \times 10^{11}$ g s^{-1}. This wide range of mass-loss rates is compatible with our results but does not significantly constrain the temperature range because, according to Fig. 12 (orange curve), the temperature varies in a wide range: 5125–11 500 K.

Other studies using hydrodynamic models have focused on thermospheric rather than exospheric simulations. In these approaches, several 1D models with spherical geometry have been developed. For example, Tian et al. (2005), in their case for an atmosphere of atomic hydrogen and a heating efficiency of $\eta = 0.6$, predicted a maximum substellar mass-loss rate of 2.4×10^{11} g s^{-1} for a temperature profile that grows monotonously with altitude from 800 K at 1 R_P to ~20 000 K at 3 R_P. For this mass-loss rate, we derive from Fig. 12 a temperature close to 10 500 K, which is significantly lower than most of the values predicted by Tian et al. (2005). Nevertheless, Shematovich et al. (2014) concluded (see discussion below) that heating efficiencies smaller than 0.2 probably yield more accurate mass-loss rates. Thus, the results from Tian et al. (2005) probably represent an overestimation of temperature.

Also, using atomic hydrogen thermospheric models and assuming heating efficiencies of 0.6 and 0.1, Penz et al. (2008) estimated substellar mass-loss rates of 1.4×10^{11} and 0.52×10^{11} g s^{-1}, and maximum temperatures of 9500 and 6300 K located near 1.5 R_P, respectively. For these mass-loss rates, we derive from Fig. 12 temperatures close to 9100 K (for their $\eta = 0.6$), and of 7200 K (for their $\eta = 0.1$), which is comparable for $\eta = 0.6$ but slightly higher than that of the latter authors for $\eta = 0.1$. We note, however, that they include only hydrogen. Thus, if we were to consider a lower He abundance in our analysis, our results would be in better agreement with theirs.

García-Muñoz (2007) studied the hydrodynamic escape of HD 209458 b for different atmospheric compositions. The most relevant case is that with a complete chemical scheme (H, He, C, O, N and D) and an H/He ratio of ≈91/9 (his DIV1 case), for which this latter author estimated a mass-loss rate of 5.0×10^{11} g s^{-1}. Furthermore, the maximum temperature found by this latter author is 12 500 K at radii of 1.2 R_P. For his mass-loss rate we derive from Fig. 12 (orange curve) a temperature of 11 500 K or even larger, which is in good agreement with that computed by García-Muñoz.

Koskinen et al. (2013) carried out simulations for a thermosphere composed of H, He, and heavier elements (C, O, N, Si, Mg, Na, K and S). For their C2 case, which is the most representative, these latter authors obtained a mass-loss rate of 1.6×10^{11} g s^{-1} with a heating efficiency of 0.44, and a maximum temperature of 12 000 K at a distance of 1.5 R_P. For this mass-loss rate we obtain a temperature of about 9100 K, which is significantly lower than theirs.

Table 3. Comparison of temperature and mass-loss rates with other works.

F_{XUV} (erg cm^{-2} s^{-1})	H/He	R_{XUV} (R_p)	K	η [a]	$\dot{M}$ [b] ($\times10^{11}$ g s^{-1})	T_{max} [c] ($\times10^3$ K)	$T_{This\ work}$ [d] ($\times10^3$ K)	Model [e]	References
...	100/0				>0.4 [f]		>7.0	3DP	(1)
[g]	100/0				0.04–4.0		5.1–11.5	3DP	(2)
[h]	100/0			0.6	2.4	See text	10.5	HD	(3)
1976	100/0			0.6	1.4	9.5	9.1	HD	(4)
1976	100/0			0.1	0.52	6.3	7.2	HD	(4)
2900	91/9			See text	5.0	12.5	11.5	HD	(5)
1800	...			0.44	1.6	12.0	9.1	HD	(6)
1148	90/10			See text	0.74	9.1	7.8	HD	(7)
[h]		3.0	1.0	1.0	<40 [i]		see text	EL	(8)
910		1.0	0.65	1.0	<1.8 [i]		<9.8	EL	(9)
1148		1.25	1.0	0.21	0.74		7.8	EL	(10)
2400	98/2	1.16-1.30 [j]	0.76	0.1-0.2 [k]	0.42–1.00		7.13–8.13		This work

Notes. [a]Averaged heating efficiencies. Particle models (3DP) do not include this parameter. [b]Substellar mass-loss rates. Globally averaged mass-loss rates were translated to substellar when necessary, multiplying by 4. [c]Maximum temperature. Given only for hydrodynamic (HD) models. [d]Temperature of our model for a 98/2 H/He abundance, corresponding to the $\dot{M}$ of the compared model. [e]Type of model: 3D particle estimation (3DP), Hydrodynamic model (HD) and Energy-limited (EL). [f]Lower limit of mass-loss rate. [g]Three to four times the current solar XUV flux. [h]Current solar XUV flux. [i]Upper limit of mass-loss rate. [j]R_{XUV} range derived in this work for the assumed heating efficiency range (0.1–0.2). [k]Range taken from Shematovich et al. (2014).

References. (1) Vidal-Madjar et al. (2003); (2) Bourrier & Lecavelier des Etangs (2013); (3) Tian et al. (2005); (4) Penz et al. (2008); (5) García-Muñoz (2007); (6) Koskinen et al. (2013); (7) Salz et al. (2015); (8) Lammer et al. (2003); (9) Sanz-Forcada et al. (2011); (10) Salz et al. (2016).

For an atomic hydrogen and helium thermosphere of 90/10, Salz et al. (2016) estimated a mass-loss rate of 0.74×10^{11} g s^{-1} with a maximum temperature of 9100 K near 1.4 R_P. For that mass-loss rate our He(2^3S) absorption implies a temperature of about 7750 K (Fig. 12, orange curve, H/He of 98/2), which is significantly lower than the temperature of Salz et al. (2016). It is interesting to note that Salz et al. (2016) obtained an H density that underestimates the Lyα observations. For an H/He ratio of 90/10, our H density derived from the He(2^3S) absorption also underestimates the Lyα absorption (see top panel in Fig. 11). In order to fit the Lyα observations, Salz et al. (2016) supplied the required extra H using an H-only (no helium) model. In our case, to obtain a good fit to both the He triplet and Lyα absorption, we also need to decrease the H/He ratio; suggesting that a value of 98/2 could be enough.

Overall, we observe that although the ranges of mass-loss rates and temperatures in the literature are rather broad, they generally agree well with the constrained $\dot{M}$(T) curve found in this work (orange curve in Fig. 12). Only the values derived by Tian et al. (2005) and Koskinen et al. (2013), both larger than ours, fall relatively far from the derived constraints.

4.3. Energy-limited escape models

Estimates of the evaporation mass-loss rate of HD 209458 b have also been obtained by using the energy-limited approximation (Watson et al. 1981; Erkaev et al. 2007; Lammer et al. 2009). The main assumption of this model is that the escape is limited by the F_{XUV}, and it is useful for constraining the atmospheric mass-loss rate or the heating efficiency. With this approach, the substellar mass-loss rate, $\dot{M}_{EL}$, can be written as

$$\dot{M}_{EL} = \frac{4\pi R_p R_{XUV}^2 \eta F_{XUV}}{G K(\xi) M_P}, \quad (18)$$

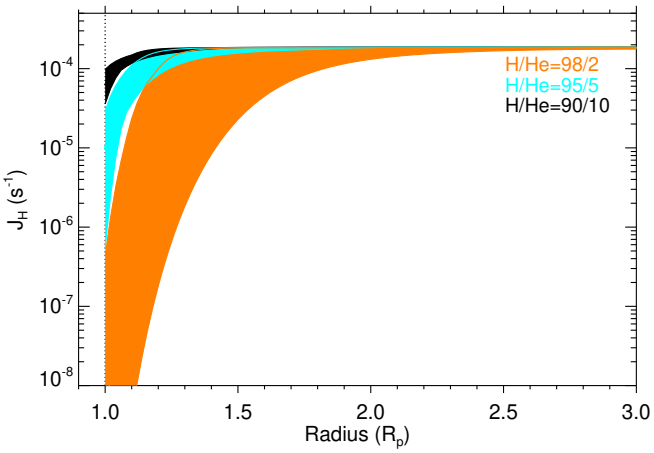

Fig. 14. Ranges of the photo-ionisation coefficient of H, J_H profiles that fit the measured absorption (Fig. 12) for the different H/He ratios.

where R_{XUV} is the atmospheric expansion radius, defined as the altitude where the optical depth is unity (Watson et al. 1981); $K(\xi) = 1 - 1.5\,\xi + 0.5\,\xi^3$ is the potential energy reduction factor, with $\xi = (M_P/M_\star)^{1/3}\,(a/R_P)$. This mass-loss rate is sometimes corrected by a factor that compensates for the underestimated kinetic and thermal energy gains. Here, however, we use uncorrected values.

We calculated the heating efficiency, η_{EL}, resulting from our He(2^3S) analysis using the aforementioned approach. To that end, we included in Eq. (18) the XUV stellar flux that we used, $F_{XUV} = 2.4\times10^3$ erg cm^{-2} s^{-1} (see Sect. 3), $K = 0.76$, and the R_{XUV} values resulting from the model fit to the He(2^3S) absorption (see Fig. 14). The resulting heating efficiencies are shown in Fig. 15.

As discussed above, Shematovich et al. (2014) modelled the thermal-escape-related heating efficiency for HD 209458 b and

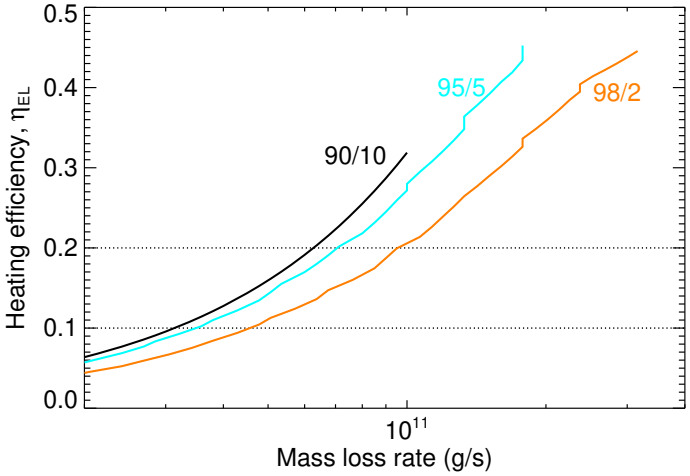

Fig. 15. Heating efficiency derived from the He(2^3S) absorption measurements (see Fig. 12) under the energy-limited escape approximation (see Eq. (18)) for H/He of 90/10, 95/5, and 98/2. Dotted lines correspond to $\eta = 0.1$ and 0.2.

concluded that η values smaller than 0.2 produce more realistic mass-loss rates. If we impose $\eta = 0.1$–0.2 and use the energy limited approach, our results of Fig. 15 limit the substellar mass-loss rate to the range of $(0.42–1.00)\times10^{11}$ g s^{-1} (on the basis that the H/He ratio of 98/2 gives the best fit to the H density), which, together with the results of Fig. 12, leads to a temperature range of 7125–8125 K (see Table 3, last row).

Depending on the values used for the different parameters in Eq. (18), we find a wide range of mass-loss rate and heating efficiency estimates for HD 209458 b. For instance, Salz et al. (2016) estimated a heating efficiency of 0.21 using a mass-loss rate of 0.74×10^{11} g s^{-1}. These values are in good agreement with those obtained in this work.

This approach has also been used to provide upper limits to the mass-loss rate, that is, when all radiation is thermalised ($\eta = 1$). Thus, Lammer et al. (2003) estimated an upper limit for the mass-loss rate of $\approx40\times10^{11}$ g s^{-1} using a calculated expansion radius of $\approx3\,R_p$ and assuming $K = 1.0$. This value is, in effect, a very high upper limit as it is much larger than those derived in this work for reasonable temperatures (<11 500 K) of $\sim4\times10^{11}$ g s^{-1} (see Fig. 12).

Sanz-Forcada et al. (2011) estimated an upper limit of 1.8×10^{11} g s^{-1} assuming $K = 0.65$, R_{XUV} equal to unity, and $F_{XUV} = 910$ erg cm^{-2} s^{-1}. This upper limit agrees with our results. We note that these latter authors used a simplified value for R_{XUV} and an F_{XUV} flux that is 2.6 times lower than ours.

5. Conclusions

We present observational constraints on the thermosphere of HD 209458 b obtained from an analysis of the mid-transit He(2^3S) spectral absorption measurements reported in Alonso-Floriano et al. (2019). Under the assumption of an upper atmosphere in blow-off escape, we modelled its thermosphere using a 1D hydrodynamic model with spherical symmetry, coupled with a non-LTE model for the population of the He(2^3S) state. The model provides, among other quantities, profiles of the He(2^3S) concentrations, which were included into a radiative transfer model to calculate He(2^3S) absorption spectra. By comparing these spectra to the measured He(2^3S) spectrum of Alonso-Floriano et al. (2019), we constrained the mass-loss rate, temperature, He(2^3S) densities, and the degree of ionisation in the upper atmosphere of HD 209458 b. We also compared the derived H densities with previous profiles derived from the Lyα absorption in order to further constrain the H density as well as the H/He ratio.

One of the main results we found is the close relationship between mass-loss rate and temperature for a wide range of these parameters (see Fig. 8). Additionally, we found that this relationship changes with the assumed H/He ratio (see Fig. 12). For a given temperature, the lighter the atmosphere, the stronger the mass-loss rate; and, for a fixed mass-loss rate, the lighter the atmosphere, the cooler the atmosphere. The H/He degeneracy was partially constrained by comparing with previous H density derived from Lyα absorption measurements. Globally, we found that an H/He ratio of 98/2 gives a better overall fit to both the He(2^3S) and Lyα measured absorption.

From the analysis performed for the considered ranges of $\dot{M} = 10^8$–10^{12} g s^{-1} and temperature of 4000 to 11 500 K, we obtain the following results: (i) we find that the He(2^3S) peak density is located in the altitude range of 1.04–1.60 R_P; (ii) we obtain an [H]/[H$^+$] transition altitude ranging from about 1.2 to 1.9 R_P; (iii) we obtain an effective radii of the XUV absorption in the range of 1.16–1.30 R_P; (iv) the averaged mean molecular weight of the gas ranges from 0.61 to 0.73 g mole^{-1}; and (v) we find that the thermospheric H/He ratio should be larger than 90/10, the most likely value being about 98/2.

Thus, the He(2^3S) absorption spectrum significantly constrains the thermospheric structure of HD 209458 b and advances our knowledge of its escaping atmosphere. In particular, we show that the H/He ratio should be larger than 90/10, that hydrogen is almost fully ionised ([H]/[H$^+$] < 0.1) at altitudes above 2.9 R_P, and that He(2^3S) is accumulated at low thermospheric altitudes.

Comparing our results with previous works we find that, overall, they generally agree well with the constrained $\dot{M}$(T) curve found in this work (orange curve in Fig. 12). Only the values derived by Tian et al. (2005) and Koskinen et al. (2013), both larger than ours, fall relatively far from the derived constraints.

Assuming the energy-limited approach, we derive the heating efficiency as a function of the mass-loss rate (see Fig. 15). If we additionally assume the heating efficiency range of 0.1–0.2 derived from the detailed study of Shematovich et al. (2014), we conclude that the most probable substellar total mass-loss rate is in the range of $(0.42–1.00)\times10^{11}$ g s^{-1}, and that the temperature ranges from 7125 to 8125 K.

Our model, as it is inherently limited by its one dimension and spherical symmetry, cannot explain any net (either blue or red) shifts. Future work on the analysis of the observed net blueshift components and on possible cometary outflows with 3D modelling is encouraged.

Acknowledgements. We thank Prof. J. Linsky for his helpful refereed report. IAA authors acknowledge financial support from the State Agency for Research of the Spanish MCIU through the "Center of Excellence Severo Ochoa" award SEV-2017-0709. CARMENES is an instrument for the Centro Astronómico Hispano-Alemán de Calar Alto (CAHA, Almería, Spain). CARMENES is funded by the German Max-Planck-Gesellschaft (MPG), the Spanish Consejo Superior de Investigaciones Científicas (CSIC), the European Union through FEDER/ERF FICTS-2011-02 funds, and the members of the CARMENES Consortium (Max-Planck-Institut für Astronomie, Instituto de Astrofísica de Andalucía, Landessternwarte Königstuhl, Institut de Ciències de l'Espai, Insitut für Astrophysik Göttingen, Universidad Complutense de Madrid, Thüringer Landessternwarte Tautenburg, Instituto de Astrofísica de Canarias, Hamburger Sternwarte, Centro de Astrobiología and Centro Astronómico Hispano-Alemán), with additional contributions by the Spanish Ministry of Economy, the German Science Foundation through the Major Research Instrumentation Programme and DFG Research Unit FOR2544

"Blue Planets around Red Stars", the Klaus Tschira Stiftung, the states of Baden-Württemberg and Niedersachsen, and by the Junta de Andalucía. We acknowledge financial support from the Agencia Estatal de Investigación of the Ministerio de Ciencia, Innovación y Universidades, funds through projects: ESP2016–76076–R, ESP2017-87143-R, BES–2015–074542, BES–2015–073500, PGC2018-098153-B-C31, AYA2016-79425-C3-1/2/3-P.

References

Allart, R., Bourrier, V., Lovis, C., et al. 2018, Science, 362, 1384
Allart, R., Bourrier, V., Lovis, C., et al. 2019, A&A, 623, A58
Alonso-Floriano, F. J., Snellen, I. A. G., Czesla, S., et al. 2019, A&A, 629, A110
Ballester, G. E., & Ben-Jaffel, L. 2015, ApJ, 804, 116
Ballester, G. E., Sing, D. K., & Herbert, F. 2007, Nature, 445, 511
Ben-Jaffel, L., & Ballester, G. E. 2013, A&A, 553, A52
Ben-Jaffel, L., & Hosseini, S. S. 2010, ApJ, 709, 1284
Benjamin, R. A., Skillman, E. D., & Smits, D. P. 1999, ApJ, 514, 307
Bourrier, V., & Lecavelier des Etangs, A. 2013, A&A, 557, A124
Bray, I., Burgess, A., Fursa, D. V., & Tully, J. A. 2000, A&AS, 146, 481
Brown, R. 1971, ApJ, 164, 387
Castelli, F., & Kurucz, R. 2004, IAU Symp. 210, A20
Claire, M. W., Sheets, J., Cohen, M., et al. 2012, ApJ, 757, 95
Drake, G. W. F. 1971, Phys. Rev. A, 3, 908
Ehrenreich, D., Lecavelier des Etangs, A., Hébrard, G., et al. 2008, A&A, 483, 933
Ehrenreich, D., Bourrier, V., Wheatley, P. J., et al. 2015, Nature, 522, 459
Erkaev, N. V., Kulikov, Y. N., Lammer, H., et al. 2007, A&A, 472, 329
Fossati, L., Haswell, C. A., Froning, C. S., et al. 2010, ApJ, 714, L222
France, K., Stocke, J. T., Yang, H., et al. 2010, ApJ, 712, 1277
García-Muñoz, A. 2007, Planet. Space Sci., 55, 1426
Glover, S. C. O., & Jappsen, A. 2007, ApJ, 666, 1
Haswell, C. A., Fossati, L., Ayres, T., et al. 2012, ApJ, 760, 79
Indriolo, N., Hobbs, L. M., Hinkle, K. H., & McCall, B. J. 2009, ApJ, 703, 2131
Jensen, A. G., Redfield, S., Endl, M., et al. 2012, ApJ, 751, 86
Jin, S., & Mordasini, C. 2018, ApJ, 853, 163
Koskinen, T., Harris, M., Yelle, R., & Lavvas, P. 2013, Icarus, 226, 1678
Kulow, J. R., France, K., Linsky, J., & Parke Loyd, R. O. 2014, ApJ, 786, 132
Lamers, H., & Cassinelli, J. 1999, Introduction to Stellar Winds, 2nd edn. (Sausalito, CA: University of Science Books)
Lammer, H., Selsis, F., Ribas, I., et al. 2003, ApJ, 598, L121
Lammer, H., Odert, P., Leitzinger, M., et al. 2009, A&A, 506, 399
Lavie, B., Ehrenreich, D., Bourrier, V., et al. 2017, A&A, 605, L7
Lecavelier des Etangs, A., Vidal-Madjar, A., McConnell, J. C., & Hébrard, G. 2004, A&A, 418, L1
Lecavelier des Etangs, A., Ehrenreich, D., Vidal-Madjar, A., et al. 2010, A&A, 514, A72
Lecavelier des Etangs, A., Bourrier, V., Wheatley, P. J., et al. 2012, A&A, 543, L4
Linsky, J. L., Yang, H., France, K., et al. 2010, ApJ, 717, 1291
Linsky, J. L., Fontenla, J., & France, K. 2014, ApJ, 780, 61
Locci, D., Cecchi-Pestellini, C., & Micela, G. 2019, A&A, 624, A101
López-Puertas, M., & Taylor, F. W. 2001, Non-LTE Radiative Transfer in the Atmosphere (Singapore: World Scientific)
Mansfield, M., Bean, J. L., Oklopčić, A., et al. 2018, ApJ, 868, L34
Moses, J. I., Fouchet, T., Bezard, B., et al. 2005, J. Geophys. Res., 110, E08001
Norcross, D. W. 1971, J. Phys. B, 4, 652
Nortmann, L., Palle, E., Salz, M., et al. 2018, Science, 362, 1388
Oklopčić, A., & Hirata, C. M. 2018, ApJ, 855, L11
Osterbrock, D. E., & Ferland, G. J. 2006, Astrophysics Of Gas Nebulae and Active Galactic Nuclei (Sausalito, CA: University Science Books)
Parker, E. N. 1958, ApJ, 128, 664
Penz, T., Erkaev, N., Kulikov, Y., et al. 2008, Planet. Space Sci., 56, 1260
Quirrenbach, A., Amado, P. J., Caballero, J. A., et al. 2016, Proc. SPIE, 12, 14
Quirrenbach, A., Amado, P. J., Ribas, I., et al. 2018, Proc. SPIE, 32, 19
Roberge, W., & Dalgarno, A. 1982, ApJ, 255, 489
Salpeter, E. E. 1973, ApJ, 181, L83
Salz, M., Schneider, P. C., Czesla, S., & Schmitt, J. H. M. M. 2015, A&A, 585, L2
Salz, M., Czesla, S., Schneider, P. C., & Schmitt, J. H. M. M. 2016, A&A, 586, A75
Salz, M., Czesla, S., Schneider, P. C., et al. 2018, A&A, 620, A97
Santos, N. C., Israelian, G., & Mayor, M. 2004, A&A, 415, 1153
Sanz-Forcada, J., Ribas, I., Micela, G., et al. 2010, A&A, 511, L8
Sanz-Forcada, J., Micela, G., Ribas, I., et al. 2011, A&A, 532, A6
Seager, S., & Sasselov, D. D. 2000, ApJ, 537, 916
Shematovich, V. I., Ionov, D. E., & Lammer, H. 2014, A&A, 571, A94
Snellen, I. A. G., de Kok, R. J., de Mooij, E. J. W., & Albrecht, S. 2010, Nature, 465, 1049
Spake, J. J., Sing, D. K., Evans, T. M., et al. 2018, Nature, 557, 68
Stevenson, D. J. 1975, Phys. Rev. B, 12, 3999
Stevenson, D. J. 1980, Science, 208, 746
Tian, F., Toon, O. B., Pavlov, A. A., & De Sterck, H. 2005, ApJ, 621, 1049
Torres, G., Winn, J. N., & Holman, M. J. 2008, ApJ, 677, 1324
Vidal-Madjar, A., des Etangs, A. L., Désert, J.-M., et al. 2003, Nature, 422, 143
Vidal-Madjar, A., Désert, J.-M., des Etangs, A. L., et al. 2004, ApJ, 604, 69
Vidal-Madjar, A., Lecavelier des Etangs, A., Désert, J.-M., et al. 2008, ApJ, 676, L57
Vidal-Madjar, A., Huitson, C. M., Bourrier, V., et al. 2013, A&A, 560, A54
Watson, A. J., Donahue, T. M., & Walker, J. C. 1981, Icarus, 48, 150
Wilson, H. F., & Militzer, B. 2010, Phys. Rev. Lett., 104, 121101
Yan, F., & Henning, T. 2018, Nat. Astron., 2, 714
Yelle, R. V. 2004, Icarus, 170, 167

Appendix A: Calculation of the average mean molecular weight

From Eq. (5), considering the constant temperature T_0, we have

$$v(r)\frac{\mathrm{d}v}{\mathrm{d}r} + \frac{kT_0}{\mu(r)}\left(-\frac{1}{v(r)}\frac{\mathrm{d}v}{\mathrm{d}r} - \frac{2}{r}\right) + k\,T_0\,\frac{\mathrm{d}(1/\mu)}{\mathrm{d}r} + \frac{G\,M_\mathrm{p}}{r^2} = 0. \tag{A.1}$$

By integrating Eq. (A.1) and re-arranging its terms, we obtain

$$\frac{G\,M_\mathrm{p}}{kT_0}\int_{r_0}^{r_\mathrm{f}}\mu(r)\,\frac{\mathrm{d}r}{r^2} + \frac{1}{kT_0}\int_{v_0}^{v_\mathrm{f}}\mu(r)\,v(r)\,\mathrm{d}v + \int_{1/\mu_0}^{1/\mu_f}\mu(r)\,\mathrm{d}(1/\mu) = \int_{v_0}^{v_f}\frac{\mathrm{d}v}{v(r)} + 2\int_{r_0}^{r_f}\frac{\mathrm{d}r}{r}, \tag{A.2}$$

where r_f is the upper boundary distance of our model (10 R_P), and v_f and μ_f are the bulk radial velocity and mean molecular weight, respectively.

The mean molecular weight, $\mu(r)$, enters in the first, second, and third terms of Eq. (A.2). Thus, we construct an expression for $\bar{\mu}$:

$$\bar{\mu} = \frac{G\,M_\mathrm{p}\int_{r_0}^{r_\mathrm{f}}\mu(r)\,\frac{\mathrm{d}r}{r^2} + \int_{v_0}^{v_f}\mu(r)\,v(r)\,\mathrm{d}v + kT_0\int_{1/\mu_0}^{1/\mu_\mathrm{f}}\mu(r)\,\mathrm{d}(1/\mu)}{G\,M_\mathrm{p}\int_{r_0}^{r_\mathrm{f}}\frac{\mathrm{d}r}{r^2} + \int_{v_0}^{v_\mathrm{f}}v(r)\,dv + kT_0\int_{1/\mu_0}^{1/\mu_\mathrm{f}}\mathrm{d}(1/\mu)}. \tag{A.3}$$

4

Characterisation of the upper atmospheres of HD 189733 b and GJ 3470 b

This Chapter has been accepted for publication in the journal Astronomy and Astrophysics with the title “Modelling the He I triplet absorption at 10 830 Å in the atmospheres of HD 189733 b and GJ 3470 b”. Lampón et al. 2021, A&A, in press, DOI 10.1051/0004-6361/202039417, reproduced with permission ©ESO.

Astronomy & Astrophysics manuscript no. output
January 31, 2021
©ESO 2021

Modelling the He I triplet absorption at 10830 Å in the atmospheres of HD 189733 b and GJ 3470 b

M. Lampón[1], M. López-Puertas[1], J. Sanz-Forcada[2], A. Sánchez-López[3], K. Molaverdikhani[4,5], S. Czesla[6], A. Quirrenbach[5], E. Pallé[7,8], J. A. Caballero[2], Th. Henning[4], M. Salz[6], L. Nortmann[9], J. Aceituno[1,10], P. J. Amado[1], F. F. Bauer[1], D. Montes[11], E. Nagel[12], A. Reiners[9], and I. Ribas[13,14]

[1] Instituto de Astrofísica de Andalucía (IAA-CSIC), Glorieta de la Astronomía s/n, 18008 Granada, Spain
e-mail: mlampon@iaa.es
[2] Centro de Astrobiología (CSIC-INTA), ESAC, Camino bajo del castillo s/n, 28692 Villanueva de la Cañada, Madrid, Spain
[3] Leiden Observatory, Leiden University, Postbus 9513, 2300 RA, Leiden, The Netherlands
[4] Max-Planck-Institut für Astronomie, Königstuhl 17, 69117 Heidelberg, Germany
[5] Landessternwarte, Zentrum für Astronomie der Universität Heidelberg, Königstuhl 12, 69117 Heidelberg, Germany
[6] Hamburger Sternwarte, Universität Hamburg, Gojenbergsweg 112, 21029 Hamburg, Germany
[7] Instituto de Astrofísica de Canarias (IAC), Calle Vía Láctea s/n, 38200 La Laguna, Tenerife, Spain
[8] Departamento de Astrofísica, Universidad de La Laguna, 38026 La Laguna, Tenerife, Spain
[9] Institut für Astrophysik, Georg-August-Universität, Friedrich-Hund-Platz 1, 37077 Göttingen, Germany
[10] Observatorio de Calar Alto, Sierra de los Filabres, 04550 Gérgal, Almería, Spain
[11] Departamento de Física de la Tierra y Astrofísica & IPARCOS-UCM (Instituto de Física de Partículas y del Cosmos de la UCM), Facultad de Ciencias Físicas, Universidad Complutense de Madrid, 28040 Madrid, Spain
[12] Thüringer Landessternwarte Tautenburg, Sternwarte 5, 07778 Tautenburg, Germany
[13] Institut de Ciències de l'Espai (CSIC-IEEC), Campus UAB, c/ de Can Magrans s/n, 08193 Bellaterra, Barcelona, Spain
[14] Institut d'Estudis Espacials de Catalunya (IEEC), 08034 Barcelona, Spain

Received 13 September 2020 / Accepted 20 January 2021

ABSTRACT

Characterising the atmospheres of exoplanets is key to understanding their nature and provides hints about their formation and evolution. High resolution measurements of the helium triplet absorption of highly irradiated planets have been recently reported, which provide a new means of studying their atmospheric escape. In this work we study the escape of the upper atmospheres of HD 189733 b and GJ 3470 b by analysing high resolution He I triplet absorption measurements and using a 1D hydrodynamic spherically symmetric model coupled with a non-local thermodynamic model for the He I triplet state. We also use the H density derived from Lyα observations to further constrain their temperatures, mass-loss rates, and H/He ratios. We have significantly improved our knowledge of the upper atmospheres of these planets. While HD 189733 b has a rather compressed atmosphere and small gas radial velocities, GJ 3470 b, on the other hand with a gravitational potential ten times smaller, exhibits a very extended atmosphere and large radial outflow velocities. Hence, although GJ 3470 b is much less irradiated in the X-ray and extreme ultraviolet radiation, and its upper atmosphere is much cooler, it evaporates at a comparable rate. In particular, we find that the upper atmosphere of HD 189733 b is compact and hot, with a maximum temperature of $12\,400^{+400}_{-300}$ K, with a very low mean molecular mass (H/He=(99.2/0.8)±0.1), which is almost fully ionised above 1.1 R_P, and with a mass-loss rate of $(1.1\pm0.1)\times10^{11}$ g s^{-1}. In contrast, the upper atmosphere of GJ 3470 b is highly extended and relatively cold, with a maximum temperature of 5100±900 K, also with a very low mean molecular mass (H/He=$(98.5/1.5)^{+1.0}_{-1.5}$), which is not strongly ionised, and with a mass-loss rate of $(1.9\pm1.1)\times10^{11}$ g s^{-1}. Furthermore, our results suggest that upper atmospheres of giant planets undergoing hydrodynamic escape tend to have a very low mean molecular mass (H/He $\gtrsim$ 97/3).

Key words. planets and satellites: atmospheres – planets and satellites: gaseous planets – planets and satellites: individual: HD 189733 b – planets and satellites: individual: GJ 3470 b

1. Introduction

Observations of atmospheres undergoing hydrodynamic escape provide critical information about their physical properties and can also offer important hints about their formation and evolution (e.g. Baraffe et al. 2004, 2005; Owen & Wu 2013, 2017; Lopez & Fortney 2013; Muñoz & Schneider 2019). Hydrodynamic atmospheric escape is the most efficient atmospheric process of mass loss (see e.g. Watson et al. 1981; Yelle 2004; Tian et al. 2005; García-Muñoz 2007; Salz et al. 2015). This process occurs when the gas pressure gradient overcomes the gravity of the planet at some atmospheric altitude, as it is heated via photo-ionisation. Therefore, the stellar irradiation, mainly X-ray and extreme ultraviolet (XUV) radiation, as well as the near-ultraviolet (NUV) radiation in exoplanets orbiting hot stars (Muñoz & Schneider 2019), triggers hydrodynamic atmospheric escape generating a strong wind that substantially expands the thermosphere of the planet and ejects the gas beyond the Roche lobe.

Lyα observations can probe hydrodynamic atmospheric escape and provide important information about the planetary upper atmosphere (Vidal-Madjar et al. 2003). However, Lyα can only be observed from space. Moreover, geocoronal emission

contamination and interstellar medium absorption dominate the core of the line, leaving only their wings with potential exoplanetary information (see e.g. Vidal-Madjar et al. 2003; Ehrenreich et al. 2008). Observations of X-ray radiation and ultraviolet lines from heavy elements (e.g. O I and C II) in exoplanets undergoing hydrodynamic atmospheric escape have similar limitations (see e.g. Vidal-Madjar et al. 2004; Ben-Jaffel & Ballester 2013; Poppenhaeger et al. 2013).

Observations of the He I 2^3S–2^3P lines[1] (hereafter He(2^3S) lines) and Hα are not seriously limited by interstellar absorption (see e.g. Spake et al. 2018; Nortmann et al. 2018; Allart et al. 2018; Mansfield et al. 2018; Allart et al. 2019; Yan & Henning 2018; Casasayas-Barris et al. 2018; Wyttenbach et al. 2020). Therefore, detailed studies of the absorption line profile are feasible. For instance, Lampón et al. (2020) have recently analysed the He(2^3S) absorption in the atmosphere of HD 209458 b and derived a well-constrained relationship between the mass-loss rate and temperature, as well as key atmospheric parameters such as the He(2^3S) density, the [H]/[H^+] transition altitude, and the XUV absorption effective radii.

In addition, as He(2^3S) measurements probe different atmospheric altitudes than the H lines, it is possible to reduce the degeneracy significantly by combining information from both elements. Indeed, by comparing the hydrogen density profile retrieved from Lyα by Salz et al. (2016) with that derived from He(2^3S) observations, Lampón et al. (2020) found H/He $\approx$ 98/2 in the upper atmosphere of HD 209458 b, which is significantly higher than the commonly used value of 90/10 (e.g. Oklopčić & Hirata 2018; Mansfield et al. 2018; Ninan et al. 2020; Guilluy et al. 2020). Moreover, by constraining the upper atmospheric H/He ratio, we can gain important insights on the formation, evolution, and nature of the planet (see, e.g. Hu et al. 2015; Malsky & Rogers 2020). Therefore, it is important to measure the H/He ratio in other evaporating atmospheres.

The exoplanets HD 189733 b and GJ 3470 b undergo hydrodynamic escape, as was probed by the Lyα and oxygen observations in HD 189733 b (Lecavelier des Etangs et al. 2010, 2012; Bourrier et al. 2013; Ben-Jaffel & Ballester 2013), and by Lyα and He(2^3S) observations for GJ 3470 b (Bourrier et al. 2018; Pallé et al. 2020; Ninan et al. 2020). These planets have rather different physical properties. Salz et al. (2016) estimated that HD 189733 b, with a high gravitational potential, has a hot thermosphere with weak winds, whereas GJ 3470 b, with lower gravitational potential, has a relatively cool atmosphere with strong winds. Both exoplanets are also rather different from HD 209458 b, as they have distinct bulk parameters and are irradiated at different XUV fluxes. To date, He(2^3S) spectral absorption has been observed in HD 189733 b by Salz et al. (2018) and Guilluy et al. (2020), as well as in GJ 3470 b by Pallé et al. (2020) and Ninan et al. (2020).

In this work we aim to improve the characterisation of the upper atmospheres of HD 189733 b and GJ 3470 b from the He(2^3S) spectral absorption measurements taken with the high–resolution spectrograph CARMENES [2] (Quirrenbach et al. 2016, 2018) by Salz et al. (2018) and Pallé et al. (2020), respectively. To that end, we applied a 1D hydrodynamic model with spherical symmetry together with an He(2^3S) non-local thermodynamic equilibrium (non-LTE) model to calculate the He(2^3S) concentration and gas radial velocity distributions. Subsequently, we used a high-resolution radiative transfer model for calculating the synthetic spectra as observed by CARMENES and compared them with the measurements. By exploring a wide range of input parameters, we derived constraints on the mass-loss rate, temperature, H/He composition, He(2^3S) density, [H]/[H^+] transition altitude, and XUV absorption effective radii. Finally, we compared our H densities with those retrieved from Lyα measurements in previous studies in order to constrain the H/He composition.

The paper is organised as follows. Sect. 2 summarises the He(2^3S) observations of HD 189733 b and GJ 3470 b; Sect. 3 briefly describes the modelling of the He(2^3S) density, the gas radial velocities, and the He(2^3S) absorption; Sect. 4 shows and discusses the results obtained; and in Sect. 6 we present a summary and our conclusions.

2. Observations of He I triplet absorption of HD 189733 b and GJ 3470 b

The He(2^3S) absorption profiles analysed here were observed in the atmospheres of HD 189733 b and GJ 3470 b by Salz et al. (2018) and Pallé et al. (2020), respectively, with the high-resolution spectrograph CARMENES. We briefly summarise these observations below.

HD 189733 b shows a significant He excess absorption at mid-transit, with a mean absorption level of 0.88 ± 0.04%, and of 0.24±0.12% and 0.46±0.06% for the ingress and egress phases, respectively. The absorption (in the planetary rest frame) appears shifted to blue wavelengths by $-3.5 \pm 0.4\,\mathrm{km\,s^{-1}}$ and $-12.6 \pm 1.0\,\mathrm{km\,s^{-1}}$ during the mid-transit and egress, respectively, and it appears shifted to red wavelengths by $6.5 \pm 3.1\,\mathrm{km\,s^{-1}}$ during the ingress. We caution, however, as Salz et al. (2018) remarked, that these velocities could be potentially affected by stellar pseudo-signals. Another important feature is that the ratio between the absorption in the stronger He(2^3S) line, caused by the two unresolved lines centred at 10833.22 and 10833.31 Å, and the weaker one centred at 10832.06 Å (hereafter He $\mathrm{I}_{\lambda 10833}$/He $\mathrm{I}_{\lambda 10832}$) is 2.8 ± 0.2, which is much smaller than expected from optically thin conditions.

GJ 3470 b shows a 1.5 ± 0.3% He absorption depth at mid-transit (Pallé et al. 2020). Unfortunately, the individual spectra during ingress or egress do not have a sufficient signal-to-noise ratio (S/N) to probe for any blue or red shifts. The mid-transit spectrum appears shifted to blue wavelengths by $-3.2 \pm 1.3\,\mathrm{km\,s^{-1}}$. The analysis of these absorption profiles is discussed in Sect. 4.1.

3. Modelling the He I triplet

3.1. Helium triplet density

We calculated the populations of the He(2^3S) by using the model described in Lampón et al. (2020). Briefly, we used a 1D hydrodynamic model together with a non-LTE model to calculate the He(2^3S) density distribution in the substellar direction (the one that connects the star-planet centres) in the upper atmosphere of the planets. We assumed that the substellar conditions are a representative of the whole planetary sphere, so that a spherical symmetry was adopted. The mass-loss rate derived under this assumption is a valid estimate for the whole atmosphere when divided by a factor of ∼4 to account for the 3D asymmetric stellar irradiation on the planetary surface (see e.g. Murray-Clay et al. 2009; Stone & Proga 2009; Tripathi et al. 2015; Salz et al. 2016).

[1] At wavelengths 10832.06, 10833.22, and 10833.31 Å in the vacuum, often referred to as their air wavelengths of 10830 Å.

[2] Calar Alto high-Resolution search for M dwarfs with Exoearths with Near-infrared and optical Échelle Spectrographs, at the 3.5 m Calar Alto Telescope.

Table 1. System parameters of HD 189733 and GJ 3470.

Parameter	Value	Reference
HD 189733		
d	19.775 ± 0.013 pc	Gaia DR2[(a)]
$R_\star$	$0.805 \pm 0.016\ R_\odot$	Boyajian et al. (2015)
$M_\star$	$0.846\ ^{+0.06}_{-0.049}\ M_\odot$	de Kok et al. (2013)
$T_{\rm eff}$	4875 ± 43 K	Boyajian et al. (2015)
$[{\rm Fe/H}]_\star$	-0.03 ± 0.05	Bouchy et al. (2005)
a[(b)]	0.0332 ± 0.0010 au	Agol et al. (2010)
$R_{\rm P}$[(c)]	$1.23 \pm 0.03\ R_{\rm Jup}$	Baluev et al. (2015)
$M_{\rm P}$	$1.162\ ^{+0.058}_{-0.039}\ M_{\rm Jup}$	de Kok et al. (2013)
GJ 3470		
d	29.45 ± 0.05 pc	Gaia DR2[(a)]
$R_\star$	$0.474 \pm 0.014\ R_\odot$	Pallé et al. (2020)
$M_\star$	$0.476 \pm 0.019\ M_\odot$	Pallé et al. (2020)
$T_{\rm eff}$	3725 ± 54 K	Pallé et al. (2020)
$[{\rm Fe/H}]_\star$	$+0.420 \pm 0.019$	Pallé et al. (2020)
a	0.0348 ± 0.0014 au	Bonfils et al. (2012)
$R_{\rm P}$	$0.36 \pm 0.01\ R_{\rm Jup}$	Pallé et al. (2020)
$M_{\rm P}$	$0.036 \pm 0.002\ M_{\rm Jup}$	Pallé et al. (2020)

Notes. [(a)] Gaia Collaboration et al. (2018). [(b)] From $a/R_\star = 8.863(20)$ by Agol et al. (2010) and $R_\star$ by Boyajian et al. (2015). [(c)] From $R_P/R_\star = 0.15712(40)$ by Baluev et al. (2015) and $R_\star$ by Boyajian et al. (2015).

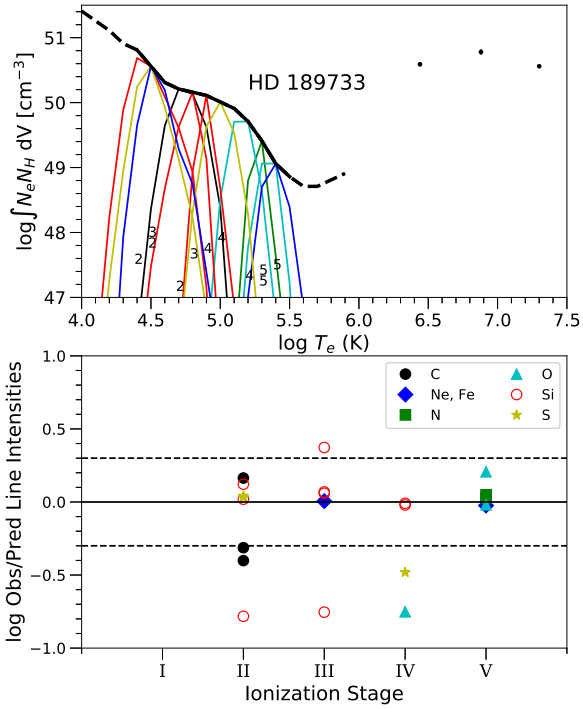

Fig. 1. *Upper panel*: Emission measure distribution of HD 189733 calculated using the line fluxes measured in the HSLA/COS summed spectrum. The 3-T model used to fit *XMM-Newton* summed EPIC spectra is also displayed. The thin lines represent the relative contribution function for each ion (the emissivity function multiplied by the EMD at each point), following same colour code as in lower panel. The small numbers indicate the ionisation stages of the species. *Lower panel*: Observed-to-predicted line flux ratios for the ion stages in the upper panel. The dotted lines denote a factor of 2.

The hydrodynamic equations were solved assuming that the escaping gas has a constant speed of sound, $v_s = \sqrt{k\,T(r)/\mu(r)}$, where k is the Boltzmann constant, $T(r)$ is temperature, and $\mu(r)$ is the mean molecular weight. This assumption leads to the same analytical solution as the isothermal Parker wind solution. However, the atmosphere is not assumed to be isothermal, but the temperature varies with altitude in such a way that the $T(r)/\mu(r)$ ratio is constant. That is to say we assume $v_s = \sqrt{k\,T_0/\bar{\mu}}$ where $\bar{\mu}$ is the average mean molecular weight, calculated in the model, and T_0 is a model input parameter which is very similar to the maximum of the thermospheric temperature profile calculated by hydrodynamic models that solve the energy balance equation (see, e.g. Salz et al. 2016). The temperature ,T_0, the mass-loss rate, $\dot{M}$ (of all species considered in the model), and the H/He mole-fraction ratio (i.e. the composition of the upper atmosphere) are input parameters to the model. The physical parameters of the planets, such as their mass, $M_{\rm P}$, and size, $R_{\rm P}$, introduced in the model, are listed in Table 1.

The model computes the radial distribution of the concentrations of the following species: neutral and ionised hydrogen, H^0 and H^+, respectively, as well as helium singlet and ionised helium, He(1^1S) and He^+, and He(2^3S). In addition, it also calculates the radial velocity of the gas. The production and loss terms and the corresponding rates are listed in Table 2 of Lampón et al. (2020). They represent a minor extension of those considered by Oklopčić & Hirata (2018), where two additional processes were included: the charge exchange reactions, $Q_{\rm He}$ and $Q_{\rm He^+}$, from Koskinen et al. (2013). Other parameters such as the H, He(1^1S), and He(2^3S) photo-ionisation cross sections were taken as in Lampón et al. (2020).

In the model we established the lower boundary conditions where hydrodynamic escape originates. This is usually assumed to occur at μbar–nbar levels (see, e.g. García-Muñoz 2007; Koskinen et al. 2013; Salz et al. 2016; Murray-Clay et al. 2009), although its geometric altitude is uncertain as it depends on the pressure, temperature, and composition below, which are normally unknown. In Sects. 4.1.1 and 4.1.3, we discuss the effects of the lower boundary conditions on the absorption profiles of these planets. Nominally, we assumed that hydrodynamic escape originates at $1.02\,R_{\rm P}$ (slightly higher than the optical radius) with a density of 10^{14} cm^{-3}. The density at the lower boundary was chosen large enough so that the XUV radiation is fully absorbed by the atmosphere above, but it is consistent with the values given by the hydrostatic models below (see, e.g. Salz et al. 2016).

3.2. Stellar fluxes

A further input parameter required by the model is the stellar XUV spectral flux. For HD 189733, a coronal model was used to obtain the stellar emission in the range of 5–1200 Å. The model is based on the addition of all the *XMM-Newton* observations available to date of this star, between 2007 and 2015 [3]. The EPIC spectra were combined for a total exposure

[3] Proposals id. 50607, 60097, 67239, 69089, 69229, 74498, 74839.

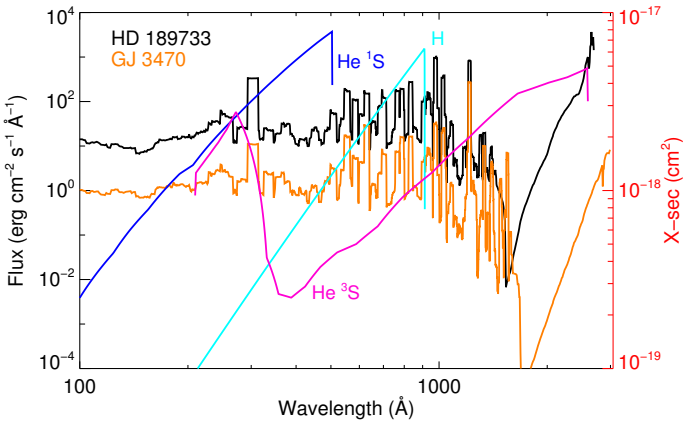

Fig. 2. Flux density (left y-axis) for HD 189733 (black) and GJ 3470 (orange) at 0.0332 au and 0.0348 au plotted at a resolution of 10 Å, respectively. The H, He singlet, and He triplet ionisation cross sections (right y-axis) are also shown.

time of 461 ks (pn), 822 ks (MOS1), and 896 ks (MOS2). The coronal 3-Temperature model (log T(K)= 6.44 ± 0.01, 6.88 ± 0.01, 7.3 ± 0.01, log EM(cm^{-3})= 50.59 ± 0.03, 50.78 ± 0.04, 50.56 ± 0.01, L_X = 2.2 × 10^{28} erg s^{-1}) is complemented with line fluxes (Table A.1) from the HST/COS FUV spectrum available from the Hubble Spectral Legacy Archive (HSLA) to extend the model (Tables A.2 and A.3) towards lower temperatures (log T(K)~ 4.0−5.9), following Sanz-Forcada et al. (2011). This model (Fig. 1) is a substantial improvement with respect to the X-exoplanets model available in Sanz-Forcada et al. (2011). The modelled spectral energy distribution (SED) fluxes now indicate an EUV luminosity of $L_{\rm EUVH}$ = 1.6 × 10^{29} erg s^{-1} and $L_{\rm EUVHe}$ = 5.1 × 10^{28} erg s^{-1} in the ranges of 100–912 Å and 100-504 Å, respectively. The SED covers the range of 5–1145 Å, and it was generated following Sanz-Forcada et al. (2011). The data include several small flares, which were not removed on purpose, in order to provide an average model of active and non-active stages. We, therefore, used the summed HST/COS spectrum in the range of 1145–1450 Å. The SED calculated using our model is consistent with the flux level observed in the actual *HST* observations of the star in the region of 1145−1200 Å.

XMM-Newton observations of GJ 3470 were used to model the corona of this star, complemented with HST/STIS spectral line fluxes, as described in Bourrier et al. (2018). The quality of the HST/COS spectra was not good enough to fix the UV continuum in the spectral range of 1150–1750 Å, due to poor statistics, while HST/STIS coverage was limited to 1195–1248 Å only. Thus, the model SED was also used in this spectral range.

In order to extend the SED of both planets to 2600 Å, we used the stellar atmospheric model of Castelli & Kurucz (2004) scaled to the corresponding temperature, surface gravity, and metallicity (see Table 1). The composite SED for the spectral range of 5−2600 Å for both planets at their respective orbital separations are shown in Fig. 2.

3.3. Spectral absorption

With the He(2^3S) calculations and gas radial velocities from the model described above, we computed the He(2^3S) absorption by using a radiative transfer code for the primary transit geometry (Lampón et al. 2020). The spectroscopic data for the three metastable helium lines were taken from the NIST Atomic Spectra Database[4]. Doppler line shapes are assumed at the atmospheric temperature used in the model density, and an additional broadening produced by turbulent velocities can be included if necessary ($v_{\rm turb} = \sqrt{5kT/3m}$, where m is the mass of an He atom, see Eq. 16 in Lampón et al. 2020). The component of the radial velocity of the gas along the line of sight (LOS) towards the observer is also included in order to account for the motion of He(2^3S) as predicted in the hydrodynamic model. In addition to the radial velocities, averaged winds (e.g. day-to-night and super-rotation winds), and planetary rotation (see e.g. Salz et al. 2018; Seidel et al. 2020) can also be included in the radiative transfer model, as required (see Eq. 15 in Lampón et al. 2020).

In this study, we performed the integration of the He(2^3S) absorption up to 10 R_P. This is motivated because we found that the He(2^3S) distribution of GJ 3470 b is rather extended (see Sect. 4.3).

3.4. Grid of simulations

Here we have analysed the mid-transit absorption profiles of HD 189733 b and GJ 3470 b (see Fig. 3) in a similar manner as in Lampón et al. (2020) for HD 209458 b. Briefly, from this model and the measured He(2^3S) absorption, we could not unambiguously determine the mass-loss rate and temperature of the planetary atmosphere as these two quantities are degenerate in most cases. Thus, for a given H/He composition, we ran the He(2^3S) model for a range of temperatures and mass-loss rates and computed the He(2^3S) absorption. As also shown by Lampón et al. (2020), the temperatures and mass-loss rates are also degenerate with respect to the H/He atomic ratio. We broke that degeneracy by also fitting the H^0 density profiles of the model to those derived from Lyα measurements. To that end, we ran several sets of models for H/He atomic ratios ranging from 90/10, our nominal case, to 99.9/0.1 and to 99/1 for HD 189733 b and GJ 3470 b, respectively.

Synthetic spectra from these simulations were compared to the measured absorption profiles, and the corresponding reduced χ^2 values were computed by (see, e.g. Press et al. 2007)

$$\chi^2_R = \frac{\chi^2}{\nu} \quad \text{with} \quad \chi^2 = \sum_i^N \frac{(Tr_{\rm mea,i} - Tr_{\rm mod,i})^2}{\sigma_i^2},$$

where $\nu = N - 2$ is the number of degrees of freedom, N is the number of fitted spectral points, $Tr_{\rm mea,i}$ and $Tr_{\rm mod,i}$ are the measured and calculated transmissions, and σ_i is the error of the transmissions (see Fig. 3). For obtaining the uncertainties in the derived parameters T and $\dot{M}$ with this method, we considered the 95% confidence levels of the χ^2 (not the reduced χ^2). In addition, we also explored the posterior probability distribution of the three model parameters for the grid of model spectra discussed above by using the Markov chain Monte Carlo (MCMC) method (Sect. 4.5).

4. Results and discussion

4.1. He I transmission spectra

Our aim is to concentrate on the mid-transit absorption, which provides information about the main structure of the thermospheric escaping gas, but not to explain all the He(2^3S) absorption features of those planets, nor their variations along the transit. In particular, the analysis of the velocity shifts in the He(2^3S)

[4] https://www.nist.gov/pml/atomic-spectra-database.

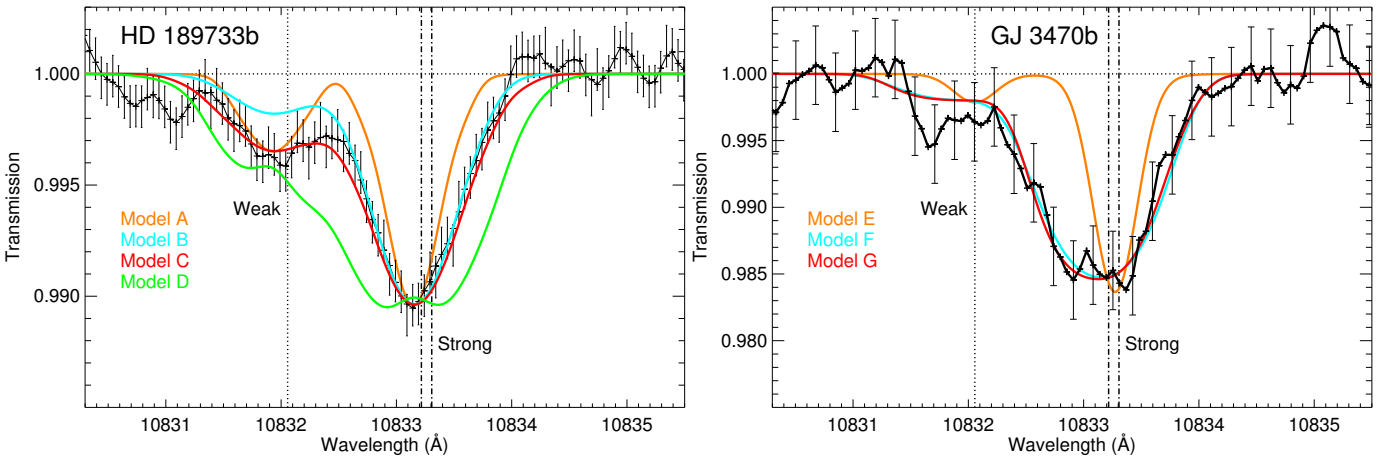

Fig. 3. Spectral transmission of the He triplet at mid-transit for HD 189733 b and GJ 3470 b (we note the different y-axis scale). Data points and their respective error bars are shown in black (adapted from Salz et al. (2018) and Pallé et al. (2020), respectively). Wavelengths are given in vacuum. The best-fit simulations are shown with red curves. For HD 189733 b, the best fit corresponds to a temperature of 10 000 K, a mass-loss rate of 10^9 g s^{-1} and an H/He mole-fraction of 90/10. For GJ 3470 b, the best fit corresponds to a temperature of 6000 K, $\dot{M}$=3.2× 10^{10} g s^{-1} and an H/He of 90/10. Other models are described in Table 2. The positions of the helium lines are marked by vertical dotted (weak) and dot-dashed (strong) lines.

Table 2. Models used for the calculation of the absorption shown in Fig. 3.

Model	Turbulent broadening[a]	LOS components	Lower boundary layer	Gas radial velocity
HD 189733 b				
A	No	–3.5 km s^{-1} (100%)	Yes	This model[b]
B	Yes	–12 km s^{-1}(25%), –3.5 km s^{-1}(47%), 5 km s^{-1}(28%),	No	This model[b]
C	Yes	–12 km s^{-1}(25%), –3.5 km s^{-1}(47%), 5 km s^{-1}(28%),	Yes	This model[b]
D	No	–3.5 km s^{-1} (100%)	Yes	40 km s^{-1} [c]
GJ 3470 b				
E	Yes	No component	Yes	No velocities
F	Yes	–3.2 km s^{-1} $\forall z$	Yes	This model
G	Yes	No component at $z < R_{\rm lobe}$, –5 km s^{-1} at $z > R_{\rm lobe}$	Yes	This model

Notes. [(a)] Doppler broadening was included in all models. [(b)] From the hydrodynamic model of this work. The gas radial velocities for this planet have negligible effects. [(c)] As in Seidel et al. (2020).

absorption is potentially interesting because it would provide information about the 3D velocity distribution, its origin (e.g. day-to-night and super-rotation winds, and planet's rotation), and it may also break some of the degeneracy between the temperature and mass-loss rates. However, as our model is spherically symmetric, it cannot explain net blue or red shifts and, hence, such analysis is beyond the scope of this paper. Nevertheless, in order to obtain the best fit to the mid-transit spectra, we need to assume some net velocities along the observational LOS superimposed on the gas radial velocities of our model. Thus, before exploring the range of temperature and mass-loss rates (see Sect. 4.2), we first discuss the shape of the mid-transit spectra and the required additional velocities.

4.1.1. He(2^3S) absorption of HD 189733 b

According to the observations by Salz et al. (2018), HD 189733 b shows a significant He excess absorption peaking at mid-transit (see Fig. 3), which is much stronger than that of HD 209458 b (see Alonso-Floriano et al. 2019; Lampón et al. 2020). The absorption profile also exhibits a more pronounced displacement to bluer wavelengths (−3.5±0.4 km s^{-1}) and it is also significantly broader. A similar net blue shift has been observed in the He(2^3S) absorption of GJ 3470 b (see below and Pallé et al. 2020). Then, in order to obtain the best possible fit, we incorporated a net blue shift of −3.5 km s^{-1} in our simulations.

A further analysis of the spectrum shows that, at typical thermospheric temperatures for this planet, ∼12 000 K (see, e.g. Guo 2011; Salz et al. 2016; Odert et al. 2020), the Doppler broadening is insufficient to explain the width of the absorption profile (see Model A in left panel of Fig. 3). To achieve a similar width, we would need temperatures much higher than 20 000 K, which do not seem very realistic. Including a turbulence broadening component (see Sect. 3.3), the profile broadens, but it is still narrower than the measured absorption. In that calculation we also included the component of the gas radial velocities of our model along the observation LOS. However, since the absorption is confined to the first few thousands of kilometres and our velocities at these altitudes are rather slow (see left panels of Figs. 6 and 7), the induced broadening is negligible. Hence, our hydrodynamic model alone is not able to explain the width of the absorption profile.

A likely explanation of the broadening emerges from the inspection of the observed shifts of the absorption profile during

the ingress and egress transit phases (Sect. 2, Salz et al. 2018). These shifts can be produced by a combination of the planetary rotation and strong net winds (probably of day-to-night and super-rotational winds) (see e.g. Salz et al. 2018; Flowers et al. 2019; Seidel et al. 2020), at altitudes ∼1–2 R_P, where the He(2^3S) absorption mainly takes place (see left panel of Fig.6). In particular, Salz et al. (2018) derived an averaged wind in the range of −11.6 to −13.6 km s^{-1} from the blue shift in the egress, and an averaged wind in the range of 3.4 to 9.6 km s^{-1} from the red shift in the ingress. Thus, we fitted the absorption by including, in addition to the main atmospheric blue component at −3.5 km s^{-1}, a blue and a red atmospheric component. By perturbing the velocity and fractional contribution of those components and minimising the χ^2, we found that the absorption profile can be well reproduced by two components at −12 km s^{-1} and 5 km s^{-1}, covering about 25% and 28% of the disk, respectively (Models B and C in the left panel of Fig.3). We note that those velocities are very similar to the mean values of the winds derived by Salz et al. (2018) from the egress and ingress phases. Also our red-shifted atmospheric fraction agrees very well, although the blue-shifted fraction is smaller in our case (mid-transit) than in the egress. These three components are included when we analyse the best fit to the spectra, for example in Model C (see Sect. 4.2).

Our model can also fit the absorption in the weaker He(2^3S) line (near 10832 Å) (see Model C in left panel of Fig. 3). This is due to the assumption of a lower boundary with a high enough density so that it absorbs all the XUV flux reaching this altitude (compare Models C, with a boundary condition, and B, without a boundary condition, in that figure). As the strong stellar radiation reaches the lower boundary of the upper atmosphere of HD 189733 b (see left panel of Fig. 8), and since the stronger lines are saturated at low altitudes, the relative absorption of the stronger lines with respect to the weaker lines decreases.

However, in order to fit the He I$_{\lambda 10833}$/He I$_{\lambda 10832}$ ratio, we had to increase the lower boundary density up to 10^{18} cm^{-3}, which agrees with the result of a very compressed annulus suggested by Salz et al. (2018). At this high concentration, collision processes become more important, increasing the production of He(2^3S) via recombination, because of the increase in He^+ by charge-exchange, and by electron collision (see Table 2 in Lampón et al. 2020). These processes are more important at high temperatures (see inset in Fig. 6). Overall, the fitting of the He I$_{\lambda 10833}$/He I$_{\lambda 10832}$ ratio in this planet requires a very compressed and hot lower boundary.

It is worth noting that our model reproduces the measured He I$_{\lambda 10833}$/He I$_{\lambda 10832}$ ratio of 2.8 better than the simple annulus model of Salz et al. (2018), who obtained a value of 4.6. The key difference is that while the annulus is optically thick to the stronger lines in all its extension, 1.2 R_P, they are only optically thick at the lower altitudes in our model.

4.1.2. Comparison with previous estimations of gas radial velocities of HD 189733 b

Seidel et al. (2020) have recently re-analysed observations of Na in HD 189733 b and have retrieved vertical upward winds, for example, radial velocity winds, of 40±4 km s^{-1} at altitudes above 1 μbar. The region probed by them, however, is limited to below ∼16 000 km (see their Fig. 8) (1.2 R_P referred to the centre of the planet), that is, the 1 μbar to ∼1 nbar or, approximately, (5–16)×10^3 km or (1.06–1.2) R_P region. They also suggest that such high radial velocities could arise from the expanding thermosphere. Our model velocities are much lower than 40 km s^{-1} (see Fig. 7, left panel); although, they could be affected by the imposed null velocity at the base of our model at 1.02 R_P.

In order to verify if the shape of the measured He(2^3S) absorption profile is compatible with the value derived by Seidel et al., we simulated an absorption profile with the He(2^3S) densities derived in this work, but by assuming that the atmosphere is escaping at a constant radial velocity of 40 km s^{-1} at all altitudes. The He(2^3S) abundances that fit the absorption (see left panel of Fig. 6) have a very pronounced peak at the lower altitudes of our model, 1–1.5 R_P. Hence, in essence, that is equivalent to imposing a constant 40 km s^{-1} velocity in that region. In order to be conservative, we did not include the turbulent component of the Doppler broadening in this calculation. The results show (see Fig. 3, Model D in green) that at such a high velocity, the He(2^3S) absorption profile would be much broader than measured. At those altitudes, (1.06–1.2) R_P, the atmosphere is still dense enough to drag all atoms at a similar radial velocity (Murray-Clay et al. 2009). That is to say the velocities derived from either He or Na should not differ significantly. Hence, we conclude that such a high radial (vertical) velocity of 40±4 km s^{-1} is not compatible with the He(2^3S) measurements, but this rather suggests that the gas radial velocities at those altitudes are significantly smaller.

4.1.3. He(2^3S) absorption of GJ 3470 b

GJ 3470 b shows a significantly larger He excess absorption than HD 189733 b (we note the different y-axis scale in Fig.3). Also, the absorption profile of the two stronger lines that are combined near 10833 Å is broader. As for HD 189733 b, we have included the Doppler and turbulence broadening in the calculation. This warm Neptune has a weaker gravity that leads to a much more extended atmosphere which expands at larger velocities (see right panels of Figs. 6 and 7). In fact, the velocities are already significant at rather low radii. Thus, in contrast to HD 189733 b, the component of the gas radial velocity along the observer LOS produces a significant broadening. We observe in Fig.3 (right panel) that the models that include the radial velocities (F and G), in contrast to E, explain very well the observed broadening without the need of blue or red components. We should also note that (not shown in the figure) the turbulent broadening is negligible compared to the broadening caused by such high radial velocities, and hence it does not have any significant impact on the line width.

As found in HD 189733 b (see above), as well as in HD 209458 b (Alonso-Floriano et al. 2019), we also observe a significant blue shift of the whole absorption, estimated to be −3.2±1.3 km s^{-1} (Pallé et al. 2020). This is intermediate between the values measured in those two planets. Unfortunately, we do not have ingress or egress spectra with a sufficient S/N (as we did for HD 189733 b) to help us in understanding its origin. A likely explanation is that it is also produced by day-to-night winds with velocities along the LOS of −3.2 km s^{-1} (see model F in Fig. 3). However, as GJ 3470 b has a very extended atmosphere, with significant He(2^3S) absorption beyond the Roche lobe (see left panel of Fig.6), another plausible interpretation is an upper atmosphere with no significant day-to-night winds below the Roche radius (3.6 R_P, see Table 3) but with the unbound gas above the Roche lobe blue-shifted by processes, such as stellar wind interactions or stellar radiation pressure (see e.g. Salz et al. 2016). Model G (red curve in right panel of Fig. 3) shows the absorption of those simulations assuming that the gas above the Roche lobe

Table 3. Planet parameters, the XUV flux, and EW(He(2^3S)) absorption.

Planet	HD 209458 b	HD 189733 b	GJ 3470 b
Mass ($M_{\rm Jup}$)	$0.685^{+0.015}_{-0.014}$	$1.162^{+0.058}_{-0.039}$	$0.036^{+0.002}_{-0.002}$
Radius ($R_{\rm Jup}$)	$1.359^{+0.016}_{-0.019}$	$1.23^{+0.03}_{-0.03}$	$0.36^{+0.01}_{-0.01}$
Gravity ($g_{\rm Jup}$)	0.371	0.768	0.278
Φ^a ($\Phi_{\rm Jup}$)	0.504	0.944	0.100
$R_{\rm lobe}$ ($R_{\rm P}$)^b	4.2	3.0	3.6
$F_{\rm XUV}{}^c$	2.358	56.74	3.928
EW (mÅ)^d	5.3±0.5	12.7±0.4	20.7±1.3

Notes. Planetary mass and radius of HD 209458 b from Torres et al. (2008). Those of HD 189733 b and GJ 3470 b are taken from Table 1 and included here for easier comparisons. $^{(a)}$ Gravitational potential. $^{(b)}$ Roche lobe of HD 209458 b, HD 189733 b, and GJ 3470 b by Salz et al. (2016), Eggleton (1983), and Bourrier et al. (2018), respectively. $^{(c)}$ XUV flux in units of 10^3 erg cm^{-2} s^{-1} at $\lambda < 912$ Å at planetary distance, calculated from Lampón et al. (2020) for HD 209458 b and from Fig. 2 for HD 189733 b and GJ 3470 b. $^{(d)}$ Equivalent width (EW) integrated in the range of 10831.0−10834.5 Å.

is escaping at an LOS velocity of -5.0 km s^{-1}. This scenario is consistent with that proposed by Bourrier et al. (2018) to explain the blue-shifted absorption signature of their Lyα observations.

The absorption of the weaker He(2^3S) line near 10832 Å is also significantly broadened, and it is well reproduced within the estimated error bars. We note though that, in contrast to HD 189733 b, the stronger lines are not saturated at any radii and hence the ratio of the strong to the weaker lines is larger in this planet. Thus, the He(2^3S) absorption of this planet is rather insensitive to its lower boundary atmospheric conditions.

4.2. Constraining the temperatures and mass-loss rates by the χ^2 analysis

The T-$\dot{M}$ curves dictated by the He(2^3S) absorption of both planets show the typical behaviour of a positive correlation (see Fig. 4). That is to say for a given He(2^3S) concentration (imposed by the measured absorption profile), if temperature increases, the He(2^3S) concentration decreases and its maximum tends to move to lower altitudes (with smaller effective absorption areas) which, in order to be balanced, requires an increase in $\dot{M}$.

Different H/He compositions of the thermospheric gas show different T–$\dot{M}$ curves, as was studied for HD 209458 b by Lampón et al. (2020). For a given mass-loss rate and temperature, the effect of increasing the H/He ratio results in a decrease in the global mass density, and the hydrogen and He(2^3S) concentrations, (see Fig. 13 of Lampón et al. 2020). Then, to compensate for the He(2^3S) absorption, the mass-loss rate has to be increased. In summary, for a fixed temperature, the higher the H/He ratio is, the higher the mass-loss rate required to reproduce the He(2^3S) absorption.

In comparing the results of HD 189733 b and GJ 3470 b (Fig. 4) with those of HD 209458 b (Fig. 8 of Lampón et al. 2020), we can appreciate that the T-$\dot{M}$ curves of HD 189733 b and GJ 3470 b are better constrained. In the case of HD 189733 b, the reduction of the degeneracy comes from the fitting of the He I$_{\lambda 10833}$/He I$_{\lambda 10832}$ ratio and from the temperature broadening, principally when including the turbulence.

The minima of χ^2_R for HD 189733 b are larger at temperatures below ∼10 000 K and above ∼12 500 K. For lower temperatures, despite the high density in the lower boundary of this planet, He(2^3S) density is too low for fitting the weaker line, similar to Model B in Fig. 3; while at high temperatures, it is well fitted (see Sect. 4.1.1). At temperatures above ∼12 500 K, the lines are too broadened, particularly when including the turbulence, and then the fitting is worse. It is interesting to look at the T/$\dot{M}$ constrain when neglecting the turbulence (see Fig. C.1). We see that the constrain changes significantly, leading in general to larger temperatures and mass-loss rates although the fit is not so good (larger minimum χ^2).

As the strong line of HD 209458 b and GJ 3470 b is not saturated at any altitude, the He I$_{\lambda 10833}$/He I$_{\lambda 10832}$ ratio does not contribute to reduce the model degeneracy for these exoplanets. For GJ 3470 b, as the broadening of the gas radial velocities is very large, the effects of the turbulence are negligible.

In the case of GJ 3470 b, the reduction of the degeneracy comes from the large radial velocities (see right panel of Fig. 7). As we can see in Fig. 4 (right panel), χ^2 is worse at temperatures below about 5400 K and higher than ∼6900 K. At lower temperatures, the velocities are smaller and the broadening of the absorption profile narrower. The opposite occurs for higher temperatures. Thus, radial velocities calculated by the hydrodynamic model help to constrain the T-$\dot{M}$ curves of GJ 3470 b. However, HD 209458 b and HD 189733 b do not have such high radial velocities, so they do not help to reduce the degeneracy in these exoplanets.

We note that as the T-$\dot{M}$ degeneracy of HD 209458 b is not reduced by fitting the He I$_{\lambda 10833}$/He I$_{\lambda 10832}$ ratio nor by the gas radial velocities, Lampón et al. (2020) reduced it by applying constraints on the heating efficiencies. This criterion, however, cannot be used to reduce the degeneracy in HD 189733 b as heating efficiencies in this exoplanet are rather uncertain because of the significant radiative cooling (see, e.g. Salz et al. 2015, 2016).

We have found that the mass-loss rates of GJ 3470 b are much larger than those of HD 189733 b (Fig. 4); they are more than a factor of 10 for similar temperatures and an H/He ratio of 90/10. For larger H/He ratios, this difference decreases. Using the T-$\dot{M}$ curve of HD 209458 b as a reference (Lampón et al. 2020, reproduced in Fig. 5), we observe that the corresponding curves for HD 189733 b and GJ 3470 b are located in opposite regions, below and above that of HD 209458 b. On the one hand, the mass-loss rate of HD 189733 b is more than one order of magnitude smaller than that of HD 209458 b, and it is located at higher temperatures. The larger XUV flux of HD 189733 b (see Table 3) favours its larger temperatures. However, its larger gravity prevents its evaporation, resulting in much lower mass-loss rates. On the other hand, GJ 3470 b is not only irradiated in the XUV at higher levels than HD 209458 b (although only slightly), but it also has a much smaller gravity (see Table 3). Both factors favour its larger mass-loss rate, although the second is by far the most important. Those factors lead to a very extended atmosphere for GJ 3470 b and a rather compressed one for HD 189733 b (see Fig. 6); while the He(2^3S) concentration drops by a factor of 10 in ∼7 $R_{\rm P}$ for GJ 3470 b, it takes only ∼0.5 $R_{\rm P}$ for HD 189733 b. Likewise, the velocities of atmospheric expansion of GJ 3470 b are significantly larger than those of HD 189733 b (see Fig. 7). It is important to note that for GJ 3470 b, the velocities are already significant at very small radii, which, together with the large He(2^3S) abundances at these distances, contribute to a significant broadening of the absorption profile (see Sect. 4.1.3).

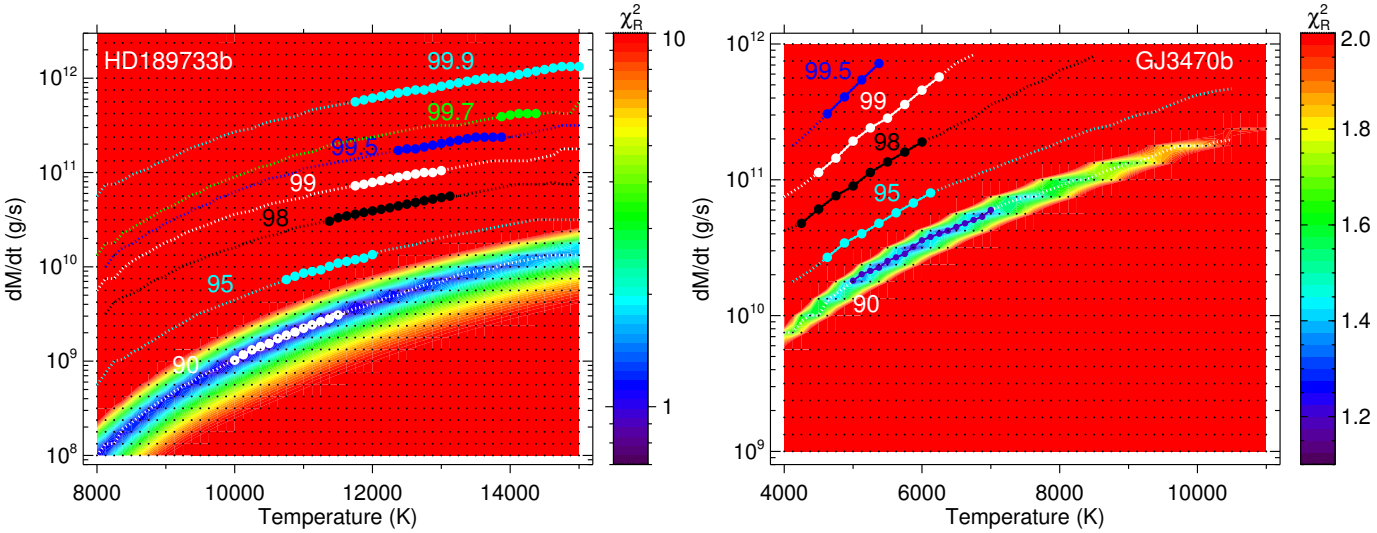

Fig. 4. Contour maps of the reduced χ^2 of the He(2^3S) absorption for HD 189733 b (left panel) and GJ 3470 b (right panel) for an H/He ratio of 90/10. We note the different scales of temperatures and $\dot{M}$. Dotted curves represent the best fits with filled circles denoting the constrained ranges for a confidence level of 95% (see Sect. 3.4). Over-plotted are also the curves and symbols for several H/He ratios, as labelled. The labels correspond to the hydrogen percentage, e.g. '90' for an H/He of 90/10 and '95' for H/He=95/5 (see Sect. 4.4). The black dots represent the grid of the simulations.

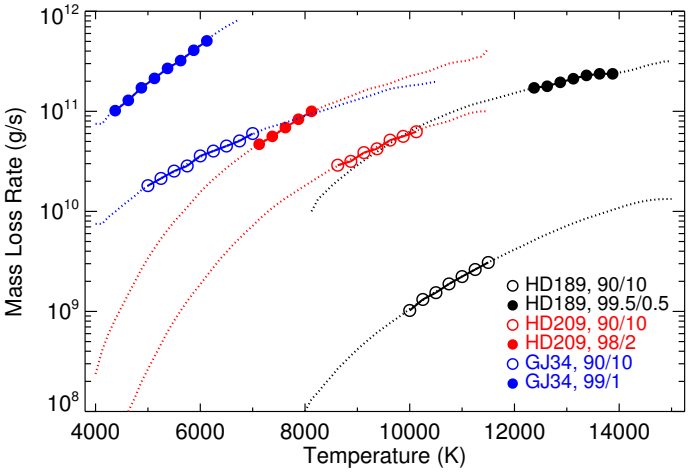

Fig. 5. Ranges of temperature and mass-loss rates for HD 209458 b, HD 189733 b, and GJ 3470 b for H/He ratios of 90/10 and 99.5/0.5, 90/10 and 98/2, as well as 90/10 and 99/1, respectively. Dotted lines show the ranges explored and symbols correspond to the constrained ranges (see Sect. 3.4). The values for HD 209458 b were taken from Lampón et al. (2020). The limited ranges (symbols) for this planet were obtained from heating efficiency considerations.

4.3. He(2^3S) density profiles and ionisation of the upper atmosphere

In this section we show the derived He(2^3S) densities, gas radial velocities, and the ionisation state of the upper atmospheres of HD 189733 b and GJ 3470 b. The He(2^3S) density profiles for our nominal case of H/He=90/10 are shown in Fig. 6 (the profiles for the derived H/He ratios are shown in Fig. B.1). The densities of HD 189733 b peak at its lower boundary. GJ 3470 b shows more extended He(2^3S) density profiles with lower values at lower altitudes and larger values at higher altitudes. The peaks of the density profiles for this planet are also well confined to the range of 1.3–1.5 R_P.

The results for the gas radial velocities are shown in Fig. 7 for the nominal H/He=90/10, and in Fig. B.2 for the derived H/He ratios. GJ 3470 b is already expanding at large velocities at rather low altitudes, which is supported by the rather wide observed absorption profile. Fig. 3 shows (right panel, Model E, orange) that if these radial velocities are not included, the He(2^3S) line profile would be significantly narrower.

The resulting ionisation fronts can be seen in the H^+ mole fractions plotted in Fig. 8 for the nominal and the derived H/He ratios. The ionisation front of HD 189733 b is closer to the planet's lower boundary and narrower than that of GJ 3470 b. That is, for HD 189733 b, the stellar flux is strongly absorbed in a narrow altitude interval near the lower boundary, while in the case of GJ 3470 b, it is absorbed progressively in a wide range of altitudes at relatively large distances. Nonetheless, the effective absorption radius, R_{XUV}, the distance where the optical depth for the XUV radiation is unity (Watson et al. 1981), is 1.02 R_P (i.e. the lower boundary) for HD 189733 b and is in the range (1.02–1.12) R_P for GJ 3470 b. As the planetary XUV cross section varies with R^2_{XUV}, the stellar radiation energy absorbed by GJ 3470 b increases due to the hydrodynamic atmospheric escape, while that of HD 189733 b remains constant.

4.4. Constraining the H/He composition by the χ^2 analysis

As in Lampón et al. (2020), we constrained the H/He ratio by matching the H^0 abundance profiles imposed by the He(2^3S) observations with those derived from Lyα absorption measurements. By constraining the H/He ratio, we also reduced the T-$\dot{M}$ degeneracy (see Fig. 4).

For HD 189733 b, we compared our H^0 abundance profiles to those retrieved by Salz et al. (2016) and Odert et al. (2020) from Lyα absorption measurements. These authors analysed the observations of Lecavelier des Etangs et al. (2012) using a 1D hydrodynamic model and assuming substellar conditions to be representative of the whole planet. While Salz et al. (2016) report a good fit of the Lyα absorption, Odert et al. slightly overestimate it. We performed Lyα absorption calculations and found, in effect, that the profile of Salz et al. (2016) fit the observations of Lecavelier des Etangs et al. (2012) better. In addition we obtained that the errors in these measurements are well embraced

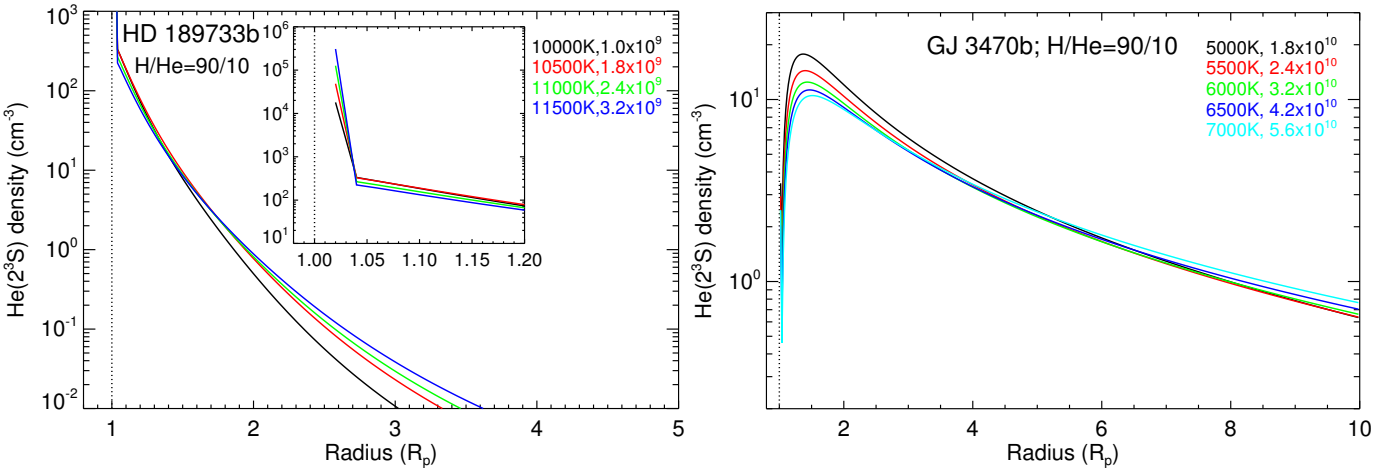

Fig. 6. He(2^3S) concentration profiles that best fit the measured absorption; i.e. for the white (HD 189733 b) and dark blue (GJ 3470 b) filled circles in Fig. 4. We note the different scale of the x-axis. The inset in the left panel shows a zoom at low radii.

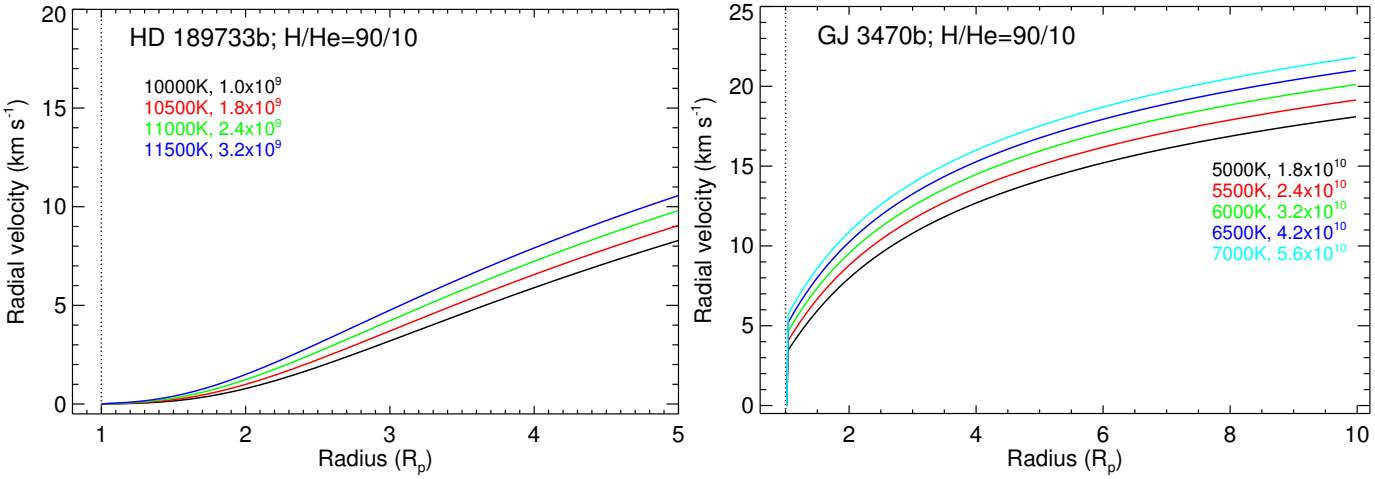

Fig. 7. Gas radial velocities of the model for the best fits of the He(2^3S) measured absorption; i.e. for the white (HD 189733 b) and dark blue (GJ 3470 b) filled circles in Fig. 4. We note the different scale of the x-axis.

by the H^0 profile of Salz et al. (2016) when scaled by factors of 0.1 and 10 (see upper panels in Fig. 9).

From the analysis of χ^2 (i.e. the profiles that fit the measured He(2^3S) within the minimum χ^2 values, see Sect. 3.4), we found that the H^0 model density profiles for H/He ratios of 90/10, 95/5, and even for 98/2 (see upper left panel of Fig. 9) are significantly lower than that of Salz et al. (2016), including their estimated uncertainties, at all altitudes. Also, for an H/He ratio of 99.9/0.1 and larger values, the H^0 Lyα density profile is clearly overestimated (upper right panel in Fig. 9). This analysis suggests that an H/He composition of ~ 99.5/0.5 is more probable (upper middle panel in Fig. 9). It is worth mentioning that using the XUV flux from the X-exoplanets model by Sanz-Forcada et al. (2011), which is about a factor of 3 smaller than that used here, we obtained a good agreement with an H/He of 98/2. That is to say, including the effects of several small flares in the stellar model (see Sect. 3.2), we obtained a more ionised atmosphere and then a higher H/He.

In the case of GJ 3470 b, Salz et al. (2016) calculated the H^0 density for this planet, but they could not verify it because of the lack of Lyα absorption measurements. More recently, however, Bourrier et al. (2018) measured the Lyα absorption and concluded that the Salz et al. model underestimates the H^0 density. As for HD 189733 b, we also performed Lyα absorption calculations and found that the profile of Salz et al. (2016) actually fit the observations of Bourrier et al. (2018) rather well. Further, we found that the errors in those observations are covered by the H^0 profile of Salz et al. (2016) when divided by $\sqrt{10}$ and multiplied by 10 (see lower panels in Fig. 9).

Our χ^2 analysis for GJ 3470 b shows that the H^0 density profiles obtained with H/He ratios of 90/10 and 95/5 are significantly lower than those of Salz et al. (2018) at all altitudes (bottom left panel in Fig. 9). They agree rather well, however, within the estimated uncertainties, for H/He ratios of 98/2 and 99/1 (bottom middle panel in Fig. 9). For H/He ratios larger than 99.5/0.5, most of the H^0 density profiles that fit the He(2^3S) absorption fall outside the estimated uncertainties of the H^0 Lyα profile and hence are rather unlikely (bottom right panel in Fig. 9).

4.5. MCMC analysis

In order to investigate the posterior probability distribution of model parameters for the described grid of models in Section 3.4, and to determine if the simultaneous MCMC fit constrains the parameters further by sampling the parameter-space effectively, we used a python implementation of `emcee` (Goodman & Weare 2010; Foreman-Mackey et al. 2013), called `MCKM`.

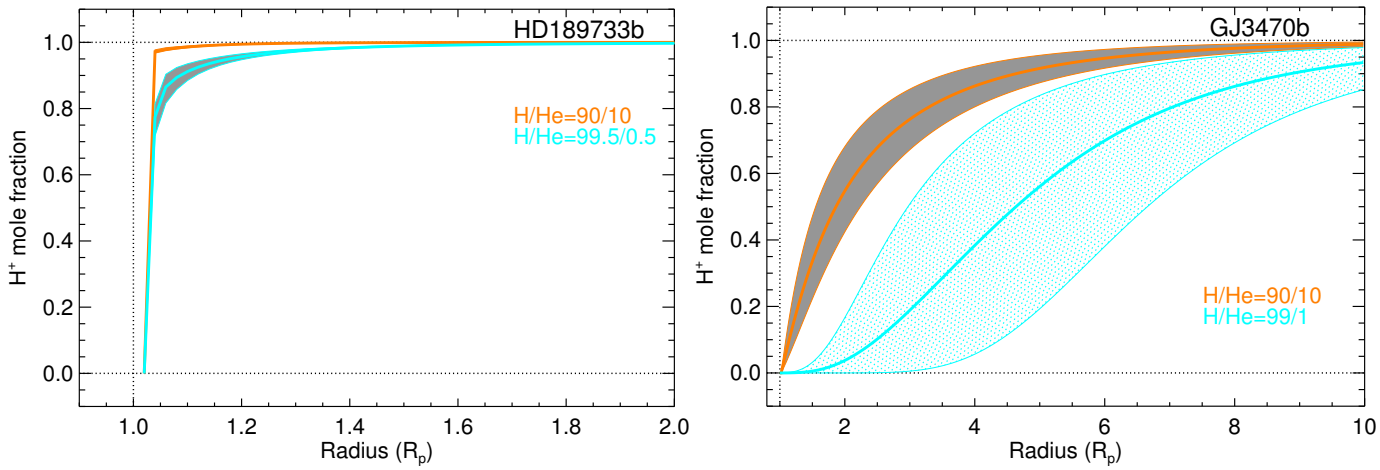

Fig. 8. H^+ mole fraction profiles resulting from the fit of the measured absorption (filled circles in Fig. 4) for H/He=90/10 and 99.5/0.5 for HD 189733 b (left panel) and 90/10 and 99/1 for GJ 3470 b (right panel). We note the different x-axis range. The solid thicker lines are the mean profiles.

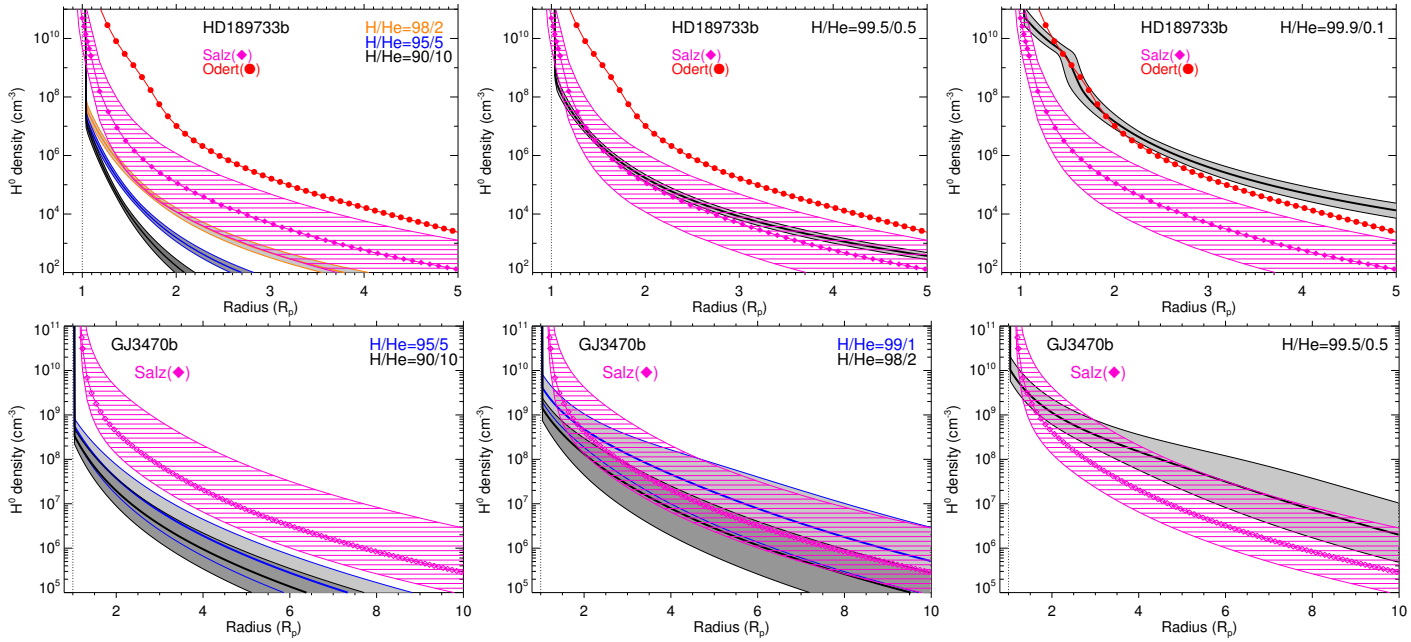

Fig. 9. Range of the neutral hydrogen concentration profiles (in grey shade areas) resulting from the fit of the measured absorption (filled circles in Fig. 4) for HD 189733 b (upper panels), GJ 3470 b (lower panels), and several H/He ratios, as labelled. The solid thicker curves are the mean profiles. The H^0 density derived from Lyα measurements for HD 189733 b and GJ 3470 b by Salz et al. (2016) and our estimated uncertainties ($\times$10 and /10 for HD 189733 b, as well as $\times$10 and / $\sqrt{10}$ for GJ 3470 b) are also shown (diamonds and hatched areas in magenta). The red profile is the H^0 density derived by Odert et al. (2020) from their SF11 model for HD 189733 b.

The `MCKM` handles any arbitrary number of model parameters over regular (Cartesian) or irregularly spaced parameters, as well as any arbitrary number of data points and their respective covariance matrices.

We simultaneously fitted the observed He spectra and the H^0 density derived from Lyα observations to constrain the temperatures, mass-loss rates, and H/He ratios of HD 189733 b and GJ 3470 b (see Fig. 10). We initialised 1000 walkers with uniform priors and with their range being the same as in the χ^2 method to avoid differences between the two methods from different priors. Overall, the best models are consistent with the observations and no systematic residual is noticeable, except for the H^0 density in the case of GJ 3470 b, where our models underestimate the density at low altitudes, R<2 R_P. This could be due to the fact that we fitted global H^0 density profiles (i.e. not at individual altitudes) and all of our modelled H^0 profiles are systematically smaller than the profile of Salz et al. (2016) at R<2 R_P. Further, because of the extended atmosphere of this planet, the atmospheric absorption at small radii is comparatively small and therefore has a weaker weight in the fitting of the whole atmosphere. Thus, both facts together could explain the underestimation.

Figure 11 shows the corner plot of the retrieved thermospheric parameters of HD 189733 b (red) and GJ 3470 b (blue). From this analysis, we find that the effective temperature, mass-loss rate, and H/He of HD 189733 b are T=12 400$^{+400}_{-300}$ K, $\dot{M} = (1.1\pm0.1) \times 10^{11}$ g s^{-1}, and H/He = (99.2/0.8)±0.1, respectively. The retrieved values for GJ 3470 b are T=6500$^{+800}_{-400}$ K, $\dot{M} = 1.74^{+0.21}_{-0.15} \times 10^{11}$ g s^{-1}, and H/He=(97.1/2.9)$^{+0.5}_{-1.6}$.

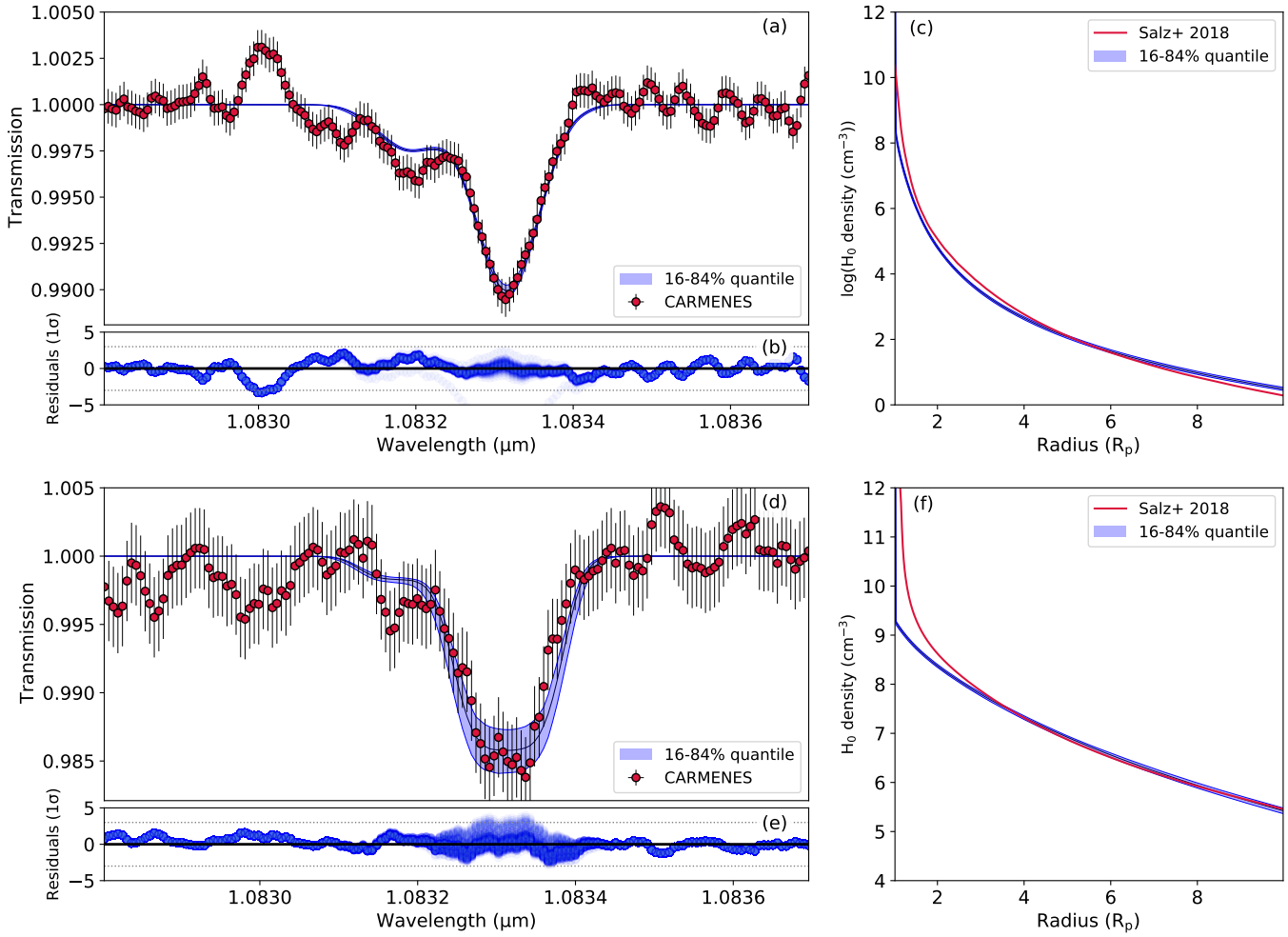

Fig. 10. Bayesian inference of upper thermospheric conditions for HD 189733 b and GJ 3470 b. (a) Comparison of the best-fit model spectra (blue shaded area) and of the measured He triplet line for HD 189733 b (red data points). (b) Residual of the fitted models for HD 189733 b. The dotted horizontal lines mark 3-σ. (c) Comparison of the best-fit model H^0 density (shaded blue area) and of the estimated H^0 density from Lyα measurements for HD 189733 b (red data points). For the models, the blue area corresponds to the region of the posteriors between the 16 and 84% quantiles. (d), (e), and (f) are similar to (a), (b), and (c), but for GJ 3470 b.

4.6. Retrieved temperatures, mass-loss rates, and H/He composition

The results obtained by both the χ^2 and the MCMC analysis are generally consistent. That is particularly clear in the case of HD 189733 b, for which the best fit of the H/He ratio derived from χ^2 is very close to 99.5/0.5 and from the MCMC method we obtained H/He = (99.2/0.8)±0.1. The small uncertainty derived from the MCMC analysis is remarkable. Generally, one would expect a larger uncertainty range from the MCMC analysis than from the χ^2 method, as the parameter space explored is wider. As explained above, a possible reason for the narrow MCMC posteriors might be that the MCMC fits the density profile at higher altitudes, but χ^2 is fit at lower altitudes, particularly in the case of GJ 3470 b. The total number of data points at higher altitudes are more than that of the lower altitudes and hence a narrower posterior from such fit is not unexpected. The χ^2 analysis suggests that they might be underestimated. Overall, as the most likely H/He ratio derived from both methods are very similar, we adopt the MCMC results of $T = 12\,400^{+400}_{-300}$ K, that is, with an uncertainty of about 400 K; a mass-loss rate of $\dot{M} = (1.1\pm0.1)\times10^{11}$ g s^{-1}, which is very well constrained (see the almost flat T/$\dot{M}$ curves for high H/He ratios in left panel of Fig. 4), and an H/He = (99.2/0.8)±0.1, with possibly slightly larger uncertainties.

For GJ 3470 b, we have seen above that the MCMC analysis systematically underestimates the H^0 density at low altitudes. This could be the reason of the significantly smaller derived H/He ratio by this method, H/He=$(97.1/2.9)^{+0.5}_{-1.6}$, than that suggested by the χ^2 analysis of 99/1 (in the range of 98/2–99.5/0.5; bottom panels in Fig. 9). The general trend is to obtain larger H^0 densities for larger H/He ratios. The H/He ratio has a rather important impact on the mass-loss rate of this planet, as well as on the temperature (see the rather steep T/$\dot{M}$ curves in the right panel of Fig. 4). Hence, the derived H/He has a significant impact on the resulting temperature and mass-loss rate ranges. Given the systematic underestimation of the H^0 density by MCMC, we are more inclined to adopt the H/He values and uncertainties derived from the χ^2 method, which also embraces the high probability peak value at H/He=97 of MCMC (see Fig. 11). Thus, we conclude with a $T = 5100\pm900$ K, an $\dot{M} = (1.9\pm1.1)\times10^{11}$ g s^{-1}, and an H/He=$(98.5/1.5)^{+1.0}_{-1.5}$ for GJ 3470 b.

It is interesting to note that of the three exoplanets undergoing hydrodynamic escape which have been analysed thus from their He(2^3S) and Lyα observations (HD 209458 b by Lampón et al. (2020), and HD 189733 b and GJ 3470 b in this work), all

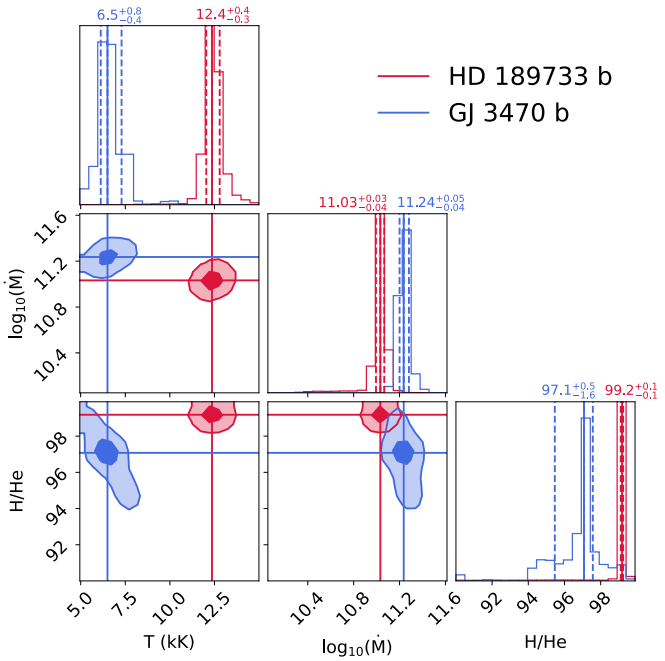

Fig. 11. Posterior probability distribution of our grid of models with respect to each of their parameter pairs as well as the marginalised distribution for each parameter for HD 189733 b (red) and GJ 3470 b (blue). The marginalised uncertainties are given as 16% to 84% quantiles. In the density maps, 1- and 2-σ are given as 1-e$^{-0.5}$~0.393 and 1-e$^{-2.0}$~0.865, respectively, as are common for multivariate MCMC results.

show higher H/He ratios than the widely assumed 90/10, despite having rather different bulk parameters. Hence, this work suggests that an enrichment of H over He seems to be common in the upper atmospheres of giant exoplanets undergoing hydrodynamic escape.

One possibility to explain our results is that the escape of these atmospheres originates above the homopause, where, due to diffusive separation, the atmosphere is enriched in H over the heavier He atoms (see, e.g. Fig. 14 in Moses et al. 2005). Our results, however, could also be consistent with an origin of the escape near the homopause, at least for GJ 3470 b, as Hu et al. (2015) have shown that such enrichment is possible in Neptune and sub-Neptune exoplanets if the H mass-loss rate is comparable to its diffusion-limited mass-loss rate. This escape of H-enriched gas can lead, in the case of Neptune and sub-Neptunes, to an He and metal enrichment in the lower atmosphere with further consequences on their composition (e.g. abundances of carbon and oxygen-bearing species) (Hu et al. 2015; Malsky & Rogers 2020). Furthermore, according to these authors, it may even change the mass-radius relationship of the planet. In addition, our results are consistent with the depletion of atmospheric He by other processes as well, for example, with the formation of an H–He immiscibility layer in the interior of giant planets, as it produces He sequestration from the upper atmosphere (Salpeter 1973; Stevenson 1975, 1980; Wilson & Militzer 2010). This result also suggests that the H/He ratio might play a more important role than expected in the detectability of He(2^3S). In addition to the spectral shape and intensity of the XUV stellar irradiation (see, e.g. Oklopčić 2019), high H/He ratios could help to explain the non-detection of the He(2^3S) in some highly irradiated exoplanets, such as GJ 1214 b and GJ 9827 d (as suggested by Kasper et al. 2020) as well as K2-100b (Gaidos et al. 2020).

5. Comparison of temperatures and mass-loss rates with previous works

5.1. HD 189733 b

Guilluy et al. (2020) observed the He(2^3S) absorption with the GIANO-B high-resolution spectrograph at the Telescopio Nazionale Galileo. They measured an He(2^3S) mid-transit absorption of 0.75±0.03%, slightly lower than the 0.88±0.04% by Salz et al. (2018); this was possibly due to the lower resolving power of GIANO-B with R ≈50 000 compared to CARMENES with R≈80 400, as argued by Guilluy et al. (2020). These authors analysed their measurements with a 1D hydrodynamic isothermal Parker wind model (Parker 1958) for the thermosphere, and with a 3D particle model (Bourrier & Lecavelier des Etangs 2013) above 1.2 R_P, the altitude where they estimated the gas becomes non-collisional. We applied a hydrodynamic model for the whole upper atmosphere because, as shown in our calculations, the altitude where the gas becomes non-collisional occurs far beyond the Roche lobe (in agreement with Salz et al. 2016; Odert et al. 2020). They estimated a T–$\dot{M}$ relationship that favoured a thermosphere with a T ≈12 000 K and an He(2^3S) density of 70 atoms cm^{-3} at 1.2 R_P assuming solar-like H/He composition. Despite the different modelling and assumptions between the two analyses, our derived He(2^3S) distribution for the case of H/He = 90/10 and T = 12 000 K (see Fig. 6) agrees well with their He(2^3S) density at 1.2 R_P. However, as we have shown in Sect. 4.6, our comparison with the Lyα measurements suggests an H/He composition of ~99.2/0.8, which leads to a higher mass-loss rate, $\dot{M}$ ≈10×10^{10} g s^{-1}(instead of $\dot{M}$ = 0.4×10^{10} g s^{-1} for H/He=90/10), for T = 12 000 K (see Fig. 4).

Salz et al. (2016) simulated the upper atmosphere of HD 189733 b assuming that it is composed by ~90/10 of H/He, and using an incident F_{XUV} ≈ 2.09×10^4 erg cm^{-2} s^{-1}. They used a comprehensive 1D hydrodynamic model and fitted the Lyα measurements of Lecavelier des Etangs et al. (2012). The resulting maximum temperature was 11 800 K and the mass-loss rate was $\dot{M}$ ≈1.7×10^{10} g s^{-1}. For the same H/He composition, mass-loss rate, and maximum temperature, we overestimated the measured He(2^3S) absorption. Our results, $\dot{M}$=(1.1±0.1) × 10^{11} g s^{-1}and T=12 400$^{+400}_{-300}$ K, show that our mass-loss rate range is larger by a factor of ~6.3 than that of Salz et al., while the maximum temperature is in good agreement. We note, however, that our stellar flux (see Table 3) is larger by a factor of 3 than that used by Salz et al., and our derived H/He composition is ≈ 99.2/0.8.

Odert et al. (2020) modelled the upper atmosphere of HD 189733 by also using a hydrodynamic approach for fitting the Lyα measurements of Lecavelier des Etangs et al. (2012). They assumed a thermosphere composed of H only and irradiated by F_{XUV} ≈ 1.8 ×10^4 erg cm^{-2} s^{-1}. They obtained a maximum temperature of 11 000 K and a mass-loss rate of 5.4×10^{10} g s^{-1}. We can see that our mass-loss rate range, $\dot{M}$=(1.1±0.1) × 10^{11} g s^{-1}, is larger by a factor of ~2; our derived H/He composition is ≈ 99.2/0.8, which is close to the H-only composition assumed by Odert et al.; and our temperature range, T=12 400$^{+400}_{-300}$ K, is slightly larger than that obtained by Odert et al. Therefore, considering that our F_{XUV} is larger by a factor of 3, our results are in good agreement with those of Odert et al.

Overall, we obtain similar mass-loss rates as Guilluy et al. (2020), when considering only the He(2^3S) absorption, but larger rates by a factor of ~ 25 when also considering the Lyα absorp-

tion. Salz et al. (2016) and Odert et al. (2020) derived mass-loss rates from Lyα measurements only. Our evaporation rates (constrained by both He(2^3S) and Lyα measurements) are larger (by a factor ~6.3) than those of Salz et al., who assumed an H/He composition of ~ 90/10; however, they are in good agreement (slightly larger by a factor of ~2) with those of Odert et al., who assumed an H-only atmosphere.

5.2. GJ 3470 b

Ninan et al. (2020) observed the He(2^3S) absorption with the Habitable Zone Planet Finder near-infrared spectrograph (HPF), on the 10 m Hobby–Eberly Telescope at the McDonald Observatory. They measured an equivalent width of the He(2^3S) mid-transit absorption of 0.012±0.002 Å, which is lower than that calculated here of 0.0207 Å from the observations of Pallé et al. (2020). We note that differences could come from the different resolution power, as HPF has R≈ 55 000, or from the different spectral integration interval (we include the absorption of the weak line, i.e. from 10831.0 to 10834.5 Å). They found that the model by Salz et al. (2016) overestimates their He(2^3S) measurements for this exoplanet, which agrees with our results.

Bourrier et al. (2018) modelled the upper atmosphere of GJ 3470 b with a parametrised thermosphere and a 3D particle model for non-collisional altitudes, assuming a thermospheric solar-like composition of H and He and a temperature of 7 000 K. They fitted their Lyα observations obtaining an H^0 mass-loss rate of $\approx 1.5\times10^{10}$ g s^{-1}. Our derived total (i.e. all neutral, ionised, and excited species) mass-loss rate is $\dot{M}=(1.9\pm1.1)\times10^{11}$ g s^{-1}, which agrees with the lower limit imposed by their H^0 mass-loss rate.

Salz et al. (2016) modelled the upper atmosphere of GJ 3470 b with a comprehensive hydrodynamic model. For an H/He composition of ~ 90/10 and a $F_{\rm XUV} \approx 7.8\times10^3$ erg cm^{-2} s^{-1}, they estimated a $\dot{M} \approx 1.9\times10^{11}$ g s^{-1} and a maximum thermospheric temperature of ≈8600 K. For the same H/He composition, mass-loss rate, and maximum temperature, we overestimated the He(2^3S) absorption, which agrees with Ninan et al. (2020). Our results, $\dot{M}=(1.9\pm1.1)\times10^{11}$ g s^{-1}, T=5100±900 K, and H/He=$(98.5/1.5)^{+1.0}_{-1.5}$, show that our mass-loss rates agree with those derived by Salz et al., although the temperature range is lower. We note, however, that our $F_{\rm XUV}$ is about a factor of 2 lower (see Table 3).

Overall, by using the same solar H/He ratio, mass-loss rate, and temperature as Salz et al. (2016), we overestimated the He(2^3S) measurements of CARMENES, which agrees with the analysis of Ninan et al. (2020) from their HPF measurements. Our mass-loss rates, constrained by He(2^3S) and Lyα observations, agree with those of Salz et al., but for a higher H/He composition $(98.5/1.5)^{+1.0}_{-1.5}$. Also, our results agree with the lower limit of the mass-loss rate derived by Bourrier et al. (2018) from their Lyα measurements.

6. Summary

In this work we have studied the hydrodynamic atmospheric escape of the hot Jupiter HD 189733 b and the warm Neptune GJ 3470 b by analysing the mid-transit He(2^3S) absorption measurements observed with CARMENES (Salz et al. 2018; Pallé et al. 2020). We used a 1D hydrodynamic model with spherical symmetry (assuming substellar conditions apply to the whole planetary surface) and a non-LTE model for computing the population of He(2^3S). As a further constraint, we also used the neutral hydrogen density derived from Lyα measurements in previous studies.

The analysis of HD 189733 b shows that the lower boundary conditions are very important in explaining the anomalously large absorption in the weaker He(2^3S) line, which is caused by the hot and rather compressed upper atmosphere of this planet. It is worth mentioning that the absorption ratio of the weaker to stronger He(2^3S) lines helps in constraining the mass-loss rate and lower boundary conditions of its atmosphere. Thus, spectrographs with sufficient resolution for discriminating the weak and strong lines provide further information about the evaporating planets.

The radial velocities of our hydrodynamic model for HD 189733 b are too low to explain the broad absorption profile of this planet. In order to fit it, we need to incorporate blue-shifted components at -3.5 km s^{-1} and -11.5 km s^{-1} covering nearly half and a quarter of the atmosphere's terminator, respectively, as well as a red component at 5.5 km s^{-1} with 28% of the terminator coverage. We also found that a thermospheric constant radial velocity of 40 km s^{-1}, as derived by Seidel et al. (2020), substantially overestimates the width of the He(2^3S) lines, suggesting that such a large velocity is unlikely.

In the case of GJ 3470 b, however, with a lower gravitational potential, our hydrodynamic model predicts gas radial velocities large enough to explain the width of the He(2^3S) absorption profile very well. This, in fact, helps in constraining its mass-loss rate and temperature. Furthermore, the measured absorption profile exhibits a net blue shift at -3.2 km s^{-1}, which we can be explained either by a net blue wind of the whole atmosphere at that velocity or by a combined atmosphere with a null blue shift below the Roche lobe and expanding at -5 km s^{-1} above.

These two planets have a similar He(2^3S) absorption, but rather different bulk parameters (see Table 3). In particular, the gravitational potential of HD 189733 b is near a factor of 10 larger and GJ 3470 b is irradiated in the XUV at about a factor of 14 smaller. In consequence, the characteristics of their upper atmospheres also differ significantly. Thus, while HD 189733 b has a rather compressed and warm atmosphere ($12\,400^{+400}_{-300}$ K) with small gas radial velocities, GJ 3470 b exhibits a very extended and cooler (5100±900 K) atmosphere with large radial velocities. Also, while the upper atmosphere of HD 189733 b is almost fully ionised beyond $\approx 1.1 R_{\rm P}$, GJ 3470 b exhibits a very wide ionisation front (from $\sim 1.25\,R_{\rm P}$ to far beyond its Roche lobe). Overall, the gravitational potential and the irradiation balance result in comparable mass-loss rates, $\dot{M}=(1.1\pm0.1)\times10^{11}$ g s^{-1} versus $\dot{M}=(1.9\pm1.1)\times10^{11}$ g s^{-1} for HD 189733 b and GJ 3470 b, respectively. The very different characteristics of these objects make them very suitable archetypes for benchmark studies on atmospheric loss.

We have further found that both planets have upper atmospheres with very low mean molecular masses (H/He=97/3–99.5/0.5). It is remarkable that the three exoplanets with evaporating atmospheres that have been studied so far by using both He(2^3S) and Lyα observations (HD 209458 b, HD 189733 b, and GJ 3470 b) all show higher H/He ratios than the commonly assumed 90/10, despite having very different bulk parameters. This H-enrichment of the upper atmospheres could be explained, on the one hand, by the escape originating above the homopause, where the atmosphere is expected to be depleted in He by diffusive separation. Another possibility, particularly in the case of the warm Neptune GJ 3470 b, is that the escape originates from deeper altitudes, around the homopause, according to the prediction of Hu et al. (2015) of an H-enriched upper atmosphere for Neptune and sub-Neptunes undergoing hydrodynamic escape.

They further predict that it could lead to an He-enrichment of the lower atmosphere, with important consequences on their atmospheric composition (abundances of carbon and oxygen-bearing species) and even on their mass-radius relationship. Our results also suggest that the H/He ratio might play a more important role than expected in the detectability of He(2^3S). The confirmation of this important result definitely calls for the study of other escaping atmospheres with concomitant He(2^3S) and Lyα measurements and for performing an independent analysis.

Here, we have analysed the He(2^3S) mid-transit absorption spectra of HD 189733 b and GJ 3470 b with a 1D spherical model. However, comprehensive multi-fluid magneto-hydrodynamic 3D models are needed to provide more detailed information about the spatial and velocity distribution of the gas, the origin of the non-radial winds, and the influence of other processes (e.g. stellar wind, radiation pressure, or magnetic field interactions). In particular, the analysis of the ingress and egress spectra of these planets would be very valuable.

Acknowledgements. We thank the referee for very useful comments. CARMENES is an instrument for the Centro Astronómico Hispano-Alemán (CAHA) at Calar Alto (Almería, Spain), operated jointly by the Junta de Andalucía and the Instituto de Astrofísica de Andalucía (CSIC). CARMENES was funded by the Max-Planck-Gesellschaft (MPG), the Consejo Superior de Investigaciones Científicas (CSIC), the Ministerio de Economía y Competitividad (MINECO) and the European Regional Development Fund (ERDF) through projects FICTS-2011-02, ICTS-2017-07-CAHA-4, and CAHA16-CE-3978, and the members of the CARMENES Consortium (Max-Planck-Institut für Astronomie, Instituto de Astrofísica de Andalucía, Landessternwarte Königstuhl, Institut de Ciències de l'Espai, Institut für Astrophysik Göttingen, Universidad Complutense de Madrid, Thüringer Landessternwarte Tautenburg, Instituto de Astrofísica de Canarias, Hamburger Sternwarte, Centro de Astrobiología and Centro Astronómico Hispano-Alemán), with additional contributions by the MINECO, the Deutsche Forschungsgemeinschaft through the Major Research Instrumentation Programme and Research Unit FOR2544 "Blue Planets around Red Stars", the Klaus Tschira Stiftung, the states of Baden-Württemberg and Niedersachsen, and by the Junta de Andalucía. We acknowledge financial support from the Agencia Estatal de Investigación of the Ministerio de Ciencia, Innovación y Universidades and the ERDF through projects ESP2016–76076–R, ESP2017–87143–R, PID2019-110689RB-I00/AEI/10.13039/501100011033, BES–2015–074542, PGC2018-099425–B–I00, PID2019-109522GB-C51/2/3/4, PGC2018-098153-B-C33, AYA2016-79425-C3-1/2/3-P, ESP2016-80435-C2-1-R, and the Centre of Excellence "Severo Ochoa" and "María de Maeztu" awards to the Instituto de Astrofísica de Canarias (SEV-2015-0548), Instituto de Astrofísica de Andalucía (SEV-2017-0709), and Centro de Astrobiología (MDM-2017-0737), and the Generalitat de Catalunya/CERCA programme. T.H. acknowledges support from the European Research Council under the Horizon 2020 Framework Program via the ERC Advanced Grant Origins 832428. A.S.L. acknowledges funding from the European Research Council under the European Union's Horizon 2020 research and innovation program under grant agreement No 694513.

References

Agol, E., Cowan, N. B., Knutson, H. A., et al. 2010, ApJ, 721, 1861
Allart, R., Bourrier, V., Lovis, C., et al. 2019, A&A, 623, A58
Allart, R., Bourrier, V., Lovis, C., et al. 2018, Science, 362, 1384
Alonso-Floriano, F. J., Snellen, I. A. G., Czesla, S., et al. 2019, A&A, 629, A110
Anders, E. & Grevesse, N. 1989, Geochim. Cosmochim. Acta, 53, 197
Asplund, M., Grevesse, N., Sauval, A. J., & Scott, P. 2009, ARA&A, 47, 481
Baluev, R. V., Sokov, E. N., Shaidulin, V. S., et al. 2015, MNRAS, 450, 3101
Baraffe, I., Chabrier, G., Barman, T. S., et al. 2005, A&A, 436, L47
Baraffe, I., Selsis, F., Chabrier, G., et al. 2004, A&A, 419, L13
Ben-Jaffel, L. & Ballester, G. E. 2013, A&A, 553, A52
Bonfils, X., Gillon, M., Udry, S., et al. 2012, A&A, 546, A27
Bouchy, F., Udry, S., Mayor, M., et al. 2005, A&A, 444, L15
Bourrier, V. & Lecavelier des Etangs, A. 2013, A&A, 557, A124
Bourrier, V., Lecavelier des Etangs, A., Ehrenreich, D., et al. 2018, A&A, 620, A147
Bourrier, V., Lecavelier des Etangs, A., Dupuy, H., et al. 2013, A&A, 551, A63
Boyajian, T., von Braun, K., Feiden, G. A., et al. 2015, MNRAS, 447, 846
Casasayas-Barris, N., Pallé, E., Yan, F., et al. 2018, A&A, 616, A151
Castelli, F. & Kurucz, R. 2004, IAU Symp. No 210,A20
de Kok, R. J., Brogi, M., Snellen, I. A. G., et al. 2013, A&A, 554, A82
Eggleton, P. P. 1983, ApJ, 268, 368
Ehrenreich, D., Lecavelier des Etangs, A., Hébrard, G., et al. 2008, A&A, 483, 933
Flowers, E., Brogi, M., Rauscher, E., Kempton, E. M.-R., & Chiavassa, A. 2019, ApJ, 157, 209
Foreman-Mackey, D., Hogg, D. W., Lang, D., & Goodman, J. 2013, PASP, 125, 306
Gaia Collaboration, Brown, A. G. A., Vallenari, A., et al. 2018, A&A, 616, A1
Gaidos, E., Hirano, T., Mann, A. W., et al. 2020, MNRAS, 495, 650
García-Muñoz, A. 2007, Planetary and Space Science, 55, 1426
Goodman, J. & Weare, J. 2010, Communications in Applied Mathematics and Computational Science, 5, 65
Guilluy, G., Andretta, V., Borsa, F., et al. 2020, A&A, 639, A49
Guo, J. H. 2011, ApJ, 733, 98
Hu, R., Seager, S., & Yung, Y. L. 2015, ApJ, 807, 8
Kasper, D., Bean, J. L., Oklopčić, A., et al. 2020, ApJ, 160, 258
Koskinen, T., Harris, M., Yelle, R., & Lavvas, P. 2013, Icarus, 226, 1678
Lampón, M., López-Puertas, M., Lara, L. M., et al. 2020, A&A, 636, A13
Lecavelier des Etangs, A., Bourrier, V., Wheatley, P. J., et al. 2012, A&A, 543, L4
Lecavelier des Etangs, A., Ehrenreich, D., Vidal-Madjar, A., et al. 2010, A&A, 514, A72
Lopez, E. D. & Fortney, J. J. 2013, ApJ, 776, 2
Malsky, I. & Rogers, L. A. 2020, ApJ, 896, 48
Mansfield, M., Bean, J. L., Oklopčić, A., et al. 2018, ApJ, 868, L34
Moses, J. I., Fouchet, T., Bezard, B., et al. 2005, Journal of Geophysical Research, 110, E08001
Muñoz, A. G. & Schneider, P. C. 2019, ApJ, 884, L43
Murray-Clay, R. A., Chiang, E. I., & Murray, N. 2009, ApJ, 693, 23
Ninan, J. P., Stefansson, G., Mahadevan, S., et al. 2020, ApJ, 894, 97
Nortmann, L., Palle, E., Salz, M., et al. 2018, Science, 362, 1388
Odert, P., Erkaev, N. V., Kislyakova, K. G., et al. 2020, A&A, 638, A49
Oklopčić, A. 2019, ApJ, 881, 133
Oklopčić, A. & Hirata, C. M. 2018, ApJ, 855, L11
Owen, J. E. & Wu, Y. 2013, ApJ, 775, 105
Owen, J. E. & Wu, Y. 2017, ApJ, 847, 29
Pallé, E., Nortmann, L., Casasayas-Barris, N., et al. 2020, A&A, 638, A61
Parker, E. N. 1958, ApJ, 128, 664
Poppenhaeger, K., Schmitt, J. H. M. M., & Wolk, S. J. 2013, ApJ, 773, 62
Press, W. H., Teukolsky, S. A., Vetterling, W. T., & Flannery, B. P. 2007, Numerical Recipes 3rd Edition: The Art of Scientific Computing, 3rd edn. (USA: Cambridge University Press)
Quirrenbach, A., Amado, P. J., Caballero, J. A., et al. 2016, in SPIE Proceedings, ed. C. J. Evans, L. Simard, & H. Takami (SPIE), 12–1–14
Quirrenbach, A., Amado, P. J., Ribas, I., et al. 2018, in SPIE Proceedings, ed. H. Takami, C. J. Evans, & L. Simard (SPIE), 32–19
Salpeter, E. E. 1973, ApJ, 181, L83
Salz, M., Czesla, S., Schneider, P. C., et al. 2018, A&A, 620, A97
Salz, M., Czesla, S., Schneider, P. C., & Schmitt, J. H. M. M. 2016, A&A, 586, A75
Salz, M., Schneider, P. C., Czesla, S., & Schmitt, J. H. M. M. 2015, A&A, 585, L2
Sanz-Forcada, J., Maggio, A., & Micela, G. 2003, A&A, 408, 1087
Sanz-Forcada, J., Micela, G., Ribas, I., et al. 2011, A&A, 532, A6
Sanz-Forcada, J., Micela, G., Ribas, I., et al. 2011, A&A, 532, A6
Seidel, J. V., Ehrenreich, D., Pino, L., et al. 2020, A&A, 633, A86
Spake, J. J., Sing, D. K., Evans, T. M., et al. 2018, Nature, 557, 68
Stevenson, D. J. 1975, Phys. Rev. B, 12, 3999
Stevenson, D. J. 1980, Science, 208, 746
Stone, J. M. & Proga, D. 2009, ApJ, 694, 205
Tian, F., Toon, O. B., Pavlov, A. A., & De Sterck, H. 2005, ApJ, 621, 1049
Torres, G., Winn, J. N., & Holman, M. J. 2008, ApJ(2008), 677
Tripathi, A., Kratter, K. M., Murray-Clay, R. A., & Krumholz, M. R. 2015, ApJ, 808, 173
Vidal-Madjar, A., des Etangs, A. L., Désert, J.-M., et al. 2003, Nature, 422, 143
Vidal-Madjar, A., Désert, J.-M., des Etangs, A. L., et al. 2004, ApJ, 604, 69
Watson, A. J., Donahue, T. M., & Walker, J. C. 1981, Icarus, 48, 150
Wilson, H. F. & Militzer, B. 2010, Phys. Rev. Lett., 104, 121101
Wyttenbach, A., Mollière, P., Ehrenreich, D., et al. 2020, A&A, 638, A87
Yan, F. & Henning, T. 2018, Nature Astronomy, 2, 714
Yelle, R. V. 2004, Icarus, 170, 167

Appendix A: Data for calculating the stellar flux of HD 189733.

Data used in the modelling of the stellar flux of HD 189733 in Sect. 3.2. The spectrum was downloaded from the Hubble Spectral Legacy Archive (HSLA); a sum of 42 HD 189733 spectra were acquired with the COS/G130M grating. The exposures were taken in 2009, 2013, and 2017 (proposals IDs 11673, 12984, and 14767).

Table A.1. *HST*/COS line fluxes of HD 189733[a].

Ion	λ_{model}	log T_{max}	F_{obs}	S/N	Ratio	Blends
Ne v	1145.5959	5.5	7.09e-17	4.5	-0.02	
Si iii	1206.5019	4.9	1.10e-14	39.9	-0.75	
O v	1218.3440	5.5	2.19e-15	39.8	0.21	
N v	1238.8218	5.4	3.32e-15	25.9	0.05	
N v	1242.8042	5.4	1.58e-15	17.6	0.03	
S ii	1253.8130	4.6	1.56e-16	9.6	0.03	
S ii	1259.5210	4.6	2.70e-16	11.7	0.04	
Si ii	1260.4240	4.6	5.00e-16	15.2	-0.78	
Si ii	1264.7400	4.5	1.95e-15	18.5	0.12	Si ii1265.0040
Si iii	1296.7280	4.9	1.13e-16	6.6	0.07	
Si iii	1298.9480	4.9	4.36e-16	7.4	0.37	Si iii1298.8940
Si iii	1303.3250	4.9	1.36e-16	7.9	0.06	
Si ii	1309.2770	4.6	6.49e-16	11.0	0.02	
C ii	1323.9080	4.8	9.90e-17	5.9	-0.40	C ii1323.9540
C ii	1334.5350	4.7	8.96e-15	33.6	-0.31	
C ii	1335.7100	4.7	1.72e-14	42.8	0.16	C ii1335.6650
Fe iii	1364.2950	4.6	1.53e-16	9.8	0.01	
O v	1371.2960	5.5	2.96e-16	11.2	-0.02	
Si iv	1393.7552	5.0	6.91e-15	25.8	-0.02	
O iv	1401.1570	5.3	4.52e-16	10.8	-0.75	
Si iv	1402.7704	5.0	3.55e-15	20.1	-0.01	
S iv	1406.0160	5.1	6.40e-17	5.8	-0.48	

[a] Line fluxes (in erg cm^{-2} s^{-1}) measured in *HST*/COS HD 189733 spectra. log T_{max} (K) indicates the maximum temperature of formation of the line (unweighted by the EMD). 'Ratio' is the log(F_{obs}/F_{pred}) of the line. Blends amounting to more than 5% of the total flux for each line are indicated.

Table A.2. Emission measure distribution of HD 189733.

log T (K)	EM (cm^{-3})[a]	log T (K)	EM (cm^{-3})
4.0	51.40:	5.0	$50.00^{+0.10}_{-0.40}$
4.1	51.25:	5.1	$49.90^{+0.10}_{-0.40}$
4.2	51.10:	5.2	$49.70^{+0.10}_{-0.40}$
4.3	$50.90^{+0.20}_{-0.20}$	5.3	$49.40^{+0.20}_{-0.10}$
4.4	$50.80^{+0.20}_{-0.20}$	5.4	$49.05^{+0.05}_{-0.05}$
4.5	$50.55^{+0.05}_{-0.15}$	5.5	$48.85^{+0.10}_{-0.10}$
4.6	$50.30^{+0.20}_{-0.20}$	5.6	$48.70^{+0.10}_{-0.10}$
4.7	$50.20^{+0.20}_{-0.30}$	5.7	48.70:
4.8	$50.15^{+0.15}_{-0.05}$	5.8	48.80:
4.9	$50.10^{+0.10}_{-0.20}$	5.9	48.90:

Notes. [a] Emission measure (EM=log $\int N_e N_H dV$), where N_e and N_H are electron and hydrogen densities, in cm^{-3}. Errors provided are not independent between the different temperatures, as explained in Sanz-Forcada et al. (2003).

Table A.3. Transition region abundances of HD 189733 (solar units[a]).

X	FIP (eV)	Solar photosphere Ref.[a]	(AG89)	HD 189733 [X/H]
Si	8.15	7.51	(7.56)	-0.57±0.15
Fe[b]	7.87	7.50	(7.67)	-0.34
S	10.36	7.12	(7.21)	-1.22±0.24
C	11.26	8.43	(8.56)	-0.87±0.29
O	13.61	8.69	(8.93)	-0.86±0.31
N	14.53	7.83	(8.05)	-0.58±0.07
Ne	21.56	7.93	(8.09)	-0.95±0.23

Notes. [a] Solar photospheric abundances from Asplund et al. (2009), adopted in this table, are expressed on a logarithmic scale. Several values have been updated in the literature since Anders & Grevesse (1989, AG89) and they have also been listed for easier comparison. [b] Fe abundance fixed to the coronal value (resulting from the fit of *XMM-Newton* EPIC data).

Appendix B: Results for different H/He compositions

Results for the T-$\dot{M}$ maps, He(2^3S) densities, and gas radial velocities for H/He compositions of 95/5, 98/2, and 99/1.

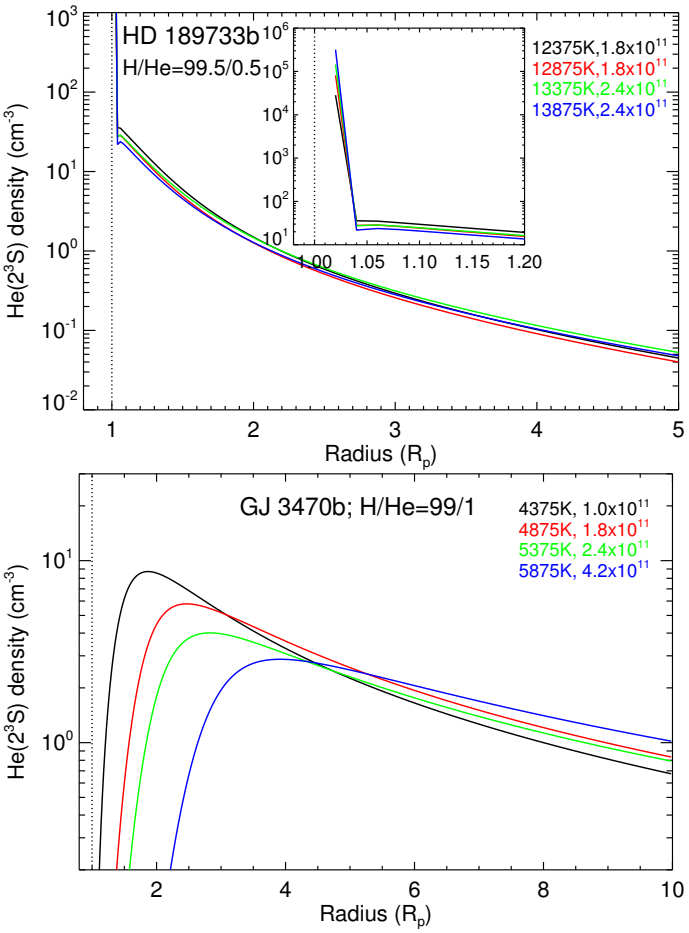

Fig. B.1. He(2^3S) concentration profiles that best fit the measured absorption (i.e. the filled circles in Fig. 4) for HD 189733 b and an H/He ratio of 99.5/0.5 (upper panel), as well as for GJ 3470 b and H/He=99/1 (lower panel).

Appendix C: Results for neglecting the broadening turbulence

Results for the T-$\dot{M}$ map for HD 189733 b when the turbulence broadening is not considered.

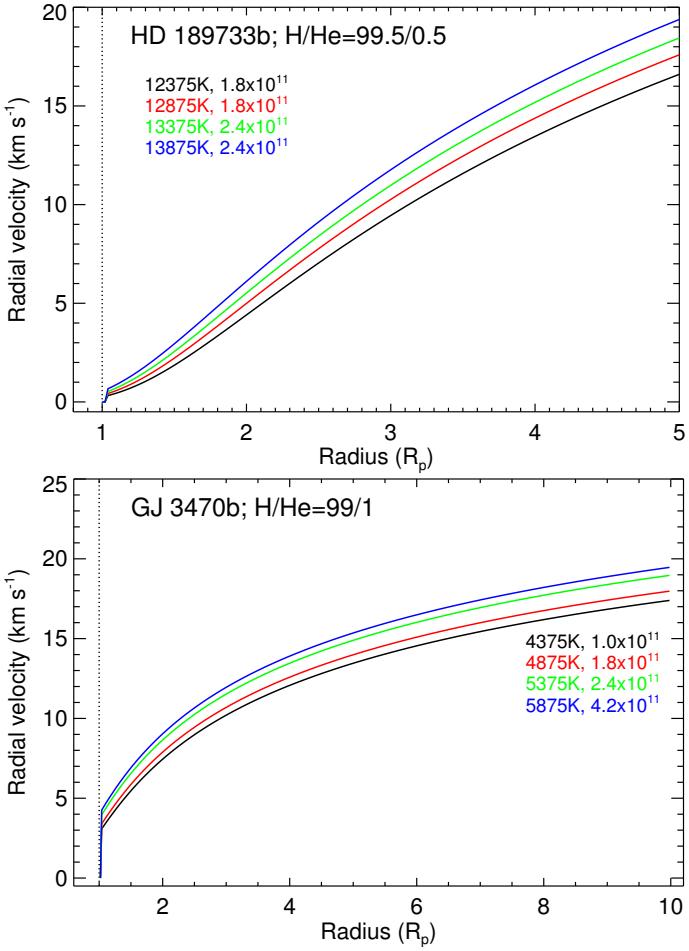

Fig. B.2. Gas radial velocities of the hydrodynamic model for the best fit of the measured absorption (i.e. the filled circles in Fig. 4) for HD 189733 b and an H/He ratio of 99.5/0.5 (upper panel), as well as for GJ 3470 b and H/He=99/1 (lower panel).

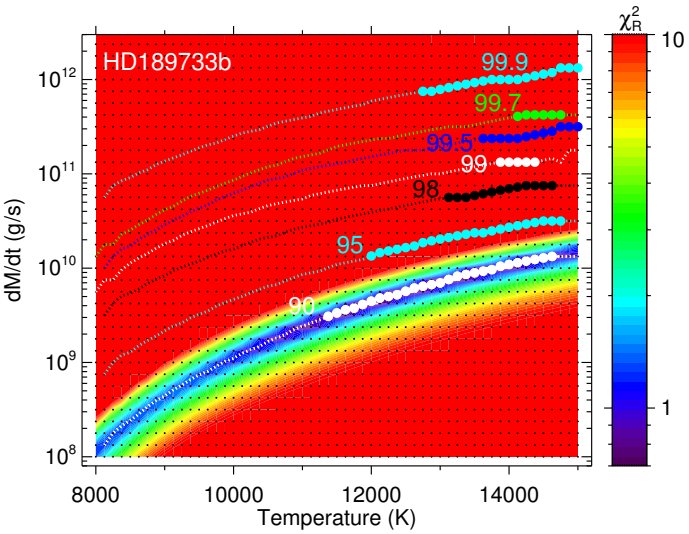

Fig. C.1. Contour maps of the reduced χ^2 of the model of the helium triplet absorption for HD 189733 b for several H/He ratios (as in Fig. 4, left panel) when the turbulence broadening is not considered. The filled circles highlight the best fits (constrained ranges). The black dots represent the grid of the models.

5 Observational evidence of hydrodynamic escape regimes

The work described in this chapter has been submitted to the journal Astronomy and Astrophysics with the title “Observational evidences of the hydrodynamic escape regimes in planetary H/He atmospheres” (Lampón et al., 2021a).

Astronomy & Astrophysics manuscript no. output
January 26, 2021
©ESO 2021

Letter to the Editor

Observational evidence of hydrodynamic escape regimes in planetary H/He atmospheres

M. Lampón[1], M. López-Puertas[1], S. Czesla[2], A. Sánchez-López[3], L. M. Lara[1], M. Salz[2], J. Sanz-Forcada[4], K. Molaverdikhani[5,6], A. Quirrenbach[6], E. Pallé[7,8], J. A. Caballero[4], Th. Henning[5], L. Nortmann[9], P. J. Amado[1], A. Reiners[9], and I. Ribas[10,11]

[1] Instituto de Astrofísica de Andalucía (IAA-CSIC), Glorieta de la Astronomía s/n, 18008 Granada, Spain
e-mail: mlampon@iaa.es
[2] Hamburger Sternwarte, Universität Hamburg, Gojenbergsweg 112, 21029 Hamburg, Germany
[3] Leiden Observatory, Leiden University, Postbus 9513, 2300 RA, Leiden, The Netherlands
[4] Centro de Astrobiología (CSIC-INTA), ESAC, Camino bajo del castillo s/n, 28692 Villanueva de la Cañada, Madrid, Spain
[5] Max-Planck-Institut für Astronomie, Königstuhl 17, 69117 Heidelberg, Germany
[6] Landessternwarte, Zentrum für Astronomie der Universität Heidelberg, Königstuhl 12, 69117 Heidelberg, Germany
[7] Instituto de Astrofísica de Canarias (IAC), Calle Vía Láctea s/n, 38200 La Laguna, Tenerife, Spain
[8] Departamento de Astrofísica, Universidad de La Laguna, 38026 La Laguna, Tenerife, Spain
[9] Institut für Astrophysik, Georg-August-Universität, Friedrich-Hund-Platz 1, 37077 Göttingen, Germany
[10] Institut de Ciències de l'Espai (CSIC-IEEC), Campus UAB, c/ de Can Magrans s/n, 08193 Bellaterra, Barcelona, Spain
[11] Institut d'Estudis Espacials de Catalunya (IEEC), 08034 Barcelona, Spain

Received 26 January 2021 / Accepted dd Month 2021

ABSTRACT

Hydrodynamic escape is the most efficient atmospheric mechanism of planetary mass-loss and has a large impact on planetary evolution. Three hydrodynamic escape regimes have been identified theoretically: energy-limited, recombination-limited, and photon-limited. However, no observational evidence of these regimes has been reported to date. Here, we report observational evidence of these three regimes from the helium I triplet at 10830 Å and Lyα absorption. In particular, we demonstrate that HD 209458 b is in the energy-limited regime, HD 189733 b is in the recombination-limited regime and GJ 3470 b is in the photon-limited regime. These exoplanets can be considered as benchmark cases for their respective regimes.

Key words. planets and satellites: atmospheres – planets and satellites: gaseous planets – planets and satellites: individual: HD 209458 b – planets and satellites: individual: HD 189733 b – planets and satellites: individual: GJ 3470 b

1. Introduction

Understanding the diversity, evolution, and formation of planets requires a profound knowledge of their atmospheric escape. This statement especially applies to planets that, at some stage in their history, experience the most effective atmospheric process of mass-loss, the hydrodynamic atmospheric escape. A planetary atmosphere is in hydrodynamic escape when the absorbed stellar high-energy flux is strong enough to produce substantial heating of the atmosphere that triggers a massive gas outflow, expelling material beyond the Roche lobe of the planet. This process can lead from a loss of a fraction of the original atmosphere to its complete removal (see e.g., Baraffe et al. 2004; Baraffe et al. 2005; Muñoz & Schneider 2019), and hence can shape the current planetary population (e.g., forming the sub-Jovian desert and the evaporation valley, Owen & Wu 2013; Lopez & Fortney 2013). Hydrodynamic escape can also significantly change the composition of the primordial atmospheres and thus affects the planetary mass-radius relationship (see e.g. Hu et al. 2015; Malsky & Rogers 2020).

Several models have been developed for studying planetary atmospheres undergoing hydrodynamic escape (e.g. Watson et al. 1981; Lammer et al. 2003; Yelle 2004; Tian et al. 2005; García-Muñoz 2007; Murray-Clay et al. 2009; Owen & Alvarez 2016; Salz et al. 2016a; Bourrier & Lecavelier des Etangs 2013; Shaikhislamov et al. 2020). In particular, Murray-Clay et al. (2009) studied the atmospheric mass-loss as a function of the incident ultra-violet (UV) flux for a typical hot Jupiter. They found that under high irradiation, the mass-loss rate was not limited by the radiative energy deposited in the atmosphere, but by the radiation-recombination equilibrium of the escaping gas. When the mass-loss rate is limited by the energy deposition, it scales linearly with the incident UV flux, which is efficiently converted into the work that lifts the gas. When the mass-loss rate is limited by the radiation-recombination equilibrium, it approximately scales to the square root of the incident UV flux since a large fraction of the absorbed energy is lost by radiative cooling. Owen & Alvarez (2016) found that the mass-loss rate of moderately irradiated low gravity planets can be limited by the number of incoming ionising photons, instead of the absorbed energy or the radiation-recombination equilibrium. In this limit, the mass-loss rate scales to the square of the effective absorption radius of the planet. Therefore, it is theoretically possible to identify three distinct hydrodynamic atmospheric escape regimes in hydrogen-dominated atmospheres: energy-limited, recombination-limited[1], and photon-limited.

[1] Also known as radiation/recombination limited.

The classification of the hydrodynamic atmospheric escape regimes is important when using the energy-limited approximation for estimating the planetary mass-loss rate (see, e.g., Murray-Clay et al. 2009; Bear & Soker 2011; Owen & Alvarez 2016; Salz et al. 2016b; Wang & Dai 2018). This approach, used together with an average heating efficiency[2] in the range of 10–20% (the most probable range in hydrogen-dominated atmospheres, Shematovich et al. 2014), largely overestimates the mass-loss rate of planets that are in the recombination-limited regime. It might also lead to significantly inaccurate results if applied to atmospheres in the photon-limited regime, as the effective absorption radius could differ considerably from the planetary radius. Hence, the applicability of this approach largely depends on the hydrodynamic escape regime.

Despite the central role of the hydrodynamic escape regimes, the lack of suitable observations has prevented their confirmation. As Solar System planets do not currently undergo hydrodynamic escape, observers have to revert to extrasolar planets. While Lyα absorption measurements are promising tracers of this process, they can only be carried out from space and are adversely affected by interstellar absorption and geocoronal emission. This is not the case for the recent observations of the He I 2^3S–2^3P triplet transitions[3], hereafter He(2^3S) transitions, that provide new opportunities to explore the hydrodynamic atmospheric escape, because these lines can be observed with ground–based telescopes and they are not affected by interstellar absorption (e.g. Spake et al. 2018; Nortmann et al. 2018; Allart et al. 2018).

By analysing high-resolution He(2^3S) absorption spectra, Lampón et al. (2020, 2021) constrained several parameters of the upper atmospheres of the hot Jupiters HD 209458 b and HD 189733 b, and of the warm Neptune GJ 3470 b. The three planets undergo hydrodynamic escape, as shown by derivation of supersonic outflow velocities (see e.g. Vidal-Madjar et al. 2004; Ben-Jaffel & Ballester 2013; Lampón et al. 2021). These planets have different bulk parameters and stellar irradiation levels and Lampón et al. (2020, 2021) found different upper atmospheric characteristics, such as temperatures, mass-loss rates, and ionisation profiles.

In this work we report observational evidence for the three regimes of the hydrodynamic atmospheric escape theoretically predicted, indicating that HD 209458 b is in the energy-limited, HD 189733 b is in the recombination-limited and GJ 3470 b is in the photon-limited regime. To this end, we analyse the neutral and ionised H distributions in the upper atmosphere of these exoplanets, derived from their observed He(2^3S) and Lyα absorption spectra, and deduce their heating efficiencies.

2. Criteria to differentiate the hydrodynamic atmospheric escape regimes

Physically, the three regimes can be distinguished by the production and losses of neutral H (see Murray-Clay et al. 2009; Bear & Soker 2011; Owen & Alvarez 2016) and also by the conversion of the absorbed stellar radiative energy into the work that drives the escape (see Murray-Clay et al. 2009; Salz et al. 2016b).

[2] Defined in Sect. 2.2

[3] At wavelengths 10832.06, 10833.22 and 10833.31 Å in vacuum; often referred to as their air wavelengths of 10830 Å.

2.1. Ratio of recombination to advection rates

The steady-state continuity equation of neutral H species, H^0, can be expressed by (see Appendix A)

$$-v_{\rm r}\frac{\partial f_{H^0}}{\partial r} + f_{H^+}\, n_{H^+}\, \alpha_H - f_{H^0}\, J_H = 0, \quad (1)$$

where r is the distance from the centre of the planet; $v_{\rm r}$ is the bulk radial velocity of the gas; $f_{\rm H^0}$ and $f_{\rm H^+}$ are the mole fractions of H^0, and the ionised H, H^+, respectively; n_{H^+} is the H^+ number density; $\alpha_{\rm H}$ and $J_{\rm H}$ are the H recombination and photo-ionisation rates. In addition, we define the recombination production rate, $P_{\rm rec} = f_{\rm H^+}\, n_{\rm H^+}\, \alpha_{\rm H}$, and the advection rate $P_{\rm adv} = -v_{\rm r}\, \partial f_{\rm H^0}/\partial\, r$.

Similarly, like Owen & Alvarez (2016), we consider the ionisation front (IF) as the region where the atmosphere is partially ionised. That is, from the altitude where $f_{\rm H^0}$ is close to one ($f_{\rm H^0} \geq 0.95$, where the optical depth of the X-ray and extreme UV (XUV) radiation, $\tau_{\rm XUV}$, is ≥ 1), up to the altitude where the atmosphere is almost fully ionised ($f_{\rm H^0} \leq 0.05$ and $\tau_{\rm XUV} \ll 1$). In this region, the photo-ionisation rate is greater than the recombination rate, and advection is not negligible.

Following Murray-Clay et al. (2009) and Owen & Alvarez (2016), the different hydrodynamic atmospheric escape regimes are characterised as follows: (1) In the recombination-limited regime, the IF region is very narrow compared with the scale of the flow. The gas is almost in radiation-recombination equilibrium (i.e., advection is negligible, $P_{\rm rec}/P_{\rm adv} \gg 1$) in practically all the upper atmosphere. (2) In the photon-limited regime, the photo-ionisation rate is much faster than the recombination rate so that the recombination process is negligible in the whole upper atmosphere and then $P_{\rm rec}/P_{\rm adv} \ll 1$. Consequently, the IF region occupies the whole upper atmosphere of the planet. (3) The energy-limited regime is an intermediate case between the recombination- and the photon-limited regimes. The IF is wide, although it does not encompass the entire flow as in the photon-limited regime. The advection and the recombination rates are not negligible in the whole upper atmosphere.

2.2. Heating efficiency criterion

The heating efficiency, η, is usually defined as the fraction of the absorbed stellar radiative energy, $W_{\rm hv}$, which is converted into kinetic energy of the gas, namely,

$$\eta = \frac{W_{\rm hv} - W_{\rm e} - W_{\rm cool}}{W_{\rm hv}}, \quad (2)$$

where $W_{\rm e}$ is the rate of energy lost by photo-ionisation and photo-electron impact processes (as excitation and ionisation of atoms by collisions with photo-electrons, see e.g., Shematovich et al. 2014); and $W_{\rm cool}$ is the radiative cooling rate, mostly produced by Lyα and free-free emission (Salz et al. 2016b). Thus, $W_{\rm hv} - W_{\rm e} - W_{\rm cool}$ represents the energy from the absorbed stellar radiation that is converted into kinetic energy of the gas species (atoms, ions and electrons), the so-called thermal heating.

In the energy- and photon-limited regimes radiative cooling is moderate or negligible, while in the recombination-limited regime it is a considerable fraction of the absorbed energy. If radiative cooling is neglected, the heating efficiency of stellar XUV radiation is about 0.1–0.2 in hydrogen-dominated planetary upper atmospheres (see e.g. Shematovich et al. 2014; Salz et al. 2016b). Consequently, the heating efficiency of the energy-limited and the photon-limited regimes is expected to be in

the range of 0.1–0.2. In contrast, the heating efficiency of the recombination-limited regime is expected to be much smaller than 0.1 (see, e.g., Salz et al. 2016b).

3. Modelling the hydrodynamic escape of HD 209458 b, HD 189733 b and GJ 3470 b

The H^0 and H^+ concentrations and heating efficiencies analysed here are based on the results obtained by Lampón et al. (2020, 2021) from the analysis of the observations of the He(2^3S) absorption taken with the high–resolution spectrograph CARMENES[4] (Quirrenbach et al. 2016, 2018) and reported by Alonso-Floriano et al. (2019), Salz et al. (2018) and Pallé et al. (2020) for HD 209458 b, HD 189733 b and GJ 3470 b, respectively. Lampón et al. (2020, 2021) used a 1D hydrodynamic model with a non-LTE treatment for the He(2^3S) state in the substellar direction[5], and derived well-constrained relationships between the mass-loss rate, $\dot{M}$, and the temperature, T, in the upper atmosphere of these exoplanets. Additionally, by comparing the H^0 density distribution with those derived from Lyα measurements, they constrained the H/He mole-fraction ratio and found values of H/He=(99.2/0.8)±0.1 for HD 189733 b, H/He ~ 98/2 for HD 209458 b, and H/He=$(98.5/1.5)^{+1.0}_{-1.5}$ for GJ 3470 b. Here we use the T-$\dot{M}$ ranges for the representative H/He ratios of 99/1 for HD 189733 b, and 98/2 for HD 209458 b and GJ 3470 b (see Fig. 1).

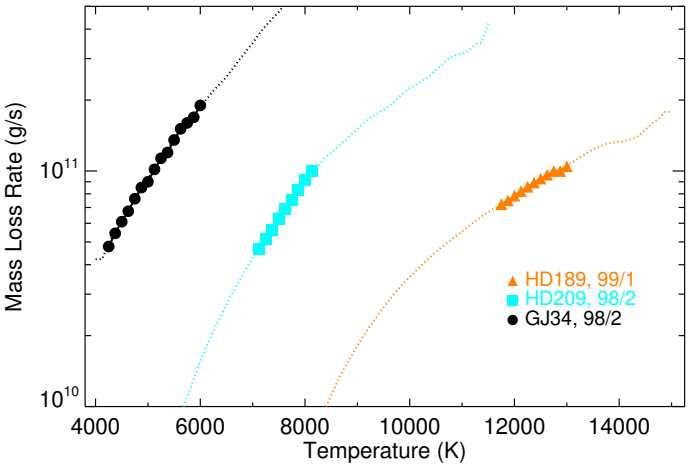

Fig. 1. Ranges of temperature and mass-loss rates for HD 209458 b, HD 189733 b, and GJ 3470 b for H/He ratios of 98/2, 99/1 and 98/2, respectively, derived by Lampón et al. (2020, 2021). Symbols show the derived ranges and dotted lines the extended ranges (see Sec.4.1).

The He(2^3S) production is controlled by the electron concentration via recombination with He^+, and by electron collision excitation of He(1^1S) (see Oklopčić & Hirata 2018; Lampón et al. 2020). As electrons are predominantly produced by photo-ionisation of H and lost by advection and H^+ recombination, the He(2^3S) concentration profile is mainly controlled by the H production and loss rates. Therefore, by constraining the He(2^3S) concentration profile, we simultaneously constrain the production and loss rates of H.

[4] Calar Alto high-Resolution search for M dwarfs with Exoearths with Near-infrared and optical Échelle Spectrographs, at the 3.5 m Calar Alto Telescope.

[5] The direction that connects the star-planet centres. They assumed that substellar conditions are representative of the whole planetary sphere, as we do here.

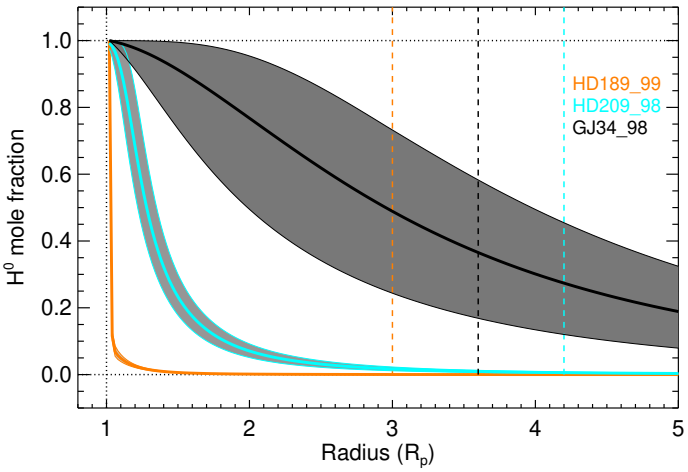

Fig. 2. Neutral H mole fraction profiles resulting from the measured He(2^3S) and Lyα absorption spectra for HD 189733 b, HD 209458 b, and GJ 3470 b with the representative H/He ratios of 99/1, 98/2 and 98/2, respectively. The shade areas correspond to the temperature and mass loss rates ranges (symbols) in Fig. 1. The solid thicker lines are the mean profiles. The vertical dashed lines indicate the mean Roche lobes.

4. Results and discussion

In this section we discuss the hydrodynamic escape regimes on the basis of the H^0 and H^+ distributions and of the heating efficiencies for the three planets.

4.1. Structure, productions and losses of the neutral H

The H^0 mole fractions that result from the derived T–$\dot{M}$ ranges (see symbols in Fig. 1) are shown in Fig. 2. The f_{H^0} profiles for HD 189733 b show a very narrow IF, confined at the lower boundary (set up at 1.02 R_P for the three planets), well below its Roche lobe located at 3.0 R_P. Accordingly, this planet shows a wide fully ionised region. In contrast, GJ 3470 b shows a very extended IF, from about 1.2 R_P to far beyond its Roche lobe at 3.6 R_P. Therefore, no atmospheric region of GJ 3470 b is fully ionised. The H^0 structure of HD 209458 b shows a relatively wide IF, extending from the lower boundary to about 2.3 R_P, which is wider than that of HD 189733 b but narrower than for GJ 3470 b, and below its Roche lobe (at 4.2 R_P). Thus, there is a region almost fully ionised below the Roche lobe, as in HD 189733 b, although narrower.

Figure 3 shows the ratio of recombination to advection terms, P_{rec}/P_{adv}, for the derived T–$\dot{M}$ range of the measured He(2^3S) and Lyα absorption spectra for HD 209458 b, HD 189733 b and GJ 3470 b (see Fig. 1). For the case of HD 189733 b, recombination dominates in practically the whole upper atmosphere. In contrast, the H^0 density is dominated by advection in the whole upper atmosphere of GJ 3470 b. In HD 209458 b, the H^0 density is dominated by advection ($P_{rec}/P_{adv} < 1$) in the lower part of the IF, but by recombination ($P_{rec}/P_{adv} > 1$) in the upper part of the IF and above. That is, neither advection nor recombination rates are negligible in the upper atmosphere of HD 209458 b. Hence, according to the criteria discussed in Sec. 2.1, these results demonstrate that HD 189733 b is in the recombination-limited, GJ 3470 b is in the photon-limited and HD 209458 b is in the energy-limited regime.

We also analysed other plausible T–$\dot{M}$ values beyond the derived interval, hereafter 'extended' T–$\dot{M}$ range (see dotted lines in Fig. 1). These T–$\dot{M}$ values are still compatible with the mea-

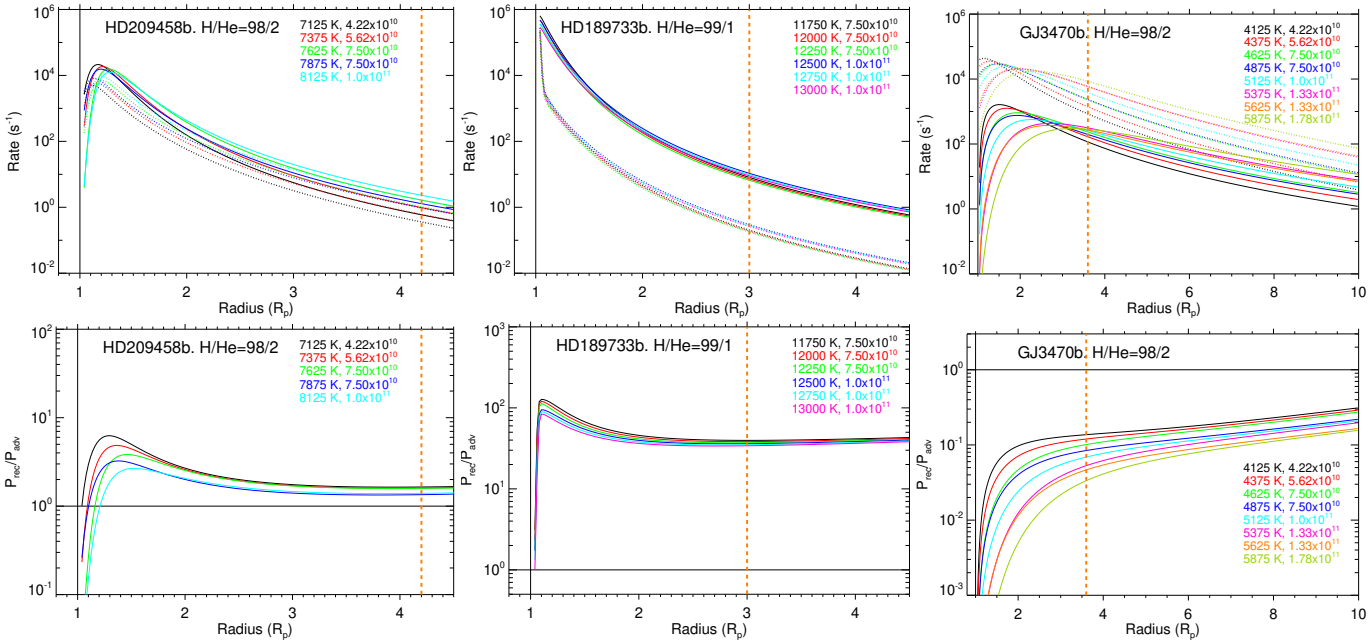

Fig. 3. Upper row: production rates of H by recombination (solid lines) and advection (dashed lines) derived from fit of the measured He(2^3S) absorption spectra (see symbols in Fig. 1) in the atmospheres of HD 209458 b (left), HD 189733 b (middle) and GJ 3470 b (right) and the representative H/He ratios of 98/2, 99/1, and 98/2, respectively. Lower row: ratios of the recombination to the advection. The vertical dashed orange lines indicate the mean Roche lobes. Note the different scales of the x and y axes for the different planets.

sured He(2^3S) and Lyα absorption although less likely, as they yield a higher χ^2. With this, we aim to find out if they would affect the classification with respect to the escape regime. Figs. B.1 and B.3 show the results for the P_{rec}/P_{adv} ratios and the corresponding H^0 mole fractions, respectively. We found that the extended T–$\dot{M}$ ranges for HD 189733 b and GJ 3470 b have the same behaviour to that of the corresponding derived T–$\dot{M}$ ranges (see Fig. 3). In contrast, production terms for HD 209458 b at temperatures below ~ 7000 K (see Fig. B.1) are at the limit between the energy-limited and recombination-limited regimes, as advection becomes less important compared to the recombination. However, when comparing the H density profiles for these conditions with those derived from the Lyα measurements by García-Muñoz (2007), Koskinen et al. (2013) and Salz et al. (2016a), we found that the H^0 density profiles are significantly smaller. We thus conclude that hydrodynamic regimes discussed above for the three planets are not altered when considering the extended T–$\dot{M}$ ranges.

We find that the classification of the escape regimes also remains unchanged in these exoplanets if the commonly used H/He fraction of 90/10 is assumed instead of the ratios derived from He(2^3S) and Lyα transmission spectroscopy (see Figs. B.2 and B.4).

For HD 189733 b, we used an XUV flux that accounts for several small flares to provide an average model of active and non-active periods (see Sect. 3.2 in Lampón et al. 2021). In order to explore the hydrodynamic regime of this planet in quiescent stages, we made a test using the XUV flux from the X-exoplanets model by Sanz-Forcada et al. (2011), which is about a factor 3 smaller than the one used here. We found that the hydrodynamic regime remains recombination-limited despite such a considerably XUV flux decrease.

4.2. Heating efficiencies

To calculate the heating efficiencies of the upper atmospheres of the planets, we follow the method of Salz et al. (2016b). Essentially, we use the relationship between the heating efficiency, η, and the mass-loss rate for the energy-limited approximation, $\dot{M}_{EL}$, (Watson et al. 1981; Erkaev et al. 2007), together with the relationship $\dot{M}/\dot{M}_{EL} = 4/5$ derived by Salz et al. (2016b) to obtain

$$\dot{M} = \frac{4}{5} \frac{4\pi R_p R_{XUV}^2 F_{XUV}}{G K(\xi) M_P} \eta, \quad (3)$$

where M_p and R_P, are the planetary mass and radius respectively, F_{XUV} is the XUV stellar flux at the planetary orbital separation, R_{XUV} is the effective absorption radius, the altitude where the XUV optical depth is unity, and G is the gravitational constant. $K(\xi) = 1–1.5\,\xi + 0.5\,\xi^3$ is the potential energy reduction factor, with $\xi = (M_P/M_\star)^{1/3}\,(a/R_P)$ where a is the planetary orbital separation and $M_\star$ the stellar mass. Therefore, taking the $\dot{M}$ and R_{XUV} obtained from the He(2^3S) measurements and the required system's parameters from Table B.1, we calculated their corresponding η values (see Fig. 4). The $\dot{M}$ values are taken from Fig. 1 (ranges limited by the symbols) and the R_{XUV} values are $\approx$1.02 R_P for HD 189733 b (i.e. the lower boundary), about 1.16–1.30 R_P for HD 209458 b, and about 1.38–2.46 R_P for GJ 3470 b.

As shown by thick lines in Fig. 4, η reaches high values in HD 209458 b and GJ 3470 b, while it remains very low ($\eta < 0.04$) for HD 189733 b. This indicates that HD 189733 b is in the recombination-limited regime, as predicted (e.g., by Salz et al. 2016b).

We note that the derived T–$\dot{M}$ range for HD 209458 b was obtained by limiting the heating efficiency to the range of 0.1–0.2 (Lampón et al. 2020), as shown in Fig. 4. Values of $\eta \leq 0.1$, would indicate a recombination-limited regime (see Sect. 2.2). However, they correspond to temperatures below T $\approx$ 7000 K, which, as discussed in Sec. 4.1, are discarded on the basis of Lyα observations. Thus, we conclude that also from the heating

efficiency argument, HD 209458 b is not in the recombination-limited regime.

Heating efficiency remains almost constant with $\dot{M}$ in GJ 3470 b, in contrast to HD 209458 b. As the upper atmosphere of GJ 3470 b is very extended, an increase of $\dot{M}$ implies higher $R_{\rm XUV}$ (i.e. higher planetary XUV cross section), that prevents η from increasing. The fact that η is nearly constant is equivalent to stating that $\dot{M} \propto R_{\rm XUV}^2$ (see Eq. 3) which, according to Owen & Alvarez (2016), indicates that GJ 3470 b is in the photon-limited regime.

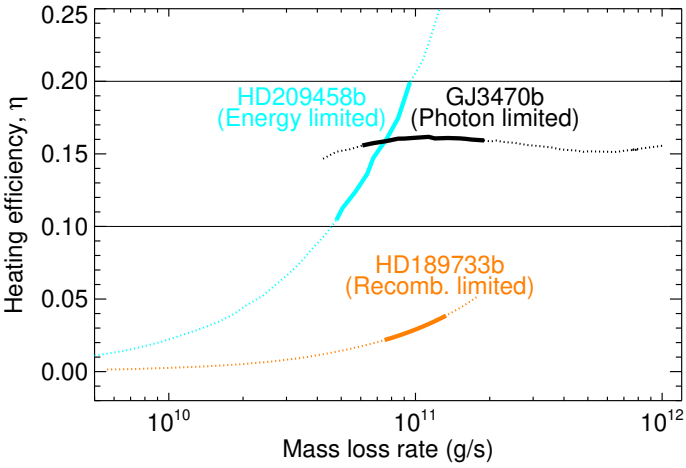

Fig. 4. Heating efficiency, η, versus mass-loss rate for HD 189733 b (orange), HD 209458 b (cyan) and GJ 3470 b (black). H/He ratios of 99/1 for HD 189733 b and of 98/2 for HD 209458 b and GJ 3470 b were used. Dotted lines show the extended T–$\dot{M}$ ranges and thick lines the derived T–$\dot{M}$ ranges (see dotted lines and symbols respectively in Fig. 1).

5. Summary

Several theoretical studies have identified three distinct hydrodynamic atmospheric escape regimes in hydrogen-dominated planetary atmospheres: energy-limited, recombination-limited, and photon-limited. In addition to the importance from the theoretical point of view, the classification of the hydrodynamic escape regimes has important consequences for the estimation of the mass-loss rate by models based on the energy-limited approach. However, no observational evidence of these regimes have been reported to date.

In this work, we studied the upper atmospheric H distribution and the heating efficiencies derived from the analysis of the measured absorption spectrum of the He I triplet lines at 10830 Å and Lyα of HD 189733 b, HD 209458 b, and GJ 3470 b. We used a 1D hydrodynamic model with spherical symmetry coupled with a non local thermodynamic model for the He triplet metastable state concentration profile. We also calculated heating efficiencies following Salz et al. (2016b).

We found that in HD 189733 b the neutral H production is governed by recombination in the whole upper atmosphere, giving rise to a very narrow ionisation front. In contrast, advection dominates the neutral H density in the entire upper atmosphere of GJ 3470 b, leading to a very extended ionisation front. HD 209458 b is an intermediate case between HD 189733 b and GJ 3470 b where the advection and the recombination processes are not negligible which forms a relatively extended ionisation front.

The derived heating efficiencies for HD 209458 b and GJ 3470 b are similar to those expected from the heating by photo-electrons, while those of HD 189733 b are much lower. Therefore, HD 209458 b and GJ 3470 b show little loss by radiative cooling, in contrast to HD 189733 b. Additionally, we found that $\dot{M} \propto R_{\rm XUV}^2$ in GJ 3470 b, which leads to a nearly constant heating efficiency in the range of 0.15–0.17.

Following two different criteria, one based on the productions and losses of the neutral H, and the other based on energy balance considerations, we demonstrate that HD 189733 b is in the recombination-limited regime, GJ 3470 b is in the photon-limited regime, and HD 209458 b is in the energy-limited regime. Thus, we provide observational evidence, based on the He(2^3S) and Lyα measured absorption, of the three hydrodynamic escape regimes theoretically predicted in hydrogen-dominated atmospheres. These exoplanets can be considered as benchmark cases for their respective regimes.

Acknowledgements. CARMENES is an instrument for the Centro Astronómico Hispano-Alemán (CAHA) at Calar Alto (Almería, Spain), operated jointly by the Junta de Andalucía and the Instituto de Astrofísica de Andalucía (CSIC). CARMENES was funded by the Max-Planck-Gesellschaft (MPG), the Consejo Superior de Investigaciones Científicas (CSIC), the Ministerio de Economía y Competitividad (MINECO) and the European Regional Development Fund (ERDF) through projects FICTS-2011-02, ICTS-2017-07-CAHA-4, and CAHA16-CE-3978, and the members of the CARMENES Consortium (Max-Planck-Institut für Astronomie, Instituto de Astrofísica de Andalucía, Landessternwarte Königstuhl, Institut de Ciències de l'Espai, Institut für Astrophysik Göttingen, Universidad Complutense de Madrid, Thüringer Landessternwarte Tautenburg, Instituto de Astrofísica de Canarias, Hamburger Sternwarte, Centro de Astrobiología and Centro Astronómico Hispano-Alemán), with additional contributions by the MINECO, the Deutsche Forschungsgemeinschaft through the Major Research Instrumentation Programme and Research Unit FOR2544 "Blue Planets around Red Stars", the Klaus Tschira Stiftung, the states of Baden-Württemberg and Niedersachsen, and by the Junta de Andalucía. We acknowledge financial support from the Agencia Estatal de Investigación of the Ministerio de Ciencia, Innovación y Universidades and the ERDF through projects ESP2016–76076–R, ESP2017–87143–R, BES–2015–074542, PID2019-110689RB-I00/AEI/10.13039/501100011033, PGC2018-099425–B–I00, PID2019-109522GB-C51/2/3/4, PGC2018-098153-B-C33, AYA2016-79425-C3-1/2/3-P, ESP2016-80435-C2-1-R, and the Centre of Excellence "Severo Ochoa" and "María de Maeztu" awards to the Instituto de Astrofísica de Canarias (SEV-2015-0548), Instituto de Astrofísica de Andalucía (SEV-2017-0709), and Centro de Astrobiología (MDM-2017-0737), and the Generalitat de Catalunya/CERCA programme. T.H. acknowledges support from the European Research Council under the Horizon 2020 Framework Program via the ERC Advanced Grant Origins 832428. A.S.L. acknowledges funding from the European Research Council under the European Union's Horizon 2020 research and innovation program under grant agreement No 694513.

References

Agol, E., Cowan, N. B., Knutson, H. A., et al. 2010, ApJ, 721, 1861
Allart, R., Bourrier, V., Lovis, C., et al. 2018, Science, 362, 1384
Alonso-Floriano, F. J., Snellen, I. A. G., Czesla, S., et al. 2019, A&A, 629, A110
Baluev, R. V., Sokov, E. N., Shaidulin, V. S., et al. 2015, MNRAS, 450, 3101
Baraffe, I., Chabrier, G., Barman, T. S., et al. 2005, A&A, 436, L47
Baraffe, I., Selsis, F., Chabrier, G., et al. 2004, A&A, 419, L13
Bear, E. & Soker, N. 2011, MNRAS, 414, 1788
Ben-Jaffel, L. & Ballester, G. E. 2013, A&A, 553, A52
Bonfils, X., Gillon, M., Udry, S., et al. 2012, A&A, 546, A27
Bourrier, V. & Lecavelier des Etangs, A. 2013, A&A, 557, A124
Bourrier, V., Lecavelier des Etangs, A., Ehrenreich, D., et al. 2018, A&A, 620, A147
de Kok, R. J., Brogi, M., Snellen, I. A. G., et al. 2013, A&A, 554, A82
Eggleton, P. P. 1983, ApJ, 268, 368
Erkaev, N. V., Kulikov, Y. N., Lammer, H., et al. 2007, A&A, 472, 329
García-Muñoz, A. 2007, Planetary and Space Science, 55, 1426
Hu, R., Seager, S., & Yung, Y. L. 2015, ApJ, 807, 8
Koskinen, T., Harris, M., Yelle, R., & Lavvas, P. 2013, Icarus, 226, 1678
Lammer, H., Selsis, F., Ribas, I., et al. 2003, ApJ, 598, L121
Lampón, M., López-Puertas, M., Lara, L. M., et al. 2020, A&A, 636, A13
Lampón, M., López-Puertas, M., Sanz-Forcada, J., et al. 2021 [arXiv:2101.09393]
Lopez, E. D. & Fortney, J. J. 2013, ApJ, 776, 2
Malsky, I. & Rogers, L. A. 2020, ApJ, 896, 48

Muñoz, A. G. & Schneider, P. C. 2019, ApJ, 884, L43
Murray-Clay, R. A., Chiang, E. I., & Murray, N. 2009, ApJ, 693, 23
Nortmann, L., Palle, E., Salz, M., et al. 2018, Science, 362, 1388
Oklopčić, A. & Hirata, C. M. 2018, ApJ, 855, L11
Owen, J. E. & Alvarez, M. A. 2016, ApJ, 816, 34
Owen, J. E. & Wu, Y. 2013, ApJ, 775, 105
Pallé, E., Nortmann, L., Casasayas-Barris, N., et al. 2020, A&A, 638, A61
Quirrenbach, A., Amado, P. J., Caballero, J. A., et al. 2016, in SPIE Proceedings, ed. C. J. Evans, L. Simard, & H. Takami (SPIE), 12–1–14
Quirrenbach, A., Amado, P. J., Ribas, I., et al. 2018, in SPIE Proceedings, ed. H. Takami, C. J. Evans, & L. Simard (SPIE), 32–19
Salz, M., Czesla, S., Schneider, P. C., et al. 2018, A&A, 620, A97
Salz, M., Czesla, S., Schneider, P. C., & Schmitt, J. H. M. M. 2016a, A&A, 586, A75
Salz, M., Schneider, P. C., Czesla, S., & Schmitt, J. H. M. M. 2016b, A&A, 585, L2
Sanz-Forcada, J., Micela, G., Ribas, I., et al. 2011, A&A, 532, A6
Shaikhislamov, I. F., Khodachenko, M. L., Lammer, H., et al. 2020, MNRAS, staa2367
Shematovich, V. I., Ionov, D. E., & Lammer, H. 2014, A&A, 571, A94
Spake, J. J., Sing, D. K., Evans, T. M., et al. 2018, Nature, 557, 68
Tian, F., Toon, O. B., Pavlov, A. A., & De Sterck, H. 2005, ApJ, 621, 1049
Torres, G., Winn, J. N., & Holman, M. J. 2008, ApJ, 677
Vidal-Madjar, A., Désert, J.-M., des Etangs, A. L., et al. 2004, ApJ, 604, 69
Wang, L. & Dai, F. 2018, ApJ, 860, 175
Watson, A. J., Donahue, T. M., & Walker, J. C. 1981, Icarus, 48, 150
Yelle, R. V. 2004, Icarus, 170, 167

Appendix A: The steady-state continuity equation of neutral H

The hydrodynamic continuity equation of mass can be expressed by

$$\dot{M} = 4\,\pi\,r^2\,\rho_{\rm r}\,v_{\rm r}, \tag{A.1}$$

where $\rho_{\rm r} = n_{\rm H}\,m_{\rm H} + n_{\rm He}\,m_{\rm He}$; $n_{\rm H}$ and $n_{\rm He}$ are the number density of H and He; and $m_{\rm H}$ and $m_{\rm He}$ are the atomic mass of H and He, respectively. Assuming that $n_{\rm H}/n_{\rm He}$ (hereafter H/He) is constant with respect to r, then $n_{\rm He} = (H/He)^{-1}\,n_{\rm H}$. Therefore, $\rho_{\rm r} = n_{\rm H}\,x$, where $x = m_{\rm H} + (H/He)^{-1}\,m_{\rm He}$, is constant. Thus, the mass-loss rate can be expressed by

$$\dot{M} = 4\,\pi\,r^2\,n_{\rm H}\,x\,v_{\rm r}. \tag{A.2}$$

The continuity equation of H^0 can be written as

$$\frac{1}{r^2}\frac{\partial(r^2\,n_{\rm H^0}\,v_{\rm r})}{\partial r} = n_{\rm H^+}\,n_{\rm e}\,\alpha_{\rm H} - n_{\rm H^0}\,J_{\rm H}, \tag{A.3}$$

and, deriving,

$$\frac{2\,n_{\rm H^0}\,v_{\rm r}}{r} + v_{\rm r}\,\frac{\partial n_{\rm H^0}}{\partial r} + n_{\rm H^0}\,\frac{\partial v_{\rm r}}{\partial r} = n_{\rm H^+}\,n_{\rm e}\,\alpha_{\rm H} - n_{\rm H^0}\,J_{\rm H}. \tag{A.4}$$

Taking $v_{\rm r} = \dot{M}/(4\,\pi\,r^2\,n_{\rm H}\,x)$ from Eq. A.2, and re-arranging, we have

$$v_{\rm r}\,\frac{1}{n_{\rm H}}\left[n_{\rm H}\,\frac{\partial n_{\rm H^0}}{\partial r} - n_{\rm H^0}\,\frac{\partial n_{\rm H}}{\partial r}\right] = n_{\rm H^+}\,n_{\rm e}\,\alpha_{\rm H} - n_{\rm H^0}\,J_{\rm H}. \tag{A.5}$$

Taking into account that

$$\frac{\partial f_{\rm H^0}}{\partial r} = \frac{\partial\,(n_{\rm H^0}/n_{\rm H})}{\partial r} = \frac{1}{n_{\rm H}^2}\left(n_{\rm H}\,\frac{\partial n_{\rm H^0}}{\partial r} - n_{\rm H^0}\,\frac{\partial n_{\rm H}}{\partial r}\right), \tag{A.6}$$

and including it in Eq. A.5, we obtain

$$v_{\rm r}\,n_{\rm H}\,\frac{\partial f_{\rm H^0}}{\partial r} = n_{\rm H^+}\,n_{\rm e}\,\alpha_{\rm H} - n_{\rm H^0}\,J_{\rm H}. \tag{A.7}$$

Assuming $n_{\rm e} = n_{\rm H^+}$, and re-arranging Eq. A.7, we finally obtain Eq. 1.

Appendix B: Other tables and figures

In Table B.1 we provide the most relevant systems' parameters used in our calculations. In Figures B.1 to B.4 we show ratios of recombination to advection and H^0 mole fraction profiles for the extended T–$\dot{M}$ ranges (dotted lines in Fig. 1), and for H/He composition of 90/10 (see symbols in Fig. 5 in Lampón et al. 2021).

Table B.1. System's parameters.

System	HD 209458	HD 189733	GJ 3470
$M_\star$ ($M_\odot$) [(a)]	$1.119^{+0.033}_{-0.033}$	$0.846^{+0.06}_{-0.049}$	$0.476^{+0.019}_{-0.019}$
a (au) [(b)]	$0.04707^{+0.00046}_{-0.00047}$	$0.0332^{+0.001}_{-0.001}$	$0.0348^{+0.0014}_{-0.0014}$
M_P (M_{Jup}) [(c)]	$0.685^{+0.015}_{-0.014}$	$1.162^{+0.058}_{-0.039}$	$0.036^{+0.002}_{-0.002}$
R_P (R_{Jup}) [(c)]	$1.359^{+0.016}_{-0.019}$	$1.23^{+0.03}_{-0.03}$	$0.360^{+0.01}_{-0.01}$
Φ (Φ_{Jup}) [(d)]	0.504	0.944	0.100
R_{lobe} (R_P) [(e)]	4.2	3.0	3.6
F_{XUV} [(f)]	2.358	56.740	3.928

Notes. [(a)] Stellar masses of HD 209458, HD 189733 and GJ 3470 from Torres et al. (2008), de Kok et al. (2013) and Pallé et al. (2020) respectively. [(b)] Orbital separation from Torres et al. (2008), Agol et al. (2010) and Bonfils et al. (2012). [(c)] Planetary mass and radius of HD 209458 b from Torres et al. (2008); of HD 189733 b from de Kok et al. (2013) and Baluev et al. (2015); and of GJ 3470 b from Pallé et al. (2020). [(d)] Gravitational potential. [(e)] Roche lobe of HD 209458 b, HD 189733 b and GJ 3470 b by Salz et al. (2016a), Eggleton (1983) and Bourrier et al. (2018) respectively. [(f)] XUV flux in units of 10^3 erg cm^{-2} s^{-1} at $\lambda < 912$ Å at planetary separation calculated by Lampón et al. (2020) for HD 209458 b and from Lampón et al. (2021) for HD 189733 b and GJ 3470 b.

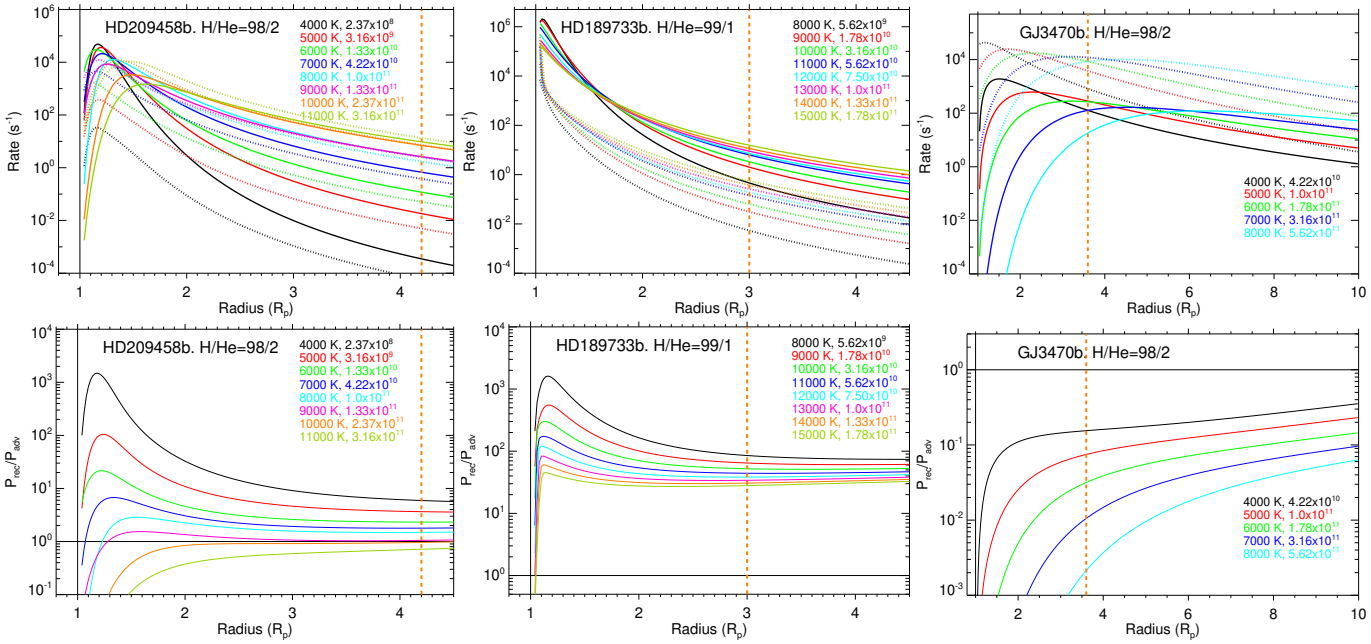

Fig. B.1. As Fig. 3 but for the extended T–$\dot{M}$ ranges (see dotted lines in Fig. 1). Upper row: rates of H by recombination (solid lines) and advection (dotted lines). Lower row: ratios of recombination to advection. The vertical dashed orange lines indicate the mean Roche lobes. Note the different scales of the x and y axes.

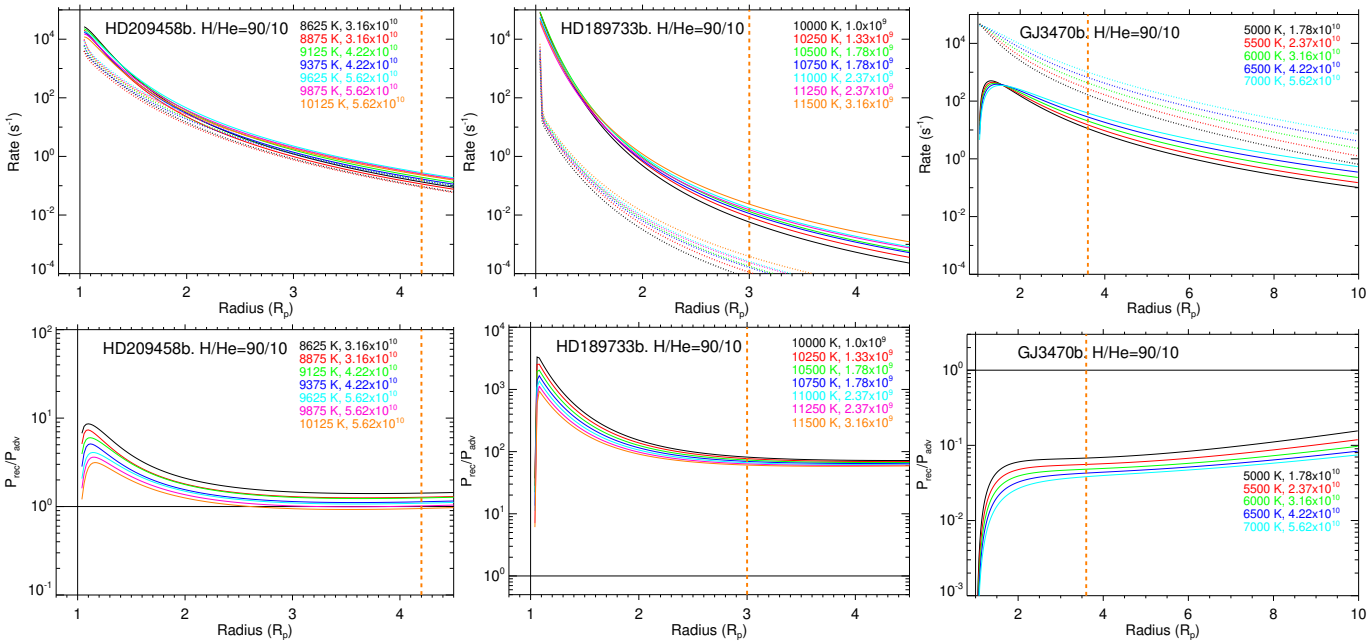

Fig. B.2. As Fig. 3 but for an H/He ratio of 90/10 (see Fig. 5 in Lampón et al. 2021). Upper row: rates of H by recombination (solid lines) and advection (dotted lines). Lower row: ratios of recombination to advection. The vertical dashed orange lines indicate the mean Roche lobes. Note the different scales of the x and y axes.

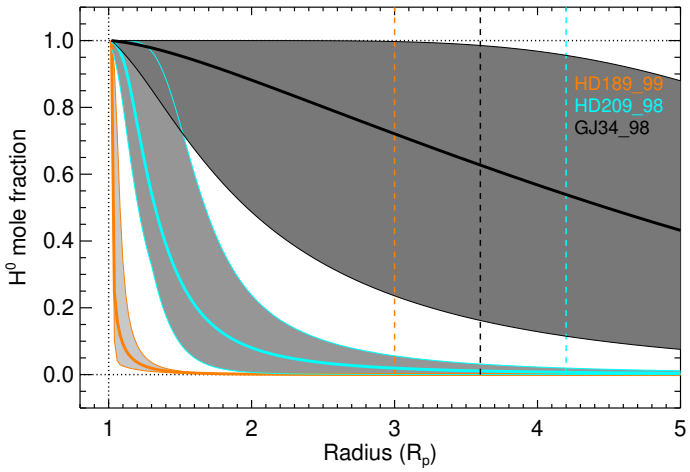

Fig. B.3. As Fig. 2 but for the extended T–$\dot{M}$ ranges (see dotted lines in Fig. 1). The solid thicker lines are the mean profiles. The vertical dashed lines are the mean Roche lobes.

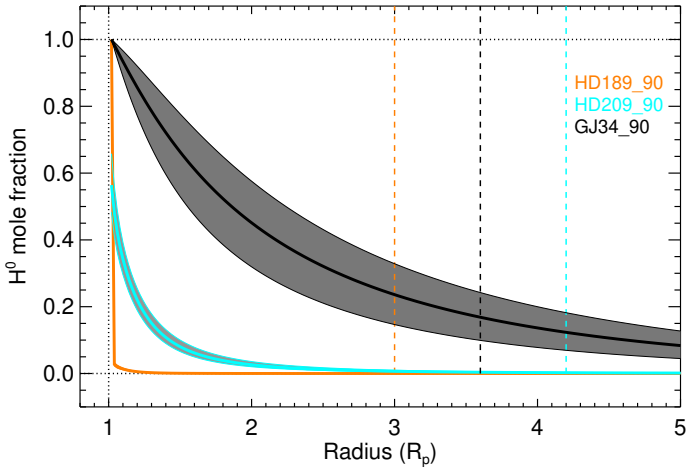

Fig. B.4. As Fig. 2 but for an H/He mole fraction of 90/10 (see Fig. 5 in Lampón et al. 2021). The solid thicker lines are the mean profiles. The vertical dashed lines are the mean Roche lobes.

6 Conclusions

6.1 Summary

The characterisation of exo-atmospheres currently undergoing hydrodynamic escape provides critical information of their nature, hints about their origin and evolution, and also give us key clues to understand the observed planetary population and the formation and evolution of the Solar System. However, only a few observations of the hydrodynamic escape were available until very recently. Consequently, our knowledge of this process is very limited.

The new observations of the He I triplet lines at 10830 Å of highly irradiated planets provide a new means of studying their atmospheric escape allowing to significantly improve the characterisation of the upper atmosphere of exoplanets undergoing hydrodynamic escape. Detailed studies of the absorption line profile are nowadays feasible and the diversity in bulk parameters of exoplanets with the recent available observations of He(2^3S) and Lyα lines, allows us to perform deeper studies and to investigate their hydrodynamic regimes. In this thesis we exploit these new measurements of He(2^3S) in conjunction with previous measurements of the H Lyα line. This constitutes one of the very first (if not the first) dedicated studies of the evaporating atmospheres of gas giants by using the recent He(2^3S) and Lyα absorption measurements.

In this thesis we present observations of the He(2^3S) absorption spectra of the atmosphere of GJ 3470 b with the high-resolution spectrograph CARMENES, obtaining a 1.5 ± 0.3% absorption depth. In our research, within the framework of the CARMENES He I survey, we also observed the He(2^3S) absorption spectra from HD 189733 b, and HD 209458 b (by Salz et al. (2018) and Alonso-Floriano et al. (2019), respectively). However, we have not included these publications as we aim to present a concise work focussed on the physical interpretation of the observations.

We obtain observational constraints on the upper atmospheres of the hot Jupiters HD 209458 b and HD 189733 b, and of the warm Neptune GJ 3470 b, from the analysis of the mid-transit He(2^3S) spectral absorption reported by Alonso-Floriano et al. (2019); Salz et al. (2018) and Pallé et al. (2020), respectively. This sample

of planets are especially interesting because all of them undergo hydrodynamic escape, have very different planetary and stellar bulk parameters, and the absorption measurements of both He(2^3S) and Lyα lines are available.

We modelled the upper atmospheres of these planets using a 1D hydrodynamic model with spherical symmetry, coupled with a non-LTE model for calculating the population of the metastable He(2^3S) state. We assumed that substellar conditions apply to the whole planet. The He(2^3S) concentration profiles were included into a radiative transfer model to calculate He(2^3S) absorption spectra. Our model allows the inclusion of Doppler broadening due to temperature and turbulence, and the broadening induced by the gas radial velocities, non-radial winds (e.g., day-to-night and super-rotation winds) and the rotation of the planet. By comparing the calculated and measured He(2^3S) spectra, we constrained key parameters of the upper atmosphere of these planets as the mass-loss rate, the thermospheric temperature, the He(2^3S) density profile, and the degree of ionisation. We also compared our derived H densities with previous profiles derived from the Lyα absorption and hence we were able to further constrain the H/He ratio.

We find that the upper atmosphere of HD 189733 b is compact and hot, with a maximum temperature of $12\,400^{+400}_{-300}$ K, with a very low mean molecular mass (H/He=(99.2/0.8)$\pm$0.1), with small gas radial velocities, which is almost fully ionised above 1.1 $R_{\rm P}$, and with a mass-loss rate of $1.07^{+0.08}_{-0.09} \times 10^{11}$ g s^{-1}. Regarding production and losses of neutral H, H^0, in the outflow, we find that H^0 density is produced by recombination in the whole upper atmosphere, giving rise to a very narrow ionisation front and a low gas heating efficiency.

In contrast to HD 189733 b, the upper atmosphere of GJ 3470 b is highly extended and relatively cold, with a maximum temperature of 5100$\pm$900 K. Thermosphere of this planet also has a very low mean molecular mass, H/He=$(98.5/1.5)^{+1.0}_{-1.5}$, but large radial outflow velocities, and is not strongly ionised. We highlight that our derived supersonic radial velocities demonstrate that GJ 3470 b undergoes hydrodynamic escape, which is not obvious if the whole parameters space is not fully explored. Despite having a gravitational potential near a factor of 10 lower than HD 189733 b, GJ 3470 b has a comparable mass-loss rate of $(1.87\pm1.13) \times 10^{11}$ g s^{-1}. It is clear that the XUV irradiation of GJ 3470 b, $\sim$14 times smaller than that of HD 189733 b, compensates the gravitational effect. The H^0 density is widely dominated by advection in all the upper atmosphere of GJ 3470 b, leading to a very extended ionisation front and a large gas heating efficiency.

HD 209458 b seems an intermediate case between HD 189733 b and GJ 3470 b, as its upper atmosphere is extended, although not as GJ 3470 b, with an intermediate temperature of 7625$\pm$500 K, a mean molecular weight of $\sim$98/2, with intermediate

gas radial velocities. The mass-loss rate of this planet is also comparable to those of HD 189733 b and GJ 3470 b, with a value of $(0.71 \pm 0.29) \times 10^{11}$ g s^{-1}. Our analysis of this planet provides the first observational derivation of the H/He ratio of an exoplanet and the first hint about the unexpected very low mean molecular weight. Concerning the H^0 productions and losses, both processes, recombination and advection, are not negligible in this planet, which leads to a large gas heating efficiency.

It is remarkable that the three exoplanets with evaporating atmospheres so far studied by using together their He(2^3S) and Lyα observations, (HD 209458 b by Lampón et al. (2020), HD 189733 b by Lampón et al. (2021b) and GJ 3470 b by Lampón et al. (2021b) and Shaikhislamov et al. (2020)), all show higher H/He ratios than the widely assumed solar-like $\sim$90/10, despite of having very different bulk parameters. Hence, our results suggest that the upper atmospheres of giant exoplanets undergoing hydrodynamic escape are very light (H/He $\gtrsim$ 97/3). It is interesting to note that our derived mean molecular weight for GJ 3470 b agrees very well with one estimated by Shaikhislamov et al. (2020). These authors used a 3D hydrodynamic model and, although their parameters space study is not as wide as ours, they reached the same conclusion.

The knowledge of the atmospheric mean molecular mass is key in planetary studies. A very low mean molecular mass in the upper atmosphere agrees with the scenario studied by Hu et al. (2015), who showed that fractionation between He and H is important in short-period exoplanets undergoing hydrodynamic escape. Fractionation can produce a considerable depletion of He in the escaping gas, which could lead to He and metals enrichment (i.e., H depletion) in the lower atmosphere (Hu et al., 2015; Malsky and Rogers, 2020). A significant H depletion in the lower atmosphere could change the abundances of carbon and oxygen-bearing species. Furthermore, it may change the mass-radius relationship of the planet. Besides, our results are also consistent with the depletion of atmospheric He by other processes as the formation of an H–He immiscibility layer in the interior of giant planets, as it produces He sequestration from the upper atmosphere (Salpeter 1973; Stevenson 1975, 1980; Wilson & Militzer 2010). In addition, this result also suggests that the H/He ratio might plays a more important role than expected on the detectability of the He(2^3S), with the subsequent consequences for future observations.

One of the main gaps in the knowledge of the hydrodynamic escape is the lack of confirmation of the three regimes theoretically identified: energy-limited, recombination-limited, and photon-limited. No observational evidence of these regimes has been reported to date. In this thesis we provide observational evidence of the hydrodynamic escape regimes in H/He atmospheres. Investigating the H^0 production and loss processes, and the heating efficiencies of the upper atmospheres from the He(2^3S)

and Lyα observations and our modelling, we have demonstrated that HD 209458 b is in the energy-limited regime, HD 189733 b is in the recombination-limited regime and GJ 3470 b is in the photon-limited regime. Accordingly, we think that these exoplanets can be considered as benchmark cases of their respective regimes for future studies.

6.2 Conclusion remarks

The main goal of this thesis is to contribute to the knowledge in planetary science through the study of the upper atmospheres of giant exoplanets undergoing hydrodynamic atmospheric escape.

The main achievements by this research can be summarised in:

1. We significantly improve the characterisation of the upper atmosphere of the warm Neptune GJ 3470 b and of the hot Jupiters HD 209458 b and HD 189733 b.

2. We demonstrate that GJ 3470 b undergoes hydrodynamic escape.

3. We propose these three exoplanets as benchmark cases for evaporation studies.

4. We provide the first observational derivation of the H/He ratio from an exoplanet.

5. We show the first observational evidence of an escaping outflow with very low mean molecular weight.

6. We suggest there is a very low mean molecular weight tendency in upper atmospheres of H/He planets undergoing hydrodynamic escape. This challenges the current status of outflows with solar-like composition.

7. We provide the first observational evidence of the three different hydrodynamic escape regimes theoretically predicted.

Accordingly, we conclude that this research significantly contributes to the knowledge of the exoplanets of the sample; strengthens hydrodynamic atmospheric escape theory; and provides important hints that could help to understand the current planetary population, the planetary evolution and formation, and the origin of the Solar System.

6.3 Future work

As shown in this thesis, hydrodynamic atmospheric escape plays a primary role in planetary science. However, the knowledge of this process is very limited. To advance our understanding of this process it is crucial to improve the hydrodynamic escape theory; build more comprehensive and computationally efficient hydrodynamic models; and to observe large samples of different classes of planets undergoing hydrodynamic escape.

The success of CARMENES observing high-resolution He(2^3S) absorption spectra point to a fast progress on the characterisation of exoplanets undergoing hydrodynamic escape, as it demonstrates that key observations are feasible from ground based telescopes. Indeed, several other high-resolution spectrographs (e.g. the GIANO-B and the HPF spectrographs) began very recently to observe He(2^3S) in evaporating atmospheres. Furthermore, new space telescopes (e.g. the *James Webb Space Telescope*) will bring the possibility to continue collecting absorption spectra of Lyα and heavy species lines as HST, but in a wider spectral range and higher resolution.

In this thesis we suggest that there is a very low mean molecular weight tendency in the upper atmospheres of H/He planets undergoing hydrodynamic escape, but more observational evidence from a larger sample of exoplanets are needed for confirmation. He(2^3S) and Lyα observations are especially valuable for this end, although Hα observations (in planets highly irradiated by stellar NUV) could be also important for this objective. The CARMENES group is currently undertaking a significant survey of planets with potential He I, and possibly Hα signatures. Such observations, if successful in detecting these features in more exoplanets, will significantly contribute to this end.

Computationally efficient 1D models are key for exploiting observational data and retrieve key information about hydrodynamic escape, as shown in this thesis. Nevertheless, more detailed studies about interactions between host star and planet (e.g., stellar wind, radiation pressure or magnetic field interactions); spatial and velocity distribution of the gas; and the origin of the non-radial winds, require comprehensive multi-fluid magneto-hydrodynamic 3D models. Their main problem is the computational cost, and therefore advances in computational techniques and the increase of processing power will benefit significantly to the field.

In short, because of observations of high-resolution spectra of He(2^3S), Lyα, Hα and heavy species lines became feasible very recently; new instruments with improved sensitivity and large telescopes are expected in the recent future; and computational

power is continuously increasing; detecting and characterising planets undergoing hydrodynamic atmospheric escape promise a significant advance in planetary science in the next years.

Bibliography

Allart, R., V. Bourrier, C. Lovis, et al. (2018). “Spectrally resolved helium absorption from the extended atmosphere of a warm Neptune-mass exoplanet”. In: *Science* 362(6421), pp. 1384–1387 (cit. on p. 17).

Allart, R., V. Bourrier, C. Lovis, et al. (2019). “High-resolution confirmation of an extended helium atmosphere around WASP-107b”. In: *Astronomy & Astrophysics* 623, A58 (cit. on p. 17).

Alonso-Floriano, F. J., I. A. G. Snellen, S. Czesla, et al. (2019). “He I λ 10830 Å in the transmission spectrum of HD209458 b”. In: *Astronomy & Astrophysics* 629, A110 (cit. on pp. 17, 19, 20, 77).

Baraffe, I., Chabrier, G., Barman, T. S., et al. (2005). “Hot-Jupiters and hot-Neptunes: A common origin?” In: *Astronomy & Astrophysics* 436(3), pp. L47–L51 (cit. on p. 11).

Baraffe, I., F. Selsis, G. Chabrier, et al. (2004). “The effect of evaporation on the evolution of close-in giant planets”. In: *Astronomy & Astrophysics* 419(2), pp. L13–L16 (cit. on p. 11).

Bear, E. and N. Soker (2011). “Evaporation of Jupiter-like planets orbiting extreme horizontal branch stars”. In: *Monthly Notices of the Royal Astronomical Society* 414(2), pp. 1788–1792 (cit. on p. 7).

Ben-Jaffel, L. and G. E. Ballester (2013). “HubbleSpace Telescope detection of oxygen in the atmosphere of exoplanet HD 189733 b”. In: *Astronomy & Astrophysics* 553, A52 (cit. on p. 15).

Bourrier, V. and A. Lecavelier des Etangs (2013). “3D model of hydrogen atmospheric escape from HD 209458 b and HD 189733 b: radiative blow-out and stellar wind interactions”. In: *Astronomy & Astrophysics* 557, A124 (cit. on p. 9).

Bourrier, V., A. Lecavelier des Etangs, D. Ehrenreich, Y. A. Tanaka, and A. A. Vidotto (2016). “An evaporating planet in the wind: stellar wind interactions with the radiatively braked exosphere of GJ 436 b”. In: *Astronomy & Astrophysics* 591, A121, A121 (cit. on p. 14).

Bourrier, V., A. Lecavelier des Etangs, D. Ehrenreich, et al. (2018). “Hubble PanCET: an extended upper atmosphere of neutral hydrogen around the warm Neptune GJ 3470b”. In: *Astronomy & Astrophysics* 620, A147, A147 (cit. on p. 14).

Brogi, M. (2018). “Escaping Atmospheres of Extrasolar Planets”. en. In: *Science* 362(6421), pp. 1360–1361 (cit. on p. 18).

Bryson, S., M. Kunimoto, R. K. Kopparapu, et al. (2021). “The Occurrence of Rocky Habitable-zone Planets around Solar-like Stars from Kepler Data”. In: *The Astronomical Journal* 161(1), 36, p. 36 (cit. on p. 2).

Cabot, S. H. C., N. Madhusudhan, L. Welbanks, A. Piette, and S. Gandhi (2020). “Detection of neutral atomic species in the ultra-hot Jupiter WASP-121b”. In: *Monthly Notices of the Royal Astronomical Society* 494(1), pp. 363–377 (cit. on p. 16).

Casasayas-Barris, N., E. Pallé, F. Yan, et al. (2020). “Is There Na I in the Atmosphere of HD 209458b? - Effect of the Centre-to-Limb Variation and Rossiter-McLaughlin Effect in Transmission Spectroscopy Studies”. en. In: *Astronomy & Astrophysics* 635, A206 (cit. on p. 3).

Casasayas-Barris, N., Pallé, E., Yan, F., et al. (2018). “Na I and Horption features in the atmosphere of MASCARA-2b/KELT-20b”. In: *Astronomy & Astrophysics* 616, A151 (cit. on p. 16).

Cassan, A., D. Kubas, J. P. Beaulieu, et al. (2012). “One or more bound planets per Milky Way star from microlensing observations”. In: *Nature* 481(7380), pp. 167–169 (cit. on p. 1).

Catling, D. C., K. J. Zahnle, and C. P. McKay (2001). “Biogenic Methane, Hydrogen Escape, and the Irreversible Oxidation of Early Earth”. In: *Science* 293(5531), pp. 839–843 (cit. on p. 13).

Chamberlain, J. W. (1963). “Planetary coronae and atmospheric evaporation”. In: *Planetary and Space Science* 11(8), pp. 901 –960 (cit. on p. 5).

Charbonneau, D., T. M. Brown, D. W. Latham, and M. Mayor (2000). “Detection of Planetary Transits Across a Sun-like Star”. In: *The Astrophysical Journal* 529(1), pp. L45–L48 (cit. on p. 2).

Charbonneau, D., T. M. Brown, R. W. Noyes, and R. L. Gilliland (2002). “Detection of an Extrasolar Planet Atmosphere.” In: *The Astrophysical Journal* 568(1), p. 377 (cit. on p. 3).

Chen, G., Casasayas-Barris, N., Pallé, E., et al. (2020). “Detection of Na, K, and Horption in the atmosphere of WASP-52b using ESPRESSO”. In: *Astronomy & Astrophysics* 635, A171 (cit. on p. 16).

Ehrenreich, D., V. Bourrier, P. J. Wheatley, et al. (2015). “A giant comet-like cloud of hydrogen escaping the warm Neptune-mass exoplanet GJ 436b”. In: *Nature* 522(7557), pp. 459–461 (cit. on pp. 14, 15).

Ehrenreich, D., A. Lecavelier des Etangs, G. Hébrard, et al. (2008). “New observations of the extended hydrogen exosphere of the extrasolar planet HD 209458b”. In: *Astronomy & Astrophysics* 483(3), pp. 933–937 (cit. on p. 14).

Fressin, F., G. Torres, D. Charbonneau, et al. (2013). “The false positive rate of Kepler and the occurrence of planets”. In: *The Astrophysical Journal* 766(2), p. 81 (cit. on pp. 1, 2).

García Muñoz, A. (2007). “Physical and chemical aeronomy of HD 209458b”. In: *Planetary and Space Science* 55(10), pp. 1426 –1455 (cit. on p. 9).

García Muñoz, A. and P. C. Schneider (2019). “Rapid Escape of Ultra-hot Exoplanet Atmospheres Driven by Hydrogen Balmer Absorption”. In: *The Astrophysical Journal* 884(2), p. L43 (cit. on pp. 5, 11, 16).

Gaudi, B. S., J. L. Christiansen, and M. R. Meyer (2020). “The Demographics of Exoplanets”. In: *arXiv e-prints*, arXiv:2011.04703, arXiv:2011.04703 (cit. on pp. 2, 3).

Guilluy, G., Andretta, V., Borsa, F., et al. (2020). “The GAPS programme at TNG - XXII. The GIARPS view of the extended helium atmosphere of HD 189733 b accounting for stellar activity”. In: *Astronomy & Astrophysics* 639, A49 (cit. on p. 17).

Henry, G. W., G. W. Marcy, R. P. Butler, and S. S. Vogt (2000). “A Transiting “51 Peg–like” Planet”. In: *The Astrophysical Journal* 529(1), pp. L41–L44 (cit. on p. 2).

Hsu, D. C., E. B. Ford, and R. Terrien (2020). “Occurrence rates of planets orbiting M Stars: applying ABC to Kepler DR25, Gaia DR2, and 2MASS data”. In: *Monthly Notices of the Royal Astronomical Society* 498(2), pp. 2249–2262 (cit. on p. 2).

Hu, R., S. Seager, and Y. L. Yung (2015). “Helium atmospheres on warm neptune- and sub-neptune-sized exoplanets and applications to GJ 436b”. In: *The Astrophysical Journal* 807(1), p. 8 (cit. on pp. 13, 79).

Hunten, D. M., R. O. Pepin, and J. C.G. Walker (1987). “Mass fractionation in hydrodynamic escape”. In: *Icarus* 69(3), pp. 532 –549 (cit. on p. 13).

Indriolo, N., L. M. Hobbs, K. H. Hinkle, and Benjamin J. McCall (2009). “Interestellar metastable helium absorption as a probe of the cosmic-ray ionization rate”. In: *The Astrophysical Journal* 703(2), pp. 2131–2137 (cit. on p. 16).

Jackson, A. P., T. A. Davis, and P. J. Wheatley (2012). “The coronal X-ray–age relation and its implications for the evaporation of exoplanets”. In: *Monthly Notices of the Royal Astronomical Society* 422(3), pp. 2024–2043 (cit. on p. 11).

Jeans, J. H. (1905). “The Dynamical Theory of Gases”. In: *Nature* 71(1852), p. 607 (cit. on p. 5).

Jensen, A. G., P. W. Cauley, S. Redfield, W. D. Cochran, and M. Endl (2018). “Hydrogen and Sodium Absorption in the Optical Transmission Spectrum of WASP-12b”. In: *The Astronomical Journal* 156(4), p. 154 (cit. on p. 16).

Jensen, A.G., Redfield, S., Endl, M., et al. (2012). “A detection of H alpha in an exoplanetary atmosphere”. In: *The Astrophysical Journal* 751(2), p. 86 (cit. on p. 16).

Johnson, R. E., M. R. Combi, J. L. Fox, et al. (2009). “Exospheres and Atmospheric Escape”. In: *Comparative Aeronomy*. Vol. 29, p. 355 (cit. on pp. 5, 6, 9).

Koskinen, T.T., M.J. Harris, R.V. Yelle, and P. Lavvas (2013). “The escape of heavy atoms from the ionosphere of HD209458b. I. A photochemical–dynamical model of the thermosphere”. In: *Icarus* 226(2), pp. 1678 –1694 (cit. on p. 7).

Kulow, J. R., K. France, J. Linsky, and R. O. Parke Loyd (2014). “Lyα transit spectroscopy and the neutral hydrogen tail of the hot Neptune GJ 436 b”. In: *The Astrophysical Journal* 786(2), p. 132 (cit. on p. 15).

Kurbatov, E. P. and D. V. Bisikalo (2021). “The role of atmospheric outflows in the migration of hot Jupiters”. In: *arXiv:2101.04112* (cit. on p. 12).

Kurbatov, E. P., D. V. Bisikalo, and I. F. Shaikhislamov (2020). “Migration of Hot Jupiters Induced by Atmosphere Outflow”. In: *Astronomy Reports* 64(12), pp. 1016–1025 (cit. on p. 12).

Lammer, H., M. Leitzinger, M. Scherf, et al. (2020a). “Constraining the early evolution of Venus and Earth through atmospheric Ar, Ne isotope and bulk K/U ratios”. In: *Icarus* 339, 113551, p. 113551 (cit. on p. 13).

Lammer, H., M. Scherf, H. Kurokawa, et al. (2020b). “Loss and fractionation of Noble Gas Isotopes and Moderately Volatile Elements from Planetary Embryos and Early Venus, Earth and Mars”. In: *Space Science Reviews* 216(4), 74, p. 74 (cit. on p. 13).

Lammer, H., F. Selsis, I. Ribas, et al. (2003). “Atmospheric Loss of Exoplanets Resulting from Stellar X-Ray and Extreme-Ultraviolet Heating”. In: *The Astrophysical Journal* 598(2), pp. L121–L124 (cit. on p. 9).

Lampón, M., López-Puertas, M., Czesla, S., et al. (2021a). “Observational evidence of hydrodynamic escape regimes in planetary H/He atmospheres”. In: *Astronomy & Astrophysics*, "submitted" (cit. on pp. 7, 19, 20, 67).

Lampón, M., López-Puertas, M., Lara, L. M., et al. (2020). “Modelling the He triplet absorption at 10 830 the atmosphere of HD 209458 b”. In: *Astronomy & Astrophysics* 636, "A13" (cit. on pp. 19, 20, 79).

Lampón, M., López-Puertas, M., Sanz-Forcada, J., et al. (2021b). “Modelling the He I triplet absorption at 10 830 Åthe atmospheres of HD 189733 b and GJ3470 b”. In: *Astronomy & Astrophysics*, "In press", DOI 10.1051/0004–6361/202039417 (cit. on pp. 19, 20, 79).

Lavie, B., D. Ehrenreich, V. Bourrier, et al. (2017). “The long egress of GJ 436b’s giant exosphere”. In: *Astronomy & Astrophysics* 605, p. L7 (cit. on p. 15).

Lecavelier des Etangs, A., D. Ehrenreich, A. Vidal-Madjar, et al. (2010). “Evaporation of the planet HD 189733 b observed in H I Lyman-α”. In: *Astronomy & Astrophysics* 514, A72 (cit. on p. 14).

Lopez, E. D. and J. J. Fortney (2013). “The role of core mass in controling evaporation: the Kepler radius distribution and the Keppler-36 density dichotomy”. In: *The Astrophysical Journal* 776(1), p. 2 (cit. on p. 12).

Madhusudhan, N. (2019). “Exoplanetary Atmospheres: Key Insights, Challenges, and Prospects”. In: *Annual Review of Astronomy and Astrophysics* 57(1), pp. 617–663 (cit. on p. 3).

Malsky, I. and L. A. Rogers (2020). “Coupled Thermal and Compositional Evolution of Photoevaporating Planet Envelopes”. In: *The Astrophysical Journal* 896(1), p. 48 (cit. on pp. 13, 79).

Mansfield, M., J. L. Bean, A. Oklopčić, et al. (2018). “Detection of Helium in the Atmosphere of the Exo-Neptune HAT-P-11b”. In: *The Astrophysical Journal* 868(2), p. L34 (cit. on p. 17).

Mayor, M. and D. Queloz (1995). “A Jupiter-mass companion to a solar-type star”. In: *Nature* 378(6555), pp. 355–359 (cit. on p. 1).

Mazeh, T., T. Holczer, and S. Faigler (2016). “Dearth of short-period Neptunian exoplanets: A desert in period-mass and period-radius planes”. In: *Astronomy & Astrophysics* 589, A75, A75 (cit. on p. 12).

Murray-Clay, R. A., E. I. Chiang, and N. Murray (2009). “Atmospheric escape from hot Jupiters”. In: *The Astrophysical Journal* 693(1), pp. 23–42 (cit. on pp. 6, 7, 9, 10).

Ninan, J. P., G. Stefansson, S. Mahadevan, et al. (2020). “Evidence for He I 10830 Å Absorption during the Transit of a Warm Neptune around the M-dwarf GJ 3470 with the Habitable-zone Planet Finder”. In: *The Astrophysical Journal* 894(2), p. 97 (cit. on p. 17).

Nortmann, L., E. Palle, M. Salz, et al. (2018). “Ground-based detection of an extended helium atmosphere in the Saturn-mass exoplanet WASP-69b”. In: *Science* 362(6421), p. 1388 (cit. on pp. 17–19).

Oklopčić, A. and C. M. Hirata (2018). “A New Window into Escaping Exoplanet Atmospheres: 10830 Å Line of Helium”. In: *The Astrophysical Journal* 855(1), p. L11 (cit. on p. 17).

Öpik, E. J. and S. F. Singer (1961). “Distribution of Density in a Planetary Exosphere. II”. In: *Physics of Fluids* 4, pp. 221–233 (cit. on p. 5).

Owen, J. E. (2019). “Atmospheric Escape and the Evolution of Close-In Exoplanets”. In: *Annual Review of Earth and Planetary Sciences* 47(1), pp. 67–90 (cit. on pp. 11, 12, 14, 15).

Owen, J. E. and M. A. Alvarez (2016). “UV driven evaporation of close-in planets: energy-limited, recombination-limited, and photon-limited flows”. In: *The Astrophysical Journal* 816(1), p. 34 (cit. on pp. 6, 7, 9).

Owen, J. E. and D. Lai (2018). “Photoevaporation and high-eccentricity migration created the sub-Jovian desert”. In: *Monthly Notices of the Royal Astronomical Society* 479(4), pp. 5012–5021 (cit. on p. 12).

Owen, J. E., I. F. Shaikhislamov, H. Lammer, L. Fossati, and M. L. Khodachenko (2020). “Hydrogen Dominated Atmospheres on Terrestrial Mass Planets: Evidence, Origin and Evolution”. In: *Space Science Reviews* 216(8), 129, p. 129 (cit. on pp. 3, 10).

Owen, J. E. and Y. Wu (2013). “Kepler planets: a tale of evaporation”. In: *The Astrophysical Journal* 775(2), p. 105 (cit. on pp. 11, 12).

Pallé, E., Nortmann, L., Casasayas-Barris, N., et al. (2020). “A He I upper atmosphere around the warm Neptune GJ 3470 b”. In: *Astronomy & Astrophysics* 638, A61 (cit. on pp. 17, 19, 20, 77).

Parke Loyd, R. O., T. T. Koskinen, K. France, C. Schneider, and S. Redfield (2017). “Ultraviolet C ii and Si iii Transit Spectroscopy and Modeling of the Evaporating Atmosphere of GJ436b”. In: *The Astrophysical Journal* 834(2), p. L17 (cit. on p. 10).

Pierrehumbert, R. T. (2010). *Principles of Planetary Climate*. Cambridge University Press (cit. on p. 4).

Poppenhaeger, K., J. H. M. M. Schmitt, and S. J. Wolk (2013). “Transit Observations of the Hot Jupiter HD 189733b at X-Ray Wavelengths”. In: *The Astrophysical Journal* 773(1), 62, p. 62 (cit. on p. 16).

Quirrenbach, A, P J Amado, J A Caballero, et al. (2016). “CARMENES: an overview six months after first light”. In: *SPIE Proceedings*. Ed. by Christopher J Evans, Luc Simard, and Hideki Takami. SPIE, pp. 12–1–14 (cit. on p. 16).

Quirrenbach, A., P. J. Amado, I. Ribas, et al. (2018). “CARMENES: high-resolution spectra and precise radial velocities in the red and infrared”. In: *SPIE Proceedings*. Ed. by Hideki Takami, Christopher J Evans, and Luc Simard. SPIE, pp. 32–19 (cit. on p. 16).

Rogers, L. A. and S. Seager (2010). “A framework for quantifying the degeneracies of exoplanet interior compositions”. In: *The Astrophysical Journal* 712(2), pp. 974–991 (cit. on p. 13).

Salz, M., S. Czesla, P. C. Schneider, and J. H. M. M. Schmitt (2016). “Simulating the escaping atmospheres of hot gas planets in the solar neighborhood”. In: *Astronomy & Astrophysics* 586, A75 (cit. on pp. 9, 10).

Salz, M, S Czesla, P C Schneider, et al. (2018). “Detection of He I λ10830 Å absorption on HD 189733 b with CARMENES high-resolution transmission spectroscopy”. In: *Astronomy & Astrophysics* 620, A97–13 (cit. on pp. 17, 19, 20, 77).

Salz, M., P. C. Schneider, S. Czesla, and J. H. M. M. Schmitt (2015). “Energy-limited escape revised”. In: *Astronomy & Astrophysics* 585, p. L2 (cit. on p. 7).

Schneider, J., Dedieu, C., Le Sidaner, P., Savalle, R., and Zolotukhin, I. (2011). “Defining and cataloging exoplanets: the exoplanet.eu database”. In: *Astronomy & Astrophysics* 532, A79 (cit. on p. 1).

Seager, S. and D. Deming (2010). “Exoplanet Atmospheres”. In: *Annual Review of Astronomy and Astrophysics* 48(1), pp. 631–672 (cit. on p. 4).

Seager, S. and D. D. Sasselov (2000). “Theoretical Transmission Spectra during Extrasolar Giant Planet Transits”. In: *The Astrophysical Journal* 537(2), pp. 916–921 (cit. on p. 16).

Shaikhislamov, I. F., M. L. Khodachenko, H. Lammer, et al. (2020). “Global 3D hydrodynamic modeling of absorption in Lyα and He 10830 A lines at transits of GJ3470b”. In: *Monthly Notices of the Royal Astronomical Society*. staa2367 (cit. on pp. 9, 10, 79).

Shematovich, V. I., D. E. Ionov, and H. Lammer (2014). “Heating efficiency in hydrogen-dominated upper atmospheres”. In: *Astronomy & Astrophysics* 571, A94 (cit. on p. 7).

Spake, J. J., D. K. Sing, T. M. Evans, et al. (2018). “Helium in the eroding atmosphere of an exoplanet”. In: *Nature* 557(7703), pp. 68–70 (cit. on pp. 16, 17).

Stone, J. M. and D. Proga (2009). “Anisotropic winds from close-in estrasolar planets”. In: *The Astrophysical Journal* 694(1), pp. 205–213 (cit. on p. 10).

Szabó, Gy. M. and L. L. Kiss (2011). “A short period censor of sub-Jupiter mass exoplanets with low density”. In: *The Astrophysical Journal* 727(2), p. L44 (cit. on p. 12).

Tian, F. (2015). “Atmospheric Escape from Solar System Terrestrial Planets and Exoplanets”. In: *Annual Review of Earth and Planetary Sciences* 43(1), pp. 459–476 (cit. on p. 6).

Tian, F., O. B. Toon, A. A. Pavlov, and H. De Sterck (2005). “Transonic Hydrodynamic Escape of Hydrogen from Extrasolar Planetary Atmospheres”. In: *The Astrophysical Journal* 621(2), pp. 1049–1060 (cit. on p. 9).

Tripathi, A., K. M. Kratter, R. A. Murray-Clay, and M. R. Krumholz (2015). “Simulated photoevaporative mass loss from hot Jupiters in 3D”. In: *The Astrophysical Journal* 808(2), p. 173 (cit. on pp. 9, 10).

Vidal-Madjar, A., J.-M. Désert, A. Lecavelier des Etangs, et al. (2004). “Detection of Oxygen and Carbon in the Hydrodynamically Escaping Atmosphere of the Extrasolar Planet HD 209458b”. In: *The Astrophysical Journal* 604, p. 69 (cit. on p. 15).

Vidal-Madjar, A., A. Lecavelier des Etangs, J.-M. Désert, et al. (2003). “An extended upper atmosphere around the extrasolar planet HD209458b”. In: *Nature* 422(6928), pp. 143–146 (cit. on p. 14).

Volkov, A. N. (2016). “On the hydrodynamic model of thermal escape from planetary atmospheres and its comparison with kinetic simulations”. In: *Monthly Notices of the Royal Astronomical Society* 459(2), pp. 2030–2053 (cit. on pp. 5, 6, 9).

Wang, L. and F. Dai (2018). “Evaporation of Low-mass Planet Atmospheres: Multidimensional Hydrodynamics with Consistent Thermochemistry”. In: *The Astrophysical Journal* 860(2), p. 175 (cit. on p. 7).

Watson, A. J., T. M. Donahue, and J. C.G. Walker (1981). “The dynamics of a rapidly escaping atmosphere: Applications to the evolution of Earth and Venus”. In: *Icarus* 48(2), pp. 150–166 (cit. on pp. 9, 13).

Wolszczan, A. and D. A. Frail (1992). “A planetary system around the millisecond pulsar PSR1257 + 12”. In: *Nature* 355(6356), pp. 145–147 (cit. on p. 1).

Wright, J. T., G. W. Marcy, A. W. Howard, et al. (2012). “The frequency of hot Jupiters orbiting nearby solar-type stars”. In: *The Astrophysical Journal* 753(2), p. 160 (cit. on p. 2).

Wyttenbach, A., Mollière, P., Ehrenreich, D., et al. (2020). “Mass-loss rate and local thermodynamic state of the KELT-9 b thermosphere from the hydrogen Balmer series”. In: *Astronomy & Astrophysics* 638, A87 (cit. on p. 16).

Yan, F. and Th. Henning (2018). “An extended hydrogen envelope of the extremely hot giant exoplanet KELT-9b”. In: *Nature Astronomy* 2(9), pp. 714–718 (cit. on p. 16).

Yan, F., Wyttenbach, A., Casasayas-Barris, N., et al. (2021). “Detection of the hydrogen Balmer lines in the ultra-hot Jupiter WASP-33b”. In: *Astronomy & Astrophysics* 645, A22 (cit. on p. 16).

Yelle, R. V. (2004). “Aeronomy of extra-solar giant planets at small orbital distances”. In: *Icarus* 170(1), pp. 167 –179 (cit. on p. 9).

Zahnle, K. J. and J. F. Kasting (1986). “Mass fractionation during transonic escape and implications for loss of water from Mars and Venus”. In: *Icarus* 68(3), pp. 462 –480 (cit. on p. 13).

Zhang, X. (2020). “Atmospheric regimes and trends on exoplanets and brown dwarfs”. In: *Astronomy & Astrophysics* 20(7), p. 099 (cit. on pp. 5, 6).

Zhou, G., C. X. Huang, G. Á. Bakos, et al. (2019). “Two New HATNet Hot Jupiters around A Stars and the First Glimpse at the Occurrence Rate of Hot Jupiters from TESS”. In: *The Astronomical Journal* 158(4), 141, p. 141 (cit. on p. 2).

List of publications

First author refereed articles

1. **Modelling the He I triplet absorption at 10830 Å in the atmosphere of HD 209458 b**
   M. Lampón, M. López-Puertas, L. M. Lara, A. Sánchez-López, M. Salz, S. Czesla, J. Sanz- Forcada, K. Molaverdikhani, F. J. Alonso-Floriano, L. Nortmann, J. A. Caballero, F. F. Bauer, E. Pallé, D. Montes, A. Quirrenbach, E. Nagel, I. Ribas, A. Reiners, P. J. Amado.
   Astronomy and Astrophysics, 636, A13 (2020).

2. **Modelling the He I triplet absorption at 10830 Å in the atmospheres of HD 189733 b and GJ 3470 b**
   M. Lampón, M. López-Puertas, J. Sanz-Forcada, A. Sánchez-López, K. Molaverdikhani, S. Czesla, A. Quirrenbach, E. Pallé, J. A. Caballero, Th. Henning, M. Salz, L. Nortmann, J. Aceituno, P. J. Amado, F. F. Bauer, D. Montes, E. Nagel, A. Reiners, and I. Ribas.
   Accepted by the Astronomy and Astrophysics.

3. **Observational evidence of hydrodynamic escape regimes in planetary H/He atmospheres**
   M. Lampón, M. López-Puertas, S. Czesla, A. Sánchez-López, L. M. Lara, M. Salz, J. Sanz-Forcada, K. Molaverdikhani, A. Quirrenbach, E. Pallé, J. A. Caballero, Th. Henning, L. Nortmann, P. J. Amado, A. Reiners, and I. Ribas.
   Submitted at Astronomy and Astrophysics.

Co-author refereed articles

1. **A He I upper atmosphere around the warm Neptune GJ 3470 b**
   E. Palle, L. Nortmann, N. Casasayas-Barris, **M. Lampón**, M. López-Puertas, J. A. Caballero, J. Sanz-Forcada, L. M. Lara, E. Nagel, F. Yan, F. J. Alonso-Floriano, P. J. Amado, G. Chen, C. Cifuentes, M. Cortés-Contreras, S. Czesla, K. Molaverdikhani, D. Montes, V. M. Passegger, A. Quirrenbach, A. Reiners, I. Ribas, A. Sánchez-López, A. Schweitzer, M. Stangret, M. R. Zapatero Osorio, and M. Zechmeister
   Astronomy and Astrophysics, 638, A61 (2020).

2. **Ground-based detection of an extended helium atmosphere in the Saturn-mass exoplanet WASP-69b**
   L. Nortmann, E. Pallé, M. Salz, J. Sanz-Forcada, E. Nagel, F. J. Alonso-Floriano, S. Czesla, F. Yan, G. Chen, I. A. G. Snellen, M. Zechmeister, J.H.M.M. Schmitt, M. López-Puertas, N. Casasayas-Barris, F. F. Bauer, P. J. Amado, J. A. Caballero, S. Dreizler, Th. Henning, **M. Lampón**, D. Montes, K. Molaverdikhani, A. Quirrenbach, A. Reiners, I. Ribas, A. Sánchez-López, P. C. Schneider, M. R. Zapatero Osorio.
   Science, 362, 1388 (2018)

3. **Detection of He I λ 10830 Å absorption on HD 189733 b with CARMENES high-resolution transmission spectroscopy**
   M. Salz, S. Czesla, P.C. Schneider, E. Nagel, J.H.M.M. Schmitt, L. Nortmann, F.J. Alonso-Floriano, M. López-Puertas, **M. Lampón**, F.F. Bauer, I.A.G. Snellen, E. Pallé, J.A. Caballero, F. Yan, G. Chen, J. Sanz-Forcada, P.J. Amado, A. Quirrenbach, I. Ribas, A. Reiners, V.J.S. Béjar, N. Casasayas-Barris, M. Cortés-Contreras, S. Dreizler, E.W. Guenther, Th. Henning, S.V. Jeffers, A. Kaminski, M. Kürster, M. Lafarga, L.M. Lara, K. Molaverdikhani, D. Montes, J.C. Morales, A. Sánchez-López, W. Seifert, M.R. Zapatero Osorio, M. Zechmeister Astronomy and Astrophysics, 620, A97 (2018)

4. **Multiple water band detections in the CARMENES near-infrared transmission spectrum of HD 189733 b**
   F.J. Alonso-Floriano, A. Sánchez-López, I.A.G. Snellen, M. López-Puertas, E. Nagel, P.J. Amado, F.F. Bauer, J.A. Caballero, S. Czesla, L. Nortmann, E. Pallé, M. Salz, A. Reiners, I. Ribas, A. Quirrenbach, J. Aceituno, G. Anglada-Escudé, V.J.S. Béjar, E.W. Guenther, Th. Henning, A. Kaminski, M. Kürster, **M. Lampón**, L.M. Lara, D. Montes, J.C. Morales, L. Tal-Or, J.H.M.M. Schmitt, M.R. Zapatero Osorio, M. Zechmeister.
   Astronomy and Astrophysics, 621, A74 (2019)

5. **He I λ 10 830 Å in the transmission spectrum of HD 209458 b**
F.J. Alonso-Floriano, I.A.G. Snellen, S. Czesla, F.F. Bauer, M. Salz, **M. Lampón**, L.M. Lara, E. Nagel, M. López-Puertas, L. Nortmann, A. Sánchez-López, J. Sanz-Forcada, J.A. Caballero, A. Reiners, I. Ribas, A. Quirrenbach, P.J. Amado, J. Aceituno, G. Anglada-Escudé, V.J.S. Béjar, M. Brinkmöller, A.P. Hatzes, Th. Henning, A. Kaminski, M. Kürster, F. Labarga, D. Montes, E. Pallé, J.H.M.M. Schmitt, M.R. Zapatero Osorio.
Astronomy and Astrophysics, 629, A110 (2019)

6. **Water vapor detection in the transmission spectra of HD 209458 b with the CARMENES NIR channel**
A. Sánchez-López, F.J. Alonso-Floriano, M. López-Puertas, I.A.G. Snellen, B. Funke, E. Nagel, F.F. Bauer, P.J. Amado, J.A. Caballero, S. Czesla, L. Nortmann, E. Pallé, M. Salz, A. Reiners, I. Ribas, A. Quirrenbach, G. Anglada-Escudé, V.J.S. Béjar, N. Casasayas-Barris, D. Galadí-Enríquez, E.W. Guenther, Th. Henning, A. Kaminski, M. Kürster, **M. Lampón**, L.M. Lara, D. Montes, J.C. Morales, M. Stangret, L. Tal-Or, J. Sanz-Forcada, J.H.M.M. Schmitt, M.R. Zapatero Osorio, M. Zechmeister. Astronomy and Astrophysics, 630, A53 (2019)

7. **Analysis of the origin of water, carbon monoxide, and carbon dioxide in the Uranus atmosphere**
L.M. Lara, R. Rodrigo, R. Moreno, **M. Lampón**.
Astronomy and Astrophysics, 621, A129 (2019)

8. **A giant exoplanet orbiting a very-low-mass star challenges planet formation models**
J.C. Morales, A.J. Mustill, I. Ribas, M.B. Davies, A. Reiners, F.F. Bauer, D. Kossakowski, E. Herrero, E. Rodríguez, M.J. López-González, C. Rodríguez-López, V.J.S. Béjar, L. González-Cuesta, R. Luque, E. Pallé, M. Perger, D. Baroch, A. Johansen, H. Klahr, C. Mordasini, G. Anglada-Escudé, J.A. Caballero, M. Cortés-Contreras, S. Dreizler, M. Lafarga, E. Nagel, V.M. Passegger, S. Reffert, A. Rosich, A. Schweitzer, L. Tal-Or, T. Trifonov, M. Zechmeister, A. Quirrenbach, P.J. Amado, E.W. Guenther, H.J. Hagen, Th. Henning, S.V. Jeffers, A. Kaminski, M. Kürster, D. Montes, W. Seifert, F.J. Abellán, M. Abril, J. Aceituno, F.J. Aceituno, F.J. Alonso-Floriano, M. Ammler-von Eiff, R. Antona, B. Arroyo-Torres, M. Azzaro, D. Barrado, S. Becerril-Jarque, D. Benítez, Z.M. Berdiñas, G. Bergond, M. Brinkmöller, C. del Burgo, R. Burn, R. Calvo-Ortega, J. Cano, M.C. Cárdenas, C. Cardona Guillén, J. Carro, E. Casal, V. Casanova, N. Casasayas-Barris, P. Chaturvedi, C. Cifuentes, A. Claret, J. Colomé, S. Czesla, E. Díez-Alonso, R. Dorda, A. Emsenhuber, M. Fernández, A. Fernández-Martín, I.M. Ferro, B. Fuhrmeister, D. Galadí-Enríquez, I. Gallardo Cava, M.L. García Vargas, A. Garcia-Piquer, L. Gesa, E. González-Álvarez, J.I. González Hernández, R.

González-Peinado, J. Guàrdia, A. Guijarro, E. de Guindos, A.P. Hatzes, P.H. Hauschildt, R.P. Hedrosa, I. Hermelo, R. Hernández Arabi, F. Hernández Otero, D. Hintz, G. Holgado, A. Huber, P. Huke, E.N. Johnson, E. de Juan, M. Kehr, J. Kemmer, M. Kim, J. Klüter, A. Klutsch, F. Labarga, N. Labiche, S. Lalitha, **M. Lampón**, L.M. Lara, R. Launhardt, F.J. Lázaro, J.L. Lizon, M. Llamas, N. Lodieu, M. López del Fresno, J.F. López Salas, J. López-Santiago, H. Magán Madinabeitia, U. Mall, L. Mancini, H. Mandel, E. Marfil, J.A. Marín Molina, E.L. Martín, P. Martín-Fernández, S. Martín-Ruiz, H. Martínez-Rodríguez, C.J. Marvin, E. Mirabet, A. Moya, V. Naranjo, R.P. Nelson, L. Nortmann, G. Nowak, A. Ofir, J. Pascual, A. Pavlov, S. Pedraz, D. Pérez Medialdea, A. Pérez-Calpena, M.A.C. Perryman, O. Rabaza, A. Ramón Ballesta, R. Rebolo, P. Redondo, H.W. Rix.
Science, 365, 6460 (2019).

9. **The CARMENES search for exoplanets around M dwarfs - Two temperate Earth-mass planet candidates around Teegarden's Star**
M. Zechmeister, S. Dreizler, I. Ribas, A. Reiners, J.A. Caballero, F.F. Bauer, V.J.S. Béjar, L. González-Cuesta, E. Herrero, S. Lalitha, M.J. López-González, R. Luque, J.C. Morales, E. Pallé, E. Rodríguez, C. Rodríguez López, L. Tal-Or, G. Anglada-Escudé, A. Quirrenbach, P.J. Amado, M. Abril, F.J. Aceituno, F.J. Alonso-Floriano, M. Ammler-von Eiff, R. Antona Jiménez, H. Anwand-Heerwart, B. Arroyo-Torres, M. Azzaro, D. Baroch, D. Barrado, S. Becerril, D. Benítez, Z.M. Berdiñas, G. Bergond, P. Bluhm, M. Brinkmöller, C. del Burgo, R. Calvo Ortega, J. Cano, C. Cardona Guillén, J. Carro, M.C. Cárdenas Vázquez, E. Casal, N. Casasayas-Barris, V. Casanova, P. Chaturvedi, C. Cifuentes, A. Claret, J. Colomé, M. Cortés-Contreras, S. Czesla, E. Díez-Alonso, R. Dorda, M. Fernández, A. Fernández-Martín, B. Fuhrmeister, A. Fukui, D. Galadí-Enríquez, I. Gallardo Cava, J. Garcia de la Fuente, A. Garcia-Piquer, M.L. García Vargas, L. Gesa, J. Góngora Rueda, E. González-Álvarez, J.I. González Hernández, R. González-Peinado, U. Grözinger, J. Guàrdia, A. Guijarro, E. de Guindos, A.P. Hatzes, P.H. Hauschildt, R.P. Hedrosa, J. Helmling, Th. Henning, I. Hermelo, R. Hernández Arabi, L. Hernández Castaño, F. Hernández Otero, D. Hintz, P. Huke, A. Huber, S.V. Jeffers, E.N. Johnson, E. de Juan, A. Kaminski, J. Kemmer, M. Kim, H. Klahr, R. Klein, J. Klüter, A. Klutsch, D. Kossakowski, M. Kürster, F. Labarga, M. Lafarga, M. Llamas, **M. Lampón**, L.M. Lara, R. Launhardt, F.J. Lázaro, N. Lodieu, M. López del Fresno, M. López-Puertas, J.F. López Salas, J. López-Santiago, H. Magán Madinabeitia, U. Mall, L. Mancini, H. Mandel, E. Marfil, J.A. Marín Molina, D. Maroto Fernández, E.L. Martín, P. Martín-Fernández, S. Martín-Ruiz, C.J. Marvin, E. Mirabet, P. Montañés-Rodríguez, D. Montes, M.E. Moreno-Raya, E. Nagel, V. Naranjo, N. Narita, L. Nortmann, G. Nowak, A. Ofir, M. Oshagh, J. Panduro, H. Parviainen, J. Pascual, V.M. Passegger, A. Pavlov, S. Pedraz, A. Pérez-Calpena, D. Pérez Medialdea, M.

Perger, M.A.C. Perryman, O. Rabaza, A. Ramón Ballesta, R. Rebolo, P. Redondo, S. Reffert, S. Reinhardt, P. Rhode, H.W. Rix, F. Rodler, A. Rodríguez Trinidad. Astronomy and Astrophysics, 627, A49 (2019).

10. **The CARMENES search for exoplanets around M dwarfs-HD 147379 b: A nearby Neptune in the temperate zone of an early-M dwarf**
A. Reiners, I. Ribas, M. Zechmeister, J.A. Caballero, T. Trifonov, S. Dreizler, J.C. Morales, L. Tal-Or, M. Lafarga, A. Quirrenbach, P.J. Amado, A. Kaminski, S.V. Jeffers, J. Aceituno, V.J.S. Béjar, J. Guàrdia, E.W. Guenther, H.J. Hagen, D. Montes, V.M. Passegger, W. Seifert, A. Schweitzer, M. Cortés-Contreras, M. Abril, F.J. Alonso-Floriano, M. Ammler-von Eiff, R. Antona, G. Anglada-Escudé, H. Anwand-Heerwart, B. Arroyo-Torres, M. Azzaro, D. Baroch, D. Barrado, F.F. Bauer, S. Becerril, D. Benítez, Z.M. Berdiñas, G. Bergond, M. Blümcke, M. Brinkmöller, C. del Burgo, J. Cano, M.C. Cárdenas Vázquez, E. Casal, C. Cifuentes, A. Claret, J. Colomé, S. Czesla, E. Díez-Alonso, C. Feiz, M. Fernández, I.M. Ferro, B. Fuhrmeister, D. Galadí-Enríquez, A. Garcia-Piquer, M.L. García Vargas, L. Gesa, V. Gómez Galera, J.I. González Hernández, R. González-Peinado, U. Grözinger, S. Grohnert, A. Guijarro, E. de Guindos, J. Gutiérrez-Soto, A.P. Hatzes, P.H. Hauschildt, R.P. Hedrosa, J. Helmling, Th. Henning, I. Hermelo, R. Hernández Arabí, L. Hernández Castaño, F. Hernández Hernando, E. Herrero, A. Huber, P. Huke, E.N. Johnson, E. de Juan, M. Kim, R. Klein, J. Klüter, A. Klutsch, M. Kürster, F. Labarga, A. Lamert, **M. Lampón**, L.M. Lara, W. Laun, U. Lemke, R. Lenzen, R. Launhardt, M. López del Fresno, M.J. López-González, M. López-Puertas, J.F. López Salas, J. López-Santiago, R. Luque, H. Magán Madinabeitia, U. Mall, L. Mancini, H. Mandel, E. Marfil, J.A. Marín Molina, D. Maroto Fernández, E.L. Martín, S. Martín-Ruiz, C.J. Marvin, R.J. Mathar, E. Mirabet, M.E. Moreno-Raya, A. Moya, R. Mundt, E. Nagel, V. Naranjo, L. Nortmann, G. Nowak, A. Ofir, R. Oreiro, E. Pallé, J. Panduro, J. Pascual, A. Pavlov, S. Pedraz, A. Pérez-Calpena, D. Pérez Medialdea, M. Perger, M.A.C. Perryman, M. Pluto, O. Rabaza, A. Ramón, R. Rebolo, P. Redondo, S. Reffert, S. Reinhart, P. Rhode, H.W. Rix, F. Rodler, E. Rodríguez, C. Rodríguez-López, A. Rodríguez Trinidad, R.R. Rohloff, A. Rosich, S. Sadegi, E. Sánchez-Blanco, M.A. Sánchez Carrasco, A. Sánchez-López, J. Sanz-Forcada, P. Sarkis, L.F. Sarmiento
Astronomy and Astrophysics, 609, L5 (2018).

11. **The CARMENES search for exoplanets around M dwarfs-First visual-channel radial-velocity measurements and orbital parameter updates of seven M-dwarf planetary systems**
T. Trifonov, M. Kürster, M. Zechmeister, L. Tal-Or, J.A. Caballero, A. Quirrenbach, P.J. Amado, I. Ribas, A. Reiners, S. Reffert, S. Dreizler, A.P. Hatzes, A. Kaminski, R. Launhardt, Th. Henning, D. Montes, V.J.S. Béjar, R. Mundt, A.

Pavlov, J.H.M.M. Schmitt, W. Seifert, J.C. Morales, G. Nowak, S.V. Jeffers, C. Rodríguez-López, C. del Burgo, G. Anglada-Escudé, J. López-Santiago, R.J. Mathar, M. Ammler-von Eiff, E.W. Guenther, D. Barrado, J.I. González Hernández, L. Mancini, J. Stürmer, M. Abril, J. Aceituno, F.J. Alonso-Floriano, R. Antona, H. Anwand-Heerwart, B. Arroyo-Torres, M. Azzaro, D. Baroch, F.F. Bauer, S. Becerril, D. Benítez, Z.M. Berdiñas, G. Bergond, M. Blümcke, M. Brinkmöller, J. Cano, M.C. Cárdenas Vázquez, E. Casal, C. Cifuentes, A. Claret, J. Colomé, M. Cortés-Contreras, S. Czesla, E. Díez-Alonso, C. Feiz, M. Fernández, I.M. Ferro, B. Fuhrmeister, D. Galadí-Enríquez, A. Garcia-Piquer, M.L. García Vargas, L. Gesa, V. Gómez Galera, R. González-Peinado, U. Grözinger, S. Grohnert, J. Guàrdia, A. Guijarro, E. de Guindos, J. Gutiérrez-Soto, H.J. Hagen, P.H. Hauschildt, R.P. Hedrosa, J. Helmling, I. Hermelo, R. Hernández Arabí, L. Hernández Castaño, F. Hernández Hernando, E. Herrero, A. Huber, P. Huke, E. Johnson, E. de Juan, M. Kim, R. Klein, J. Klüter, A. Klutsch, M. Lafarga, **M. Lampón**, L.M. Lara, W. Laun, U. Lemke, R. Lenzen, M. López del Fresno, M.J. López-González, M. López-Puertas, J.F. López Salas, R. Luque, H. Magán Madinabeitia, U. Mall, H. Mandel, E. Marfil, J.A. Marín Molina, D. Maroto Fernández, E.L. Martín, S. Martín-Ruiz, C.J. Marvin, E. Mirabet, A. Moya, M.E. Moreno-Raya, E. Nagel, V. Naranjo, L. Nortmann, A. Ofir, R. Oreiro, E. Pallé, J. Panduro, J. Pascual, V.M. Passegger, S. Pedraz, A. Pérez-Calpena, D. Pérez Medialdea, M. Perger, M.A.C. Perryman, M. Pluto, O. Rabaza, A. Ramón, R. Rebolo, P. Redondo, S. Reinhardt, P. Rhode, H.W. Rix, F. Rodler, E. Rodríguez, A. Rodríguez Trinidad, R.R. Rohloff, A. Rosich, S. Sadegi, E. Sánchez-Blanco, M.A. Sánchez Carrasco, A. Sánchez-López, J. Sanz-Forcada, P. Sarkis, L.F. Sarmiento, S. Schäfer
Astronomy and Astrophysics, 609, A117 (2018).

12. **The CARMENES search for exoplanets around M dwarfs-High-resolution optical and near-infrared spectroscopy of 324 survey stars**
A. Reiners, M. Zechmeister, J.A. Caballero, I. Ribas, J.C. Morales, S.V. Jeffers, P. Schöfer, L. Tal-Or, A. Quirrenbach, P.J. Amado, A. Kaminski, W. Seifert, M. Abril, J. Aceituno, F.J. Alonso-Floriano, M. Ammler-von Eiff, R. Antona, G. Anglada-Escudé, H. Anwand-Heerwart, B. Arroyo-Torres, M. Azzaro, D. Baroch, D. Barrado, F.F. Bauer, S. Becerril, V.J.S. Béjar, D. Benítez, Z.M. Berdiñas, G.Bergond, M. Blümcke, M. Brinkmöller, C. del Burgo, J. Cano, M.C. Cárdenas Vázquez, E. Casal, C. Cifuentes, A. Claret, J. Colomé, M. Cortés-Contreras, S. Czesla, E. Díez-Alonso, S. Dreizler, C. Feiz, M. Fernández, I.M. Ferro, B. Fuhrmeister, D. Galadí-Enríquez, A. Garcia-Piquer, M.L. García Vargas, L. Gesa, V. Gómez Galera, J.I. González Hernández, R. González-Peinado, U. Grözinger, S. Grohnert, J. Guàrdia, E.W. Guenther, A. Guijarro, E. de Guindos, J. Gutiérrez-Soto, H.J. Hagen, A.P. Hatzes, P.H. Hauschildt, R.P. Hedrosa, J. Helmling, Th. Henning, I. Hermelo, R. Hernández Arabí, L. Hernández Castaño, F. Hernández

Hernando, E. Herrero, A. Huber, P. Huke, E.N. Johnson, E. de Juan, M. Kim, R. Klein, J. Klüter, A. Klutsch, M. Kürster, M. Lafarga, A. Lamert, **M. Lampón**, L.M. Lara, W. Laun, U. Lemke, R. Lenzen, R. Launhardt, M. López del Fresno, J. López-González, M. López-Puertas, J.F. López Salas, J. López-Santiago, R. Luque, H. Magán Madinabeitia, U. Mall, L. Mancini, H. Mandel, E. Marfil, J.A. Marín Molina, D. Maroto Fernández, E.L. Martín, S. Martín-Ruiz, C.J. Marvin, R.J. Mathar, E. Mirabet, D. Montes, M.E. Moreno-Raya, A. Moya, R. Mundt, E. Nagel, V. Naranjo, L. Nortmann, G. Nowak, A. Ofir, R. Oreiro, E. Pallé, J. Panduro, J. Pascual, V.M. Passegger, A. Pavlov, S. Pedraz, A. Pérez-Calpena, D. Pérez Medialdea, M. Perger, M.A.C. Perryman, M. Pluto, O. Rabaza, A. Ramón, R. Rebolo, P. Redondo, S. Reffert, S. Reinhart, P. Rhode, H.W. Rix, F. Rodler, E. Rodríguez, C. Rodríguez-López, A. Rodríguez Trinidad, R.R. Rohloff, A. Rosich, S. Sadegi, E. Sánchez-Blanco, M.A. Sánchez Carrasco, A. Sánchez-López, J. Sanz-Forcada, P. Sarkis, L.F. Sarmiento, S. Schäfer, J.H.M.M. Schmitt.
Astronomy and Astrophysics, 612, A49 (2018).